

Controlled Motion of Polymeric Microparticles at Interfaces and in Solution

Alireza Sadeghi



University of Sheffield
Faculty of Engineering
Department of Chemical and Biological Engineering

Thesis submitted to the University of Sheffield for the Degree
of Doctor in Philosophy

May 2014

Declaration

The work described in this thesis was undertaken at the University of Sheffield between June 2010 and June 2013, under the supervision of Dr Jonathan Howse. Unless otherwise stated, it is the work of the author and has not been submitted in whole or in any part for any other degree at this or any other institute.

Alireza Sadeghi

Department of Chemical and Biological Engineering

University of Sheffield

Sheffield

May 2014

Publications and Presentations

Autonomous Navigation Strategies for Responsive Size Changing Catalytic Swimmers

S. J. Ebbens, G. A. Buxton, A. Alexeev, A. Sadeghi, J. R. Howse
RSC Soft Matter, **2012**, **8**, 3077-3082

Goldlocks Swimmers: Designing Optimum Devices for Drug Delivery and Microfluidic Transport

S. J. Ebbens, J. R. Howse, R. Golestanian, G. A. Buxton, A. Sadeghi
Materials Research Society, Spring Meeting Proceedings 2012, San Francisco, USA.

Surface Interactions for Controlling the Microfluidic Separation of Polymeric Microspheres

A. Sadeghi, J. R. Howse, S. J. Ebbens
Materials Research Society, Spring Meeting Proceedings 2011, San Francisco, USA.
MRSS11-1357-LL06-08.R1

Designing Magnetically Controllable Phoretic Swimmers

A. Sadeghi, J. R. Howse, S. J. Ebbens
Oral Presentation at Materials Research Society's Spring Meeting 2012
San Francisco, USA.

Controlled motion of propulsive and non-propulsive microparticles on the surface and in the bulk

A. Sadeghi, J. R. Howse, S. J. Ebbens
Oral Presentation at the Royal Society of Chemistry's Macro Group - Young Researchers' Meeting 2012
Cambridge, UK.

Autonomous micromixers: spiralling nanoswimmers as a route to achieve enhanced diffusion in low Reynolds Number Environments

A. Sadeghi, S. J. Ebbens, R. Golestanian, J. R. Howse
In preparation

3D Ferromagnetic Colloidal Self-Diffusiophoretic Nanoswimmers

A. Sadeghi, S. J. Ebbens, M. T. Bryan, P. D. Topham, G. Dunderdale, J. R. Howse,
In preparation

Abstract

The research scope of this thesis is the study and the characterisation of the motion of polymeric non-propulsive and propulsive microparticles on the surface and in the bulk. Characterising the motion of these particles as well as investigating different methods to control their motion and to perform useful tasks (e.g. in vivo drug delivery, cargo transport in microfluidic systems and device assembly) has provoked great interest among scientists in recent years. Since the introduction of catalytic nanorods and colloidal nanoswimmers, many attempts have been made to transform the random motion of these particles (due to Brownian phenomena) into a controlled motion, towards a desired location. The work described here is divided into three main categories: Regulating the speed and direction of the particles by modifying the substrate they move upon, steering the particles to a target using gradients of fields such as magnetic, electric, concentration, etc. and controlling the inherent propulsion direction of the particles by fabricating swimmers that are capable of producing a range of trajectories from rotation to linear translation. These methods involve controlling the speed of rolling particles by altering their affinity to the substrate, exploiting the trajectories of pH-responsive particles to produce statistical accumulation within a gradient, directing propulsive magnetic particles via an external uniform magnetic field, utilising the motion of spiralling swimmers to achieve mixing at the microscale and adjusting the area-to-volume ratio of catalytic swimmers to optimise their propulsion speed which is a function of reaction rate on their surface. In addition, the characteristics of these techniques such as their reproducibility, accuracy, autonomy and complexity are also discussed.

Acknowledgements

First and foremost I offer my sincerest gratitude to Dr Jonathan Howse, who supported me throughout my studies with patience and knowledge. I attribute the level of my PhD degree to his encouragement and effort and without him this thesis, too, would not have been completed or written. One simply could not wish for a better or friendlier supervisor.

My special thanks go to Dr Stephen Ebbens for his help and guidance from the beginning of my research to its end. I would also like to extend my appreciations to the Department of Chemical and Biological Engineering's technical staff, namely Mr Keith Penny, Mr Andy Patrick and Mr Mark McIntosh for their help and support.

I gratefully acknowledge the funding received towards my PhD from the University of Sheffield's Faculty of Engineering Prize Scholarship.

I have to thank my parents for their love and support throughout my life. Thank you both for giving me the strength to follow my dreams. My younger sister who was my first best friend deserves my wholehearted thanks as well.

And last but not least, a special thanks to my dearest friends in Sheffield who made life in the Steel City an amazing experience for me.

List of abbreviations and symbols

ACCN	- 1,1'-Azobis cyclohexane-1-carbonitrile
AFM	- atomic force microscopy
APS	- ammonium persulfate
BA	- N,N'-methylenebisacrylamide
D	- diffusion coefficient
DAR	- diazos resin
dex	- dextran
DMAEMA	- dimethyl aminoethyl methacrylate
DNA	- deoxyribonucleic acid
DVB-80	- divinylbenzene-80
HEMA	- hydroxyethyl methacrylate
k	- Boltzmann constant
KPS	- potassium persulfate
LbL	- Layer-by-Layer
MAA	- methacrylic acid
MUA	- mercaptoundecanoic acid
PEG	- poly(ethylene glycol)
PMAA	- poly(methacrylic acid)
PS	- poly(styrene)
PSS	- poly(styrene sulfonate)
R	- radius
Re	- Reynolds number
SAM	- self-assembled monolayer
T	- absolute temperature
TEM	- transmission electron microscopy
TEMED	- N,N,N',N'-tetramethylethylenediamine
UV	- ultra violet
η	- viscosity
ϵ_a	- adhesive strength

Contents

Chapter 1: The motion of particles in fluids at the micro- and nanoscale	1
1.1 Brownian motion	2
1.2 One- and two-dimensional random walks	3
1.3 Propulsive motion	14
1.4 Analysing propulsive and non-propulsive motion	20
1.5 Propulsive nanomotors: fabrication, motion mechanism and applications	24
1.5.1 Remotely powered nanomotors	28
1.5.2 Synthetic catalytic particles	29
1.6 Strategies for controlling the motion of colloidal microparticles	33
Chapter 2: Synthetic running and tumbling: an autonomous navigation strategy for controlling pH-responsive catalytic microswimmers	40
2.1 Synthesis of pH responsive polymers	41
2.2 Preparation of poly(methacrylic acid) microparticles	43
2.2.1 Inverse suspension polymerisation	45
2.2.2 Precipitation polymerisation	46
2.3 Particle size measurement	48
2.4 Reversibility of the pH response	51
2.5 Particle size measurement over a pH gradient	52
2.6 Preparation of pH responsive microswimmers	55
2.6.1 Desalination of the particles via dialysis	55
2.6.2 Platinum deposition on emulsion products	56
2.6.3 Platinum deposition on precipitation products	57
2.6.4 Fabricating PS-PMAA nanodimer swimmers	58
2.6.5 Growing PMAA around platinum coated PS spheres	59
2.7 Computational modelling	60
Chapter 3: 3D ferromagnetic colloidal self-diffusiophoretic nanoswimmers	70
3.1 Introduction and Background	71
3.2 Orientation control using external field	74
3.2.1 Magnetic polymer beads: synthesis and applications	74

3.2.1.1 Polymer core–magnetic shell beads	75
3.2.1.2 Magnetic core–polymer shell beads	76
3.2.1.3 Magnetic beads with homogeneously dispersed magnetic particles	77
3.2.2 Preparation of magnetic catalytic swimmers	78
3.3 Helmholtz coils: producing a region of nearly uniform magnetic field	79
3.4 Characterising the motion microparticles in the bulk	84
3.5 Analysing the 1D data	87
3.6 Customized trapping of magnetic microswimmers: a new route for autonomous steering of propulsive particles	107
3.7 Magnetic micro-coils: fabrication and properties	108
3.7.1 Fabrication method of magnetic microcoils	109
3.8 Realisation of magnetic microtracks	112
3.9 Preparation of magnetic microtracks	113
3.9.1 Printed Circuit Boards (PCBs)	113
3.9.2 TEM grids	114
3.9.3 Chrome mask	115
Chapter 4: Catalytic Micromixers	121
4.1 Mixing in microfluidics	122
4.2 Catalytic micromixers	125
4.3 Experimental	126
4.3.1 Preparation of spiralling catalytic microswimmers	126
4.3.2 Particle mixing experiment	126
4.4 Result and discussion	128
4.5 Summary	130
Chapter 5: High surface area structures - a route for increasing the number of reaction sites in catalytic swimmers	133
5.1 Fabrication methods of colloidal cluster	134
5.2 Catalyst deposition via redox reactions	139
5.3 Experimental	140
5.3.1 Preparation of polystyrene spheres	140
5.3.2 Preparation of colloidal clusters	142
5.3.2.1 SDS, water, toluene (Oil-in-Water emulsion)	142

5.3.2.2 Fabrication of colloidal aggregates via partial melting	146
5.3.2.3 Fusing 6 μm PS particles to platinum coated colloids	150
5.3.3 Electroless platinum plating of colloidal particles	152
Chapter 6: Controlling the separation of polymeric microspheres via surface interactions in microfluidic devices	156
6.1 Particle-substrate interactions	156
6.2 Computational Simulations	159
6.3 Self-assembled monolayers (SAMs): structure, preparation and patterning	164
6.4 Preparation of alkanethiol SAMs	165
6.5 Patterning alkanethiol SAMs	168
6.5.1 Patterning self-assembled monolayers using soft lithography	170
6.5.2 Patterning SAMs with energetic beams	172
6.6 Polymeric microcapsules	173
6.7 Experimental	175
6.7.1 Microfluidic flow cell design and substrate patterning using SAMs	175
6.7.2 Dex-HEMA polymeric Microcapsules	176
6.8 Particle rolling experiments and results	178
Chapter 7: Conclusions & Future work	185
7.1 Conclusions	185
7.2 Future work	186
7.2.1 Chapter 2: fabricating pH-responsive catalytic devices	186
7.2.2 Chapter 3: fabrication and navigation of magnetic catalytic swimmers	186
7.2.3 Chapter 4: Mixing efficiency of spiralling catalytic swimmers	187
7.2.4 Chapter 5: Utilising high surface area porous polymeric particles in fabricating catalytic swimmers	187
7.2.5 Chapter 6: Separation of polymeric microspheres via surface interactions	188
Appendices	189
A. CCD Camera	189
B. UV spectroscopy: decomposition reaction of H_2O_2 in presence of Ni and Pt	190
C. Particle sizing: DLS and laser diffraction technique	191
D. Fluorescence microscopy	192

Chapter 1: The motion of particles in fluids at the micro- and nanoscale

This chapter provides a brief overview to motion at small length scales where viscous forces are dominant and inertia does not play a significant role. It begins by discussing 1D and 2D random walks from a mathematical viewpoint, followed by giving physical examples of a random walk such as diffusion and Brownian motion in microparticles and further discusses how the motion of living microorganisms is directly related to these phenomena. After explaining how rotational and translational diffusion affect a particle's motion in short and long timescales, the concepts of ballistic steps and propulsion are introduced and presented through simplified models which relate back to simple random walks.

Subsequent to the discussion on random walk and its related terms, the differences between the motion of micro- and macroscale objects are explained by introducing the Reynolds number and how parameters such as viscosity and density can influence this motion. After describing the mechanism that biological microorganism employ to compensate for the effects of their dimension on their motion so as to achieve propulsion in a low Reynolds numbers environment, a brief review is provided on the propulsion mechanism of various types of artificial microswimmers and their fabrication methods followed by a discussion on how the random propulsive motion of these swimming devices can be converted into a controlled motion capable of getting utilised in tasks such as cargo transport, drug delivery and diagnosis of diseases. These techniques can generally be divided into two main categories: manual control via external fields and autonomous control via coupling a navigation or response module to the swimming devices. Comparing the advantages and

disadvantages of each of these techniques and assessing their potential in offering a straightforward and accurate solution for directing microscale objects, provides the fundamental background to the work undertaken and presented in this thesis.

1.1 Brownian motion

Among the transport phenomena that occur in nature, diffusion is distinguished by its unique feature in generating mass transport or mixing, without requiring bulk motion [1]. As a result, studying this phenomenon has been of interest to scientists since the 18th century. In 1765, Jan Ingenhousz made the first known documented observations of fluctuating movements of carbon dust particles in alcohol but it was Robert Brown who developed the theory of Brownian motion in 1827 to explain the random walk of small particles in suspension in a fluid. This theory demonstrated how suspended particles move, as they collide with, then invisible molecules, or atoms surrounding them in the liquid or gas. Since then the concept of diffusion has been widely employed in all fields of science and even economics [2].

Nearly seventy years after the concept of Brownian motion by Robert Brown, Albert Einstein published a paper in 1905 [3] explaining the atomistic backgrounds of diffusion. He showed that a particle at absolute temperature T has, on average, a kinetic energy associated with movement along each axis of $kT/2$, where k is Boltzmann's constant and this is true regardless of the size of the particle. This theory explains that for a particle of mass m and velocity v_x on the x axis has a kinetic energy of $mv_x^2/2$. This quantity fluctuates, but on the average $\langle mv_x^2/2 \rangle = kT/2$, where $\langle \rangle$ denotes an average over time or over an ensemble of similar particles.

From this relationship, mean-square velocity can be calculated,

$$\langle v_x^2 \rangle = kT/m \quad (1)$$

and from this we can derive root-mean-square velocity,

$$\langle v_x^2 \rangle^{1/2} = (kT/m)^{1/2} \quad (2)$$

and this value can be used to estimate the instantaneous velocity of micron sized particles but this estimation is only valid where there are no obstructions on the particles' path. Since motion of particles is often studied while they are suspended inside a fluid, they do not go very far before bumping into molecules of liquid or gas. As a result, particle's orientation changes rapidly as it wanders about in all directions and thus executes a random walk.

1.2 One- and two-dimensional random walks

In order to characterise the diffusion of a particle, it is prudent to begin by considering its motion along one axis only, say the x axis. The particle starts at time $t = 0$ at position $x = 0$ and executes a random walk according to these rules:

1. Each particle steps to the right or to the left once every τ seconds, moving at velocity $\pm v_x$ a distance of $\delta = \pm v_x \tau$. Note, in practice, τ and δ depend on the size of particle, the viscosity of the liquid and the absolute temperature T .
2. The probability of going to the right at each step is equal to the probability of going to the left and by interacting with the molecules of fluid, the particle forgets what it did on the previous leg of its journey. That is, successive steps are statistically independent and the walk is not biased.
3. Each particle moves independently of all other particles. The particles do not interact with one another providing the suspension of particles is reasonably dilute.

These rules have two remarkable outcomes. First, the particles go nowhere on average. Second, as the particles execute n steps in a time $t = n\tau$, n is proportional to t . It follows that the mean-square displacement is proportional to t . Therefore, the root-mean-square displacement is proportional to the square-root of the time and not to the time [4].

To see this more explicitly, it should be noted that as $n = t/\tau$,

$$\langle x^2(t) \rangle = (t/\tau)\delta^2 = (\delta^2/\tau)t \quad (3)$$

For convenience, we define a diffusion coefficient, $D = \delta^2/2\tau$ in units $\text{cm}^2.\text{s}^{-1}$. This gives us

$$\langle x^2(t) \rangle = 2Dt \quad (4)$$

At this time, the migration of particles of a given kind in a given medium at a given temperature can be characterized by the diffusion coefficient, D .

Moreover, by knowing that motions in the x and y directions are statistically independent, it can be concluded that if $\langle x^2 \rangle = 2Dt$ then,

$$\langle y^2 \rangle = 2Dt \quad (5)$$

As a result, in two dimensions, where the square of the distance from the origin to the point (x,y) is $r^2 = x^2 + y^2$,

$$\langle r^2 \rangle = 4Dt \quad (6)$$

Based on the above described concepts, a 10000 step, 2D random walk can be simulated for an imaginary particle undergoing a random walk equivalent to Brownian motion (Figure 1.1). The particle starts at time $t = 0$ at position $(x,y) = (0,0)$ and has a choice of three velocities ($v = -1, 0$ or $+1 \mu\text{m}.\text{s}^{-1}$) along each axis at each time step ($\tau = 1\text{s}$), resulting in steps of $-1, 0$ or $+1$.

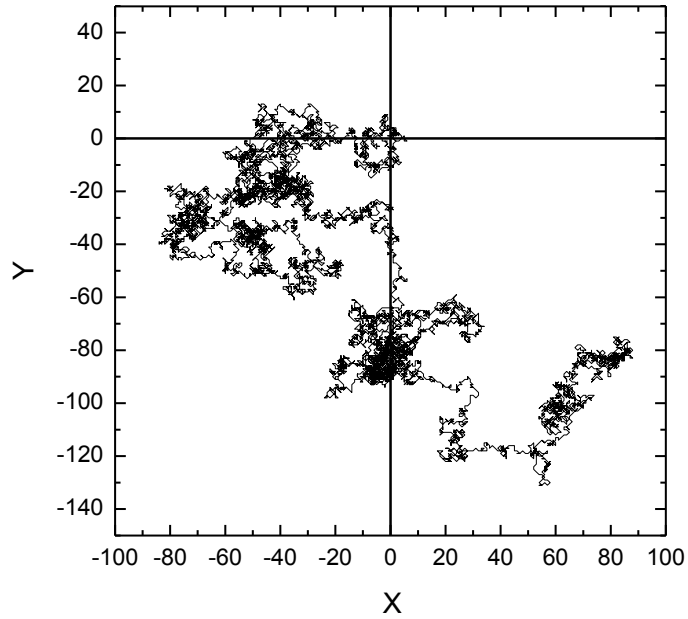


Figure 1.1 – Simulated 10000 step random walk in 2D for an imaginary particle undergoing Brownian motion with a choice of three steps sizes ($v = -1, 0$ or $+1 \mu\text{m} \cdot \text{s}^{-1}$)

To simplify and better understand how the motion of this particle behaves, the first 100 steps of this random walk are shown below in figure 1.2.

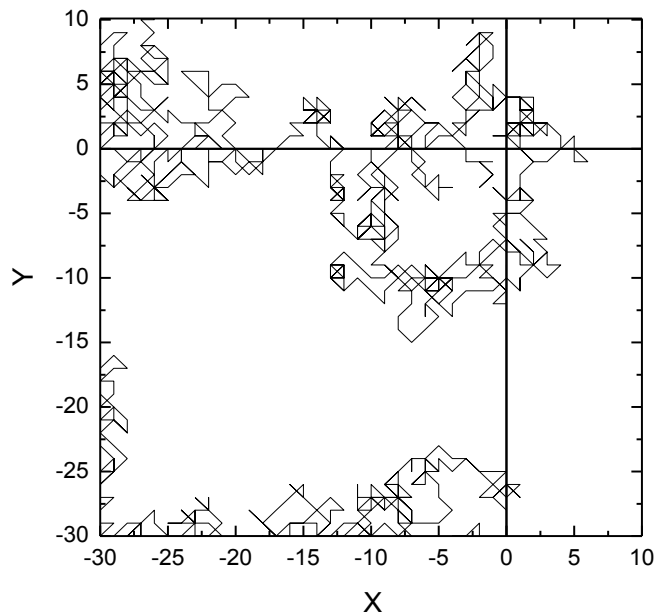


Figure 1.2 – Simulated first 100 step random walk (or the 10,000 random walk) in 2D for an imaginary particle undergoing Brownian motion with a choice of three velocities ($v = -1, 0$ or $+1 \mu\text{m} \cdot \text{s}^{-1}$)

Any two dimensional random walk is essentially the sum of two one dimensional walks in X and Y. As such each of these components can then be plotted against time (step) (Figure 1.3).

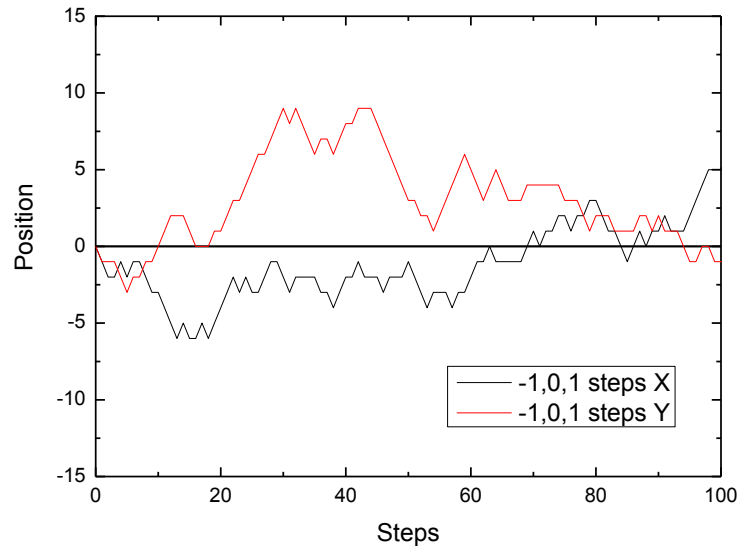


Figure 1.3 - Simulated first 100 step random walk for an imaginary particle undergoing Brownian motion with a choice of three velocities ($v = -1, 0$ or $+1 \mu\text{m. s}^{-1}$), resolved into motion along the x and y axes

Likewise, the full motion of over 10000 steps can also be plotted as shown in Figure 1.4.

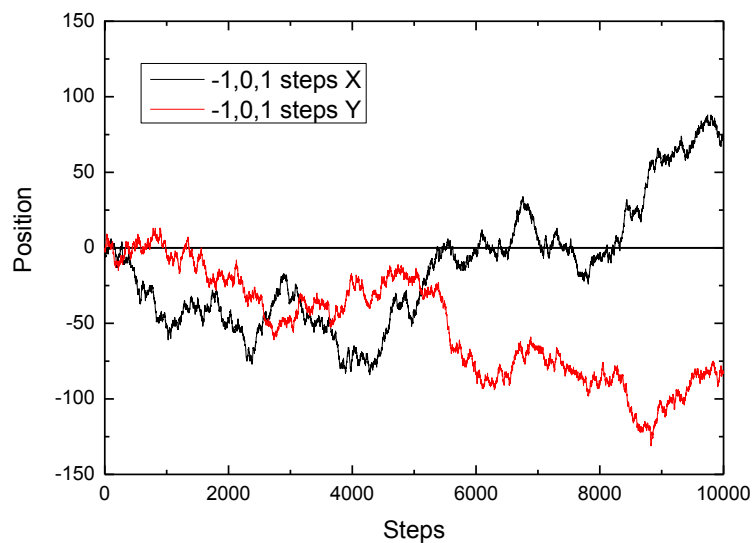


Figure 1.4 - Simulated 10000 step random walk for an imaginary particle undergoing Brownian motion with a choice of three velocities ($v = -1, 0$ or $+1 \mu\text{m. s}^{-1}$), resolved into motion along the x and y axes

In reality, the distance (δ) a particle travels at each time step (τ) is not constant and for a pure Brownian motion, δ and τ depend on the size of particle, the viscosity of the liquid and the thermal energy of the neighbouring molecules. For this motion, the diffusion coefficient is defined as $D = kT / (6\pi\eta R)$ where k is the Boltzmann constant, R is the radius of the particle, T is the absolute temperature and η is the viscosity of the surrounding fluid. Not all collisions with the surrounding fluid result in translational diffusion as some collisions also impart a "spin" to the particles, and the particle also carries out rotational diffusion $D_R = kT / (8\pi\eta R^3)$ which is independent from its translational diffusion (D) and represents the rate at which the orientation of the particle undergoes its random walk in orientation, effectively a random walk in which the steps are $-\theta$, 0 , $+\theta$. The rotational diffusion coefficient D_R is often discussed in terms of Rotational Diffusion Time (τ_R) where $\tau_R = D_R^{-1}$ and represents the time after which a singularly ordered system or ensemble has no relationship to its original orientation. A slightly more realistic random walk can be simulated by changing the velocity of the particle at each time step from three choices ($v = -1, 0$ and $+1 \mu\text{m. s}^{-1}$) to the more realistic value of ($-1 < v < 1 \mu\text{m. s}^{-1}$). With this assumption, the xy graphs of a 10000 step and a 100 step 2D random walk will be similar to Figures 1.5 and 1.6. The data for both sets (quantized steps and random steps) are based on the same data set, with difference resulting from round issues. For example, a step of 0.6 in the random step data set results in a step size of +1. As a result, the trajectories, and macroscopic motion are similar by differ in magnitude to these roundings.

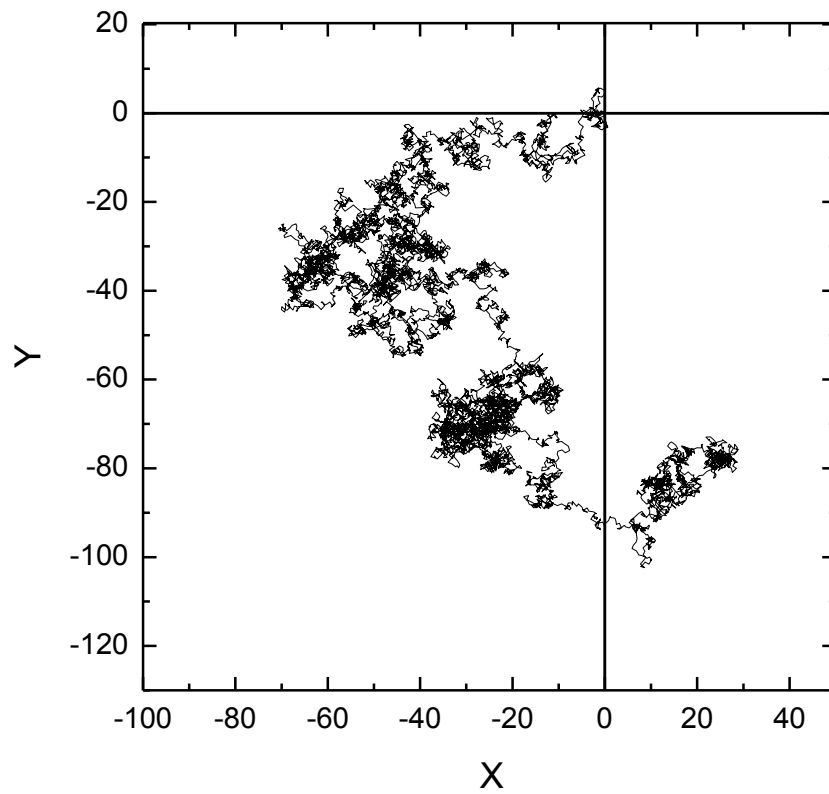


Figure 1.5 – Simulated 10000 step random walk in 2D for an imaginary particle undergoing Brownian motion with velocities at each time step between -1 and +1 ($-1 < v < 1 \mu\text{m. s}^{-1}$)

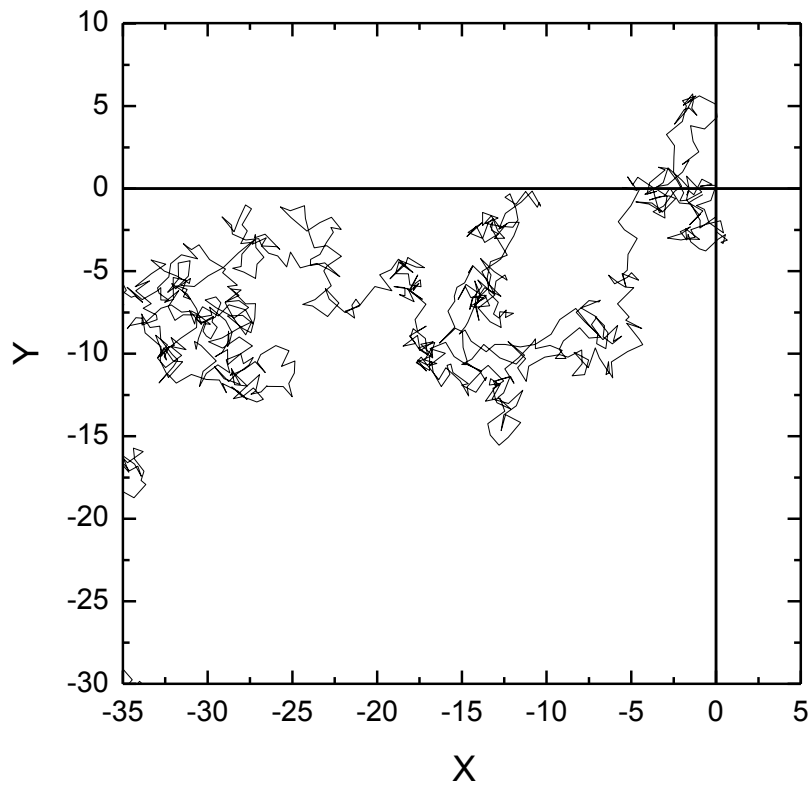


Figure 1.6 – Simulated 100 step random walk in 2D for an imaginary particle undergoing Brownian motion with velocities at each time step between -1 and +1 ($-1 < v < 1 \mu\text{m. s}^{-1}$)

Similar to the simplified random walk ($v = -1, 0$ and $+1 \mu\text{m. s}^{-1}$), these 10000 step and 100 step 2D random walks can also be resolved into two components (Figures 1.7 and 1.8), motion along the x axis and motion along the y axis and each of these components can then be plotted against time (step).

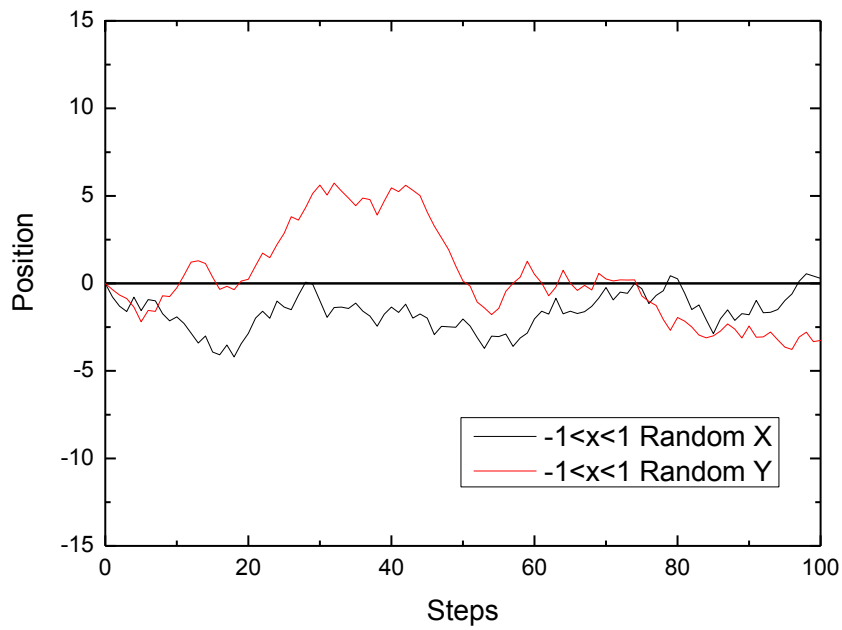


Figure 1.7 - Simulated 100 step random walk for an imaginary particle undergoing Brownian motion with velocities at each time step between -1 and +1 ($-1 < v < 1 \mu\text{m} \cdot \text{s}^{-1}$), resolved into motion along the x and y axes

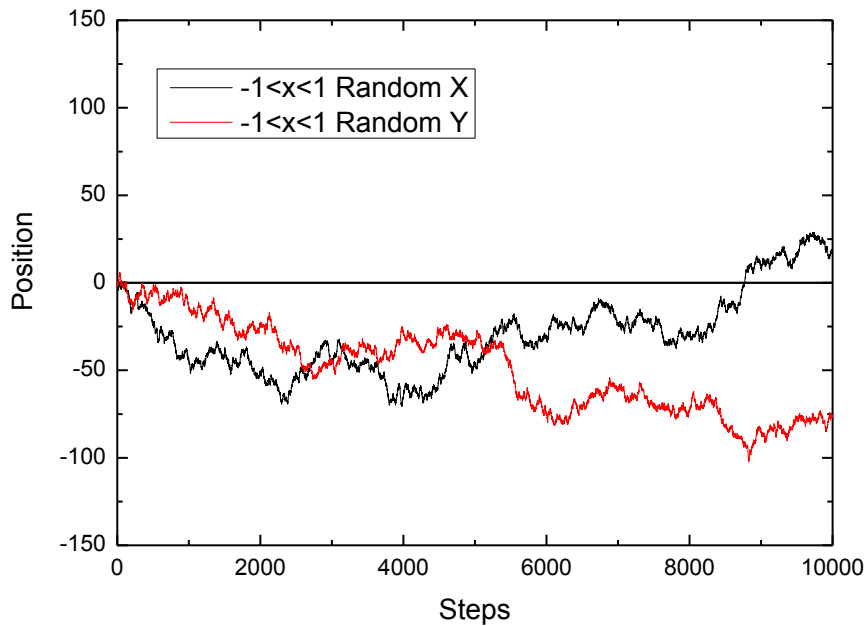


Figure 1.8 Simulated 10000 step random walk for an imaginary particle undergoing Brownian motion with velocities at each time step between -1 and +1 ($-1 < v < 1 \mu\text{m} \cdot \text{s}^{-1}$), resolved into motion along the x and y axes

As the time step (τ) for the simplified random walk ($v = -1, 0$ and $+1 \mu\text{m. s}^{-1}$) and the random walk more comparable to the Brownian motion ($-1 < v < 1 \mu\text{m. s}^{-1}$) is equal ($\tau = 1$ s), the mean-square displacement (MSD) for different step sizes of both random walks is calculated in the same fashion.

For example, to calculate the overall MSD (MSD_{xy}) for 10000 steps of the simplified random walk for 1000 time steps ($\Delta t_1 = \tau = 1$ s, $\Delta t_2 = 2\tau = 2$ s, ..., $\Delta t_{1000} = 1000\tau = 1000$ s), first 1D mean square displacements for the x and y axes should be calculated separately. For a step size of 1 ($\Delta t_1 = \tau = 1$ s), the MSD for the motion of the particle along the x axis can be calculated by averaging the square displacements corresponding to it:

$$\text{MSD}_x(\Delta t_1) = \frac{1}{10000} [(x_1-x_2)^2 + (x_2-x_3)^2 + \dots + (x_{9999}-x_{10000})^2]$$

And similarly, for the motion of the particle along the y axis for the step size of 1,

$$\text{MSD}_y(\Delta t_1) = \frac{1}{10000} [(y_1-y_2)^2 + (y_2-y_3)^2 + \dots + (y_{9999}-y_{10000})^2]$$

1D MSD for other time steps can be calculated using the equation below with n being the number of possible steps for a given time step size.

$$\langle (\text{MSD}_x(\Delta t))^2 \rangle = \frac{1}{n} \sum_{i=1}^n \Delta x_i^2(\Delta t) \quad (7)$$

$$\langle (\text{MSD}_y(\Delta t))^2 \rangle = \frac{1}{n} \sum_{i=1}^n \Delta y_i^2(\Delta t) \quad (8)$$

As in the 2D Cartesian coordinate system $r^2 = x^2 + y^2$,

$$\langle (\text{MSD}_{xy}(\Delta t))^2 \rangle = \langle (\text{MSD}_x(\Delta t))^2 \rangle + \langle (\text{MSD}_y(\Delta t))^2 \rangle = \frac{1}{n} \sum_{i=1}^n \Delta r_i^2(\Delta t) \quad (9)$$

Based on these considerations, the MSD vs step number for the simplified random walk ($v = -1, 0$ and $+1 \mu\text{m. s}^{-1}$) and the random walk comparable to the Brownian motion ($-1 < v < 1 \mu\text{m. s}^{-1}$) can be plotted in 1D (MSD_x) and in 2D (MSD_{xy}) (Figure 1.9).

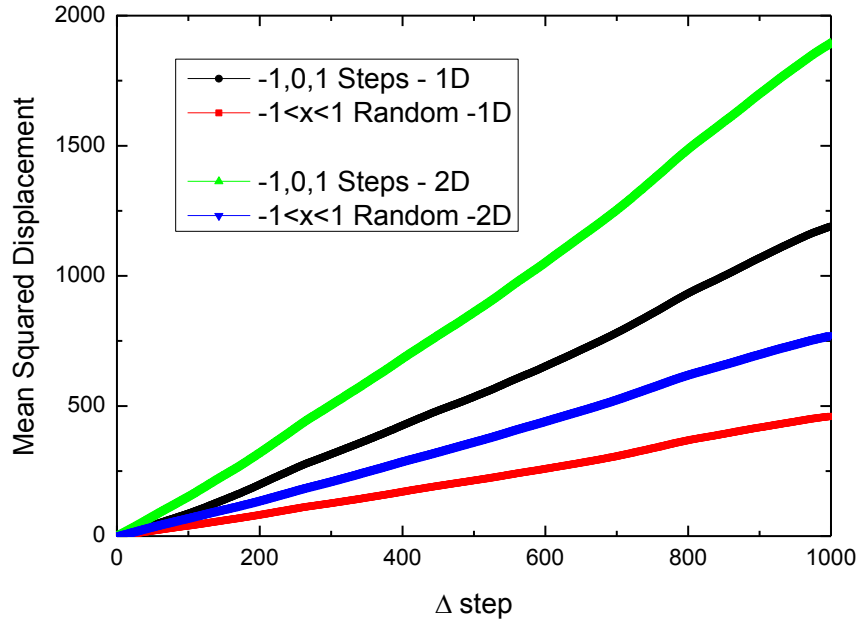


Figure 1.9 - MSD vs step size graph for the simplified random walk ($v = -1, 0$ and $+1 \mu\text{m. s}^{-1}$) and the random walk comparable to the Brownian motion ($-1 < v < 1 \mu\text{m. s}^{-1}$) in 1D (MSD_x) and in 2D (MSD_{xy}) for $\Delta t = 1000\text{s}$ which represents only 10% of the total trajectory.

As discussed earlier, in MSD graphs the slope of the line is related to the diffusion coefficient for the studied 1D or 2D random walks where $\text{MSD}_x = 2D_x t$ (10) and $\text{MSD}_{xy} = 4D_{xy} t$ (11).

In the example random walks shown here where the MSD was calculated for a 10000 steps trajectory and calculated for $0 < \Delta t < 1000$ step sizes), a straight line cannot be fitted accurately to the plotted graphs. (Slight non-linear behaviour is shown in Figure 1.9) This is due to the relatively large time period considered (10% of the total trajectory) and as such MSD calculations are dependent upon the random, macroscopic motion of the random walk.

However, if the MSD for both random walks is calculated over $0 < \Delta t < 50$ steps instead of 1000 steps, as the number of steps corresponding to the step size of 50 increases, the MSD is averaged over a larger set of data points, therefore the linear fit is more accurate and the extracted diffusion coefficient is a better represented. Figure 1.10 shows the MSD for these two walks over the $0 < \Delta t < 50$ steps. This plots clearly shows the linear behaviour for both data sets. Likewise it is clear that the gradient for 1D data ($= 2D_x$) is half that of the 2D ($= 4D_{xy}$) data and that, due to rounding errors the gradient for the quantized random walk is larger than the purely random steps random walk.

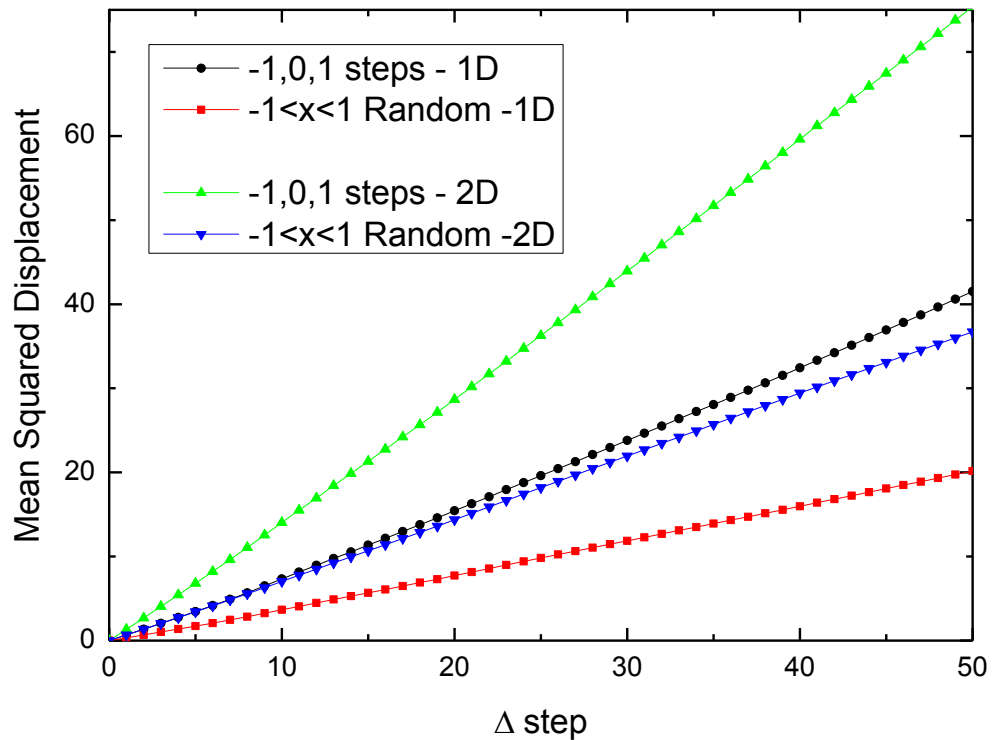


Figure 1.10 - MSD vs step size graph for the simplified random walk ($v = -1, 0$ and $+1 \mu\text{m} \cdot \text{s}^{-1}$) and the random walk comparable to the Brownian motion ($-1 < v < 1 \mu\text{m} \cdot \text{s}^{-1}$) in 1D (MSD_x) and in 2D (MSD_{xy}) for $\Delta t = 50$ s

1.3 Propulsive motion

In addition to Brownian motion, some particles and microorganisms carry out propulsion. In order to discuss the propulsion mechanism of these particles and microorganisms, it is essential to understand why propulsion is required for their motion within a fluidic environment. To achieve this, the concept of Reynolds number and its overall influence on the motion of small scale objects in fluids must be initially explained.

For a particle with a representative diameter (D) moving through a fluid with velocity (v), the Reynolds number is defined as $Re = \rho v D / \mu$ where ρ and μ are the density and dynamic viscosity of the fluid respectively. This dimension-less number indicates the ratio of inertial forces to viscous forces [5] and consequently a small Reynolds number is indicative of an environment where viscous forces dominate. For instance, considering reasonable dimensions, the Reynolds number for a human swimming in water is in the order of 10^4 where the value for a small fish in the same environment gets down to 10^2 and for a microorganism with an average speed of $30 \mu\text{m} \cdot \text{s}^{-1}$ it gets as low as 10^{-4} . This suggests that in a given fluidic environment with constant density and viscosity, the size and the velocity of the objects moving through it play a significant role on the inertial and viscous forces affecting the motion. In other words, the bigger the dimensions of an object and the higher its velocity, the longer it will coast before it slows down after the forces that move it forward are stopped. An easily imagined example would be a cruise ship going in an ocean at full speed which can take several miles to stop compared to a small plankton, both moving in the same fluidic environment, but both at considerably different ends of the Reynold's Number scale.

Based on this description, in low Reynolds numbers, inertia does not play a role and a

particle's motion at each moment is entirely the result of the forces exerted on it at that moment. To visualise the low Reynolds numbers environment that microorganisms swim in, a setting can be pictured where a large object moves slowly in a high viscosity environment. Consider, for example, a man fully submerged and trying to move in a pool filled with a highly viscous fluid like honey or molasses but he is forbidden to move faster than 1 cm. min^{-1} . For this man, motion simply means deforming his body in some manner without any displacement from his initial starting point. The only procedure that results in a displacement in this condition is a reciprocal motion where the body deforms into a certain shape then goes back to its original shape by repeating the motion in reverse.

The simplest object that can perform in this fashion is a three legged hypothetical swimmer with two hinges connecting the legs together. To execute a reciprocal motion, this swimmer should go through the sequence below:

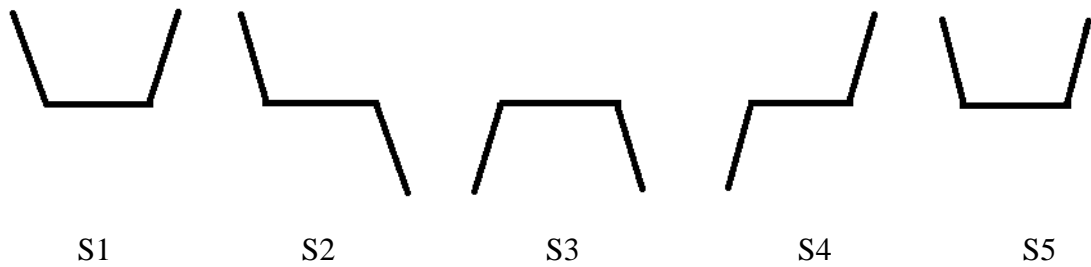


Figure 1.11 – Schematic drawing of a three legged hypothetical swimmer executing a cycle of possible configurations

By going through the sequence shown above, this swimmer goes around in a loop within its 2D configuration space with two degrees of freedom (θ_1, θ_2):

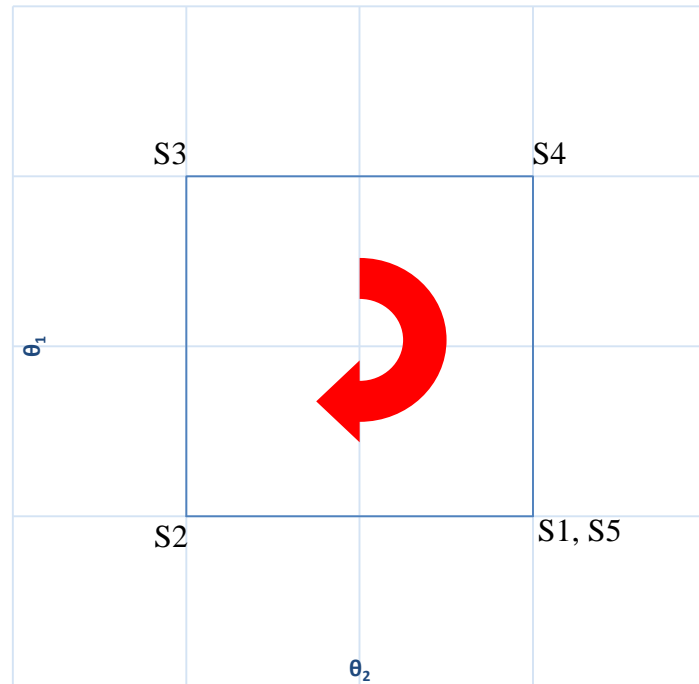


Figure 1.12 – Schematic graph demonstrating the reciprocal motion of a hypothetical three legged swimmer with two degrees of freedom, progressing around a rectangular loop

If this hypothetical swimmer only had one degree of freedom, for example if it only had two legs and one hinge joining them together, in a low Reynolds number environment, it was bound to retrace its trajectory at its initial point. Therefore, asymmetrical motion (or asymmetry in some other form) is one of the necessities for swimming in low Reynolds numbers.

In nature, microorganisms employ different strategies to swim in low Reynolds numbers to overcome the dominance of viscous forces. One of these strategies which has been studied the most is called corkscrew propulsion.

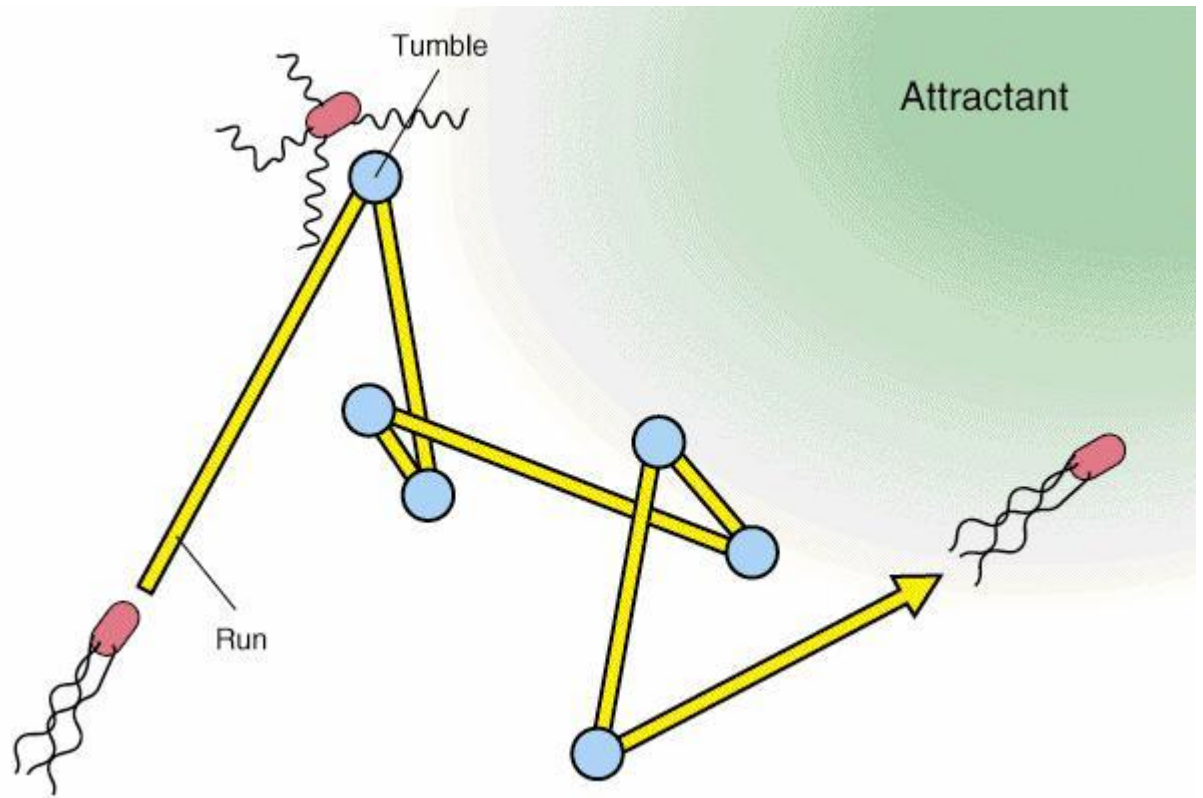


Figure 1.13 – Schematic design of E. coli bacteria employing showing both states of its propulsion system. Whilst running (bottom left) all tails act in unison to lengthen the overall dimension and reduce rotational diffusion, whilst when tumbling, the reverse is true.

For example, a group of bacteria called E. coli, propel by the spiralling wave motion running down their flagella. The foremost research on how the flagellum works was conducted by Sir Geoffrey Taylor in 1951[6]. In contrast with the common belief among scientists (who were almost certain that the flagellum has a wavelike motion), with the help of a working prototype made of a cylindrical body with a rotating helical tail powered by a rubber-band motor inside the cylinder, he proved that E. coli propel by the rotational corkscrew motion of the tail and not a spiralling wave.

However, motion in low Reynold number environments is only one obstacle to overcome. The overall motion of *E. coli*, and the key to its survival, is its ability to move in response to chemical signals. Such motion is the result of "intelligent" and autonomous motion in which controlled motion is achieved through alternating run and tumble phases. This motion is similar to a random walk and consists of straight swim periods (run) with random tumble intervals that make the bacteria capable of altering their orientation. Due to its microscale dimensions, the movement of a bacterium in water is affected by rotational diffusion. In other words, after swimming in a direct path for a few seconds, the Brownian phenomena leads to variation in *E. coli*'s orientation and as a result, it "forgets" its previous direction of motion. To overcome this effect, the bacteria frequently evaluates its course and adjusts it by switching between the run and tumble phases to direct itself towards attractants (usually sugars) while avoiding repellents (usually toxin chemicals). This mechanism is called chemotaxis.

Bacteria execute chemotaxis based on the presence of a chemical gradient in the bulk. For example, if the bacterium senses that it is directed towards a higher concentration of attractants or a lower concentration of toxins, it will continue its direct motion (running) but in the case of swimming towards a high concentration of toxins or a location where the concentration of attractants is minimal, it will tumble earlier to alter its direction and try a new random path. *E. coli* continues this sequential motion until it finds the source of attractants (the location with the highest concentration) or the position with the lowest concentration of toxins.

To carry out the running-tumbling motion and to detect the gradients of attractants/toxin, a bacterium utilises protein-based lash-like attachments called flagella. These nanoscale hollow tubes that are connected to a rotary engine located

inside the bacteria's cell membrane, and consist of two main modules, the filament (which is a long string that acts as a propeller) and the hook (which is a link that transfers the engine's torque to the filament). When the bacterium is moving towards an attractant or away from a toxin, the engine rotates clockwise, signalling the filaments to form a long coil consisting of a large bundle of flagella, allowing the bacterium to propel on a straight line (Figure 1.13, bottom left). When the bacterium wants to tumble and change its direction, the engine rotates anti-clockwise, this signals the filaments to disassemble their coil-shaped formation. As a result, the independent motion of several flagella in various random directions leads to the tumbling motion. Essentially, when the bacterium wishes to run, the flagella are bundled in a long assembly which not only acts as a propulsion mechanism, but also greatly increases the major length of bacterium itself, thus greatly reducing its rotational diffusion, and increasing its propensity for linear motion. Conversely, tumbling recedes propulsion whilst also reducing the dimension of the bacteria and increasing its rotational diffusion rate.

To execute these two modes of motion, *E. coli* and other small-scale biological propulsive systems require a source of chemical energy and a means to convert this chemical energy into mechanical energy which provides the ballistic driving force to generate net propulsion. *E. coli* employ enzymes to ferment sugars such as glucose, ribose and maltose into lactic acids and uses the energy released from this chemical reaction for propulsion. This mechanism that also enables *E. coli* to move toward these sources of energy and away from noxious molecules such as fatty acids and alcohols is an example of chemotaxis. Inspired by the biological propulsion mechanism of *E. coli* and similar living cells, various designs for fabricating micro- and nanosized machines capable of propulsion at low Reynolds numbers (where viscous forces

dominate and inertia does not play a significant role) have been proposed in the past few years. These designs promise futuristic applications such as drug delivery inside the body, cargo delivery in microfluidic systems and ultimately more complicated tasks like microsurgery.

1.4 Analysing propulsive and non-propulsive motion

As stated earlier, for a particle of radius R which is undergoing a pure Brownian motion in 2D, the squared displacement is linear in time with the slope controlled by the particle's transitional diffusion coefficient (D):

$$MSD_{xy} = 4D\Delta t \quad (11)$$

Where $D = kT/6\pi\eta R$ and R is the radius of the particle, η is the viscosity of the solution and kT is the thermal energy. The particle also carries out rotational diffusion $D_R = \tau_R^{-1} = kT/8\pi\eta R^3$ which is independent from its transitional diffusion (D).

Figure 1.13-a shows the 2D trajectories for five $1.62 \mu\text{m}$ colloidal particles (taken from [7]) undergoing Brownian motion in water for 25 seconds. The motion of particles is entirely random in all directions and as a result particles move little from their initial position and the mean squared displacement is minimal. On the other hand, the trajectories of the same particles undergoing additional propulsion (similar to the motion executed by *E. coli*) in the same period of time are shown in Figure 1.13-b. In the latter case, the particles' Brownian motion is enhanced by a ballistic effect and most particles have ended up far off from their initial position. Consequently, the mean squared displacements are considerably higher compared to their pure Brownian motion but in total (for time scales longer than particles' τ_R) the

motion is still random as particles still undergo rotational diffusion.

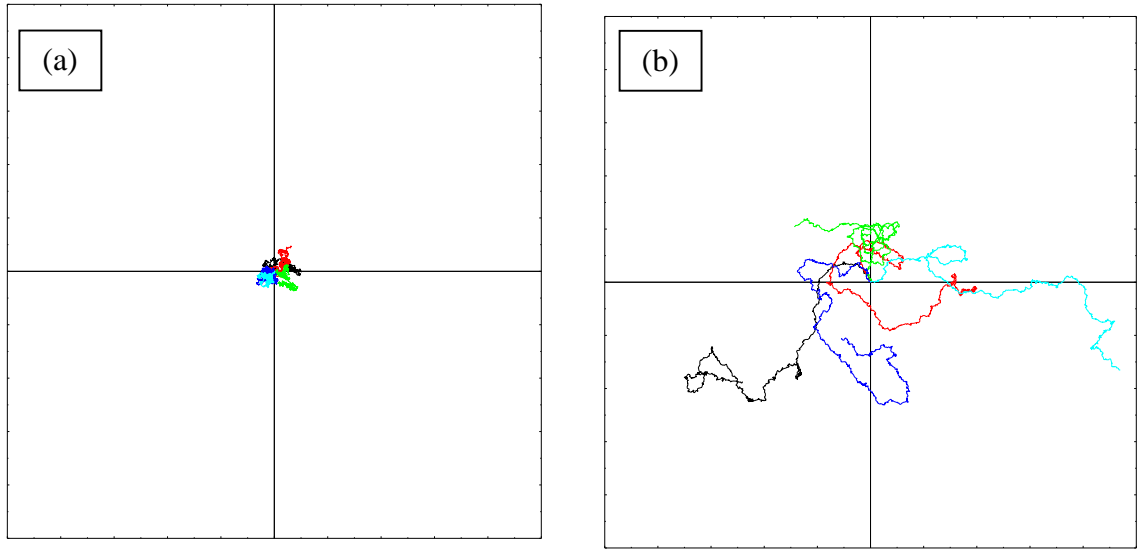


Figure 1.14 - 2D trajectories for five 1.62 μm colloidal particles undergoing (a) Brownian motion and (b) propulsive motion (taken from [7], Full x-axis=y-axis=100 μm and Time=25 s.)

To analyse the motion of these particles in different environments, qualitative observation of the trajectories is not sufficient as the overall motion is the product of natural diffusion and ballistic (artificial) effects. Thus, a method is required to quantify the differences between the motion of the swimmers in each condition which also takes into account any Brownian effects. Golestanian *et al.* [8] proposed a method for quantitative analysis of a particle's trajectory which is valid for both propulsive and non-propulsive motion. This method is also able to separate ballistic effects from purely Brownian effects. Similar to the method described in (section 1.2) for analysing the motion of a particle undergoing purely Brownian motion, from the recorded trajectory of a propulsive particle, the average value of the mean squared displacement can be plotted as a function of time but in this case (where the particle propels with velocity V). Golestanian *et al.* [8] have demonstrated that instead of fitting the MSD vs. Δt graph to $MSD_{xy} = 4D_{xy}\Delta t$ (10), the (2D projection) mean squared displacement vs. Δt must be fitted to:

$$MSD_{xy} = 4D\Delta t + \frac{V^2\tau_R^2}{2} \left[\frac{2\Delta t}{\tau_R} + e^{2\Delta t/\tau_R} - 1 \right] \quad \text{for all values of } \Delta t \quad (12)$$

For time scales longer than τ_R ($\Delta t > \tau_R$), where the exponential term has decayed to zero, the mean squared displacement reduces to:

$$\Delta L^2 = (4D + v^2\tau_R)\Delta t - \frac{v^2\tau^2}{2} \quad \text{for } \Delta t > \tau_R \quad (13)$$

For time scales much shorter than τ_r ($\Delta t \ll \tau_r$) where the mean squared displacement is dominated by ballistic propulsion, and the exponential term may be approximated as a series and we obtain:

$$\Delta L^2 = 4D\Delta t + v^2\Delta t^2 \quad \text{for } \Delta t \ll \tau_R \quad (14)$$

This allows for the determination and deconvolution of the diffusion coefficient of the particle and its average velocity in that particular time scale. What is apparent from equations 12 and 13, and their respective appropriate time scales is that the mean squared displacement begins as parabolic (ballistic) in nature, moving to a linear behaviour (enhanced diffusion) at a time larger than the rotational diffusion time. As such, equation 12 (for long time scales) may be approximated or fitted to a $y = Ax - B$ linear form at long time scales, whilst for shorter time scales, less than the rotational diffusion time, the MSD is represented through a $y = Ax + Bx^2$ form.

An example for demonstrating the difference between propulsive motion and Brownian motion is presented in Figure 1.15 where the MSD of five 1.62 μm propulsive catalytic colloidal particles is plotted against time in different fuel

concentrations (propulsion mechanism of these devices is explained in 1.5.2). As it can be seen in Figure 1.15, in the absence of the fuel, the motion of the particles is purely Brownian and the MSD graphs can be fitted to a straight line. This situation does not change for larger step sizes and longer time periods. On the other hand, the motion of the particles is propulsive in the presence of fuel and, for short periods of time a straight line cannot be fitted to the exponential MSD graph. Therefore equation (14) is employed for determining the diffusion coefficient of the particles and their propulsion velocity. On the other hand, for time periods bigger than the particles' τ_r (approximately 4 s for 1.62 μm particles), the MSD graph is more comparable to a line than a parabolic curve.

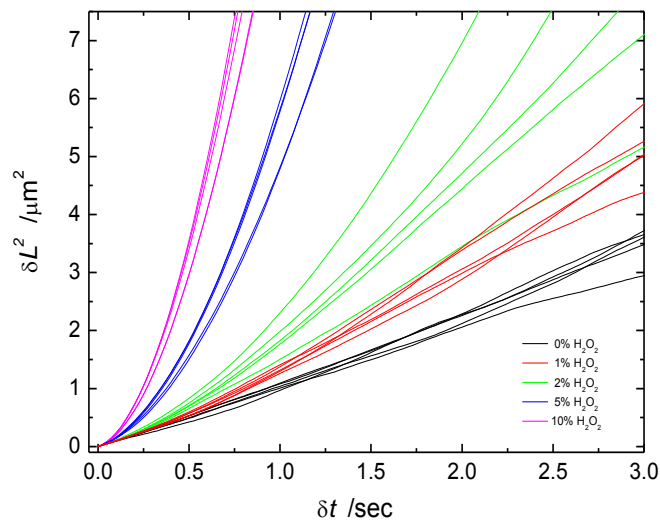


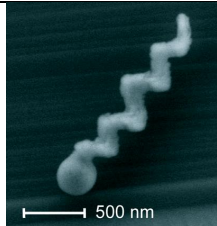
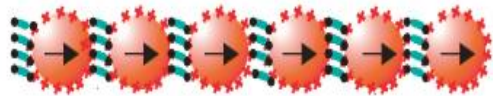
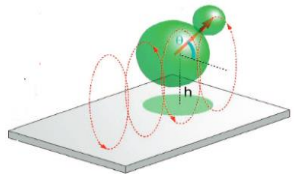
Figure 1.15 - MSD for non-propulsive (black, fuel = 0%) and propulsive particles (fuel > 0) showing the transition from a linear to a parabolic relationship. (taken from [7].)

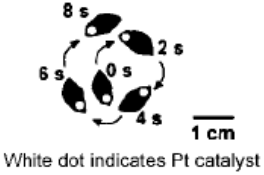
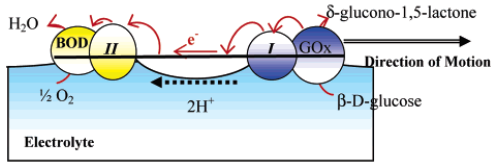
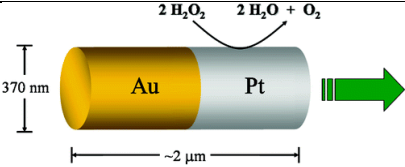
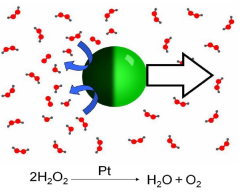
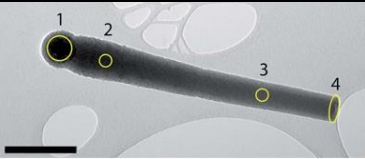
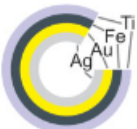
1.5 Propulsive nanomotors: fabrication, motion mechanism and applications

Fabricating micro- and nano-sized devices capable of propulsion inside a liquid media is difficult due to the predominating viscous effects at these length scales [9-11]. Existing swimming devices that are capable of propulsion at low Reynolds number environments require some form of asymmetry (be that in time or in physical make-up) and can be divided into two main categories based on the mechanism they employ to create the asymmetric force that leads to their motion. The first group requires an external energy source (such as an electric or a magnetic field) and is remotely powered by it from the outside [12]. In the second group, one or more parts of the device function in a way that they promote a chemical reaction asymmetrically across themselves in the media [13]. These *catalytic nanomotors* propel by converting the chemical energy of a *fuel* into mechanical energy. *Natural protein-based nanomotors* (e.g. dyneins, myosins and kinesins) use the energy released from the catalytic hydrolyzation of energy-rich molecules such as adenosine triphosphate (ATP) for propulsion [14]. On a similar basis, *hybrid nanomotors* have been fabricated by coupling artificial structures to these natural catalysts. For instance, Mano et al. [15] have designed a nanoswimmer by modifying one end of a carbon fiber with bilirubin oxidase (BOD) and the other end with glucose oxidase (GOx) in order to convert the chemical energy released from the reaction of glucose with oxygen (which is catalyzed by these enzymes) into the mechanical energy required for propulsion. Furthermore, *Manmade catalytic nanomotors* have been manufactured by adjoining a catalyst within or on the surface of an inorganic structure or a polymeric particle [7,16]. The most common fuel these artificial nanoswimmers studied so far hydrogen peroxide (H_2O_2) which is catalyzed through a decomposition reaction into water and oxygen and enables these devices to gain mobility. The fabrication process of these synthetic

swimming devices and their propulsion mechanism is further discussed in the following sections and summarized in Table 1.1.

Table 1.1 - A selection of remotely powered and autonomous nanoswimmers made to date

Swimmer	Category	Schematic/ Image	Dimensions	Structure	Driven by	Swim in	Max. velocity
Chang et al. [12]	Remotely powered		1.5 cm diameters	Miniature semiconductor diode	External a.c. electric field	Aqueous meniscus	$\sim 1 \text{ cm. s}^{-1}$
Ghosh and Fischer [17]	Remotely powered		1-2 μm length	Co coated Silicon	Rotating homogeneous magnetic field	Free aqueous solution	$\sim 40 \mu\text{m. s}^{-1}$
Dreyfus et al. [18]	Remotely powered		24 μm length	Magnetic particles linked with DNA	Oscillating magnetic field	Free aqueous solution	$\sim 100 \mu\text{m. s}^{-1}$
Tierno et al. [19]	Remotely powered		3.8 μm axial length	PS paramagnetic colloids linked with DNA strands	Rotating magnetic field	Near surface in aqueous solution	$\sim 3 \mu\text{m. s}^{-1}$
Mair et al. [20]	Remotely powered		2 μm length	Ni/Pd coated Au nanorod	External magnetic field	Near surface in aqueous solution	2-4 $\mu\text{m. s}^{-1}$

Swimmer	Category	Schematic/ Image	Dimensions	Catalyst	Fuel	Swim in	Max. velocity
Whitesides <i>et al.</i> [22]	Synthetic catalytic	 White dot indicates Pt catalyst	1 cm length	Pt	H ₂ O ₂	Aqueous meniscus	2 cm. s ⁻¹
Mano and Heller [15]	Synthetic catalytic		Diameter: 7 μm Length: 0.5 – 1 cm	Glucose oxidase and Bilirubin oxidase	Glucose	Aqueous meniscus	1 cm. s ⁻¹
Paxton <i>et al.</i> [23]	Synthetic catalytic		Diameter: 370 nm Length: 2 μm	Pt (+ cathodic reactions at Au)	H ₂ O ₂	Near surface in aqueous solution	~ 6.5 μm. s ⁻¹
Howse <i>et al.</i> [7]	Synthetic catalytic		Diameter: 1.62 μm	Pt	H ₂ O ₂	Free aqueous solution	~ 3 μm. s ⁻¹
Morgan <i>et al.</i> [16]	Synthetic catalytic		Length: 2 μm	Mn _x O _y	H ₂ O ₂	Free aqueous solution	2 – 4 μm. s ⁻¹
Mei <i>et al.</i> [33]	Synthetic catalytic		Diameter: 1 μm Length: 5 μm	Ag	H ₂ O ₂	Free aqueous solution	> 200 μm. s ⁻¹

1.5.1 Remotely powered nanomotors

The conventional approach for manipulating small objects involves the application of external macroscopic fields. Apart from the pioneering externally powered swimming devices developed by Ghosh and Fischer [17], Dreyfus, et al. [18] and Tierno, et al. [19], two relatively recent noteworthy papers have reported more advanced designs where microscale propulsion was achieved by electric and magnetic fields. In the first paper published by Chang, et al. [12], self-propelling particles made from semiconductor diodes acquire their energy from an external a.c. electric field. The swimming mechanism of these particles is based on rectification of this field into a constant d.c. voltage that after induction between particle's electrodes generates an electro-osmotic flow, enabling particles to rotate or propel. In other words, these microdevices convert the harvested electric energy into mechanical propulsion that results flow of the adjacent liquid. In their paper, *Chang, et al.* have also remarked the potential of these devices to be used as building blocks in dynamically reconfigurable microfluidic chips.

In the work of, Miar, et al. [20] a method for fabricating magnetically driven metallic nanorods, capable of guided near-surface swimming via an externally applied magnetic field is discussed. These Janus nanorods are fabricated by electrodepositing gold into the pores of anodized aluminium oxide (AAO) templates and thermally evaporating 50 nm of Ni and 15 nm of Pd onto the nanorods subsequent to releasing them from the template by dissolving AAO in 1 M NaOH. A permanent NdFeB magnet attached to a rotating motor positioned above the sample is employed for actuating these magnetic nanorods and the angular velocity of the particles is controlled by altering the motor drive voltage.

1.5.2 Synthetic catalytic particles

While externally powered swimmers are advantageous in nano-assembly applications where real-time monitoring is possible in microfluidic cells, due to the impracticality of tracking swimming devices in many biological environments and the challenges of providing external powering fields for *in-vivo* applications, micro- and nanoscale swimmers should ideally be capable of autonomous propulsion, and potentially directional control.

One alternative for creating autonomous propulsion at the nanoscale is to take advantage of the *phoretic* effects. In 1989, Anderson, et al [21] discovered that slip velocity can be created by coupling surface properties of particles to gradients of fields such as temperature and concentration. Based on this theory, various designs have been proposed for fabricating propulsive micro- and nano-particles. As discussed in (section 1.3), asymmetry is essential for generating net progress in low Reynolds numbers, therefore propulsion in these devices is achieved via asymmetrical incorporation of the catalyst for a chemical reaction to a particle and then suspending it in an environment where the reaction takes place. This asymmetry results in a higher reaction rate in areas where the catalyst is present therefore a concentration gradient of reaction products is formed around the particle and this leads to its propulsion as the system attempts to reach equilibrium again, through solvent flow.

The first experimental realisation of this concept for generating propulsion via asymmetrical conversion of chemical energy into motion was demonstrated by Whitesides, et al [22] who developed a surface swimmers at the millimetre scale that combined two processes: individual propulsive motion powered by the catalytic decomposition reaction of hydrogen peroxide, and self-assembly via the capillary interactions at the water-air interface.

However, the pioneering steps in experimental realisation of autonomous microswimming were taken by Paxton, et al. [23]. In a paper published in 2004, they reported that 2 μm long rod-shaped particles (370 nm in diameter), consisting of 1 μm long platinum and gold segments, propel autonomously in aqueous hydrogen peroxide solutions by catalyzing the formation of oxygen at the Pt end. These rod swimmers were fabricated electrochemically using a method previously described in ref [20]. Similar to the fabrication process of magnetically driven nanorods, striped platinum/gold (Pt/Au) nanorods were synthesised in Anopore alumina membranes via an initial silver (Ag) vacuum deposition stage followed by electrodeposition of Au and Pt. The rods were subsequently freed by dissolving Ag in HNO_3 and alumina in NaOH [24]. Paxton, et al. [23] also demonstrated that these rods move predominantly along their axis in the direction of the Pt end at speeds of up to 10 $\mu\text{m} \cdot \text{s}^{-1}$.



Figure 1.16 – Schematic design showing the structure of a catalytic metallic nanorod

The next notable development to achieve propulsion at nanoscale in catalytic swimmers was made when colloidal polymer particles were employed in synthesising these devices. As colloidal particles were available in a wide range of sizes, with densities that enabled them to propel in liquid media (as opposed to the near-surface propulsion of metallic devices due to their high densities), they were selected for this purpose. Moreover, colloidal particles could be functionalised via simple processes and the modified particles could be readily manipulated via electric [25, 26], magnetic [27,28], optical [29,30] and thermal fields [31,32], making them suitable candidates for cargo transport in microfluidic cells and *in-vivo* drug delivery.

Following the work by Paxton [23], Howse, et al. [7] proposed a straightforward method for fabricating polymer-based self-diffusiophoretic micro-swimmers based on the catalytic decomposition reaction of hydrogen peroxide. This technique, that does not involve a multi-stage electrodeposition/dissolution fabrication, consists of drawing a droplet of a dilute suspension (0.05 wt%) of micron-sized polystyrene spheres in isopropanol over a glass slide to produce a scattered monolayer of particles which were half-coated with platinum via thermal vacuum deposition. In contrast with rod-shaped microswimmers, these spherical swimmers move in a direction opposite to the orientation of the catalytic cap and their average speed is lower for a given size but, as the density of these swimmers is much lower than the density of metallic nano-rods, they perform 3D motion in the bulk where as high density rod swimmers are only capable of 2D propulsion on the bottom surface of a petri dish.

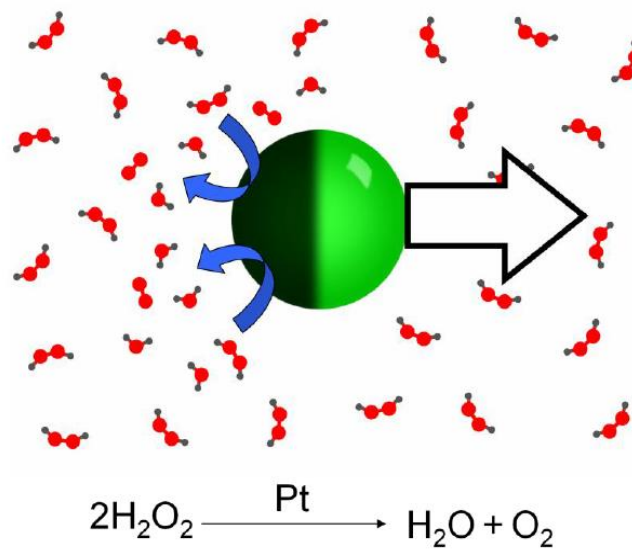


Figure 1.17 – Schematic design demonstrating the propulsion mechanism of colloidal microswimmers based on the catalysed decomposition reaction of hydrogen peroxide

The most recent generation of catalytic nano- and microengines that offer distinct advantages in comparison with metallic nanorods and spherical colloidal swimmers are tubular microstructures [33]. These microengines propel autonomously via a bubble-induced motion mechanism and compared to the maximum velocity reported for other classes of swimmers ($10 \mu\text{m} \cdot \text{s}^{-1}$) their speed can go up to $3 \text{mm} \cdot \text{s}^{-1}$ [34]. Moreover, unlike the propulsion of metallic nanorods and colloidal swimming devices that only takes place in a salt-free media, propulsive motion of tubular microengines is independent from the presence of salts in the solution and this promises various potential application for these devices in biomedical applications [35]. Two methods have been reported for fabricating tubular microengines. K. Mantesh et al. [35] utilised template-assisted electrosynthesis where conical Ag microwires were used as templates for electrodepositing polyaniline (PANI) and Pt respectively subsequent to the dissolution of Ag in acid.

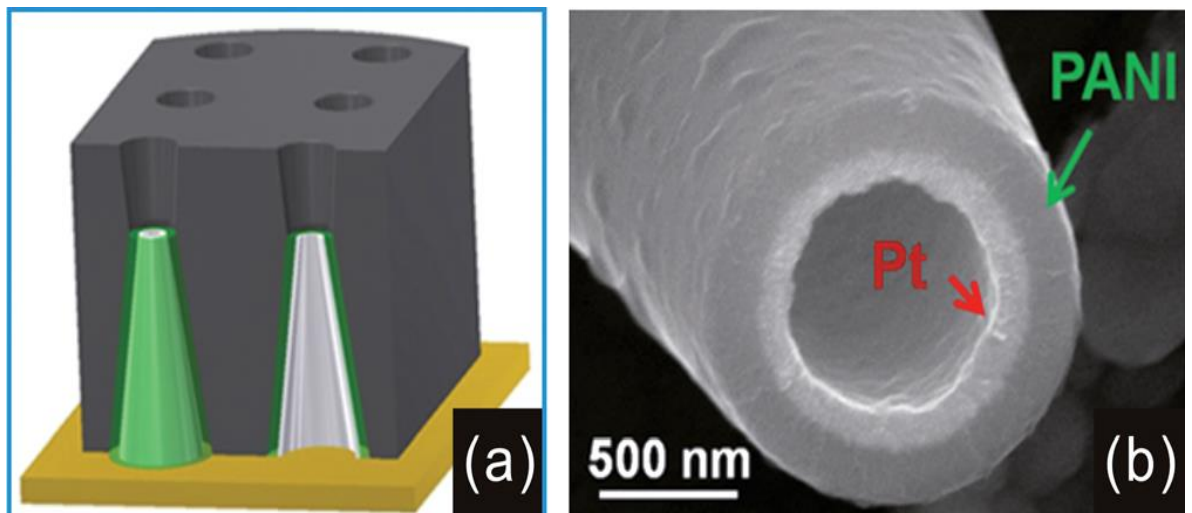


Figure 1.18 – (a) schematic design demonstrating the template-assisted electrosynthesis of tubular microengines. (b) SEM image of a template based tubular microengine (taken from Ref. 33)

V. Prinz, et al. [36] took an alternative approach. They utilised the intrinsic strain gradients in nanomembranes to prepare tubular structures. In their so-called rolled-up technique, lattice mismatch in a bi-layer semiconductor nanomembrane results in a strain gradient perpendicular to the surface. This will ultimately cause the membrane to bend/roll after the sacrificial layer that keeps the membrane flat is chemically etched. The other method is using a photoresist as the sacrificial layer, evaporating the multi-layer metallic membrane via vacuum deposition and dissolving the photoresist in an organic solvent in the final stage [37]. Since the photoresists can be easily patterned via photolithography, they can serve as a means for transferring patterns to nanomembranes and tubular structures.

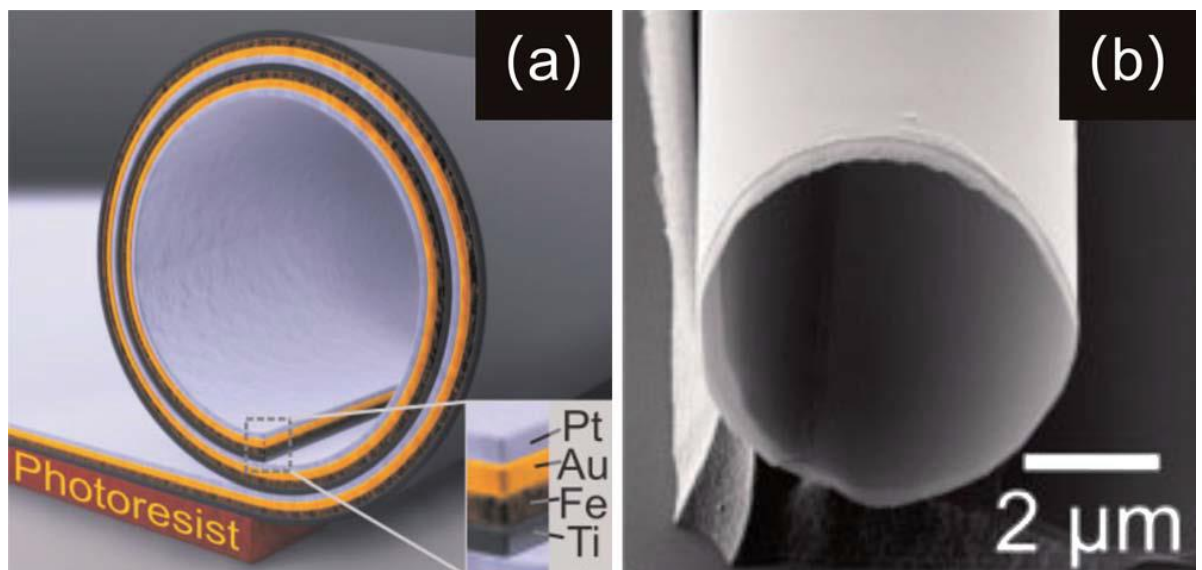


Figure 1.19 – (a) schematic design demonstrating the metallic layers of a tubular microengine fabricated via the rolled-up technique (b) SEM image of a tubular microengine fabricated via the rolled-up technique (taken from Ref. 34)

1.6 Strategies for controlling the motion of colloidal microparticles

To this point we have discussed that due to their simple synthesis and functionalisation process, simple colloidal particles hold a considerable promise to be utilised in tasks such as drug delivery, cargo transport and sensing at the micro- and nano-scale.

Converting these particles to asymmetric catalytic swimming devices, makes them capable of propulsion in low Reynolds number environments and this enhanced motion increases their ability in performing useful transport tasks. As for both propulsive and non-propulsive particles the position results from translational diffusion (D) and also the rotational diffusion (D_R), essentially, at any realistic time scales (>10 s), the motion is random and directed motion towards a desired location i.e. for cargo delivery, is therefore difficult to achieve. To overcome this issue, different strategies have been proposed for navigating and directing motile microparticles inside a liquid media. The first strategy focuses on modifying the substrate upon which the particles are in motion. By creating regions on the substrate that alter the motion of the particles when they pass upon them, particles can be guided to a location via these “tracks” [38,39]. The second strategy demonstrates the potential to exploit the trajectories of ensembles of particles (that react differently in various regions of a concentration gradient) to produce statistical accumulation, in higher concentration regions [40]. The third strategy is based on controlling the particle’s orientation via external fields such as electric [12] and magnetic [41]. Particles responsive to these fields can be directed manually towards a target by changing the direction and/or the strength of the associated external field. The fourth strategy shows the ability to fabricate propulsive devices that produce a range of trajectories from linear translation to tight on the spot rotation by modifying the technique used for adjoining the catalytic module to the particles with the aim of employing particles with linear motion in transport tasks and the rotating particles in tasks such as mixing or pumping [42, 43]. Finally, the fifth strategy studies different methods for increasing the area-to-volume ratio of catalytic swimmers in order to boost their propulsion speed which is a function of reaction rate on their surface. This approach can also potentially increase the time period at which

the catalytic device predominantly moves in a directed way. Despite their advantages, these methods have their own shortcomings. For example, navigation via surface modification can only be employed for near-surface swimmers and using external fields for steering the particles requires manual control which imposes additional errors. In the upcoming chapters, the attempts made to overcome these issues by optimising these strategies in terms of reproducibility, accuracy, autonomy and complexity are reported.

Chapter 2

In this chapter a method is proposed to benefit from the size changing capability of pH-responsive hydrogels in navigating catalytic microswimmers and to overcome and gain from the effects of rotational diffusion on the propulsive motion of these devices. The results of this chapter were obtained from experimental trials and computational modelling.

Chapter 3

The progress made towards navigating a new type of polymeric self-diffusiophoretic microswimmers via a uniform external magnetic field is discussed. To study the effects of magnetic field on the orientation and motion of these particles, their trajectories have been recorded and analysed in a variety of constant fuel concentrations, and in the presence and the absence of a uniform magnetic field. Based on the outcomes of this study, a new technique with potential capability in autonomous navigation of magnetic catalytic swimmers has also been examined.

Chapter 4

This chapter provides the experimental data that demonstrate the potential of utilising specially fabricated colloidal microswimmers which have an inherent spin as nanoscale and microscale mixing devices. To determine the degree of mixing imparted to the solution surrounding these mixing devices, the average velocity of colloidal tracer particles adjacent to the micromixers is determined in the absence and presence of hydrogen peroxide fuel and plotted against their distance to the spiralling micromixer.

Chapter 5

As the propulsion of catalytic swimming devices is dependent on the asymmetric decomposition reaction which takes place on the surface, having a higher surface area with more catalysis sites leads to a faster reaction rate and potentially a higher propulsion velocity. To examine this hypothesis, in this chapter various methods for fabricating structures with high surface areas have been examined. These methods include assembling colloidal clusters in oil-in-water emulsions, fusing polymeric particles via partial melting and growing catalytically active platinum branches on the surface of spherical particles.

Chapter 6

Surface interactions between layer-by-layer polymeric microcapsules (with charged functional groups on their surface) rolling on adhesive, non-adhesive, and conductive substrates were studied in this chapter with the aim of physically realising a computational model that demonstrated the capability of highly adhesive regions

located on a non-adhesive substrate in deviating elastic particles from their path. The outcomes of this study revealed the potential of this feature in developing a method for separating microparticles based on their mechanical stiffness and their adhesion to the surface.

Chapter 7

Finally, the future work arising from the studies conducted in previous chapters is discussed in this section.

References

1. H. Mehrer, N. A. Stolwijk, *Diffusion Fundamentals* **2009**, 11, 1-32.
2. E. M. Rogers, *Journal of Consumer Research*. **1976**, 2, 290-301.
3. A. Einstein, *Ann. Phys.* **1905**, 17 (8), 549-560.
4. H. C. Berg, *Random walks in biology* Princeton, USA: Princeton University Press, 1934.
5. E. M. Purcell, *Am. J. Phys.* **1977**, 45, 3-11.
6. G. I. Taylor, *Proc. R. Soc. A.* **1952**, 211, 225-239.
7. J. R. Howse, R. A. L. Jones, A. J. Ryan, T. Gough, R. Vafabakhsh, R. Golestanian, *Phys. Rev. Lett.*, **2007**, 99, 048102.
8. R. Golestanian, T. B. Liverpool, A. Ajdari, *New J. Phys.* **2007**, 9, 126.
9. J. P. Brody, P. Yager, R. E. Goldstein, R. H. Austin, *Biophys. J.* **1996**, 71, 3430–3441.
10. A. Shapere, F. Wilczek, *Phys. Rev. Lett.* **1987**, 58, 2051–2054.
11. L. E. Becker, S. A. Koehler, H. A. Stone, *J. Fluid Mech.* **2003**, 490, 15–35.
12. S. T. Chang, V. N. Paunov, D. N. Petsev, O. D. Velev, *Nat. Mater.* **2007**, 6, 235-240.
13. J. Gibbs, Y. Zhao, 2011, *Front. Mater. Sci.* **2011**, 5 (1): 25–39.
14. E. Gajewski, D. K. Steckler, R. N. Goldberg, *J. Bio. Chem.* **1986**, 261 (27): 12733–12737
15. N. Mano, A. Heller, *J. Am. Chem. Soc.* **2005**, 127, 11574–11575.
16. A. R. Morgan, A. B. Dawson, H. S. Mckenzie, T. S. Skelhon, R. Beanland, H. P. W. Franks, S. A. F. Bon, *Mater. Horiz.* **2014**, 1, 65.
17. A. Ghosh, P. Fischer, *Nano Lett.* **2009**, 9(6), 2243.
18. R. Dreyfus, J. Baudry, M. L. Roper, M. Fermigier, H. A. Stone and J. Bibette, *Nature* **2005**, 437, 862.
19. P. Tierno, R. Golestanian, I. Pagonabarraga and F. Sagues, *J. Phys. Chem. B* **2008**, 112, 16525.
20. L. O. Mair, B. Evans, A. R. Hall, J. Carpenter, A. Shields, K. Ford, M. Millard, R. Superfine, *J. Phys. D: Appl. Phys.* **2011**, 44, 125001.
21. J.L. Anderson, *Ann. Rev. Fluid Mech.* **1989**, 21, 61.
22. G. M. Whitesides, R. F. Ismagilov, A. Schwartz, N. Bowden, *Angew. Chem. Int. Ed.*, 2002, **41**, 652.
23. W.F. Paxton, et al. *J. Am. Chem. Soc.* **2004**, 126, 13424.

24. Martin, B. R.; Dermody, D. J.; Reiss, B. D.; Fang, M.; Lyon, L. A.; Natan, M. J.; Mallouk, T. E. *Adv. Mater.* **1999**, 11, 1021-1025.
25. R. C. Hayward, D. A. Saville and I. A. Aksay, *Nature*, **2000**, 404, 56.
26. A. Yethiraj and A. van Blaaderen, *Nature*, **2003**, 421, 513.
27. G. Helgesen, P. Pieranski, A. T. Skjeltop, *Phys. Rev. Lett.*, **1990**, 64, 1425.
28. S. Melle, O. G. Caldero, M. A. Rubio, G. G. Fuller, *Phys. Rev. E: Stat., Nonlinear, Soft Matter Phys.*, **2003**, 68, 041503.
29. A. Chowdhury, B. J. Ackerson and N. A. Clark, *Phys. Rev. Lett.*, **1985**, 55, 833.
30. M. P. MacDonald, G. C. Splading and K. Dholakia, *Nature*, **2003**, 426, 421.
31. Z. D. Cheng, W. B. Russell and P. M. Chaikin, *Nature*, **1999**, 401, 893.
32. R. Piazza, *J. Phys.: Condens. Matter*, **2004**, 16, S4195.
33. Y. F. Mei, G. S. Huang, A. A. Solovev, E. Bermudez Urena, I. Moench, F. Ding, T. Reindl, R. K. Y. Fu, P. K. Chu, O. G. Schmidt, *Adv. Mater.*, **2008**, 20, 4085.
34. W. Gao, S. Sattayasamitsathit, J. Orozco, J. Wang, *J. Am. Chem. Soc.*, **2011**, 133, 11862.
35. K. M. Manesh, M. Cardona, R. Yuan, M. Clark, D. Kagan, S. Balasubramanian, J. Wang, *ACS Nano*, **2010**, 4, 1799.
36. V. Ya. Prinz, V. A. Seleznev, A. K. Gutakovsky, A. V. Chehovskiy, V. V. Preobrazhenskii, M. A. Putyato, T. A. Gavrilova, *Phys. E.*, **2000**, 6, 828.
37. A. A. Solovev, Y. F. Mei, E. Bermudez Urena, G. S. Huang, O. G. Schmidt, *Small*, **2009**, 5, 1688.
38. Karnik R., Hong S., Zhang H., Mei Y., Anderson D. G., Karp J. M., Langer R. *Nano Lett.* **2008**, 8 (4), 1153-1158.
39. Q. Ramadan, D. P. Poenar, C. Yu, *Microfluid Nanofluid* **2009**, 6:53–62.
40. Y. Hong, N. Blackman, N. Kopp, A. Sen and D. Velegol, *Phys. Rev. Letts.*, **2007**, 99, 1–4.
41. L. Baraban, D. Makarov, R. Streubel, I. Mönch, D. Grimm, S. Sanchez, O. G. Schmidt, *ACS Nano* **2012**, 6 (4), 3383–3389.
42. J. G. Gibbs, S. Kothari, D. Saintillan, Y.-P. Zhao, *Nano Lett.*, **2011**, 11, 2543–50.
43. S. Ebbens, R. Jones, A. Ryan, R. Golestanian and J. Howse, *Phys. Rev. E.*, **2010**, 82, 6–9.

Chapter 2: Synthetic running and tumbling: an autonomous navigation strategy for controlling pH-responsive catalytic microswimmers

In this chapter a method is proposed to benefit from the size changing capability of pH-responsive hydrogels in navigating catalytic microswimmers and to overcome the complexity of studying their motion. In essence, as a particle's rotational diffusion $\left(\tau_R^{-1} = \frac{k_B T}{8\pi\eta R^3}\right)$ is inversely proportional to its radius cubed, the rotational rate varies as $1/R^3$ suggesting that contracted devices may act as spinners while expanded devices could have a higher tendency to run and therefore the size changing responsive polymer nanoswimmers enables us to control the particle's τ_R^{-1} and thus its orientation variation frequency. In other words, switching between these states could provide a navigational capability which is similar to E. Coli's running and tumbling. pH-responsive polymers are polymers whose volume, conformation, configuration and solubility can be manipulated reversibly by changing the pH of the environment they are in [1,2]. The variations in the external pH modifies the hydrophobic interactions, hydrogen bonding and ionic interactions of the polymer and results in a reversible self-organization or microphase separation in its structure. Due to the presence of certain charged functional groups in their polymer network, the dimensions of some hydrogels vary in different pHs. In other words, depending on the pH of the media they are suspended in, these materials can either be in a swollen or a collapsed state. Among different types of microgels, hydrogel particles that swell in water have received significant attention among scientists in the past

few years because of their exceptional potential in drug delivery [3], biotechnology [4-8] and tissue engineering [9] applications as they provide the opportunity of fabricating functional materials with tailor-made properties [10,11]. For example, as the pH of most cancer cells is acidic (5.5 – 6.9) [12], pH-responsive polymers can be employed for fabricating smart delivery systems for anti-cancer drugs, reducing the side effects of currently used drugs by only targeting the infected cells.

The issue investigated here is the efficiency of an approach for directing microswimmers that combines the concepts of controlling individual swimmer trajectory, with the idea of navigation in response to solution borne stimuli. This was achieved by considering the behaviour of ensembles of catalytic swimming devices made from hydrogel materials that can change size in response to solution stimuli [13,14]. The ultimate goal was to produce devices that can follow concentration gradients for a wide range of signalling chemicals in addition to rapid and autonomous accumulation at high (or low) concentration regions. The main complication in studying and modelling the behaviour of such size-changing ensembles was that both velocity and trajectory of these swimming devices have been shown to change with size [15]. Velocity changes are due to features of the fundamental mechanism producing propulsion, while trajectory changes are due to the size dependence of translational and rotational diffusion phenomena.

2.1 Synthesis of pH responsive polymers

Synthesis techniques for preparing pH-responsive hydrogels have been extensively studied so far. These materials can be fabricated by straightforward reactions between one or more monomers, or by association bonds such as strong van der Waals interactions and hydrogen bonds between polymer chains [16]. In 1935, Staudinger and Husemann [17] polymerised divinylbenzene (DVB) at high dilution

in a good solvent to achieve swollen cross-linked polymer particles. Since then, a large amount of research has been conducted on new microgel systems and some older systems have also been revised using advanced techniques or novel methods.

The main methods for fabricating microgel particles are: emulsion polymerisation [18,19], cross-linking neighbouring polymer chains [20], anionic copolymerisation [21] and inverse suspension polymerisation [22]. Among these methods, emulsion polymerisation is more commonly used due to its flexibility in solvent and monomer selection and the narrow particle size distribution of the products. A typical emulsion polymerization system is normally composed of water, water-insoluble monomer(s), surfactant and a water-soluble initiator [23]. Through an emulsion polymerization reaction, monomer is emulsified in water and small monomer droplets surrounded by surfactant molecules are formed by mechanical stirring creating micelle like drops in the water phase. After introducing the water-soluble initiator to the system, free-radical polymerization begins within the formed droplets. At this stage, monomer in the droplets reacts with the initiator and a polymer chain begins growing. The polymerization reaction continues until the growing chain terminates and the micelle like droplets transforms into a polymer particle.

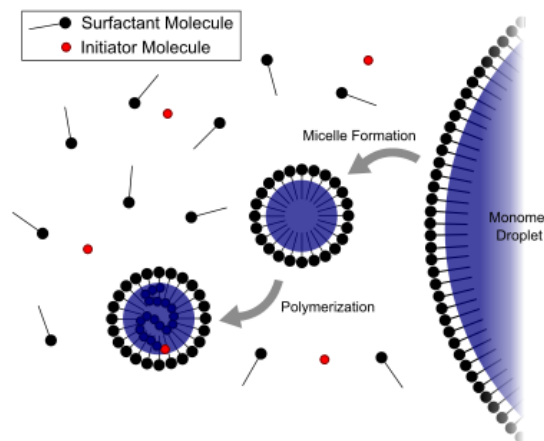


Figure 2.1 - Schematic diagram of emulsion polymerization taking place in a continuous water phase

Conventional emulsion polymerisation allows fabrication of high molecular weight polymer particles with a fast rate and a high yield with diameters starting from less than 150 nm to 100 μm . However, extracting the residual surfactant from the system after completion of the reaction is difficult and requires desorption or dialysis. Therefore, Goodwin, et al.[24] proposed conducting emulsion polymerisation in a surfactant-free environment via using a continuous phase with a high dielectric constant and an ionic initiator. For example, non-swollen polystyrene (PS) particles can be produced by using water as the media and $\text{K}_2\text{S}_2\text{O}_8$ as the initiator as the charged polymer chains formed during polymerisation will act as surfactant molecules and result a stable particle growth. Similar methods have been reported for preparing poly methyl methacrylate (PMMA) [25] and poly N-isopropylacrylamide (PNIPAA) [26] microgel systems.

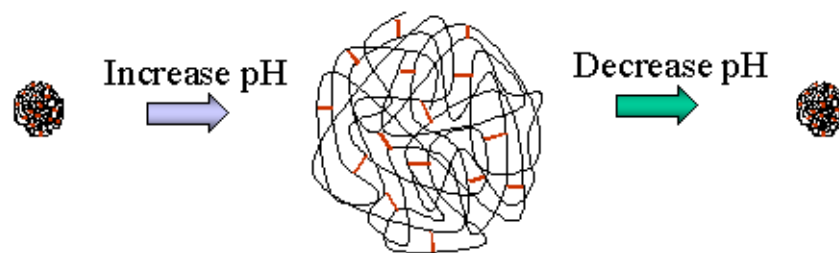


Figure 2.2 - A schematic diagram of a pH responsive PMAA particle showing its response to pH variations

2.2 Preparation of poly(methacrylic acid) microparticles

Two polymerisation techniques were employed in order to fabricate micron-sized pH-responsive particles. Initially, inverse suspension polymerisation was chosen for synthesising poly (methacrylic acid) (PMAA) microgel spheres due to the high rate of the red-ox reaction and the simplicity of the process. However, as in this technique the droplets containing the monomer were formed by mechanical stirring, the diameter of the fabricated particles varied between 50 to 700 μm and this wide size

distribution was not suitable for obtaining consistent results in the subsequent motion tracking stage. Consequently, PMAA particles were fabricated via precipitation polymerisation. Although this method had a lower reaction rate compared to emulsion polymerisation and involved continuous solvent refluxing over-night, the particles produced via this method were chosen for the pH-response studies as they had a narrow size distribution (as for this study it was necessary to distinguish the difference between the swollen and the collapsed states of the particles in different pHs) and did not require surfactant or salt extraction.

Tables 2.1 and 2.2 show the components and the summary of particle fabrication experiments via emulsion and precipitation polymerisation. More details about the fabrication process and particle size measurements are provided in the upcoming sections.

Table 2.1 – Fabrication recipe for emulsion and precipitation PMAA particles

Polymerization	Emulsion		Precipitation	
Monomer	MAA	2 ml	MAA	4 ml
Continuous phase	Xylene	100 ml	Acetonitrile	100 ml
Initiator	APS - TEMED	1 ml 1 M – 1 ml	ACCN	0.3 gr
Initiation type	Redox initiation	-	Thermal initiation	-
Crosslinker	BA	0.1 g	DVB-80	0.4 ml
Core	Rhodamine 6G	0.02 g	Rhodamine 6G	0.02 gr
Other components	Span-80	1 g	-	-
	NaOH	0.5 ml 1 M	-	-

Table 2.2 – Summary of the particle fabrication experiments via emulsion and precipitation polymerisation

Particle type	Size	Range (D)	Modulus	Core
PMAA microgel (emulsion)	250 μm (pH 10) 120 μm (pH 2)	100-700 μm 50-300 μm	pH dependent (soft to hard)	Rhodamine 6G
PMAA microgel (precip.) [0.04 wt% initiator]	525 nm (pH 10)	500-550 nm	pH dependent (soft to hard)	Rhodamine 6G
PMAA microgel (precip.) [0.04 wt% initiator]	3 μm (pH 10) 1.5 μm (pH 2)	2.9-3.1 μm 1.4-1.6 μm	pH dependent (soft to hard)	Rhodamine 6G

2.2.1 Inverse suspension polymerisation

PMAA microgels were prepared by the inverse suspension polymerisation method where MAA monomers were polymerized by (ammonium persulfate) (APS) - (TEMED) (tetramethylethylenediamin) red-ox initiators and crosslinked by BA (N,N'-methylenebisacrylamide) in a stirred flask under nitrogen purging in the presence of xylene as the continuous phase and Span-80 as the surfactant. By employing this method, PMAA microgel spheres with a mean diameter of 100 μm were fabricated and they were made visible under fluorescence mode by adding Rhodamine 6G ($\lambda_{\text{ex}}=526$ nm, $\lambda_{\text{em}}= 555$ nm) to their structure during the polymerisation [27].

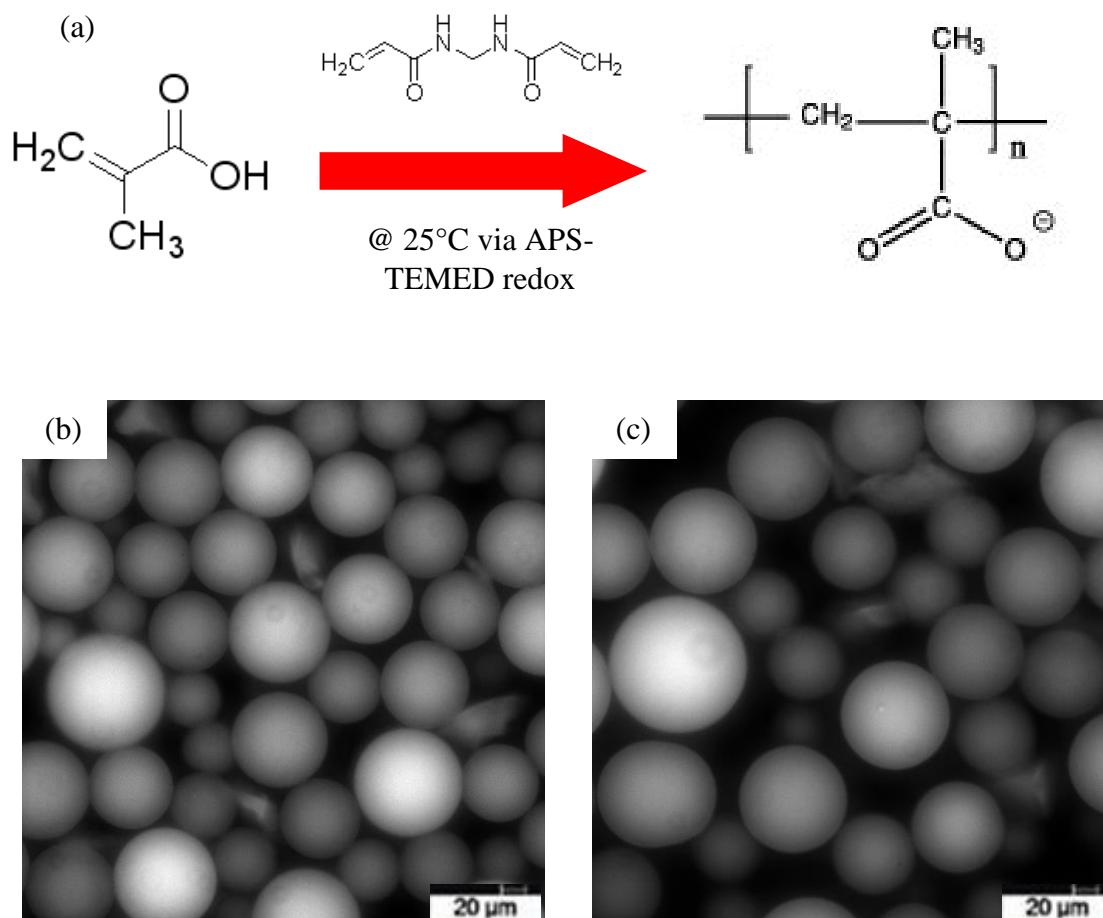


Figure 2.3 – (a) polymerisation reaction of MMA via APS-TEMED redox initiation – (b), (c) fluorescent images taken from suspension polymerisation products which demonstrates their polydispersity

2.2.2 Precipitation polymerisation

In a second attempt, PMAA microspheres were prepared by precipitation polymerization using the method described by Huang et al [28]. MAA was polymerized using 1,1'-azobis cyclohexane-1-carbonitrile (ACCN) as a thermal, water soluble azo-initiator and cross-linked using divinylbenzene-80 (80% DVB) in a gently agitated flask in the presence of acetonitrile. Using this method, particles with diameters around 300 nm (in the dehydrated stage) were fabricated. Although

the products of this reaction had a narrow size distribution, monodispersity and a noticeable pH response, as tracking their motion was difficult using optical microscopy due to their diameter (between 300 nm to 500 nm depending on the pH) which was very close to the limits of observing particles using this method, larger particles needed to be fabricated for the swimming experiments.

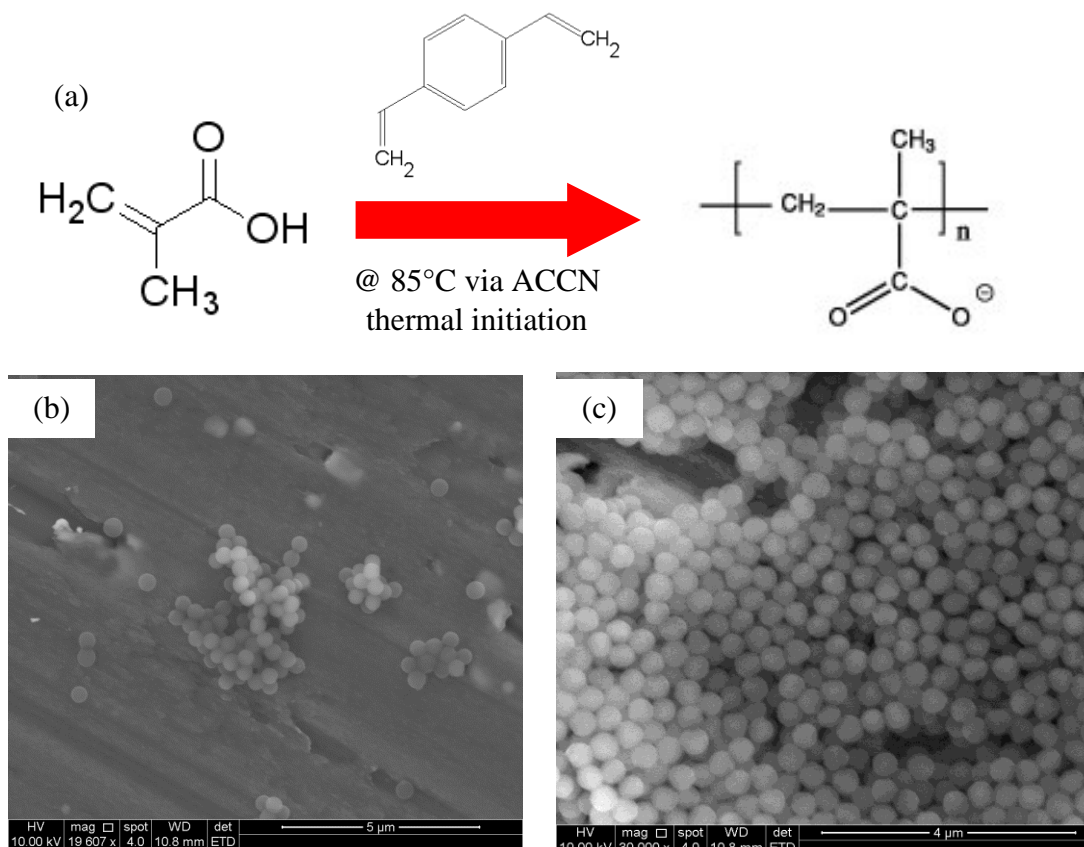


Figure 2.4 – (a) polymerisation reaction of MMA via ACCN thermal initiation – SEM images taken at 20 kX magnification (a) and 30 kX magnification (b) from precipitation polymerisation products which demonstrates their monodispersity

Series of experiments were conducted in order to find a method for fabricating precipitation PMAA spheres with an optimum diameter at which they could be easily observed and tracked using optical microscopy, in a size range between 1 to 10 μm . Firstly, by modifying the initial synthesis which was developed by Huang, et al. [28], the concentration of the initiator (ACCN) was increased from 0.04 wt% to 0.12 wt%

and the concentration of the monomer was kept constant. This resulted a higher yield in particle formation and a slight increase in particle diameter (~ 800 nm). In concentrations higher than 0.12 wt% of initiator, no significant change was seen in the size and the number of fabricated particles. Next, the concentration of monomer was increased from 2 wt% to 4 wt% and the concentration of the initiator was increased proportionally from 0.04 wt% to 0.08 wt%. In brief, 0.4 ml divinylbenzene-80 (DVB-80), 4 ml methacrylic acid (MAA), 0.3 g 1,10-azobis(cyanocyclohexane) and 100 ml acetonitrile were placed into a 250 ml round bottom flask. After submerging the flask in a water bath and gently agitating it by a magnetic stirrer bar, the temperature was raised from room temperature to 85 °C over 2 h and then kept at this temperature for 24 h. At the end of the reaction the particles were separated by centrifugation from the reaction medium then washed at least three times with acetonitrile and finally with distilled water.

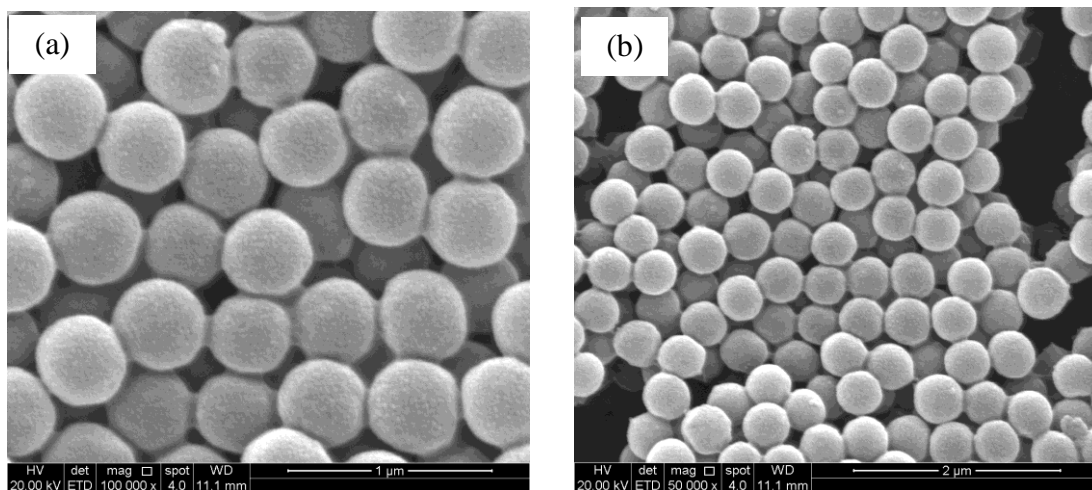


Figure 2.5 – SEM images taken at 100kX magnification (a) and 50kX magnification (b) from the precipitation polymerisation products fabricated via the modified synthesis method

2.3 Particle size measurement

Before evaporating platinum on the fabricated microspheres and utilising them as swimmers, the emulsion polymerisation products were sized using dynamic light scattering (DLS) in shrunken and swollen states in pHs lower ($\text{pH} = 2.5$) and higher ($\text{pH} = 10$) than the pK_a of methacrylic acid (MAA) ($\text{pK}_a \sim 5.5$). Figures 2.6 (a) and 2.6 (b) demonstrate the overlaid DLS graphs which exhibit the size of PMAA particles in low pH (shrunken state) and high pH (swollen state).

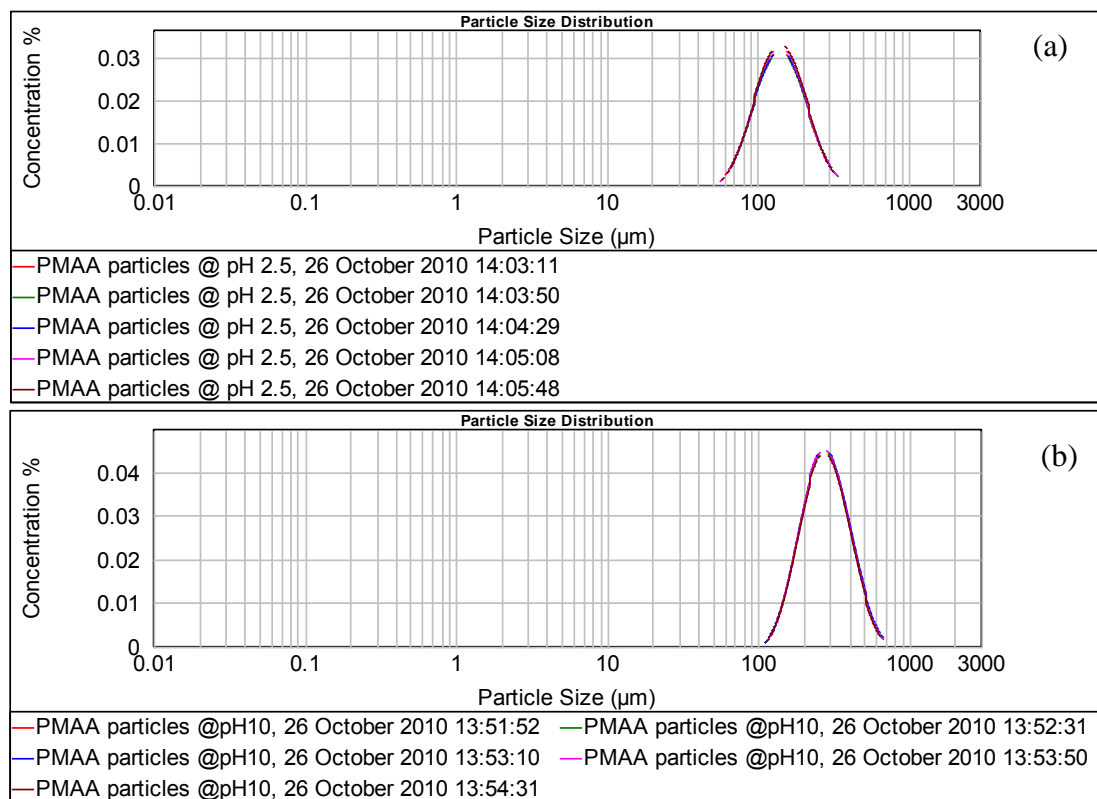


Figure 2.6 – Emulsion PMAA particles (a) shrunken at $\text{pH} = 3$ and (b) swollen at $\text{pH} = 10$

For precipitation polymerisation products, size change in different pHs was studied by preparing two dilute samples of particles in acidic ($\text{pH} = 3$) and basic ($\text{pH} = 10$) solutions.

Videos of the particles undergoing Brownian motion in solutions with different pHs were also captured and the captured videos were analyzed by a tailor-made particle

tracking program written in LabVIEW with the aim of recording the trajectories of random movements of the particles. The recorded data were then utilised to determine the diffusion coefficient of the particles suspended in the solution. Ultimately, using the calculated diffusion coefficients, the diameter of the particles in different pHs were obtained using ($D = k_B T / 6\pi\eta R$).

Results of the data analysis for 40 particles in each solution, showed a significant difference between the diffusion coefficient of the particles undergoing Brownian motion inside the acidic and the basic solutions. As in the equation above, all other parameters such as the Boltzmann constant, temperature and viscosity were the same for both solutions, the change in the diffusion coefficient of the particles could have only been due to a change in their radius (size).

Graphs 2.7 and 2.8 show the diffusion coefficient of the particles in acidic and basic solutions and the size distribution of the particles in each solution (obtained from the analysed data) respectively.

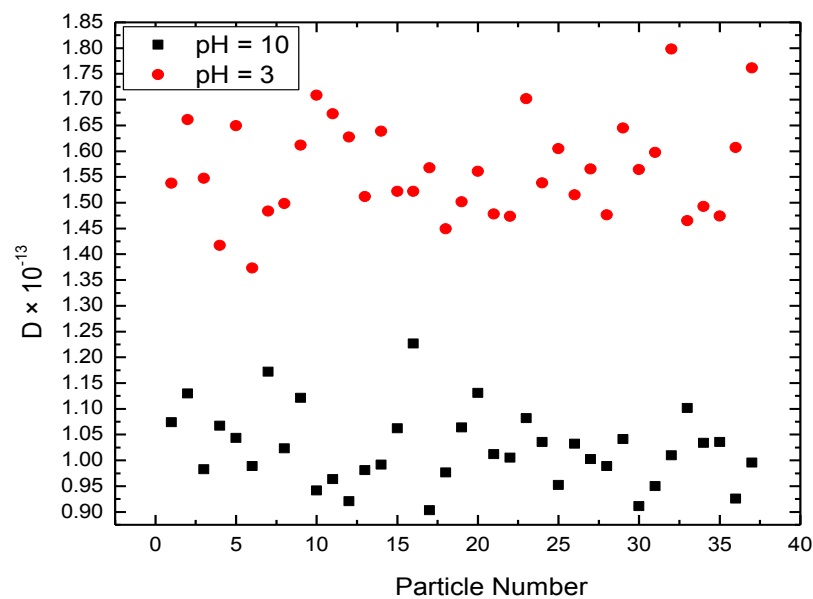


Figure 2.7 - Diffusion coefficient of PMAA particles fabricated via the modified precipitation synthesis process based on Ref. [28] representing the diameter of 1.6 μm in acid (pH = 3) and the diameter of 2.6 μm in base (pH = 10) confirming the results obtained in the ibidi[®] μ -Slide (Fig. 2.7)

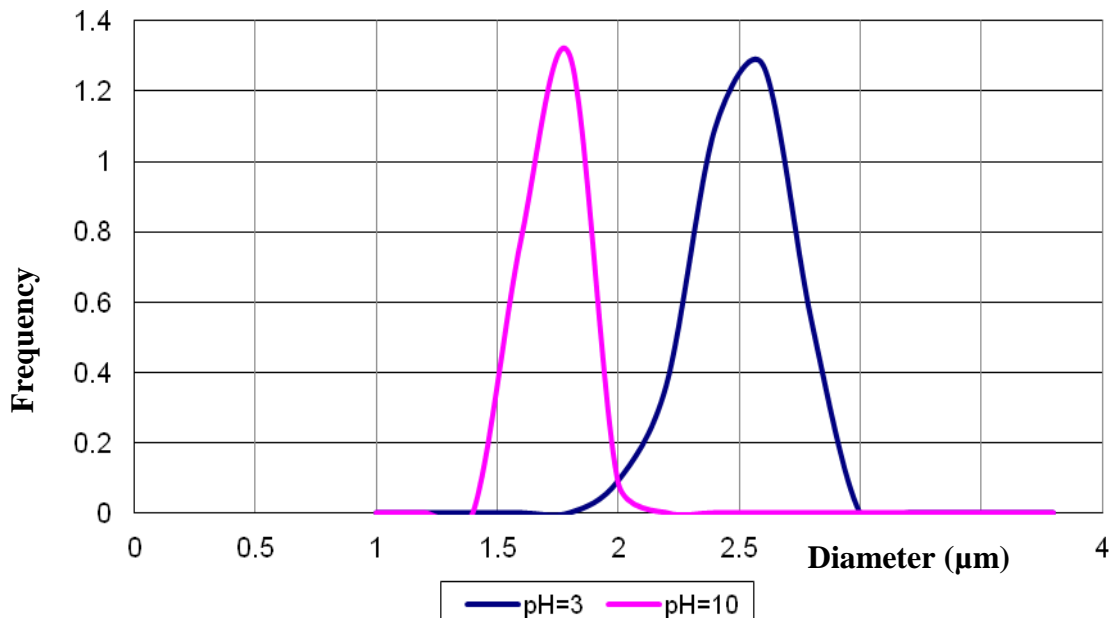


Figure 2.8 - Size distribution of PMAA particles fabricated by the modified precipitation synthesis process based on Ref. [28] in acid (pH = 3) and in base (pH = 10) based on 36 particles tracked in acid and 50 particles tracked in base

2.4 Reversibility of the pH response

Theoretically pH-responsive microgels should be capable of swelling and shrinking for an unlimited number of times in response to the variations in the pH of the solution they are suspended in. To ensure the reversibility of pH response of the PMAA particles for a reasonable number of times, in an experiment, videos were captured from around 10 particles in an acidic solution (pH = 3) and the solution was then titrated with sodium hydroxide until it turned into a basic solution at pH = 10. After capturing videos from the particles in base, the procedure was repeated again, this time by adding hydrochloric acid to the basic solution until the pH returned back to 3 again. Captured videos were analysed and the diffusion coefficient for particles of each section of the experiment was calculated. Graph 2.9 shows the reversibility of the pH response of the particles. It can be seen that the change in diffusion

coefficient of the particles is more dramatic after the first pH shift comparing to the second one and this is due to the change in the salt concentration of the solution which changes the interactions between the ions causing the size change of the particles.

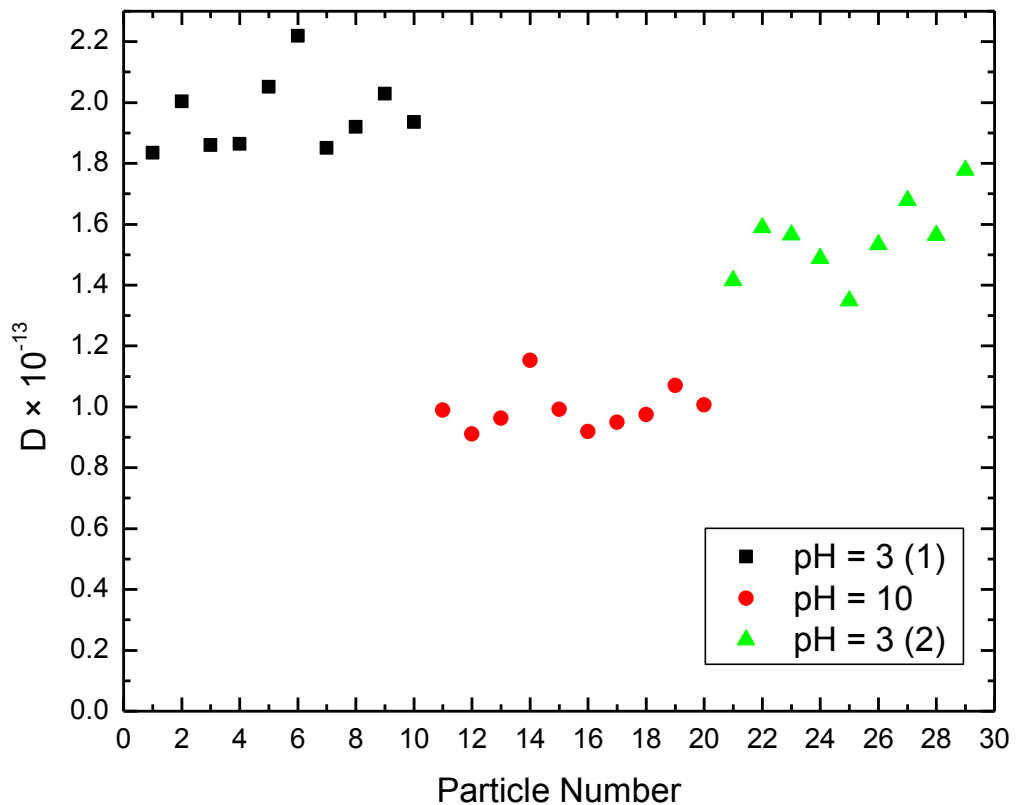


Figure 2.9 - Diffusion coefficient of PMAA particles fabricated via the modified precipitation synthesis process based on Ref. [28] in acidic and basic pHs showing the reversibility of pH response.

2.5 Particle size measurement over a pH gradient

To this point, size of the PMAA particles were only determined at certain acidic or basic pHs. To determine the rate at which this size change occurs and to find out the size of the particles in pHs between the acidic and basic pHs which the size has been determined, the particle size measurement was conducted over a pH gradient. To

achieve this, a solution of PMAA particles in a pH gradient, a 0.01 g^l⁻¹ solution of PMAA particles was prepared in distilled water. The pH of the solution was decreased from 5.52 to 1.23 by adding 1M hydrochloric acid (HCl). Next, the pH of the solution was gradually increased from 1.23 to 10.28 (while it was continuously stirred using a magnetic stirrer) by titrating the solution by adding droplets of 1M aqueous sodium hydroxide solution then 0.1M and 0.01M solutions respectively in pHs closer to the equivalence point. The pH values at which samples for size analysis were collected from the solution were 1.23, 2.68, 3.22, 4.55, 5.67, 7.33, 8.3, 9.57 and 10.28.

At each pH step, 400 µl of the solution was transferred into a spectroscopy cuvette and transmission microscopic videos were recorded for 20 suspended particles in free solution at 24 fps using a camera. Extracting the trajectory of the particles from the recorded videos enables calculating the average value of their squared displacement as a function of time. For these nonpropulsive, purely Brownian particles of radius R, the mean squared displacement is given as:

$$\Delta L^2 = 4D\Delta t \quad (1)$$

and the slope is controlled by the particle diffusion coefficient

$$D = \frac{k_B T}{6\pi\eta R} \quad (2)$$

where $k_B T$ is the thermal energy and η is the viscosity of water. For this experiment, the values for temperature and viscosity of water were 292 K and 1.00 mPa .s respectively. By plotting the calculated squared displacements as a function of time for each pH step, the obtained graphs can be fitted to eqn (1). These fits yield the diffusion coefficient of the particles at each pH and therefore the radius of the particles of each step can be calculated using eqn (2).

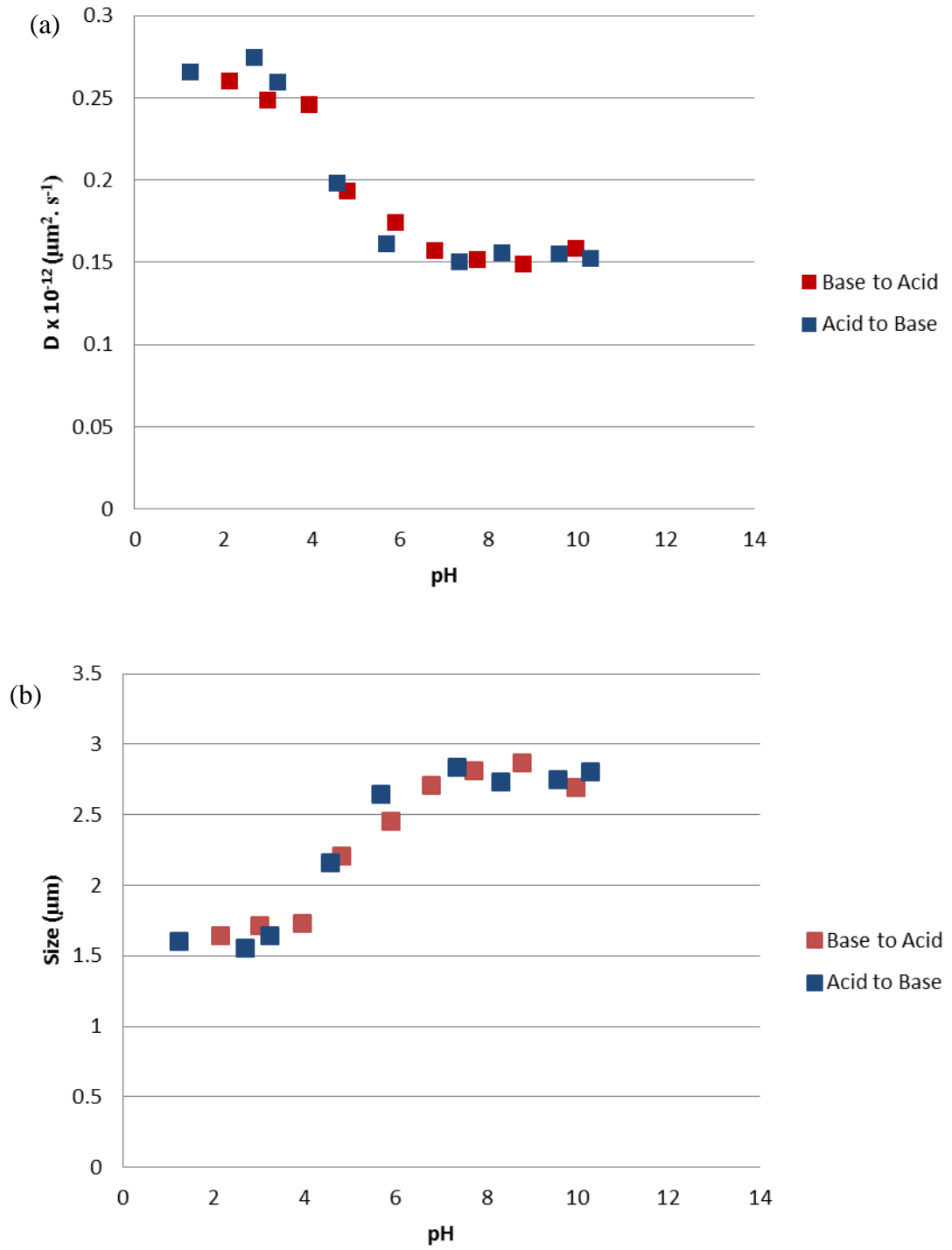


Figure 2.12 – (a) Diffusion coefficient vs pH graph and (b) size vs pH graph plotted for PMAA particles undergoing Brownian motion while the pH was gradually increased from 1.23 to 10.28

2.6 Preparation of pH responsive microswimmers

2.6.1 Desalination of the particles by dialysis

Prior to evaporating platinum onto emulsion polymerisation products, these particles required desalination. As both sodium hydroxide (NaOH) and methacrylic acid (MAA) were among the building blocks of our emulsion particles, any unreacted monomer would react with the excess NaOH to form sodium methacrylate salt. Decreasing the salt content of the particles was essential as it has been reported that presence of salt in the solution prevents the propulsion of catalytic swimmers. As it can be seen in the SEM images below, before desalination, emulsion particles were covered in salt crystals and after dialysis in deionized water for three times, each time for at least 12 h, salt concentration has been decreased significantly and no salt crystals were seen on their surface.

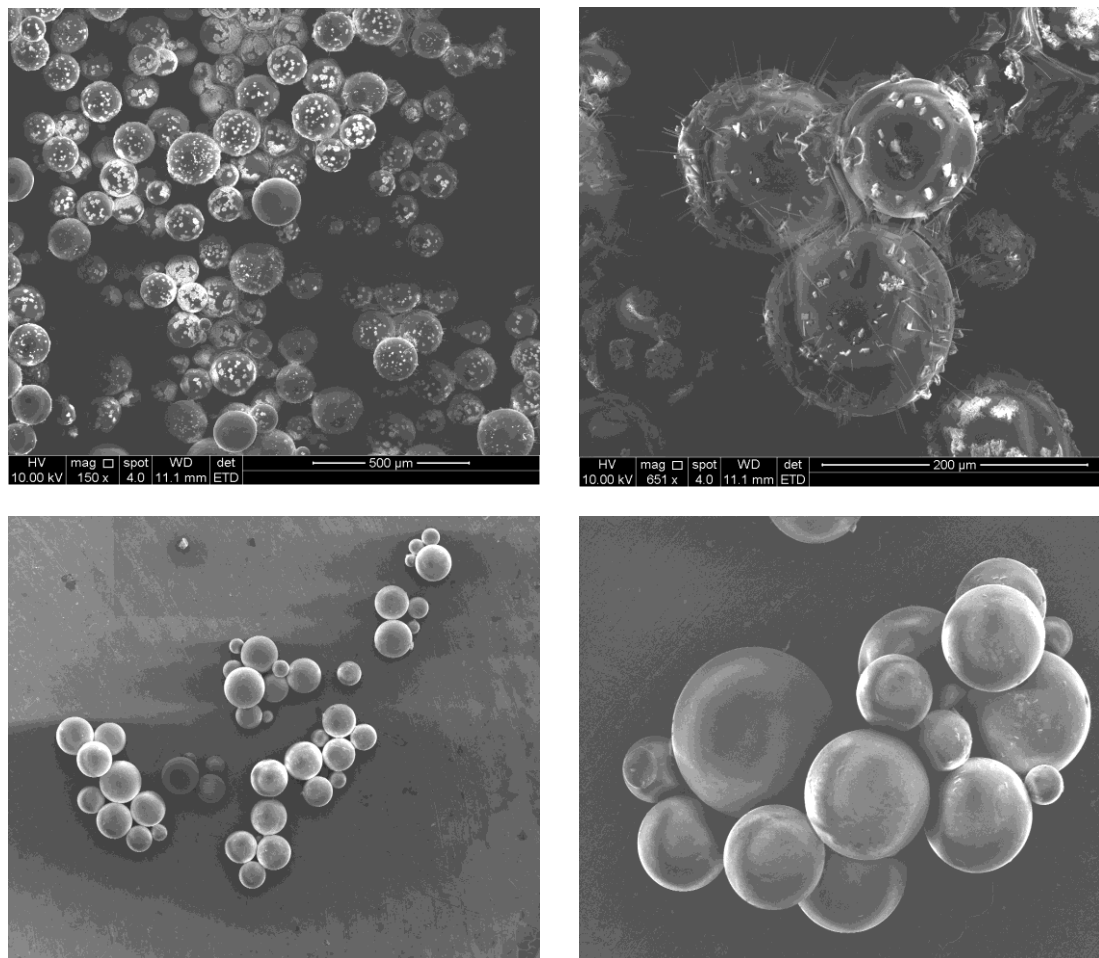


Figure 2.11 - (top) SEM images of dry emulsion PMAA particles with salt crystals on their surface (bottom) SEM image of dry emulsion PMAA particles after dialysis

2.6.2 Platinum deposition on emulsion products

As evaporating metals onto the hydrated particles was not achievable due to the high vacuum in the evaporation chamber, dried samples of emulsion particles were prepared and coated with a 20 nm thick layer of platinum. The outcome of the vacuum coating experiment showed that after rehydrating the dry samples which results a significant increase in the volume and the diameter of the microgel particles, instead of formation of particles with a stiff metal coated half and a soft swollen hydrogel half, asymmetric particles were formed with patches of platinum spreading on the half of the particle which was fully coated in the dry state. Suspending these platinum coated particles in 5% hydrogen peroxide solution unfortunately did not result in propulsion. This was probably due to the large size of these particles as increasing the concentration of hydrogen peroxide from 5% to 10% and increasing the thickness of the platinum cap from 20 nm to 30 nm did not change the outcome.

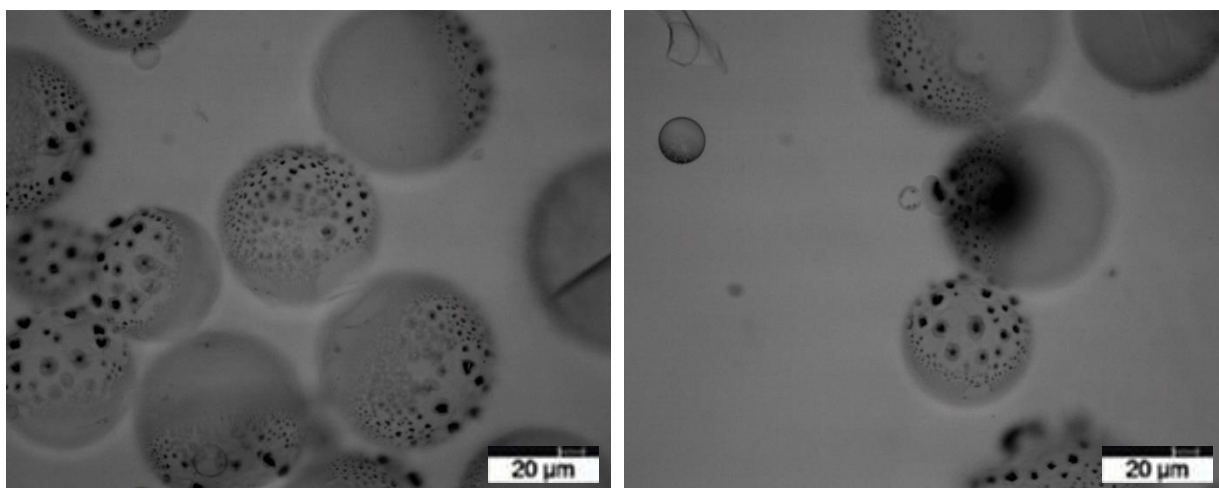


Figure 2.12 – Platinum coated emulsion PMAA spheres after rehydration with the metal cap broken into small patches extended on the surface of the particle

2.6.3 Platinum deposition on precipitation products

Precipitation PMAA particles were coated with platinum via thermal evaporation of platinum inside a vacuum coater with the aim of fabricating pH-responsive swimmers. Although SEM images and fluorescent images of the particles confirmed the presence of a platinum cap on the PMAA spheres, there were no signs of propulsion while observing and tracking the particles after they were added to 5% and 10% hydrogen peroxide solutions in neutral pH.

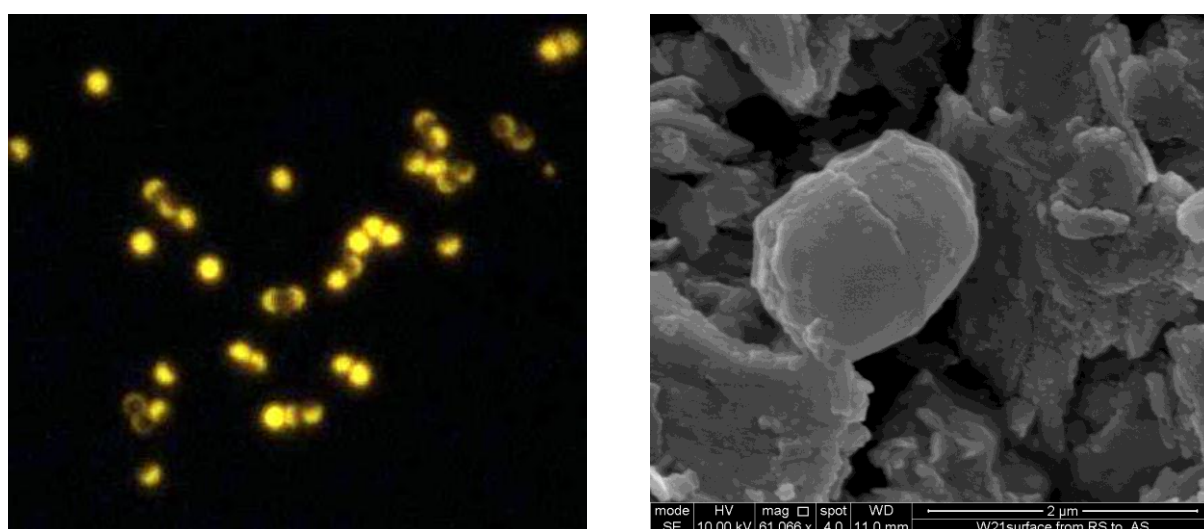


Figure 2.13 - Fluorescent and SEM images of platinum coated pH-responsive PMAA particles before hydration

After capturing videos from the particles right after hydrating them in water, it became clear that in contrast with our previous experiment with 50 μm emulsion PMAA particles, where after hydration the cap was broken into small pieces still attached to the surface of the particle, the platinum caps on the 2.5 μm precipitation PMAA particles came off completely as a result of the dramatic expansion of the particle after hydration. A second attempt was made by evaporating around 10 nm of chromium and around 20 nm of gold onto the particles in one stage before coating them with platinum, to improve the adhesion of the catalyst. This attempt failed as

well and the three layer metal cap came off from the particles shortly after they were hydrated in water.

2.6.4 Fabricating PS-PMAA nanodimer swimmers

Since the attempts for platinum coating the pH-responsive PMAA particles were not successful, the idea of fabricating nanodimer swimmers, composed of a swimming module and a size changing module was examined. For the swimming module which was in charge of propulsion, 1 μm platinum coated PS spheres (Kisker, Germany) were employed, as the platinum cap was strongly attached to the stiff surface of the particles. As asymmetry is one of the most important requirements for propulsion of the phoretic swimmers and fully Pt coated PS spheres were incapable of swimming in hydrogen peroxide solutions, we tried attaching a 2.5 μm pH-responsive PMAA to them with the aim of providing the required asymmetry plus adding a size changing unit to the swimmer to make us control the velocity of the particle by changing the pH.

At first, two solutions containing equal concentrations of platinum coated PS spheres and precipitation PMAA particles were mixed together so the particles could collide and attach to each other as a result of the interactions between their surface charges. Although a significant number dimer swimmers consisting of a PS sphere and a PMAA sphere were found in the final solution after mixing, none of them propelled after hydrogen peroxide was added to the mixture.

As we thought the reason that the fabricated swimmer do not propel might be due to the weakness of the electrostatic bonds between the two particles which does not provide the required asymmetry for propulsion, a dried sample of dimers was heated up to 160 $^{\circ}\text{C}$ for 2 minutes on a heating stage with the aim of melting the PMAA

sphere, making it attach stronger to the PS sphere. While PS and PMAA spheres seemed to be strongly attached together after heating, again the dimers did not propel either in hydrogen peroxide solution after this stage.

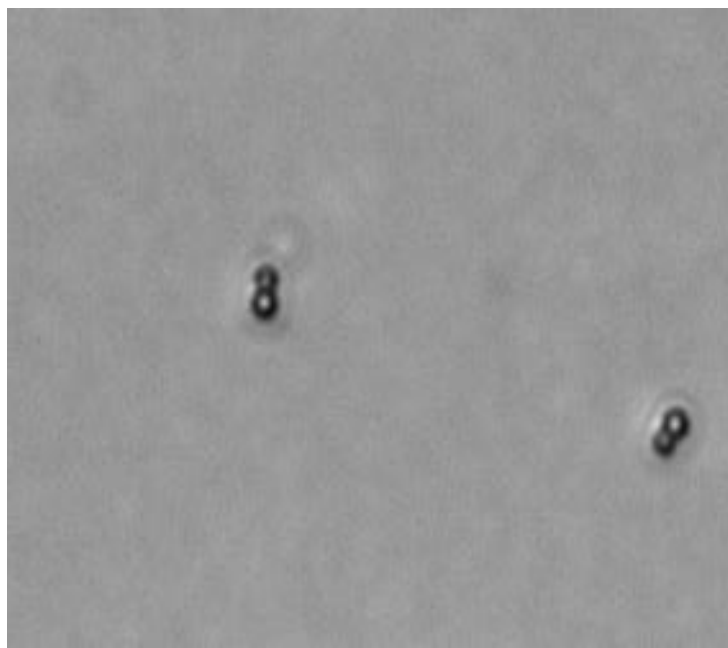


Figure 2.14 - Optical image of Pt coated PS/PMAA nanodimer swimmers in water

2.6.5 Growing PMAA around platinum coated PS spheres

In order to attach the size changing module (PMAA) to the propelling module (Pt coated PS spheres) via chemical bonds, growing PMAA around fully platinum coated PS sphere via precipitation polymerization was examined. The same procedure and recipe used for fabricating 2.5 μm PMAA spheres [28] was employed in this experiment, the only difference was adding 2 wt.% of 500 nm Pt coated PS spheres to the mixture before initiating the polymerization. The idea was, as the mixture was gently stirred during the polymerization process, some reactions would begin on the surface of the suspended PS particles in the solution and result

fabrication of either PS spheres completely coated with PMAA or asymmetrical particles with a platinum coated section and a size changing PMAA section.

SEM images taken from the products of this experiment showed that monomers (MAA) ignore the presence of the platinum coated PS spheres and grow separately during the precipitation polymerization.

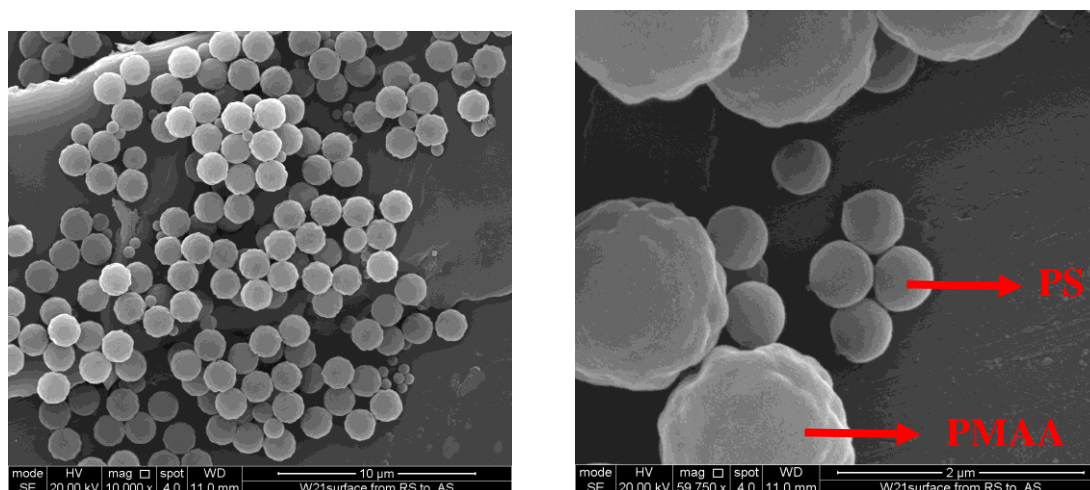


Figure 2.15 - SEM image of PMAA particles formed in presence of platinum coated PS spheres

2.7 Computational modelling

As none of the previous attempts resulted in fabrication of pH-responsive catalytic swimmers, another method examined for investigating the behaviour of plausible size changing swimmers was combining experimental data for the size response of pH responsive hydrogel beads, and the size dependency for propulsion velocity for spherical Janus swimmers in order to construct a simulation of the temporal and spatial evolution of swimmer distributions in a pH gradient. This simulation which was conducted with the assistance of Prof. Gavin Buxton (Robert Morris University), showed the factors that will influence the extent and rate of swimmer accumulation in this scenario and ascertained the interplay of both velocity and rotational motion due to size change. While the simulation parameters were chosen to closely match currently viable experimental swimmers, the obtained results also demonstrated the

great potential in expanding this approach to work with a range of stimuli, for example, the new hydrogel materials based on proteins that are currently in development [29].

To ensure the simulations were based on physically realistic swimmers, the size response of PMAA hydrogel beads was determined at different pHs based on the experiments conducted in section 2.5 of this chapter (Figure 2.16 top).

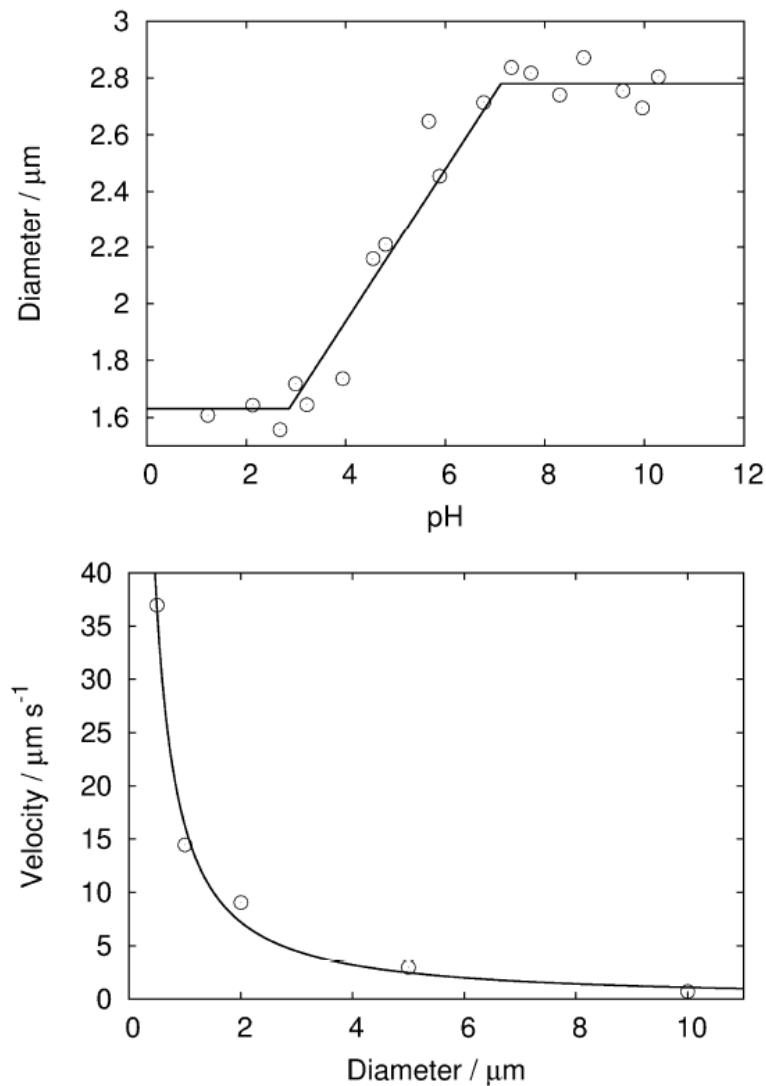


Figure 2.16 - Experimental data and numerical fits used in the simulation of pH responsive swimming devices (top) Size change as a function of pH (bottom) Propulsion velocity change as a function of diameter

Additionally, as catalytic swimmers have already been made by coating other polymeric beads (such as PS microspheres) with metallic catalysts [15], the average propulsion velocity of these type of swimmers could be plotted as a function of their diameter for constant fuel concentrations (Figure 2.16 bottom).

It has been reported that PMAA swells at higher pH and with increasing concentration of OH⁻ ions, PMAA chains in solution transform from a collapsed to stretched conformation around pH = pKa. This conformational change is induced by the electrostatic repulsion between the carboxylate anions. The equilibrium chain conformation is a balance between the electrostatic interaction of the charged carboxylate anion groups, which favours stretching, and the conformational entropy of the PMAA chains, which opposes stretching [30].

Equally, the adjustment in OH⁻ ions alters the ionic interaction and hydrophobic interaction between the carboxyl groups within the polymer chains, resulting a microphase separation or self-organizing phenomenon. Therefore, it can be seen that there is a clearly defined range of pH over which the size change occurs, and that over this range the size response is well described by a linear function according to the experimental results reported by De, et al. [31].

As a result, the size response (diameter, D) in this simulation was modelled as a continuous function returning constant size below and above the threshold values (D= 1.63 μm, pH < 2.86; D= 2.78 μm, pH >7.04), and a linear function was fitted to the experimental data in the interim (D=0.84+0.27*pH μm) (Figure 2.16, top). To determine the corresponding propulsion velocity (v) for a given sized device a numerical fit ($v=7.2.R^{-1.172} \mu\text{m} \cdot \text{s}^{-1}$) to experimental data obtained for hemi-spherical catalytic Janus particles was used for a range of diameters (Figure 2.16 bottom).

These data, combined with a model for stochastic Brownian phenomena, allowed running realistic simulations of the influence of a size changing stimulus (pH) on high densities of responsive swimmers. In all simulations a 1D periodic pH stimulus was considered, comprising equal width (0.5 mm) stripes with pH corresponding to the fully expanded and contracted states (pH=2.86 and pH =7.04), separated by the same width linear ramp of pH between these two limits. Initial concentrations of swimmers were even throughout this arrangement, permitting the evolution of any fluctuations to be monitored.

Figure 2.17a shows the time evolution of the probability density functions (pdf) of swimming devices in this periodic pH concentration. It is apparent that the devices show a statistical accumulation at the high pH (size expanded) zone, which reaches equilibrium after around 60 minutes. A control simulation in which the same size changing devices exhibited no propulsion (i.e. $v = 0 \mu\text{m} \cdot \text{s}^{-1}$) showed no response to the same pH pattern over an equivalent time-scale, revealing that propulsion is an essential requirement to produce this statistical accumulation behaviour. This simulation suggested that swimmers made from materials that can produce a size change in response to a pH gradient will exhibit a significant navigational response, which could be utilised as an autonomous navigation strategy.

As discussed earlier, two potentially competing factors determine the motion of each swimming device at a given position in the simulation: the modulation of intrinsic propulsion velocity due to the size, and the probability of being rotated within a given time step, which scales with $1/R^3$.

To further understand the roles of these two phenomena, additional simulations were run, where these effects were individually considered, (Figure 2.17 b-c). Figure 2.17 b shows the statistical response in the case where the devices velocity responds to pH

induced size change, but rotational rate remains constant: (averaged from radius at pH=2.86 and pH=7.04: $r=1.1 \mu\text{m}$; velocity only response). In this scenario, accumulation within the high pH region also evolved during the simulation. Equilibrium appeared to be established more rapidly compared to the full response simulation, after around 20 minutes, however the degree of variation induced in the pdf due to the gradient appeared rather less. On the other hand, Figure 2.17 c shows the evolution of pdf in the converse situation where device velocity was held constant (average velocity in regular simulation between pH=2.86 and pH=7.04: $v=5.68 \mu\text{m} \cdot \text{s}^{-1}$) but the rotational rate changed to reflect the pH induced size change (rotation only response). It is clear that this case also produces a pdf enhancement in the high pH regions, reaching equilibrium after around 60 minutes, however to a significantly lesser extent than in the other two cases. Figure 2.17 d compares the equilibrium probability density profiles (after 166 minutes) in these three cases (full response, velocity only, rotation only), and confirms the full response simulation produces the most significant density response to the 1D pH stripes.

The statistical response consequently appears to be due to the additive effect of both the size change induced velocity modulation, and rotational rate variation, which both act to concentrate swimmers in the expanded high pH region. Basically, the swimmers move more slowly when they are in the expanded high pH regions, and so spend more time in this zone. However, the extra contribution to the pdf enhancement made by the rotational modulation, also causing accumulation in high pH regions, is less easily visualised. As a result, although one of the driving forces for investigating size changing swimmers was to establish an analogy to *E. Coli* (based on the expectation that in the low pH, small diameter region, “tumbling” behaviour would be observed due to the rapid Brownian rotation rate, whereas in

high pH, large diameter regions “running” behaviour would be encouraged due to the slower rotational rate), this interpretation lead to an opposite response to that observed in the simulation, with swimmers having a larger probability of residing in the “tumbling” state i.e. low pH regions.

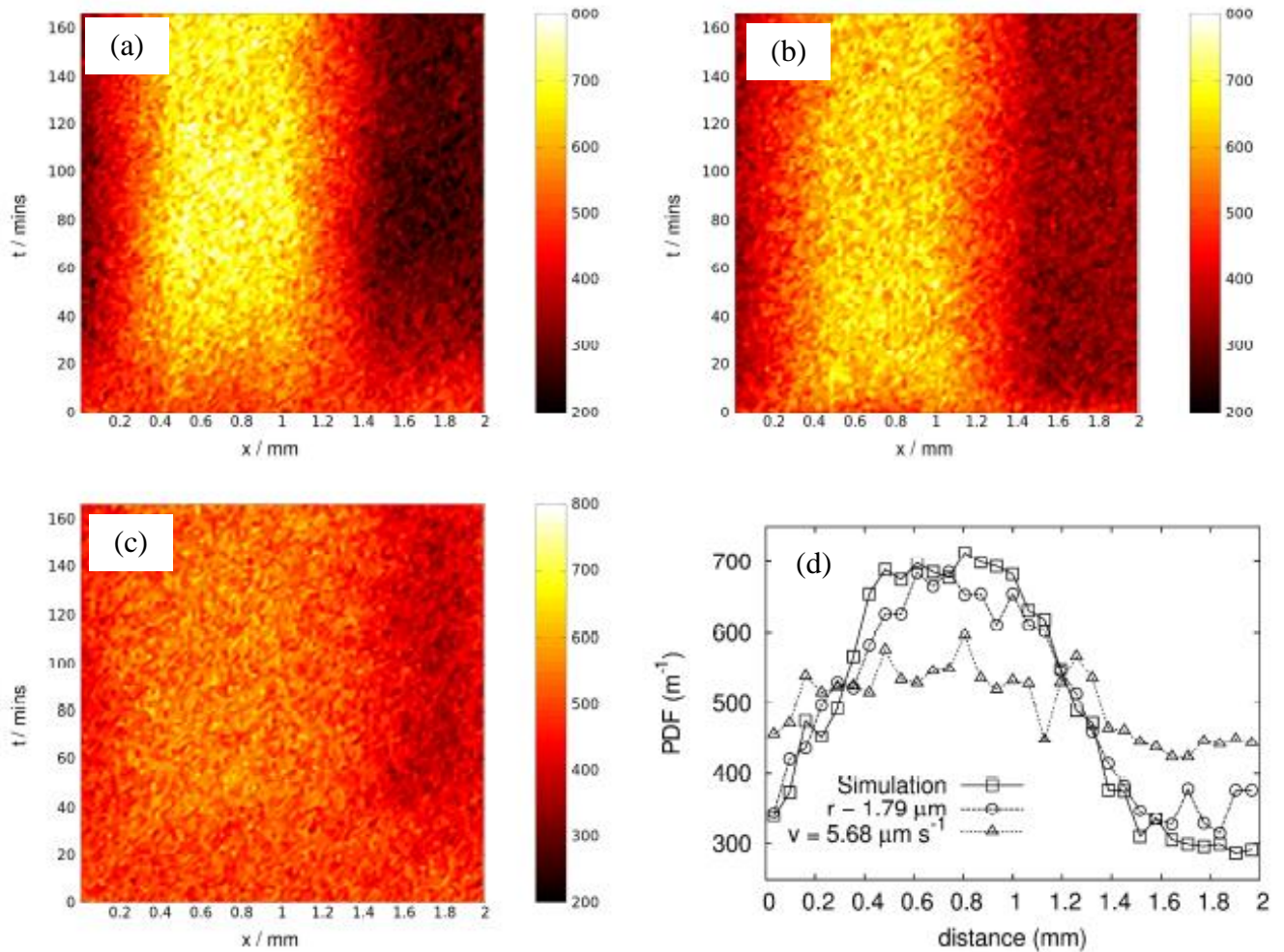


Figure 2.17 - Temporal evolution of swimming device densities in response to a 1D periodic pH (a) Full response (b) Velocity only response (rotation rate fixed at the value for a $1.1 \mu\text{m}$ swimmer) (c) Rotation rate only response (velocity fixed at $5.68 \mu\text{m} \cdot \text{s}^{-1}$) (d) Comparison of probability distribution function at equilibrium for the three response scenarios

To clarify the origin of this unexpected effect of size change on statistical accumulation for devices with no additional velocity modulation (as in Fig 2.17 c), a further simulation was run starting devices in the middle of the pH gradient region, where the pH decreases linearly from 7.04 to 2.86, to ascertain if their diffusion

behaviour shows any asymmetry, Figure 2.18 a. In this situation, as the pdf evolves, the constant velocity swimmers showed a tendency to move up the pH gradient. Figure 2.18 b shows the slice through the data at the end of the simulation ($t = 100$ s) for both constant velocity swimmers and through a similar simulation where both the velocity and rotation vary (full response). This confirms the asymmetry in the pdf for constant velocity swimmers. As these particles move down the pH gradient they rotate more and are more likely to turn around than if they head up the pH gradient. In effect, the rotation appears to provide a slight 'rattling in cage' effect where the particles are very slightly contained due to the rotational effects. However in contrast, the fully responsive swimmers do not spread out as much in this direction, presumably as they slow down as they move up the pH gradient.

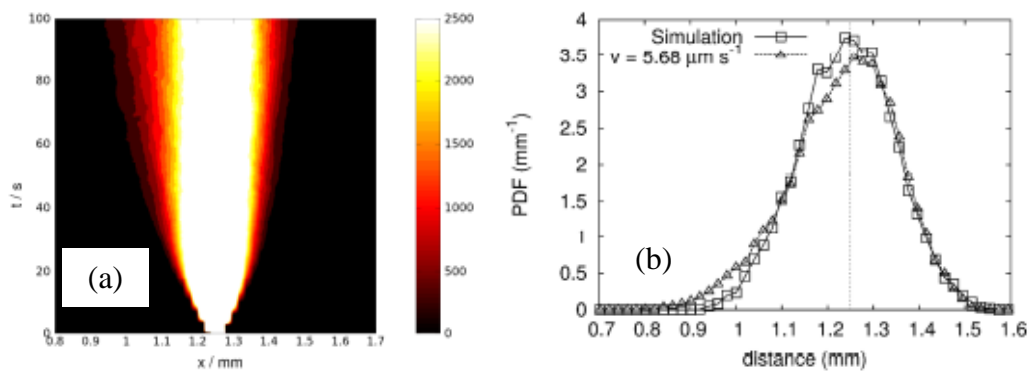


Figure 2.18: (a) pdf evolution for devices with constant velocity ($v=5.68 \mu m \cdot s^{-1}$) but varying rotational rate (rotational response) with starting positions in the middle of the pH gradient (1.25 mm; pH decreases with increasing x). (b) Comparison of pdf distributions after 100 seconds for both full response and rotation response swimming devices.

Lastly, the effect of the magnitude of the size change on the equilibrium pdf for fully responsive swimming devices was also considered (Figure 2.19). It can be seen that the statistical response to the pH gradient is significantly more pronounced with a

two-fold enhanced size change and reduced for a hypothetical half as responsive material. This is due to the more dramatic modulations in velocity and rotation rate that are associated with larger size changes.

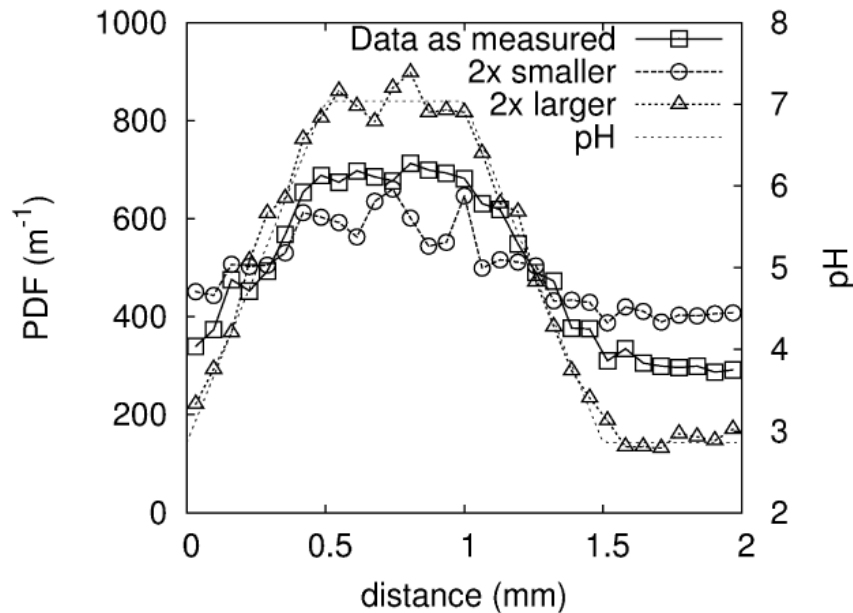


Figure 2.19 - pdf after 100 seconds for fully responsive swimming devices as a function of size response, superimposed with pH profile.

To conclude, simulations based on realistic pH responsive size changing hydrogel swimmers placed in a 1D pH stimulus predicted significant statistical accumulation in high pH (expanded) regions and in contrast to experimental reports of a very slow (days) statistical response for fixed sized swimmers in a fuel gradient [32], significant statistical response was observed within 20 minutes for the simulated size changing active swimmers. This suggests that size changing can potentially provide a more rapid navigational strategy for swimming devices. This enhanced behaviour is perhaps due to the enhanced propulsion velocity modulation possible by changing swimmer size as the relationship of swimmer velocity to fuel concentration is linear [15], whereas the reciprocal relationship of swimmer size to propulsion velocity allows a more dramatic modulation. While the velocity only simulations showed that

velocity modulation is the major, and fastest acting factor behind the observed pdf response, interestingly, the concurrent modification in rotation rate appears to act in synergy with the velocity modulation to further enhance the degree of statistical accumulation.

In summary, after a series of unsuccessful experimental trials, these simulation results clearly show a mechanism to achieve autonomous spatial control over swimming devices in response to stimuli such as pH, within a uniform fuel concentration. This is an important step closer to the goal of directing these devices towards targets, either within the body or microfluidic networks and opens up the potential to eventually use size-changing navigation methods to seek biological targets, such as a biological marker for a particular therapeutic target.

References

1. K. Park, *Controlled Drug Delivery: Challenges and Strategies*, ACS Professional Reference Book, American Chemical Society: Washington, D.C., 1997.
2. I. Roy and M. N. Gupta, *Chem. Biol.*, **2003**, 10, 1161.
3. L. J. M. Gaspar and G. Baskar, *Chem. Commun.*, **2005**, 3603.
4. P. Terech and R. G. Weiss, *Chem. Rev.*, **1997**, 97, 3133.
5. Y. Yang, M. Suzuki, S. Owa, H. Shirai and K. Hanabusa, *J. Am. Chem. Soc.*, **2007**, 129, 581.
6. X. Huang and R. G. Weiss, *Langmuir*, **2006**, 22, 8542.
7. D. Ceylan and O. Okay, *Macromolecules*, **2007**, 40, 8742.
8. F. He, Y. Tang, S. Wang, Y. Li and D. Zhu, *J. Am. Chem. Soc.*, **2005**, 127, 12343.
9. M. de Loos, B. L. Feringa and J. H. van Esch, *Eur. J. Org. Chem.*, **2005**, 17, 3615.
10. D. Schmaljohann, *Adv. Drug Delivery Rev.*, **2006**, 58, 1655.
11. B. Jeong and A. Gutowska, *Trends Biotechnol.*, **2002**, 20, 305.
12. O. Warburg, *The Metabolism of Tumours*, English translation by F. Dickens,

- Constable: London, 1930.
13. S. Dai, P. Ravi and K. C. Tam, *Soft Matter*, **2008**, 4, 435.
 14. Z. Sui, W. J. King, W. L. Murphy, *Adv.Mater.*, **2007**, 19, 3377–3380.
 15. J. Howse, R. Jones, A. Ryan, T. Gough, R. Vafabakhsh and R. Golestanian, *Phys. Rev. Lett.*, **2007**, 99, 8–11.
 16. N. A. Peppas., *Hydrogels in Medicine and Pharmacy*, CRC. Press, Boca Raion, FL, 1987.
 17. L. Baraban, M. Tasinkevych, M. N. Popescu, S. Sanchez, S. Dietrich, O. G. Schmidt, *Soft Matter*, **2012**, 8, 48–52.
 18. R.H. Pelton, P. Chibante, *Colloids Surf.* **1986**, 120, 247.
 19. J. Clarke, B. Vincent, *J. Chem. Soc. Faraday Trans. I.* **1981**, 77, 1831.
 20. M. Frank, W. Burchard, *Makromol. Chem. Rapid Commun.* **1991**, 12, 645.
 21. M. Antionietti, T. Pakula, W. Bremser, *Macromolecules* **1995**, 28, 4227.
 22. S. Neyret, B. Vincent, *Polymer* **1997**, 38, 6129.
 23. G. Odian, *Principles of Polymerization*, John Wiley & Sons Inc.: Hoboken NJ, 4th ed, 2004.
 24. J.W. Goodwin, J. Hearn, C.C. Ho, R.H. Ottewill, *Br. Polym. J.* **1973**, 5, 347.
 25. B.R. Saunders, H.M. Crowther, B. Vincent, *Macromolecules* **1997**, 30 482.
 26. R.H. Pelton, P. Chibante, *Colloids Surf.* **1986**, 120, 247.
 27. Y. Zhang *et al.* *J. Colloid & Interface Science.* **2004**, 272, 321.
 28. J.Huang, S.Wan,M.Guo, H.Yan, *J.Mater.Chem.*, **2006**, 16, 4535.
 29. W. L. Murphy, *Soft Matter*, **2011**, 7, 3679.
 30. A. J. Parnell, S. J. Martin, C. C. Dang, M. Geoghegan, R. A.L. Jones, C. J. Crook, J. R. Howse, A. J. Ryan, *Polymer* **2009**, 50, 1005-1014.
 31. S. K. De, N. R. Aluru, B. Johnson, W. C. Crone, D. J. Beebe, J. Moore, *J. Microelectromech. Syst.*, **2002**, 11, 544–555.
 32. Y. Hong, N. Blackman, N. Kopp, A. Sen and D. Velegol, *Phys. Rev. Letts.*, **2007**, 99, 1–4.

Chapter 3: 3D ferromagnetic colloidal self-diffusiophoretic nanoswimmers

Catalytic microswimmers that generate propulsion by converting chemical energy into mechanical energy have demonstrated a great potential in cargo delivery, fluidic transport and self-assembly. Among the various types of these swimmers, catalytic “Janus” colloidal particles (propelled via the asymmetrical decomposition of a fuel of hydrogen peroxide into oxygen and water) have raised more interest among scientists due to their simple fabrication method and their ability to swim in three dimensions. An unwanted consequence of the ubiquitous Brownian motion present at micro- and nanoscale is that directing these highly propulsive particles to a desired target is inherently challenging. In this chapter, the progress made towards navigating these polymeric self-diffusiophoretic microswimmers via control of the orientation of the particle using an external magnetic field has been demonstrated. This new type of propulsive magnetic particle is fabricated via evaporating a simple, thin ferromagnetic nickel “steering” layer onto one half of the particles’ surface prior to depositing the catalytic “motor” layer. The trajectories of the propulsive magnetic Janus particles have been recorded in a variety of constant fuel concentrations, and in the presence and the absence of a uniform magnetic field to determine the effects of the magnetic field on the direction and velocity of the particles. The quantitative values obtained by tracking the particles in both 2D and derived orthogonal 1D data have also been reported to reveal the effectiveness of the steering layer and the motor layers, respectively.

3.1 Introduction and Background

Among several concepts proposed for designing artificial propulsive devices including DNA-linked colloidal magnetic nano-particles [1] and three-sphere swimmers [2], phoretic swimmers possess the advantage of propelling autonomously via *in-situ* conversion of the chemical energy generated by a catalytic reaction [3]. Although autonomous propulsion permits their use in microfluidic devices employed in medical diagnostics, performing more complicated tasks, such as targeted drug delivery cannot be achieved without discovering an efficient mechanism for controlling their trajectories and turning their random walk into directed motion. To achieve this, one must overcome the Brownian motion of the particle which affects the diffusion of the particle (position) and its rotation (orientation) simultaneously [3].

To date, three main methods have been proposed for navigating propulsive particles. In the first method, instead of studying the particles individually, achieving a statistical accumulation of particles in high fuel concentration regions is pursued by exploiting the trajectories of a collection of similar propulsive particles [4]. The second method aims to design and fabricate swimming devices (via self-assembly or other fabrication techniques) capable of producing different intrinsic trajectories such as on-the-spot rotation, and linear motion [5,6]. The third approach which has raised more interest so far, focuses on orientation control using external stimuli such as electric fields [7] and magnetic fields [8,9]. For example, directing bi-metallic nano-rod swimmers has been achieved by adding two additional thin layers of nickel into their structure and employing external permanent steering magnets to align the permanent magnetic dipole present within the thin nickel layers [8]. This method provides the advantage of accurate cargo delivery when it is coupled with real-time optical monitoring.

Comparing the methods described above, in addition to the higher accuracy in targeted drug delivery, navigating particles using an external magnetic field has the most immediate scope for applications. This is because magnetic particles are extensively used in biophysical and biomedical research and being able to direct these particles is beneficial in various areas, such as biomolecular and whole cell separation techniques [10], magnetic resonance imaging contrast agents [11] and immunoassays [10].

Employing polymeric magnetic swimmers in preference to magnetic bi-metallic nanorods provides a number of additional advantages for the stated applications. In general, there is an increasing interest in employing colloidal microbeads in numerous *in vivo* and *in vitro* applications, such as biodetection [12,13], and they are proven to have great potential in efficient cancer treatment [14]. In addition, and as discussed in chapter 3, the drug delivery and release capabilities of polymeric swimmers can be significantly enhanced by using a hydrogel in their structure. Furthermore, these types of swimmers are easier to fabricate than bi-metallic nanorods with fewer processing steps to render the route more cost effective. Finally, yet equally important, in contrast with high density nanorods, which quickly settle on the surface of a container due to the large density differences, are only capable of 2D motion on the bottom of a liquid-filled container. Polymer-based swimmers have near water densities thus they suspend in the solution to afford 3D motion in the bulk, which makes their transportation easier both in microfluidic and biological systems [3]. Consequently, such systems present a fully steerable swimming device capable of motion in all three dimensions as reported here.

Of the reported methods using an external magnetic field for steering catalytic nanoswimmers a relatively complicated deposition procedure is required. One method recommends evaporating Ta or Pd as a seed layer (up to 5 nm thickness) and then

stacking up between 6 to 8 bilayers of either Co/Pd or Co/Pt before evaporating the catalyst layer in order to create an out-of-plane *perpendicular* magnetic anisotropy [15]. This has been successfully used for directing silicon Janus particles at a surface [16]. Although this method has the advantage of the fidelity of the alignment between the catalyst layer and the magnetic layers, it requires a multistage fabrication and results a significant increase in the weight of the particles. Thus the fabricated particles quickly settle on the surface and are only able to perform a 2D motion on the surface. The second method suggests adding a thin layer (up to 60 nm) of a ferromagnetic material (such as Fe or Ni) under the catalyst cap to create an *in-plane* parallel magnetic anisotropy which is perpendicular to the catalyst layer [17]. This method has been used for directing bi-metallic nano-rods [8] and “rolled-up” Ti/Fe/Pt nanotubes [18] and has the advantage of easy fabrication and “flexible” magnetization allowing for future remagnetisation. Additionally, this method does not change the weight of the particles significantly therefore they are still capable of performing 3D motion in the bulk after addition of the magnetic layer.

In the work presented here, a thin nickel “steering layer” has been combined with an “engine layer” overcoat of platinum, producing a ferromagnetic dual-coated polymeric nanoswimmer. By placing a cuvette containing a solution of the ferromagnetic nanoswimmers in dilute hydrogen peroxide, within a uniform magnetic field generated by means of a pair of Helmholtz coils, directing the motion of the particles can be achieved in three dimensions. To quantify the degree of control exhibited using this approach the propulsive trajectories have been analysed in terms of the mean squared displacement (ΔL^2), along two orthogonal axis parallel and perpendicular to the field direction, x (ΔL_x^2) and in y (ΔL_y^2) respectively, and in two dimensions (ΔL_{xy}^2).

3.2 Orientation control using external field

3.2.1 Magnetic polymer beads: synthesis and applications

Synthesis and characterisation of polymeric magnetic particles has been a rapidly developing research topic in the last 10 years as the magneto-responsive polymeric beads have the advantage of providing the combined beneficial features of both magnetic particles and polymers. Presence of magnetic materials either as nanoparticles within the polymer matrix or as a surface coating imparts the magnetic properties to the polymeric microspheres and these properties can be exploited in many applications plus, the beads can be easily extracted from the system via an external magnetic field gradient. For example, the heat generated due to hysteresis losses and relaxation processes from exposing magnetic beads to an alternating field [19] can be utilised for cancer therapy by hyperthermia [20-25]. On the other hand, the polymeric structure of the beads facilitates the stabilisation of the magnetic materials and in the instance of employing pH-responsive or other size changing polymers, it offers shrinking and swelling ability resulting the desired elasticity to the beads. Moreover, the surface of polymeric beads can be modified with different functional groups allowing them to be utilised in applications such as isolation of microorganisms [26], cells [27] and nucleic acid sequences [28], plus various immunoassay methodologies [29].

Magnetic polymer beads can be synthesized via three general methods. In the first method, the polymeric bead is either fully or partially coated with magnetic materials via electro or vacuum deposition (Figure 3.1 a). In the second method, the polymer grows around a magnetic particles and the polymerisation takes place on its surface. These particles are commonly named core-shell particles (Figure 3.1 b). Finally, in the third method, magnetic nanoparticles are evenly distributed in the polymer matrix.

This can be conducted while polymerisation is taking place or in the case of utilising porous polymeric beads, after polymerisation (Figure 3.1 c). Below some of the methods employed for fabricating magnetic polymer beads are further outlined.

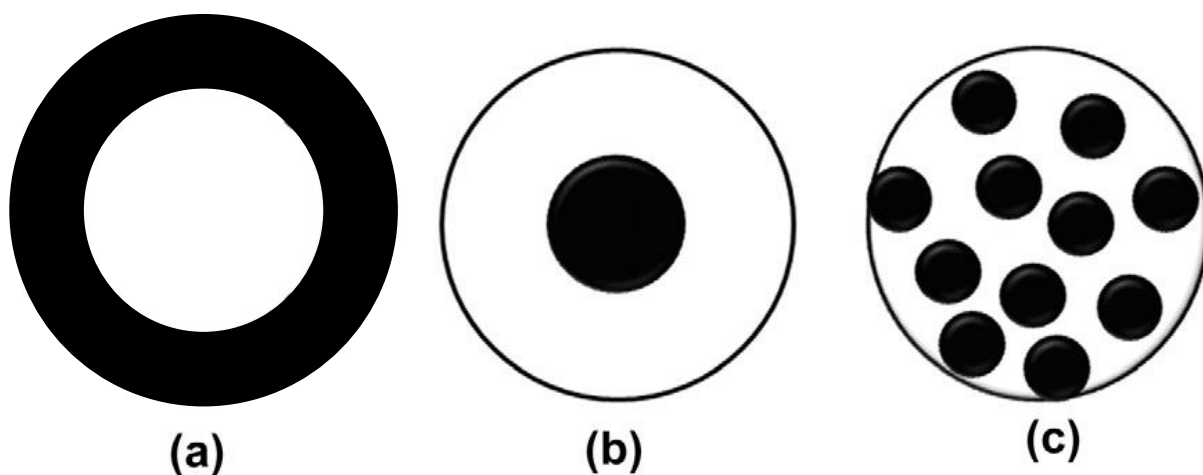


Figure 3.1 - Schematic representation of different types of magnetic colloidal particles: (a) polymer core coated with magnetic shell, (b) magnetic core with a polymer shell, (c) magnetic particles distributed in the polymer matrix.

3.2.1.1 Polymer core–magnetic shell beads

Magnetic materials can be deposited onto the surface of a polymeric bead via thermal evaporation at pressures well below atmospheric pressure (e.g. 10^{-6} mbar) [17] or through utilising the layer-by-layer (LbL) technique [30]. For example, the latter method [17] was used for fabricating Janus magnetic particles by depositing 60 nm Ni onto 2 μm diameter polystyrene beads via the previously demonstrated thermal evaporation techniques [31-33]. Moreover, the LbL technique has been used [30] for coating polystyrene beads with negatively charged maghemite particles by covering the beads with a positively charged polyelectrolyte prior to introducing the magnetic nanoparticles.

Another method for fabricating polymer core-magnetic shell beads is to polymerise monomer droplets that are stabilised by magnetic nanoparticles in a Pickering emulsion [34]. This is achieved when the self-assembly of magnetic nanoparticles takes place at the liquid-liquid interface of the droplets and promotes a solid-stabilised heterogeneous polymerisation. Gao et al. [34] have also reported that this method can be employed for fabricating more complex structures such as multihollow polymeric spheres with magnetic shells by polymerising monomers in water-oil-water (W-O-W) Pickering emulsions.

3.2.1.2 Magnetic core–polymer shell beads

Similar to polymer core–magnetic shell beads, LbL technique can be used for fabricating magnetic core-polymer shell beads. For instance, Thunemann et al. [35] have reported fabricating particles with a maghemite core and a two layer polymer shell consisting of a polyethylenimine (PEI) layer and a poly(ethylene oxide)-block-poly(glumatic acid).

In addition to the LbL technique, magnetic core-polymer shell particles can be fabricated via polymerising monomer and cross-linker molecules on the surface of magnetic particles. For instance, Luo et al. [36] have reported fabricating $\text{Fe}_3\text{O}_4/\text{SiO}_2$ core - Poly(n-isopropylacrylamide) shell particles with diameters around 500 nm via this method. Moreover, a recently developed method for these particles is a surface initiated polymerisation. In this method, *in-situ* polymer growth on the magnetic core was promoted by utilising surface-grafted initiators. This results in covalent bonds between the magnetic core and the polymeric shell and is suitable for synthesising magnetic particles with polymer brushes on their surface. For example, atom transfer

radical polymerization (ATRP) has been employed for coating magnetic particles with PS [37] and poly(2-methoxyethyl methacrylate) [38].

3.2.1.3 Magnetic beads with homogeneously dispersed magnetic particles

A straightforward method for fabricating magnetic beads with homogeneously dispersed magnetic particles in their structure is to disperse magnetic nanoparticles in a polymer solution and then emulsifying it as a disperse phase. The droplets of this dispersed phase can be transformed into spherical particles either by cross-linking or solvent evaporation. For example, Hou [39] fabricated magnetite κ -carrageenan particles by dispersing a mixture of magnetite, κ -carrageenan and hot water in oil using a non-magnetic stirrer to form a water-oil emulsion. After droplet formation, the emulsion was rapidly cooled in order to solidify the spheres and finally, the surface of the beads was hardened after reacting with poly(ethylenimine) (PEI).

Similarly, emulsion polymerisation can be employed for preparing this type of magnetic beads. In this method, magnetic micro- or nano-particles are mixed with the monomer prior to emulsification to a disperse phase. While polymerisation is taking place and the monomer molecules are joining together to form polymer spheres, magnetic particles get trapped in the polymer matrix, resulting a homogeneous dispersion. This method has been used for polymerising both hydrophobic and hydrophilic monomers in the presence of magnetic particles via oil in water and water in oil emulsions. However, as iron oxides are hydrophilic, hydrophilic monomers are mainly used for this application since utilising hydrophobic monomers results aggregation and immiscibility of magnetic particles and requires additional stages such as treating the surface of magnetic particles with sodium dodecyl sulphate or oleic acid [40].

3.2.2 Preparation of magnetic catalytic swimmers

Initial trials for fabricating magnetic catalytic swimmers involved coating half of commercially available polymeric magnetic microspheres with Pt via thermal vacuum deposition. First, 1.05 μm ProMagTM polymer-based magnetite spheres (Bangs Laboratories Inc. USA) were coated with 5 nm of Pt. Although these particles propelled with an average speed of 3 $\mu\text{m} \cdot \text{s}^{-1}$ in 5% hydrogen peroxide solution, due to their paramagnetic properties, they did not retain the magnetic alignment introduced in them by a permanent magnet after metal evaporation. Therefore they did not respond to direction changes of a uniform magnetic field. To overcome this issue, 2.0-2.9 μm SPHEROTM polymeric ferromagnetic particles (Spherotech Inc. USA) were employed in the next trial. After evaporating 5 nm Pt on to them, these particles also demonstrated propulsion in 5% hydrogen peroxide solution but since SPHEROTM particles were designed for biological applications that use gradients of magnetic field (typically generated by a permanent magnet) to separate these particles from non-magnetic substances, their magnetic material content was minimal compared to their polymer content and consequently they did not respond well to weak uniform fields generated by Helmholtz coils. As a result, although theoretically these beads should have been responsive to direction changes of a uniform magnetic field, the uniform magnetic field generated by laboratory devices was not strong enough to change their orientation.

To prepare ferromagnetic polymer spheres with stronger response to direction alteration of uniform magnetic fields, adding a relatively thick Ni layer (under the thinner Pt layer) to the surface of a polystyrene microsphere was developed. These magnetic Janus swimmers were fabricated by spin-coating a dispersed monolayer of fluorescent green (excitation/emission wavelength peaks: 468/508 nm, respectively)

Thermo Scientific polystyrene colloids with a mean diameter of 1.9 μm from ethanol on to a piranha cleaned glass slide followed by thermally evaporating 60 nm of Ni and 5 nm of Pt, respectively onto the glass slide (Figure 3.2). This evaporation procedure has been previously reported in the fabrication of other types of propulsive and non-propulsive Janus particles [31-33]. After fabrication, the particles were magnetized by a pair of 160 mT permanent magnets. After magnetization, particles were gently brushed from the glass slide using a small piece of wet lens tissue (Whatman) and then re-suspended in distilled water/aqueous hydrogen peroxide solution prior to the swimming experiments.

3.3 Helmholtz coils: producing a region of nearly uniform magnetic field

To understand and control the direction of the fabricated colloids, a uniform magnetic field is desirable. Helmholtz coils consist of two matching round coils of wire that are arranged symmetrically with a constant electrical current flowing in both of them either clockwise or anticlockwise. These coils are placed apart from each other at a distance equal to their radius and theoretically, at the center of their common axis (where the field generated by the coils adds up together) a region of nearly uniform magnetic field is present [41].

To derive the magnetic field strength as a function of axial distance for a pair of Helmholtz coils, the Biot-Savart law has to be introduced first. This law which is used for calculating the strength of a magnetic field (B) generated by a constant current for a random point (P) at any given distance from it, relates strength and

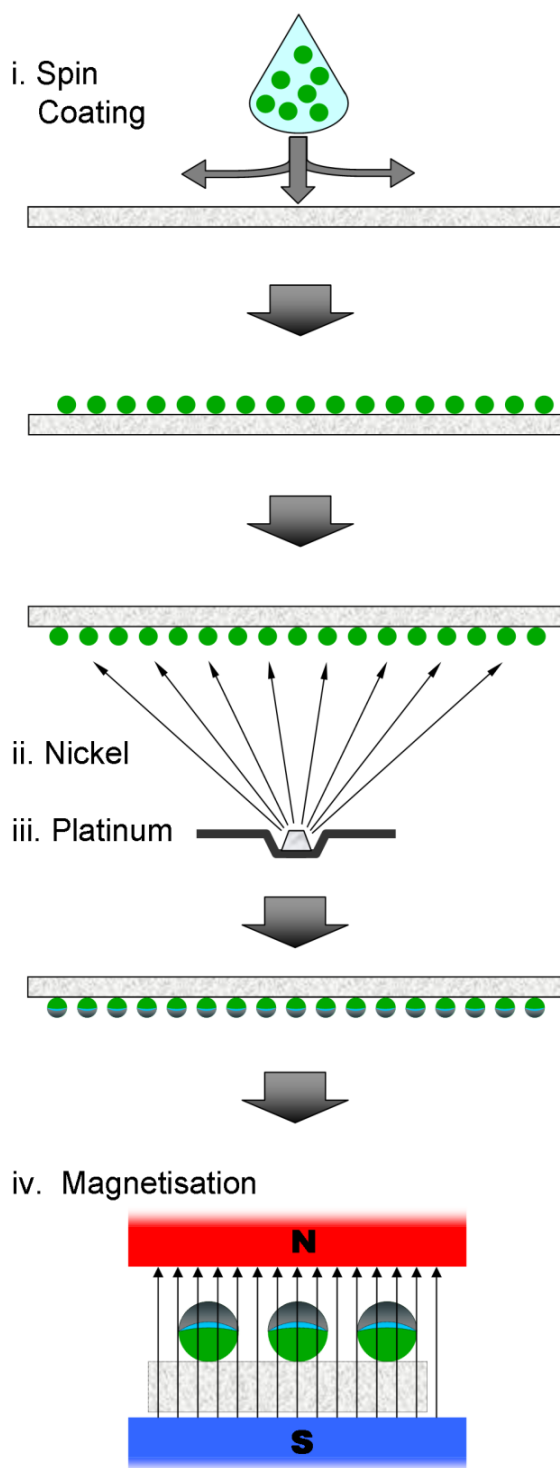


Figure 3.2 – Preparation of the ferromagnetic polymeric colloidal nanoswimmer (see text for details).

direction of the field to the distance from the increment of length to the point being studied and the strength and direction of the current running through the wire. According to the Biot-Savart law, the magnetic field ΔB , generated by the current (I) flowing in a given length of wire (Δl) for a point at the distance (r) from the wire can be determined from equation (1):

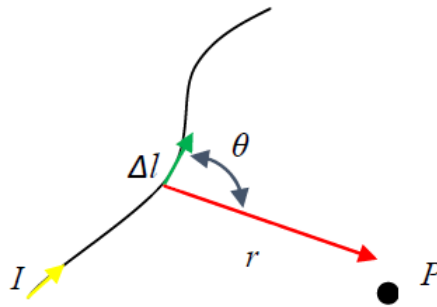


Figure 3.3 - Vectors used for calculating the magnetic field generated by a constant current

$$B = \frac{\mu_0 I \Delta l \sin \theta}{4\pi r^2} \quad (1)$$

Where μ_0 is the permeability constant ($1.257 \times 10^{-6} \text{ T} \cdot \text{m} \cdot \text{A}^{-1}$) and θ is the angle between the vector distance r to point P and the incremental vector length Δl .

For a circular loop with a constant current running through it, if the point P lies on the central axis of the plane of the loop with a distance x from it, the magnetic field can be determined with Biot-Savart law by dividing the loop into many small lengths of wire which are perpendicular to the vector distance to the point P . Next, the total magnetic field resulting from each of these small lengths can be calculated by summing up the fields generated by each incremental length.

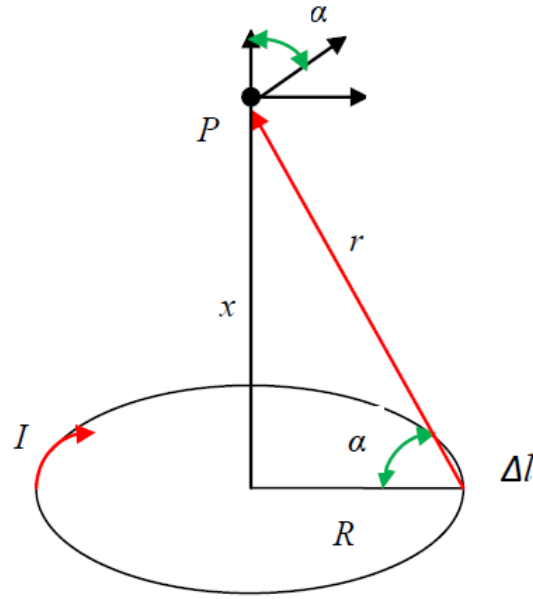


Figure 3.4 - Schematic diagram for calculating the axial magnetic field for a circular loop wire with constant current

As it can be seen in Figure 4, the magnetic field vector for point P (generated by Δl) can be resolved into perpendicular and parallel components. Therefore for the total magnetic field generated by the loop, we will have:

$$\vec{B} = \Sigma \vec{B}_{||} i + \Sigma \vec{B}_{\perp} j \quad (2)$$

Where $\vec{B}_{||} = \vec{B} \cos \alpha$ and $\vec{B}_{\perp} = \vec{B} \sin \alpha$. Since for all Δl s in the loop, the perpendicular components are equal and point to opposite directions, they cancel each other out and their sum will be zero.

Therefore:

$$\vec{B} = \Sigma \vec{B}_{||} i \quad (3)$$

Now as $\vec{B}_{||} = \vec{B} \cos \alpha$ and $B = \frac{\mu_0 I \Delta l \sin \theta}{4\pi r^2}$, we can conclude that:

$$\vec{B} = \Sigma \vec{B}_{||} i = \frac{\mu_0 I \sin \theta}{4\pi r^2} \cos \alpha \Sigma \Delta l \quad (4)$$

Since $\theta = 90^\circ$, $\sin\theta = 1$. Additionally, as $r = \sqrt{R^2 + x^2}$, therefore,

$$\cos \alpha = \frac{R}{\sqrt{R^2 + x^2}} \quad (5)$$

Finally, as the loop has been divided into many small lengths of wire (Δl), the sum of these lengths is equal to the circumference of the coil, therefore $\Sigma \Delta l = 2\pi R$.

Substituting the above parameters in equation 1 results:

$$B = \frac{\mu_0 IR}{4\pi(R^2 + x^2)^{3/2}} 2\pi R = \frac{\mu_0 IR^2}{2(R^2 + x^2)^{3/2}} \quad (6)$$

Equation 6 provides the strength of the magnetic field generated by a single loop of wire, as the diameter and the current running in all loops are equal to each other, the strength of magnetic field for a pair of Helmholtz coils with n turns will be:

$$B = \frac{\mu_0 n IR^2}{2(R^2 + x^2)^{3/2}} \quad (7)$$

In order to investigate the response of the fabricated Janus magnetic particles to an external orientating field, a pair of Helmholtz coils (diameter: 710 mm, number of turns: 332, copper wire diameter: 1.5 mm and of sufficient size to allow for an inverted microscope to be situated between the coils - see Figure 3.5) were employed to create a uniform magnetic field within the cuvette in which the particles under study were suspended. The strength of the magnetic field was modified by changing the current using a power supply and the magnetic field direction was altered by a switch which altered the direction of the current. The field had to be strong enough to overcome the Brownian effects acting upon the particles rotational diffusion but weak enough so that it does not change the initial magnetic alignment of the particles. As stated earlier, the field strength and uniformity is given by $B = \frac{\mu_0 n IR^2}{2(R^2 + x^2)^{3/2}}$ where μ_0 is the

permeability constant (1.257×10^{-6} T. m. A⁻¹), I is the coil current in amperes, n is the number of turns and R is the coil radius, and x is the position from the centre point,

both in meters. A voltage of 30V drew 0.925 amps, creating a uniform magnetic field of approximately ~ 10 mT. Particles suspended in solutions with different hydrogen peroxide concentrations were subjected to this field. The field direction was switched from (left to right) to (right to left) to also observe the response of the particles to different field directions.

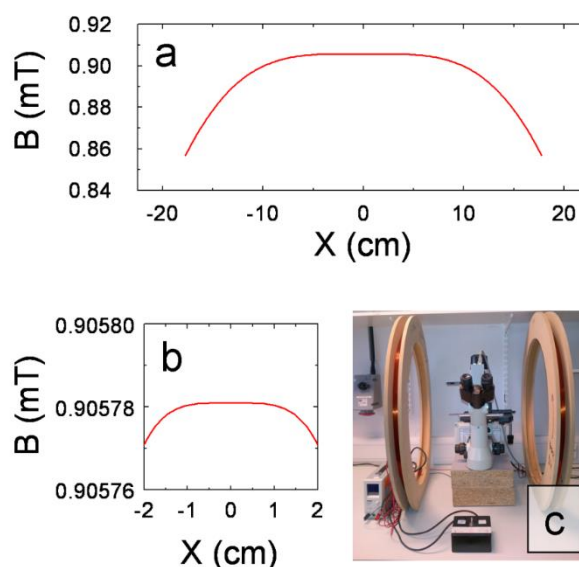


Figure 3.5 – (a) Calculated strength and uniformity of the magnetic field between the Helmholtz coils situated either side of the microscope, and (b) directly at the sample position and (c) the experimental set-up. Note, the microscope is raised so as to position the sample at the centre line of the coils.

3.4 Characterising the motion microparticles in the bulk

To determine the effect of the magnetic field on the overall motion of the swimmers, qualitative observation of the trajectories is not sufficient. Thus a method is required to quantify the differences between the motion of the swimmers in the presence and absence of any field which takes into account any Brownian effects. A method has been previously proposed (Chapter 1) for quantitative analysis of a particle trajectory which is valid for both propulsive and non-propulsive motion which is able to separate ballistic effects from Brownian effects. From the recorded trajectory of the particle, the average value of the mean squared displacement can be plotted as a function of

time, such that for a particle propelled with velocity V , the (2D projection) mean squared displacement is given as:

$$\Delta L^2 = 4D\Delta t + \frac{V^2\tau_R^2}{2} \left[\frac{2\Delta t}{\tau_R} + e^{2\Delta t/\tau_R} - 1 \right] \quad \text{for all values of } \Delta t \quad (8)$$

For time scales longer than τ_r ($\Delta t > \tau_r$), where the exponential term has decayed to zero, the mean squared displacement reduces to:

$$\Delta L^2 = (4D + v^2\tau_R)\Delta t - \frac{v^2\tau^2}{2} \quad \text{for } \Delta t > \tau_R \quad (9)$$

For time scales much shorter than τ_r ($\Delta t \ll \tau_r$) where the mean squared displacement is dominated by ballistic propulsion, and the exponential term may be approximated as a series and we obtain:

$$\Delta L^2 = 4D\Delta t + v^2\Delta t^2 \quad \text{for } \Delta t \ll \tau_R \quad (10)$$

This allows for the determination and deconvolution of the diffusion coefficient of the particle and its average velocity in that particular time scale. What is apparent from equations 9 and 10, and their respective appropriate time scales is that the mean squared displacement begins as parabolic (ballistic) in nature, moving to a linear behavior (enhanced diffusion) at a time larger than the rotational diffusion time. For a non-propulsive particle ($V=0$) undergoing purely Brownian motion, the mean squared displacement is linear in time with the slope ($=4D$) controlled by the particle's diffusion coefficient ($D = k_B T / 6\pi\eta R$), where R is the radius of the particle, η is the viscosity of the solution and $k_B T$ is the thermal energy. The particle's orientation is

also a function of its rotational diffusion ($\tau_r^{-1} = k_B T / 8\pi\eta R^3$) with a characteristic (inverse) time scale. For the 1.9 μm magnetic Janus swimmers, τ_r is approximately 5 s, and so data were fitted to the first 0.5 s. Using this method, the diffusion coefficient ($\mu\text{m}^2 \cdot \text{s}^{-1}$) and the velocity ($\mu\text{m} \cdot \text{s}^{-1}$) were determined from mean squared displacement data from the recorded trajectories of the control particles and magnetic phoretic swimmers. These are presented in Table 3.1.

Table 3.1 - 2D Particle Tracking Results. PS refers to our control particles with no coating, Ni, Pt, and Ni+Pt correspond to polystyrene particles coated with a layer(s) of the metal, respectively. The units of D are $\mu\text{m}^2 \cdot \text{s}^{-1}$ and v are $\mu\text{m} \cdot \text{s}^{-1}$. Data determined from approximately 50 particles for each value reported. The subscript in D_{XY} corresponds to the dimensionality of the trajectory used to determine D only, not a dimensionality of the diffusion coefficient. (Note, the 2D diffusion coefficient of a 1.9 micron particle in water, at 20 °C is $0.238 \mu\text{m}^2 \cdot \text{s}^{-1}$).

Particles	0% H ₂ O ₂		5% H ₂ O ₂	
	Field OFF	Field ON	Field OFF	Field ON
PS	$D_{xy} = 0.249$ $v_{xy} = 0.138$	$D_{xy} = 0.211$ $v_{xy} = 0.166$	$D_{xy} = 0.252$ $v_{xy} = 0.277$	$D_{xy} = 0.258$ $v_{xy} = 0.209$
Ni	$D_{xy} = 0.248$ $v_{xy} = 0.762$	$D_{xy} = 0.231$ $v_{xy} = 0.231$	$D_{xy} = 0.246$ $v_{xy} = 0.492$	$D_{xy} = 0.244$ $v_{xy} = 0.527$
Pt	$D_{xy} = 0.244$ $v_{xy} = 0.414$	$D_{xy} = 0.223$ $v_{xy} = 0.335$	$D_{xy} = 0.287$ $v_{xy} = 5.787$	$D_{xy} = 0.318$ $v_{xy} = 5.314$
Ni+Pt	$D_{xy} = 0.246$ $v_{xy} = 0.345$	$D_{xy} = 0.231$ $v_{xy} = 0.080$	$D_{xy} = 0.265$ $v_{xy} = 5.082$	$D_{xy} = 0.266$ $v_{xy} = 5.718$

From Table 3.1, it can be understood that only the particles with an outermost Pt cap (i.e. a pure Pt cap or a Ni sublayer with an outer Pt cap) inside a 5% hydrogen peroxide solution produce significant propulsion velocity with $v_{XY} \sim 5 \mu\text{m} \cdot \text{s}^{-1}$. Those with a Ni cap only, in the same solution, do not result in propulsion, despite having the reported ability to catalyse the decomposition of hydrogen peroxide [42]. This is likely due to a slower reaction rate in this case. As expected, optical monitoring also confirmed that

applying a magnetic field does not have an effect on the motion of propulsive particles without a magnetic Ni cap, nor does the magnetic field itself produce any noticeable propulsive effects confirming a uniform field. This verifies that the experimental set-up is not producing un-wanted thermal or magnetic gradients or other phenomena that could cause perturbations to the cuvette that would modify the particle trajectory, for example convective currents or a gradient field. Moreover, Table 1 shows that applying a uniform magnetic field does not change the overall 2D velocity of the propulsive magnetic (Ni+Pt) particles. This suggests that the total propulsive effect produced by the Ni+Pt capped beads is unaffected by the magnetic field, and only the orientation of the particles is altered. This is to be expected given that propulsion is the product of the chemical reaction which should be unaffected by the magnetic field or the orientation of the particle.

3.5 Analysing the 1D data

It is qualitatively apparent from the trajectories that the effect of the field was, as intended, to introduce asymmetrical propulsion between the axis parallel and perpendicular to the applied field direction (denoted X and Y respectively) (Figure 3.6, top, red line). Consequently, to quantify the differences between the motion of magnetic swimmers in the presence and absence of the field, the diffusion coefficient and velocity in these two directions were extracted from the 2D particle trajectories. As the overall 2D trajectory is made from two separate one dimensional trajectories it is also possible to consider the motion in purely X and Y, an example of which is

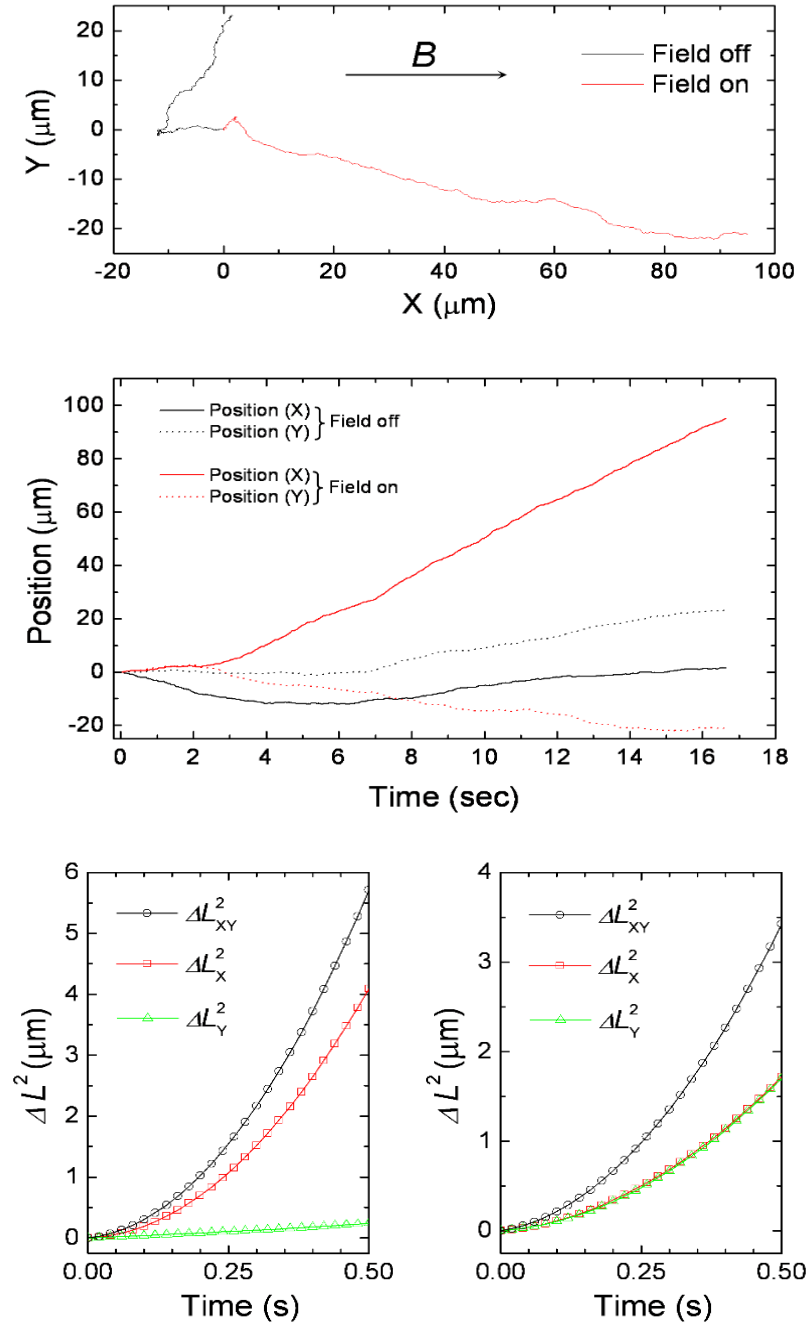


Figure 3.6 - (top) 2D trajectories for a Ni+Pt coated nanoswimmer with and without an external magnetic field, showing the expected enhanced random walk (—) and the effect of the magnetic field on the same nanoswimmer (—). (middle) 1D trajectories extracted from the 2D trajectory above with and without a field and the corresponding mean squared displacements with (bottom, left) and without an external magnetic field (bottom, right).

shown in Figure 3.6 (middle) with and without an applied field. This subsequently allowed ΔL_x^2 and ΔL_y^2 versus time graphs to be separately fitted. In the one dimensional case, equation 10 becomes:

$$\Delta L_x^2 = 2D\Delta t + v_x^2\Delta t^2 \quad \text{for } \Delta t \ll \tau_R \quad (11)$$

($\Delta L_x^2 = 2D\Delta t + v_x^2\Delta t^2$ and $\Delta L_y^2 = 2D\Delta t + v_y^2\Delta t^2$), thus obtaining component velocities along the x axis and the y axis as well as the values for the Brownian diffusion coefficients are determined from the 1D data. It should be noted that D extracted from both 1D and 2D data is the same, yet component velocities will be different. (Figure 3.6 – bottom).

Figure 3.7 shows the diffusion coefficient in the x and y direction for 46 Ni+Pt coated particles in 5% hydrogen peroxide in the presence and absence of a uniform magnetic field orientated parallel to the x axis, respectively. Comparison between the graphs above confirms that the presence of a magnetic field does not have a notable effect on the Brownian diffusion for the propulsive magnetic swimmers. For a 1.9 micron particle, in a 5% solution of hydrogen peroxide, the diffusion coefficient is $= 0.238 \mu\text{m}^2\text{s}^{-1}$ which is in close agreement with the values of D determined here. We attribute the spread in the data to a combination of experimental error and the relatively short sampling time (30 fps for 500 frames = 16.6 s). It should also be noted that the value of D, in both 1D and 2D data, are extracted from mean squared data which also contains a propulsive component (see eqns. 9 and 10) and so relatively large errors in D are often encountered when V is large, as fitting is often dominated by the squared term.

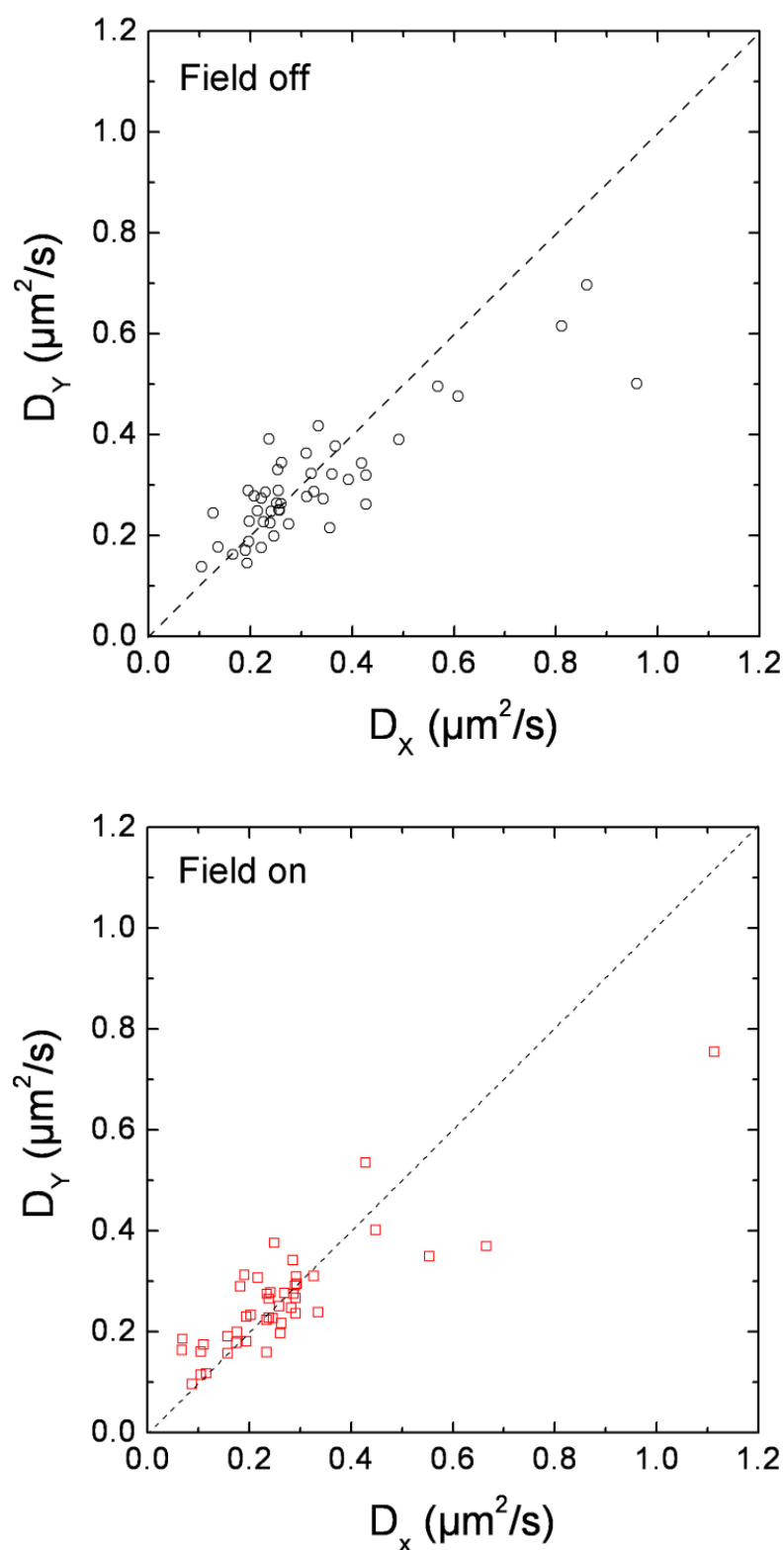


Figure 3.7 - Effect of magnetic field (parallel to x) on the measured diffusion coefficients for the Pt+Ni coated colloidal nanoswimmers ($n=46$). This data is shown for the same particles in a solution of 5% hydrogen peroxide with (bottom) and without (top) an applied field. The diffusion coefficient subscript refers to the value of D measured from a particular 1D trajectory. The dotted line is to aid the eye, showing a 1:1 correspondence.

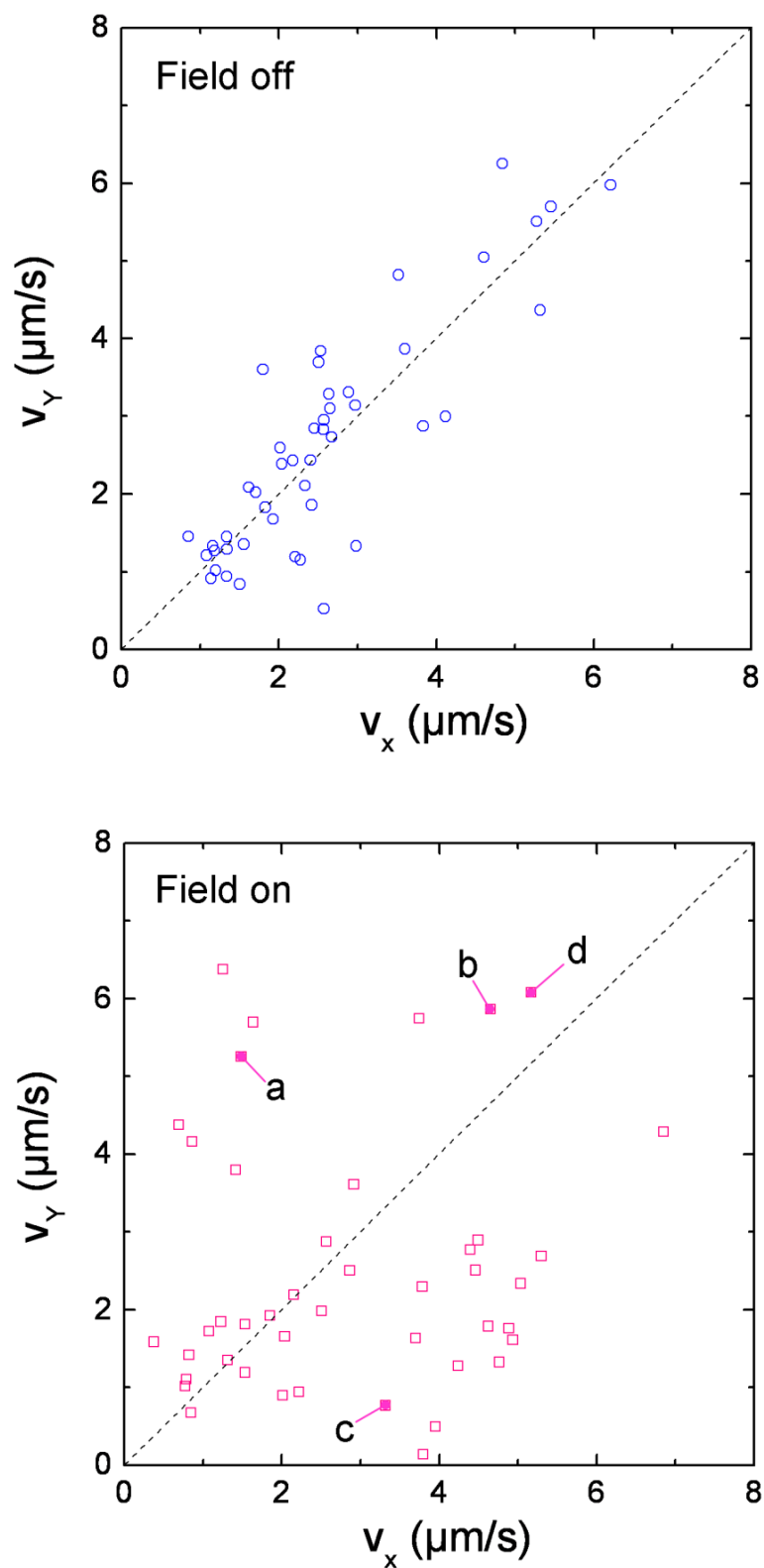


Figure 3.8 – Effect of magnetic field (parallel to x) on the 1D velocities for the Pt+Ni coated colloidal nanoswimmers ($n=46$). This data is shown for the same particles in a solution of 5% hydrogen peroxide with (bottom) and without (top) an applied field. The dotted line is to aid the eye, showing a 1:1 correspondence between V_x and V_y . Specifically labelled results are referred to in the text.

For each 2D propulsive particle, there exists a velocity in the x-direction and a velocity in the y-direction. For each particle these are plotted as an x-y graph in Figure 3.8, with and without the applied field.

Without an applied field there is near 1:1 relationship between velocities in x and in y, with an average velocity in each direction of approximately $2.5 \mu\text{m} \cdot \text{s}^{-1}$. The slight divergence from the 1:1 correlation is due to the relatively short duration for which movies are recorded, relative to the rotational diffusion time for the particle. The rotational diffusion time (τ_R) corresponds to the time taken for a singularly ordered system to become isotropic. In the case of a propulsive colloidal microswimmer this equates to the time taken for its propulsive director (the direction the chemical reaction propelling it) to bear no relationship to its starting direction. For a movie of 16 s, approximately 3-4 times its τ_R there is still some chance that propulsion may be seen to be in a single orientation, i.e. in x only, resulting in $V_X > V_Y$. The range of values for V_X and V_Y are as expected, and range from $1 \mu\text{m} \cdot \text{s}^{-1}$ to $6 \mu\text{m} \cdot \text{s}^{-1}$ and is consistent with previously reported results of similar colloids [3]. What is clear from these data is that in the absence of a field, particles are equally propulsive in x and y, and show no clear distinction between the two but when the field is turned on (Figure 8, bottom) there is a clear deviation from this 1:1 correspondence between V_X and V_Y , indicating propulsion in a single direction.

Closer inspection of this data reveals several interesting features. Firstly, there are a set of microswimmers which are unaffected by the application of the field and still $V_X \approx V_Y$ and the data points lie on, or near the 1:1 line. There is then a clear group of particles which show $V_Y \gg V_X$ and lie near to the V_Y axis with the propulsion velocity

resolved perpendicular to the applied field, and a third group in which $V_X > V_Y$ and are situated below this 1:1 correspondence line being an indication that propulsion along the applied field direction is dominant.

The observation that the application of a magnetic field in the x direction favours propulsion velocity in this direction (for this third group) for many Pt+Ni swimmers is encouraging. These data points indicate the desired effect of aligning the propulsion producing cap parallel to the field, and so producing a larger propulsion vector in this direction, while reducing the component in the y direction. Example trajectories for a swimmer showing this behaviour are shown in Figure 3.6 and more examples are available in the following pages (Figure 3.9).

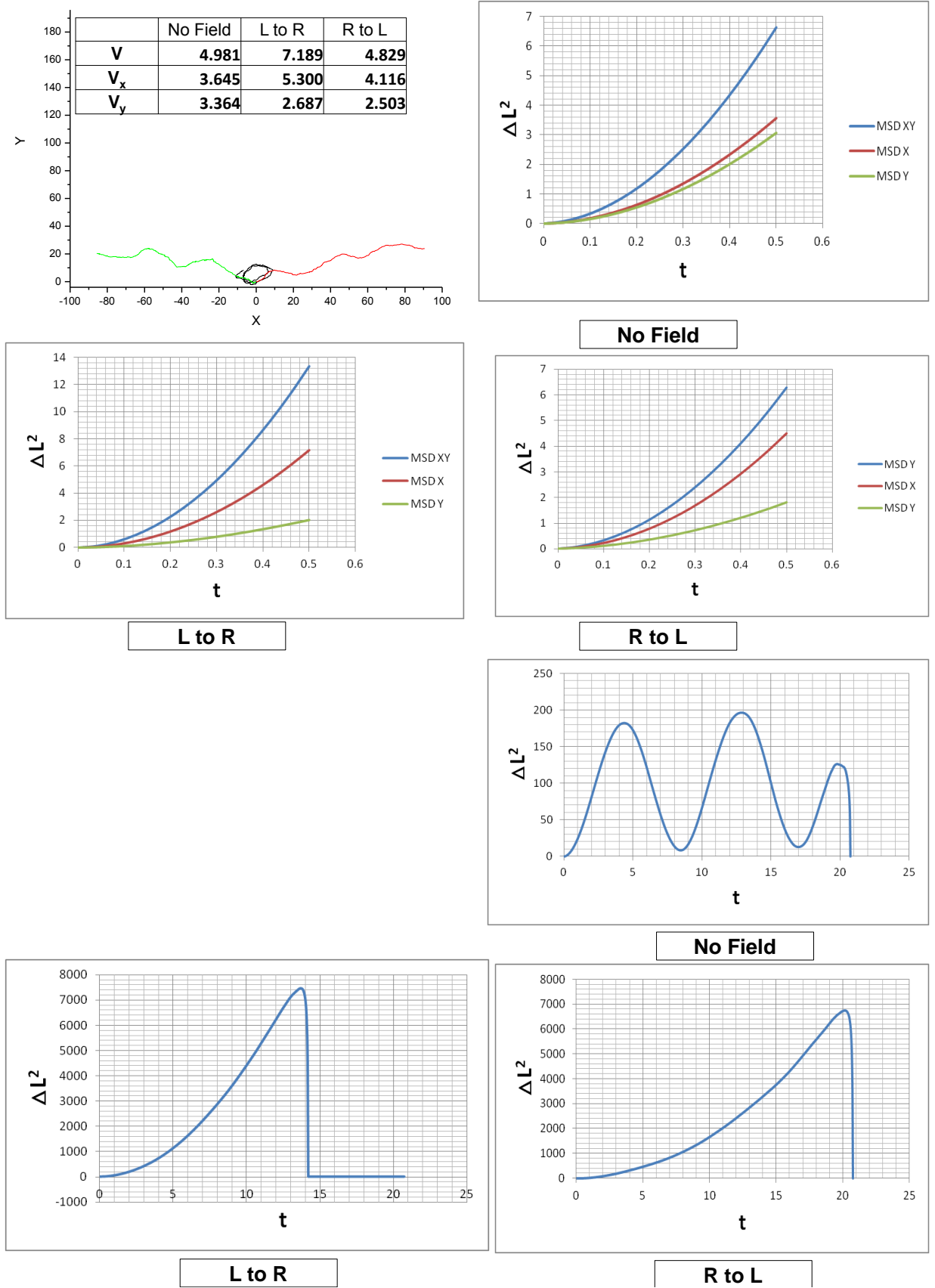


Figure 3.9 – xy trajectories and MSD vs time graphs for Ni+Pt coated magnetic swimmers in the presence and absence of a uniform magnetic field

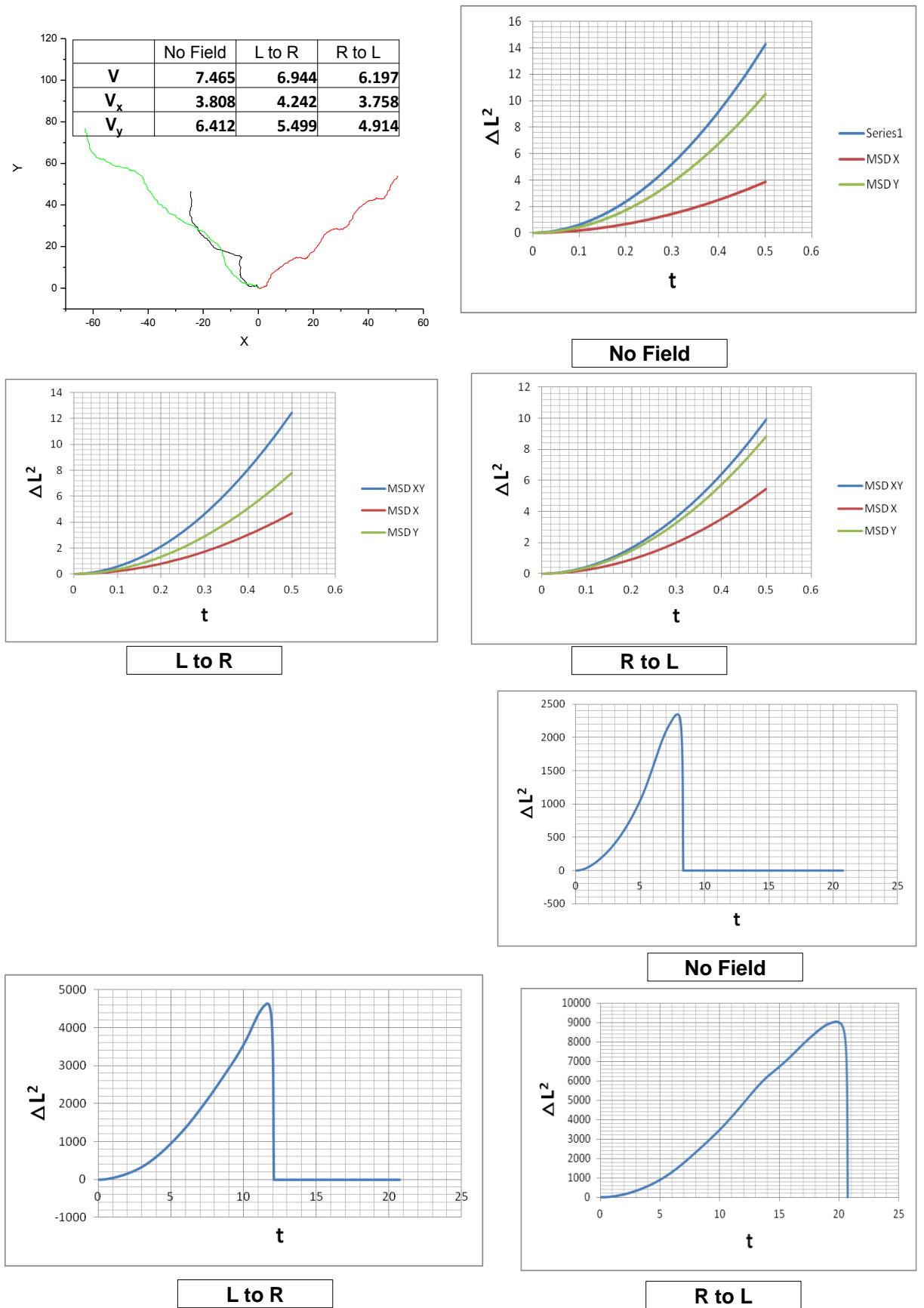


Figure 3.9 – continued

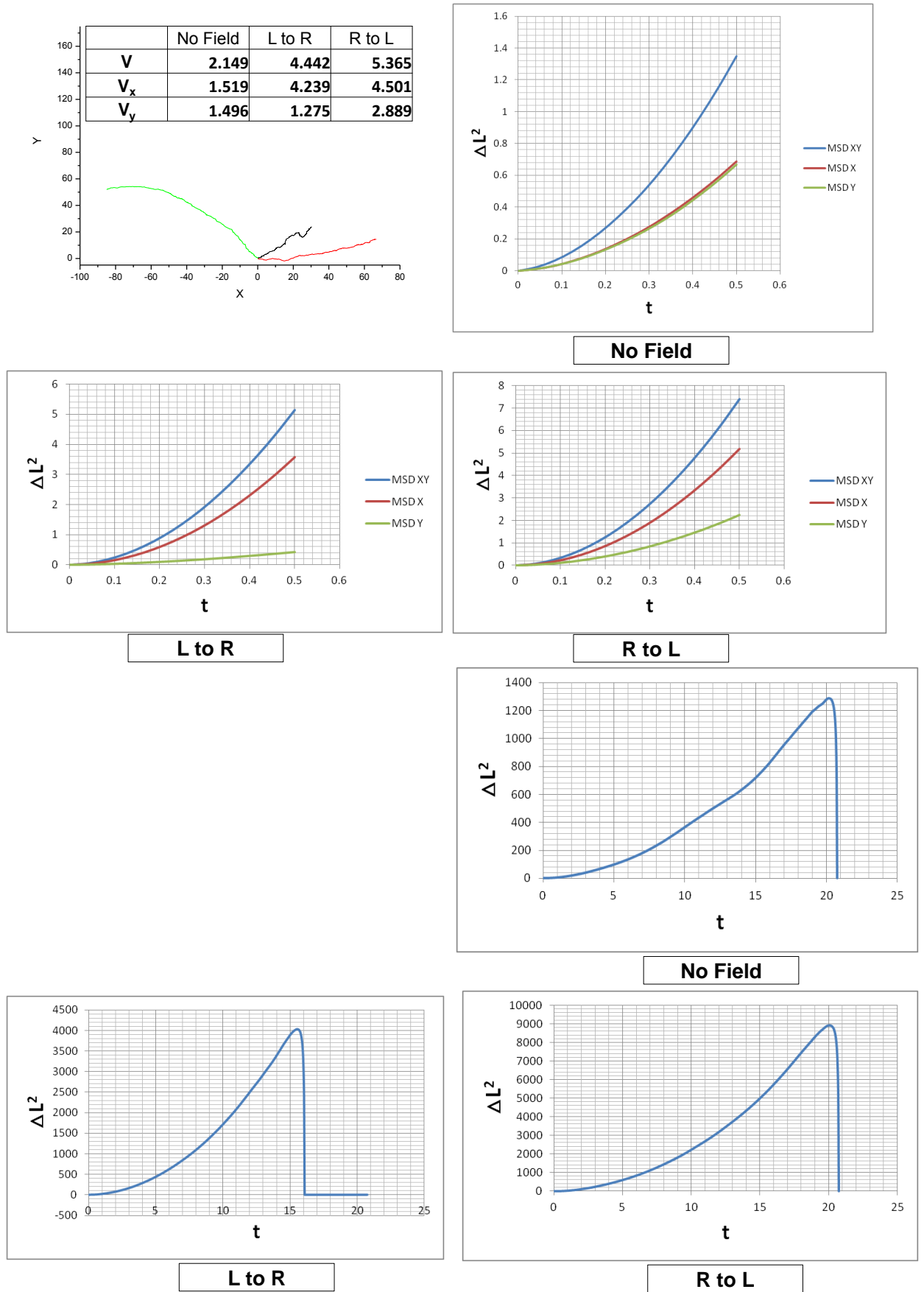


Figure 3.9 – continued

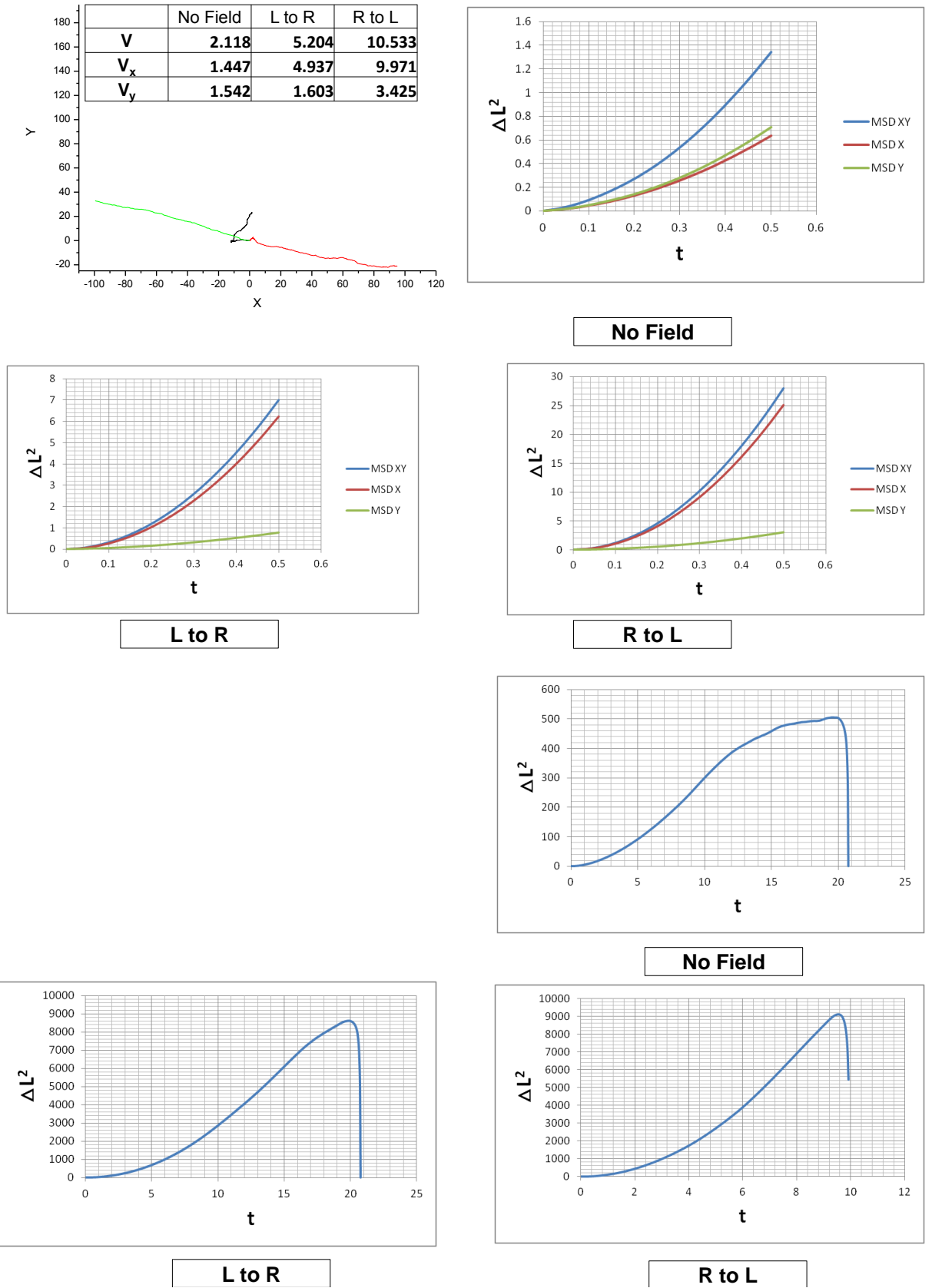


Figure 3.9 – continued

As it can be seen in the squared displacement graphs, after switching the field on, the squared displacement along the x axis (which was initially equal to the squared displacement along the y axis when the field was switched off) is significantly higher than the squared displacement along the y axis, showing that the motion in the direction of the field is dominant.

The data points in Figure 3.8 (bottom) which are still close to the $x = y$ line even after switching on the magnetic field, are effectively non-responsive swimmers as their component velocities have not changed after exposure to the magnetic field. This might be due to poor exposure to the permanent magnet during the magnetisation stage, insufficient magnetic material coating during metal deposition, or the sum of all dipoles present within the film cancelling each other out.

Although there are a significant number of data points showing $V_x > V_y$, the presence of some data-points indicating that the field is actually increasing the y component of propulsion velocity, i.e. propulsion perpendicular to the field direction, and reducing the x component is somewhat surprising. Overall, this therefore suggests three distinct types of particles from a single coating processing step. Examples of the three different types of trajectory observed (a) $v_x < v_y$, (b) $v_x \approx v_y$, and (c) $v_x > v_y$ are shown in Figure 3.10 (top), along with the corresponding the 2D and 1D mean squared displacements. The corresponding permanent dipole is also schematically represented.

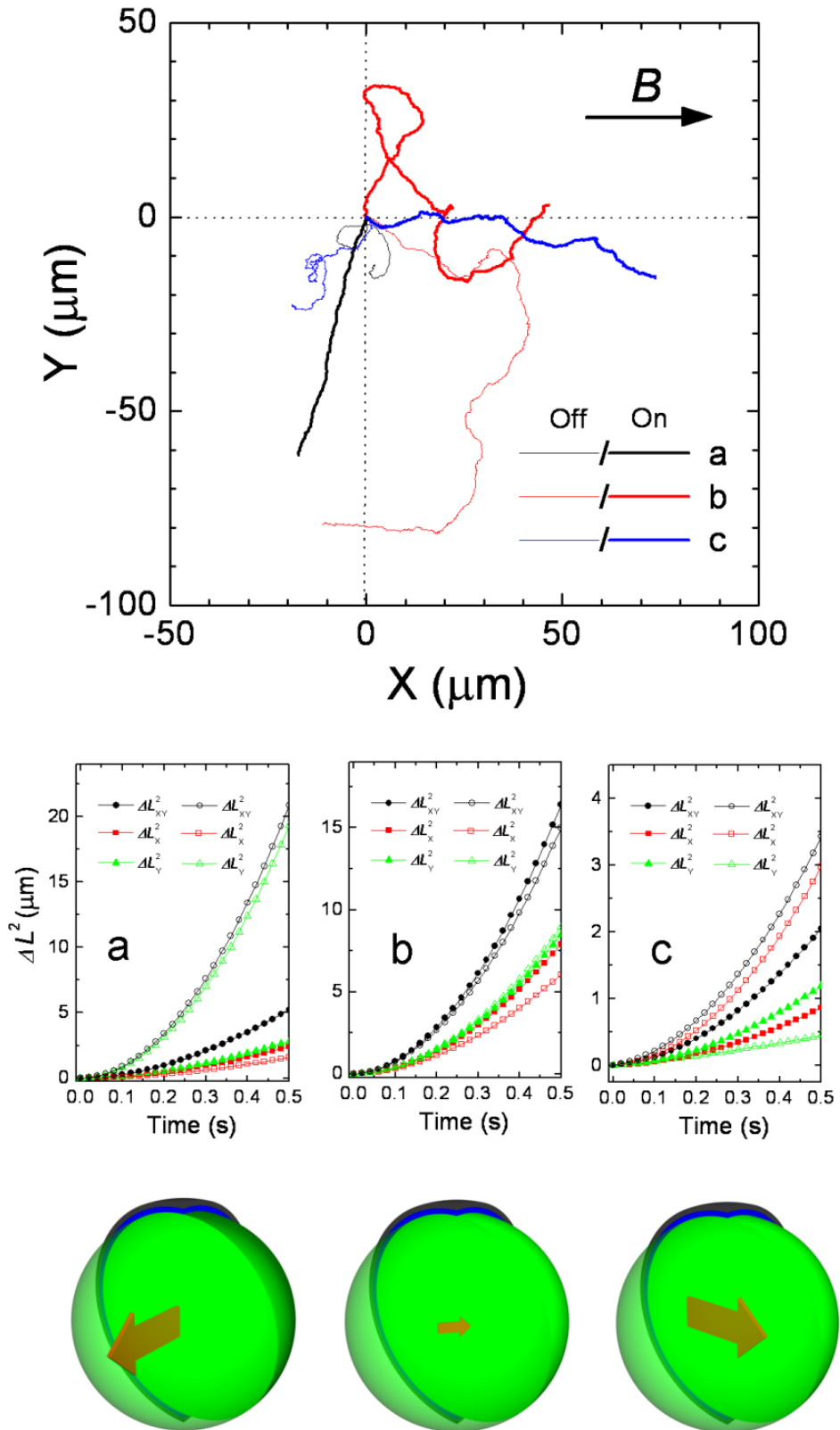


Figure 3.10 - Trajectories for the three different types of behavior observed referred to in Figure 3.8 (top) (a) $v_X < v_Y$, (b) $v_X \approx v_Y$, and (c) $v_X > v_Y$. The thicker line corresponds to the field being on. (middle) Corresponding mean squared displacements and magnetic dipole configuration (bottom).

Moreover, it is not uncommon, despite careful fabrication procedures, to create swimmers which have their own inherent spin, and which exhibit spiraling trajectories.

Figure 3.11 shows the behavior of one such particle (marked on Figure 3.8 as “d”).

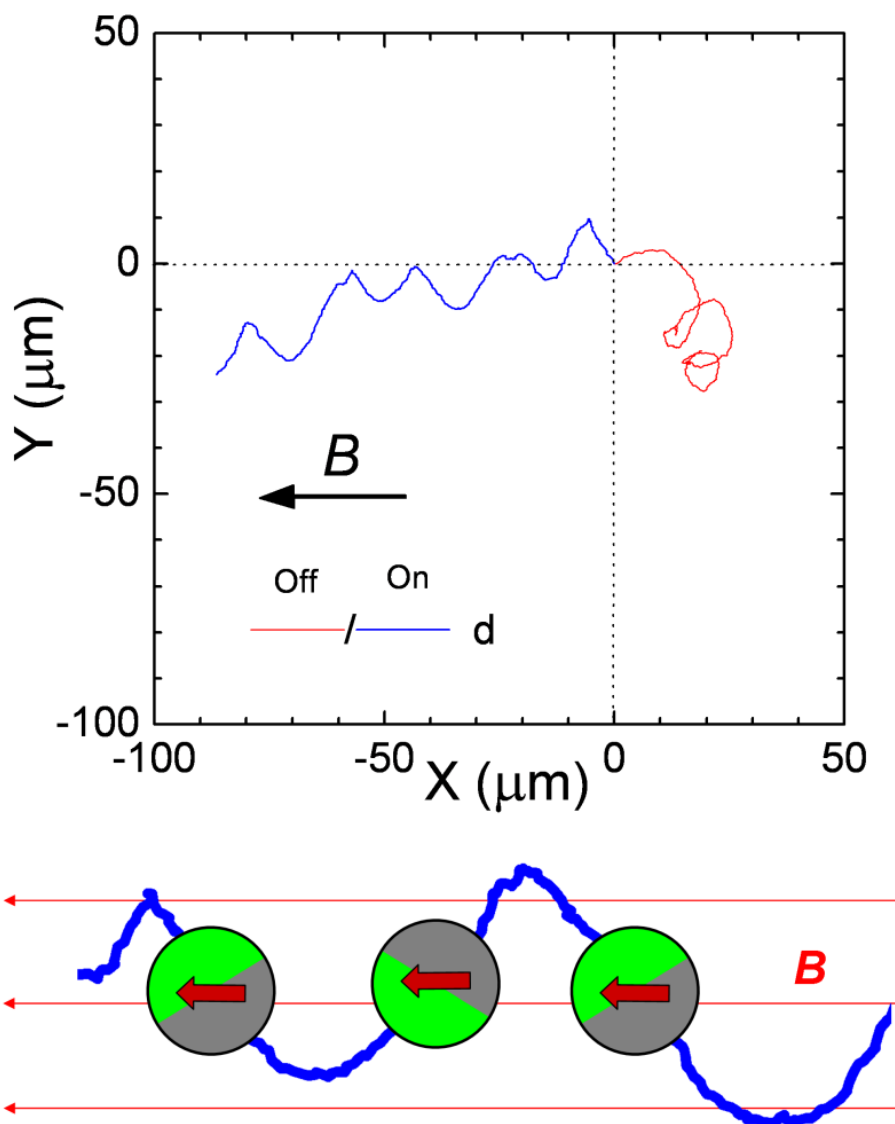


Figure 3.11 – (top) Trajectory for a spiralling swimmer with and without an applied field (swimmer “d” in Figure 3.8) and the corresponding dipole configuration (bottom). Duration of this movie is 20 s.

Under no applied field, the swimmer demonstrates circular motion, most probably caused by heterogeneity in the metal cap producing an asymmetric propulsive vector, in effect imparting a rotational torque to the swimmer. This effect is constant and always applied in the same direction and during the movie the swimmer undergoes around 4 rotations. The application of the field however causes the dipole in the nickel layer to align with the field. However, there is now both a propulsive component, producing motion to the left in this instance, but also a rotational torque which wants to rotate the particle. It is energetically unfavourable to rotate the dipole away from the field and so the particle rotates perpendicular around the field lines (Figure 3.11, bottom). This has the effect of producing trajectories which are oscillatory in 2D – with a period which is constant as it results from the rotational torque force, yet are in fact corkscrew shaped, with a fixed pitch and direction of rotation, when in 3D. More examples of this behaviour are available in the following pages (Figure 3.12).

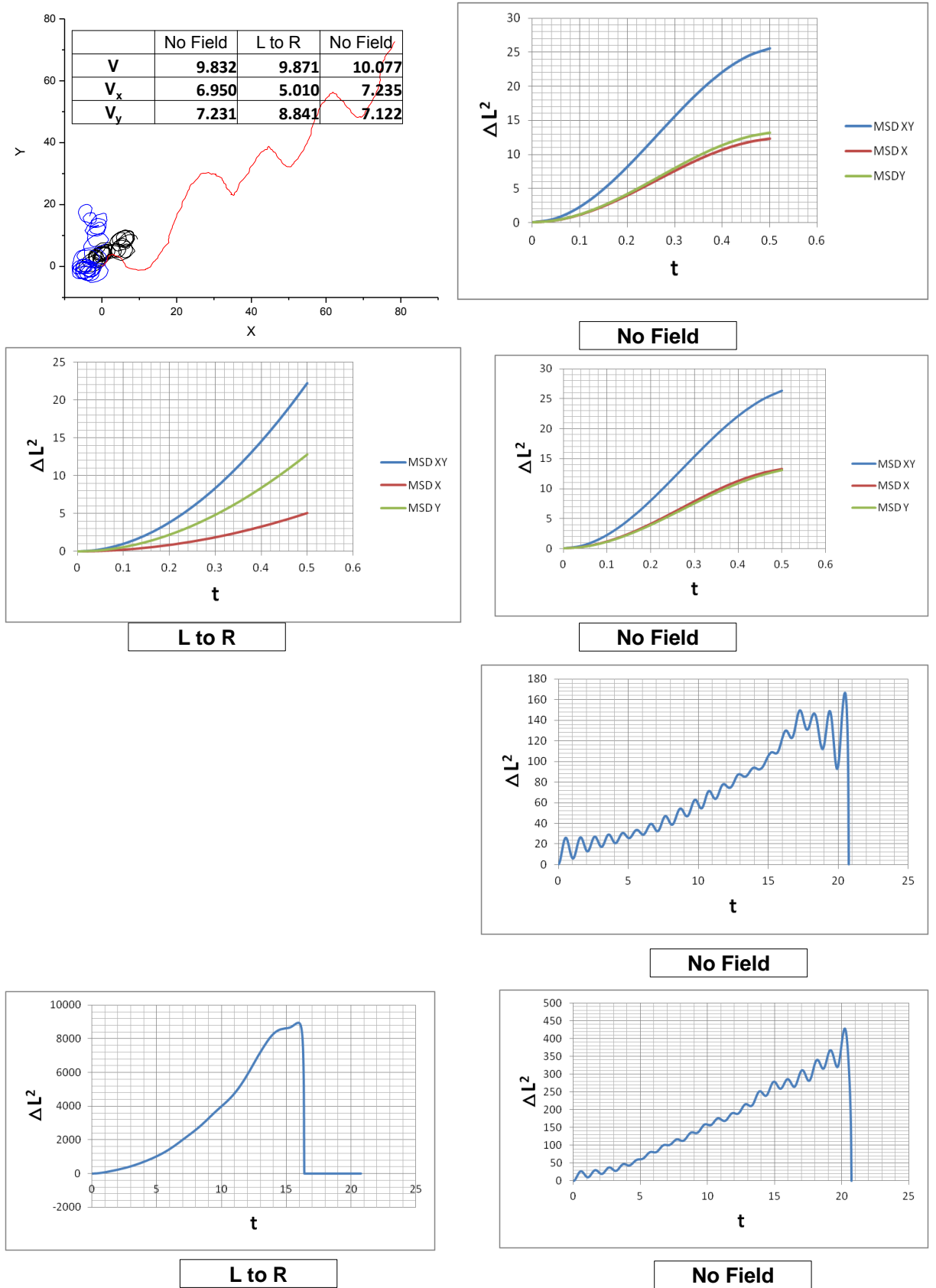


Figure 3.12 – xy trajectories and MSD vs time graphs for Ni+Pt coated spiralling magnetic swimmers in the presence and absence of a uniform magnetic field

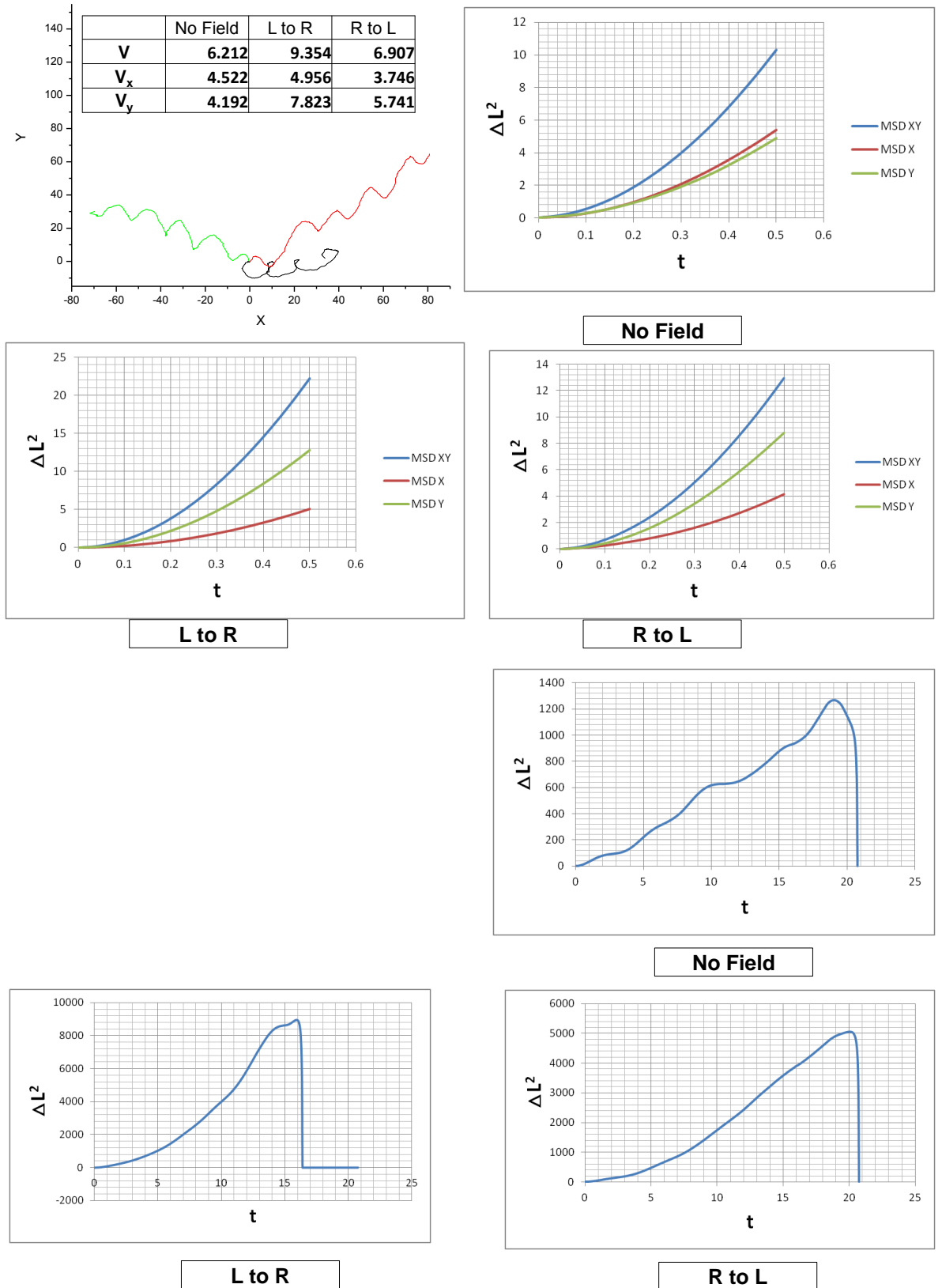


Figure 3.12 – continued

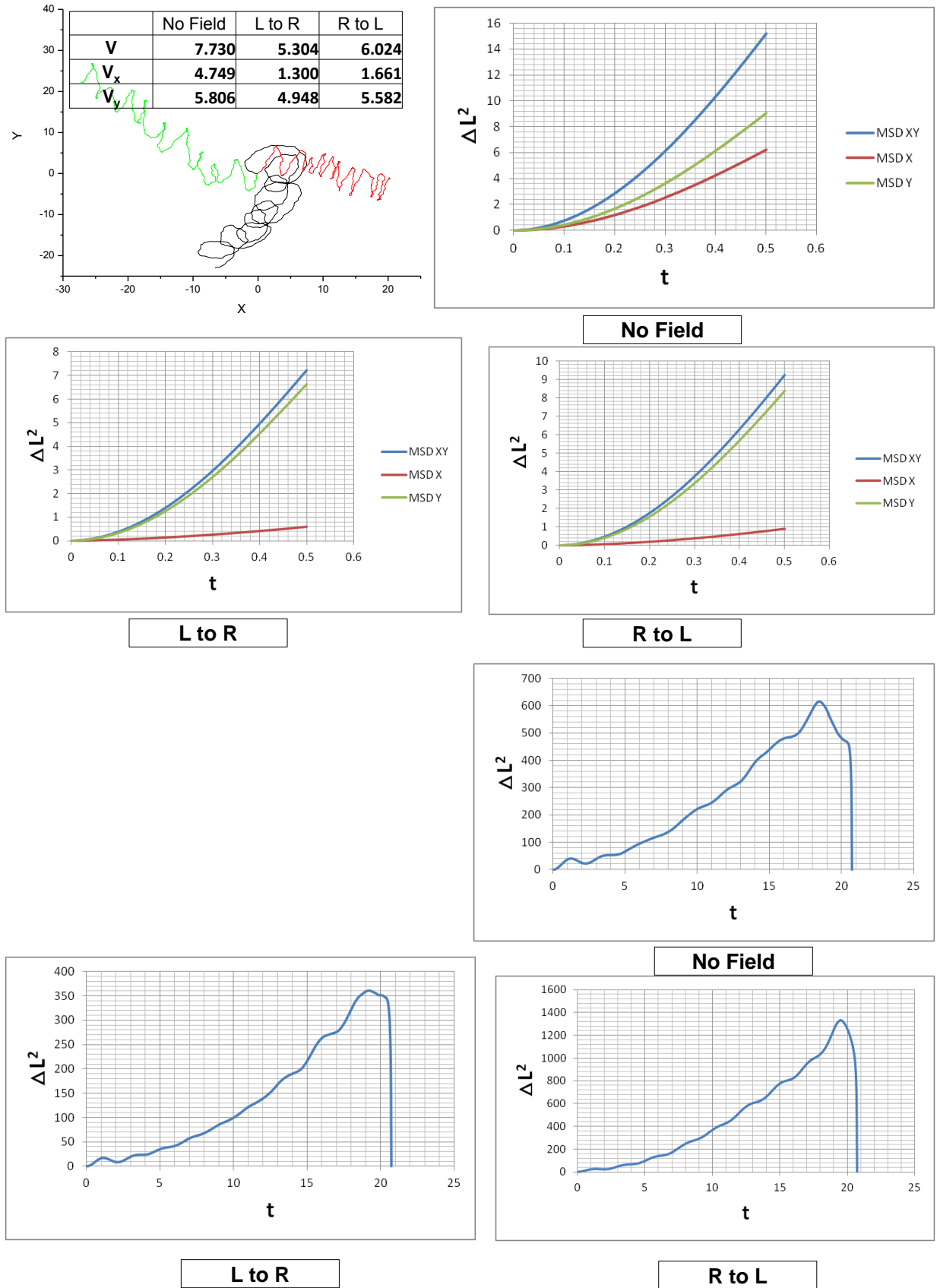


Figure 3.12 – continued

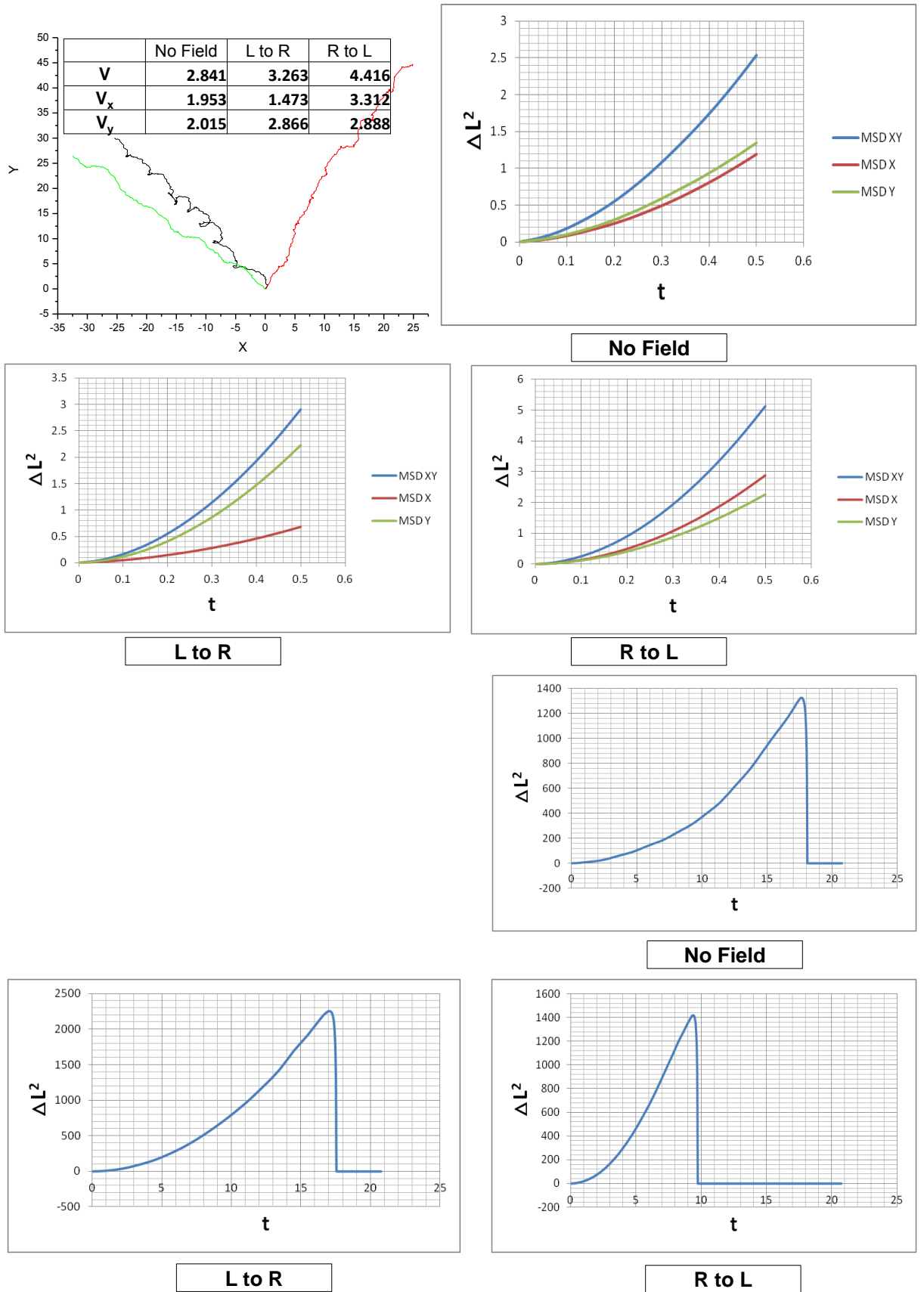


Figure 3.12 – continued

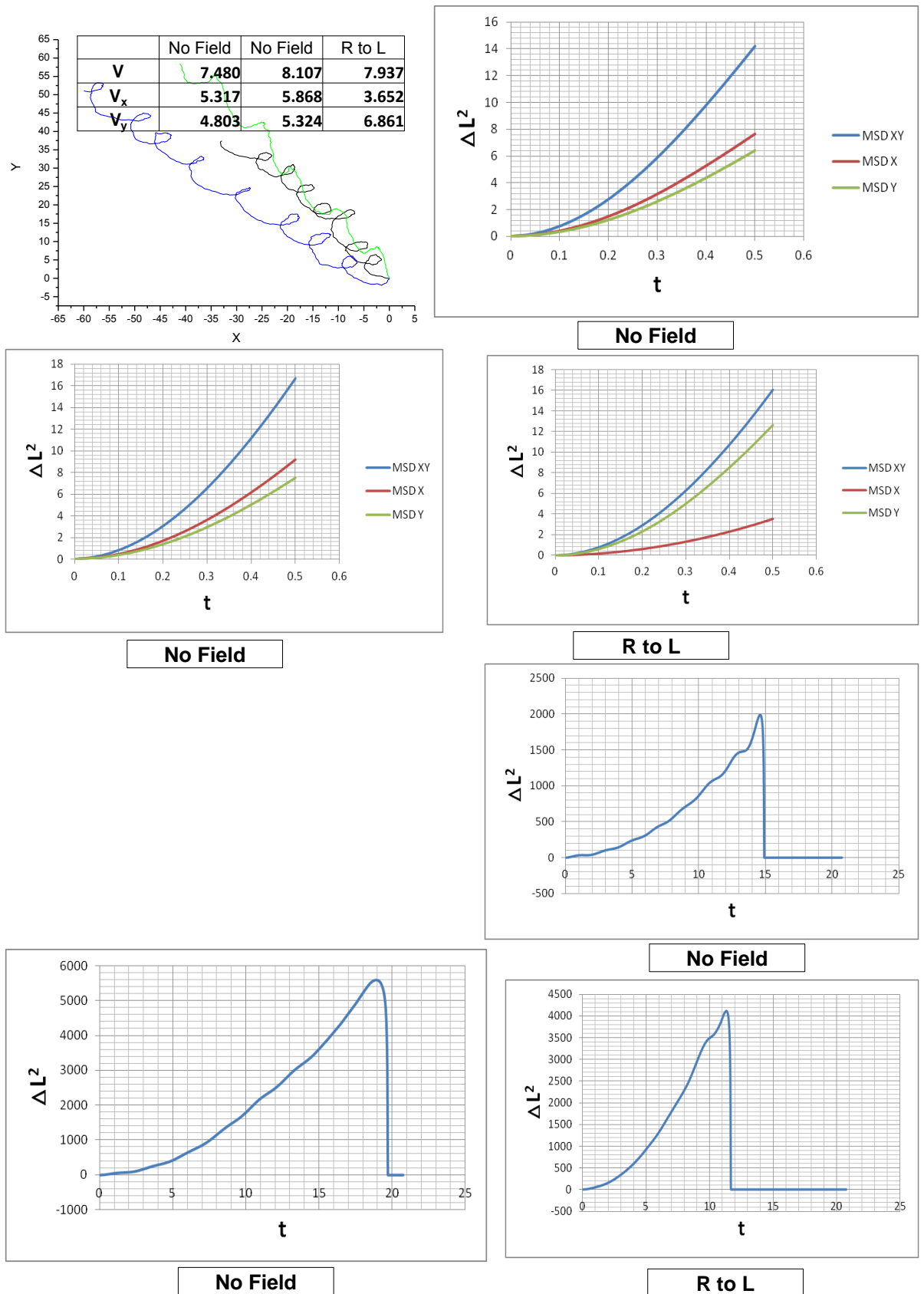


Figure 3.12 – continued

3.6 Customized trapping of magnetic microswimmers: a new route for autonomous steering of propulsive particles

Although controlling the orientation of Janus magnetic microswimmers via an external magnetic field generated by a pair of Helmholtz coils was proven to be efficient, albeit partially, the direction of the magnetic field had to be modified manually in order to steer the particle to a specific location. In general, manual trajectory control is not desirable for small scale applications due to the high probability of human errors to occur and the extensive time required for completing the process. As this technique lacks accuracy and cost efficiency, especially in applications where large numbers of micro- and nanoscale magnetic objects are required to be directed towards a specific target, various attempts have been made towards *in situ* manipulation of magnetic particles by employing microscale devices. Here, after providing a brief review on properties and fabrication methods of magnetic micro-coils (MCs), the progress made towards an autonomous technique for steering magnetic catalytic swimmers via customized magnetic entrapment using these devices is reported.

Similar to Helmholtz coils, by benefiting from the magnetic field generated by passing an electric current through wires, MCs can be employed for adjusting the alignment of magnetic particles in confined locations. With this approach, three prototypes of magnetic tracks were fabricated using printed circuit boards (PCBs), TEM grids and photolithography (chrome masks) with the aim of determining the effects of magnetic trapping on the propulsion velocity of the particles and their rotational diffusion. Therefore, each prototype was tested for its ability in altering the orientation Janus magnetic microswimmers. Although the fabricated devices did not function as efficiently as expected, the obtained results can be a good starting point for future research.

3.7 Magnetic micro-coils: fabrication and properties

Among various methods proposed for transferring microscale objects inside fluid media, utilising magnetic fields has always been desirable since such fields do not distress the activity of biological cells and effects such as electrophoresis (created by electric fields) that alter the media, are not created by magnetic fields. Due to inaccuracy of external macroscale magnetic fields in transporting small scale particles, several strategies have been proposed for generating magnetic fields that are heterogeneous on the particle scale. In contrast with Helmholtz coils that generate a region of uniform magnetic field, the microscale devices fabricated to achieve this goal, generate gradients of controllable magnetic field. This method of micro-scale magnetic manipulation has been reported by several scientists [43-47] but these studies only report magnetic trapping of particles on the surface without contributing to their transportation towards a specific location.

A more advanced approach was realised by Ramadan, et al. [48], employing steep magnetic potential wells generated by running a constant current through electroplated microcoils consisting of Cu tracks on an Si substrate to control the motion of magnetic particles.

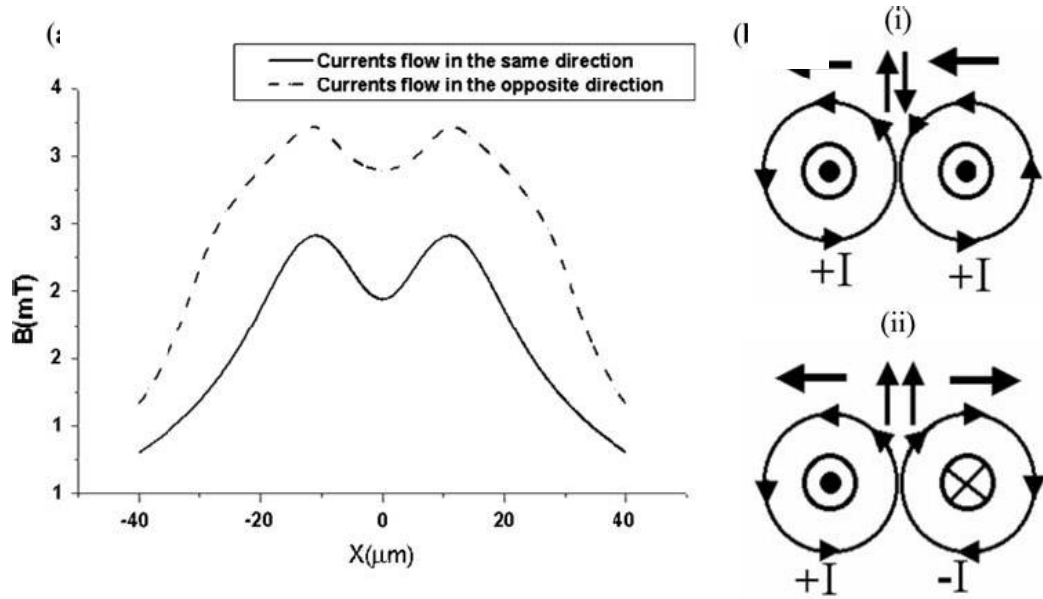


Figure 3.13 - magnetic wells generated by (i) co-current and (ii) countercurrent microwires (reprinted from Ref. 48)

The theory behind this approach (as Figure 3.13 demonstrates) is based on the magnetic field generated by parallel wires with the electric currents flowing in the same direction (i) and in the opposite direction (ii). When the electric currents flowing in the Cu tracks are in the same direction [Figure 3.13 (i)], the vertical components of the generated magnetic fields cancel each other out therefore the overall magnetic field is horizontal pointing either to left or right depending on the direction of the current. In contrast, when the electric currents flow in the opposite direction, [Figure 3.13 (ii)], the horizontal components of the generated magnetic fields cancel each other out, resulting the overall magnetic field to be vertical pointing up or down depending on the direction of the current.

3.7.1 Fabrication method of magnetic microcoils

The fabrication method of magnetic microcoils described by Ramadan, et al. [49] involved etching deep trenches in a silicon substrate followed by depositing silicon

dioxide into the trenches and filling them with copper. After covering the Si substrate with a resist while keeping the microcoil patterns exposed, the trenches were etched using SF₆ gas which provided fluorine radicals that reacted with the exposed areas. Subsequent to cleaning and resist strip processes, a 100 nm thick silicon oxide was evaporated onto the substrate via plasma enhanced chemical vapour deposition (PECVD) with the aim of isolating the forthcoming copper layer from the silicon substrate which is also conductive. Next, Cu was deposited into the trenches by initially electroplating 100 nm of copper as a seeding layer (to cover the walls and the bottom of the trenches), prior to evaporating a 30 nm layer of TiN and a 20 nm layer of Ti via physical vapour deposition (PVD) to act as adhesive layers and finally electroplating 10 µm of copper to fill the trenches. After removing excess copper using Chemical Mechanical Polishing (CMP), the 10 µm deep, 3 µm wide microcoils were used in magnetic trapping experimental trials.

The results of the magnetic trapping experiments reported by Ramadan, et al. [48] demonstrated that the magnetic field gradient generated by running a 100 mA current through the fabricated microcoils was capable of entrapping 1 µm superparamagnetic particles from Estapor® suspended in water (with a concentration around 10⁷ beads. ml⁻¹) inside the microfluidic cell where the microcoils were positioned at its bottom. Ramadan, et al. also reported that the magnetic beads entrapped between the microcoils by the field gradient are capable of confining and aligning biological cells at desired locations however, this particle-cell adhesion occurs even without presence of a magnetic field gradient.

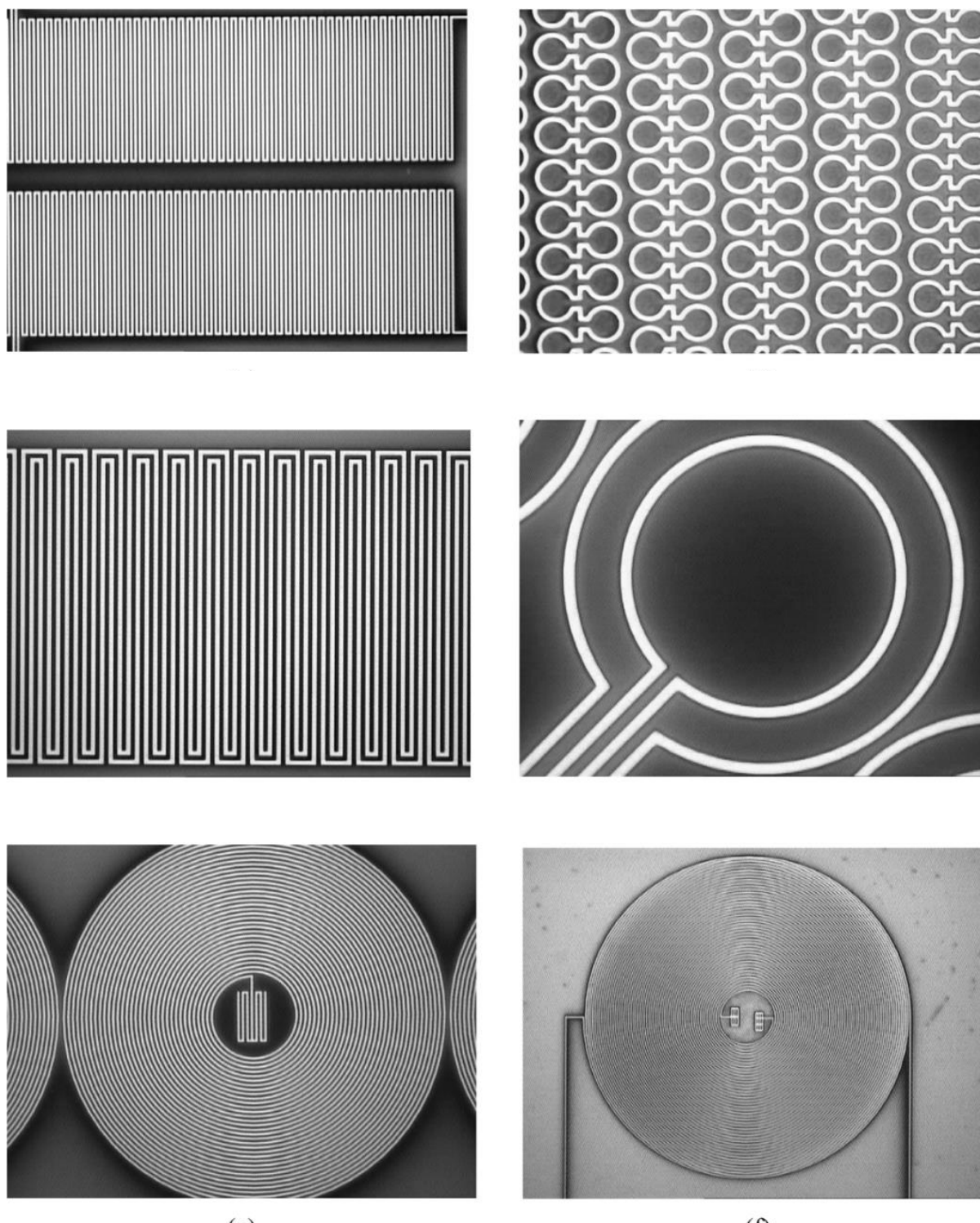


Figure 3.14 – Optical images of various designs of copper microcoils after the Chemical Mechanical Polishing (CMP) step. (reprinted from Ref. 48)

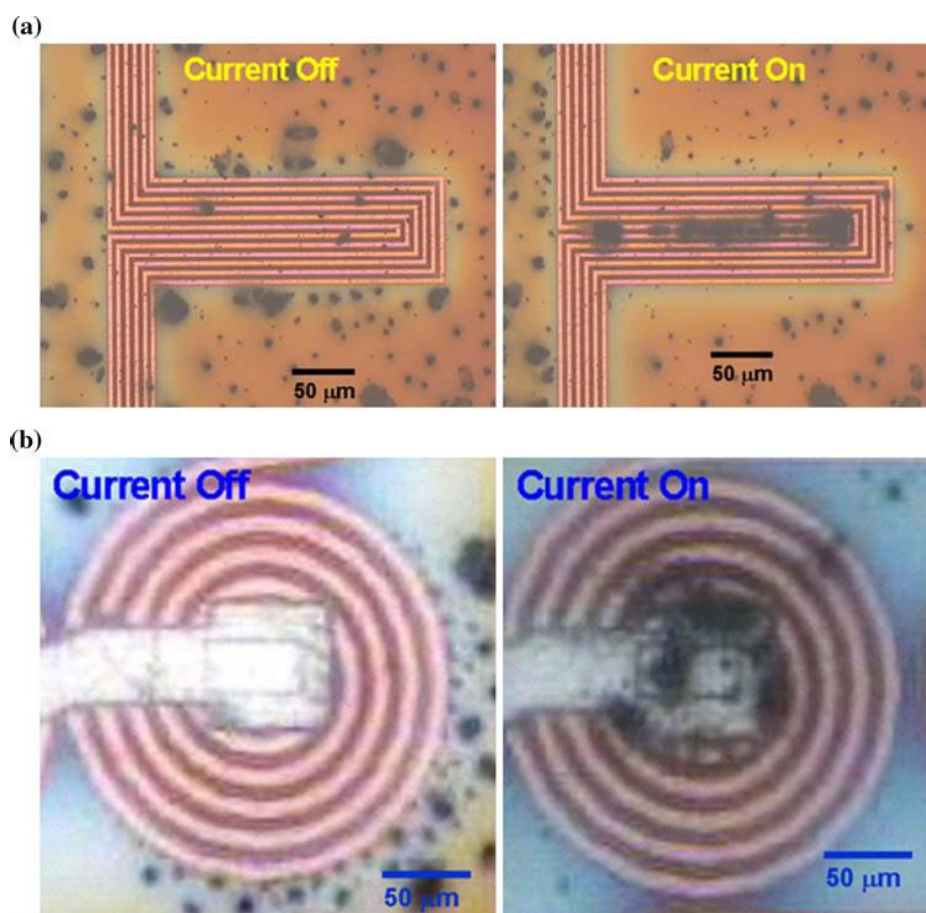


Figure 3.15 - Giardia cell trapping via (a) Meander and (b) Spiral microcoils (reprinted from ref 48)

3.8 Realisation of magnetic microtracks

The encouraging outcome of Ramadan, et al.'s [48] study on magnetic entrapment using microcoils plus the results obtained from controlling the orientation of catalytic microswimmers via an external magnetic field, were a stimulus for developing an autonomous steering method for navigating magnetic propulsive particles. As discussed earlier, if a constant electric current runs through two parallel wires in opposite directions, the horizontal components of the generated magnetic fields by the wires cancel each other out, resulting the overall magnetic field to be vertical pointing up or down depending on the direction of the current. Based on this outcome, if the

metallic cap of a magnetic catalytic swimmer is aligned parallel to the overall magnetic field generated by two parallel microwires with opposite currents, the cap will stay aligned vertical to the wires and as the direction of the magnetic field generated by the parallel wires does not alter throughout their length, theoretically the catalytic swimmer should follow the direction of the microwires towards a specific target determined by the path of the wire.

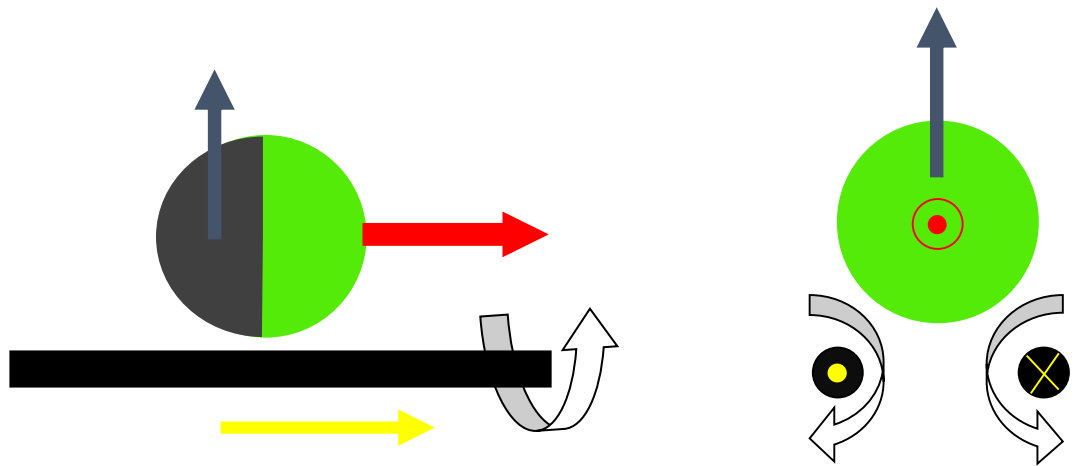


Figure 3.16 – Schematic design showing the alignment of the magnetic cap (blue) – direction of the electric current (yellow) – direction of the generated magnetic field (white) and the direction of propulsion (red)

3.9 Preparation of magnetic microtracks

3.9.1 Printed Circuit Boards (PCBs)

The first attempt towards fabricating magnetic microtracks involved cutting out a piece of PCB with parallel copper tracks and soldering the end of each track to its adjacent neighbouring track in order to have opposite running currents between the tracks. After sandwiching an adhesive sheet (with a 5×5 mm square cut out of it) between the PCB

and a cover slip, the magnetic particles suspended in water could be observed by an optical microscope in presence and absence of an electric current. Although this design was capable of handling electric currents up to 300 mA, injection of current caused undesired heating of the substrate, creating convection currents inside the cell and prevented magnetic entrapment of the colloidal particles.

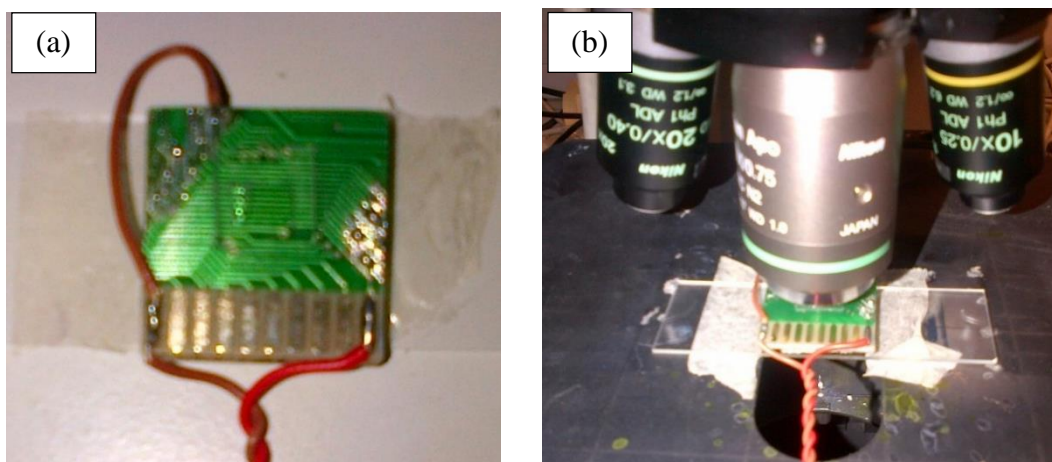


Figure 3.17 – (a) digital image of the magnetic tracks fabricated using a printed circuit board (b) the experimental setup showing the magnetic track and the microfluidic cell mounted on top under an optical microscope

3.9.2 TEM grids

In the second attempt, a copper parallel bar transmission electron microscopy (TEM) grid was employed for fabricating magnetic microtracks. In this trial, two cuts were made on the grids outer circle in order to avoid short circuiting the parallel copper bars and similar to the previous trial, a microfluidic cell was fabricated above the TEM grid using an adhesive sheet and a cover slip. As the thickness of the conductive copper in the TEM grid was considerably less than the PCB, the maximum current that could be injected into the cell was less than 100 mA therefore the generated magnetic field was

much weaker than the PCB. Additionally, as there were no isolating layers covering the conductive TEM grid, injecting the current resulted in electrophoretic effects in the microfluidic cell, preventing particle entrapment and after covering the TEM grid with an insulator layer, the generated magnetic field was incapable of entrapping the particles.

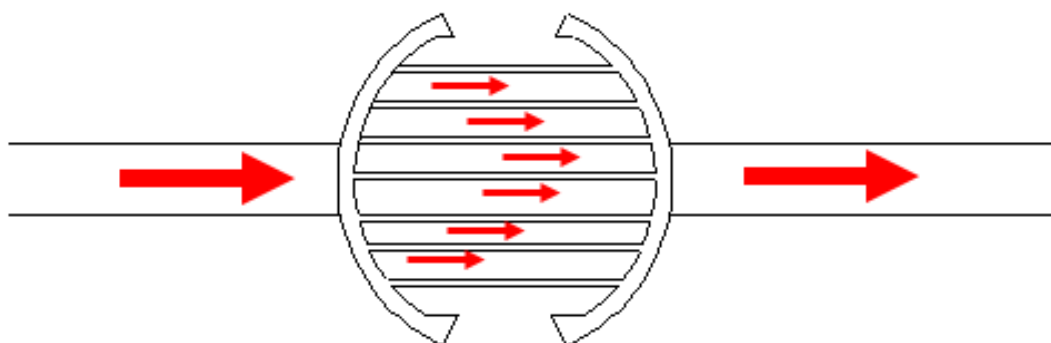


Figure 3.18 – Schematic design showing the direction of the current (red arrows) in the TEM grid magnetic microtracks

3.9.3 Chrome mask

As the microcoil fabrication method developed by Ramadan, et al. involved several etching, striping, electroplating and vapour deposition, in the third trial a simpler method was employed for preparing conductive microtracks with similar properties. In this trail, after sketching various microtrack designs using AutoCAD, a tailor-made chromium mask was produced by JD Photo-Tools (Oldham, UK). These masks that are opaque plates of fused silica (quartz) with transparent areas that allow light to shine through, are fabricated via sophisticated lithography tools and are mainly utilised in microminiaturisation of computer chips. To fabricated these masks, the quartz substrate is coated with 500 nm of chrome followed by deposition of a layer of anti-

reflective and a layer of photoresist (Figure 3.19 a). Next, the sketched patterns are printed on the photoresist using high energy flashes of light. This creates a latent image in the photoresist layer (Figure 3.19 b). Subsequently, the resist is developed and the unexposed parts of the resist are softened and dissolved out of the mask layer, leaving just the pattern on the substrate (Figure 3.19 c). In the etching process (Figure 3.19 d), chrome is selectively removed from parts of the mask with no patterns on them. Finally, in the stripping process, the remaining photoresist is removed, leaving a conductive chrome pattern on the quartz substrate with a thin layer of anti-reflective coating on top (Figure 3.19 e).

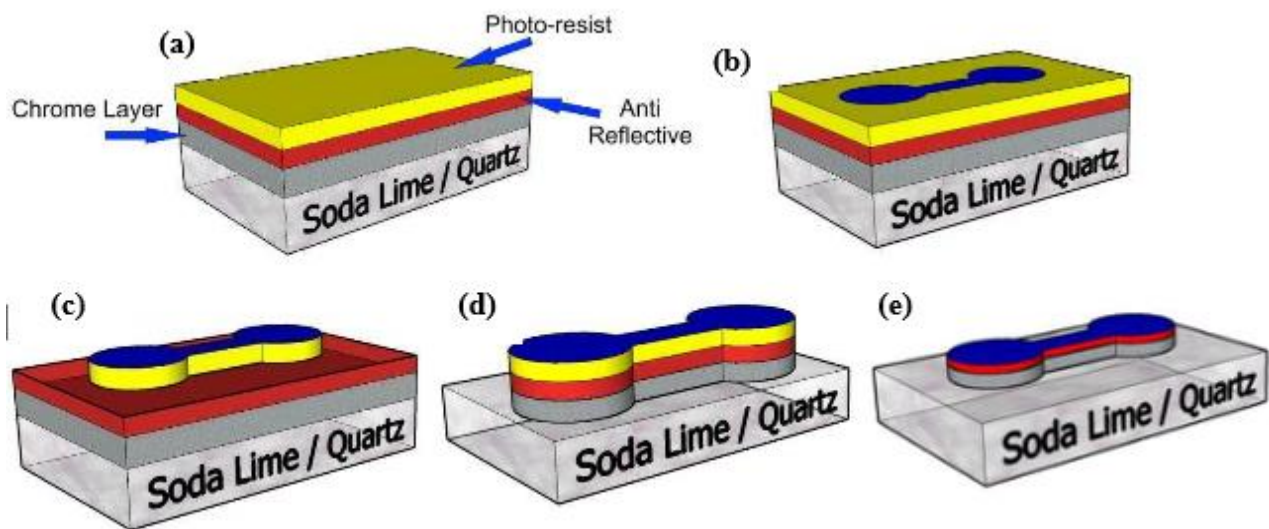


Figure 3.19 – schematic design showing different stages of chrome mask fabrication: (a) substrate preparation, (b) pattern printing, (c) resist development, (d) etching, (e) stripping

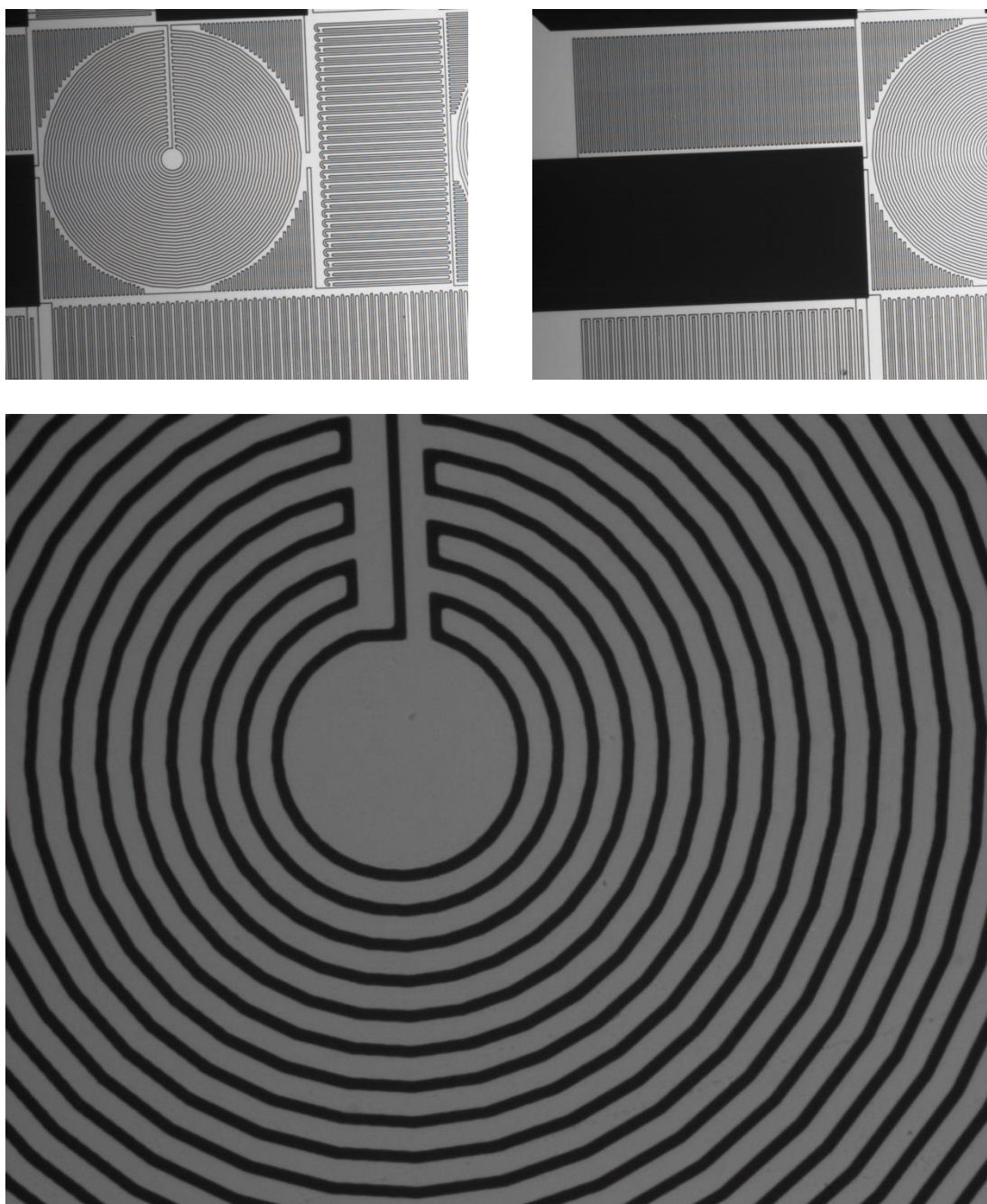


Figure 3.20 – optical image of the chrome mask produced by JD Photo-Tools

Although the fabricated chrome mask possessed features similar to Ramadan, et al.'s microcoils, as the conductive layer was much thinner compared to their design (500 nm height, 3 μm width chrome mask compared to 10 μm depth, 3 μm width copper microcoil), the maximum injected current that the photo mask was capable of handling was much less than the 100 mA current which was used for generating magnetic field

gradient in microcoils. As a result, the magnetic field generated by running a current through the chrome mask was extremely weak and was not able to entrap ferromagnetic or paramagnetic particles. Injecting stronger currents lead to melting of the chrome tracks and further attempts to thicken the chrome layer by electroplating and vacuum deposition proved to be inefficient.

References

1. R. Dreyfus et al., *Nature*, **2005**, 437, 862.
2. A. Najafi, R. Golestanian, *Phys. Rev. E*, **2004**, 69, 062901.
3. J. R. Howse et al., *Phys. Rev. Lett.*, **2007**, 99, 048102.
4. Y. Hong, N. Blackman, N. Kopp, A. Sen and D. Velegol, *Phys. Rev. Letts.*, **2007**, 99, 1.
5. S. Ebbens et al., *Phys. Rev. E.*, **2010**, 82, 6.
6. J. G. Gibbset al., *Nano Lett.*, **2011**, 11, 2543.
7. O. D. Velev et al., *Annu. Rep. Prog. Chem., Sect. C*, **2009**, 105, 213.
8. T. R. Kline et al., *Angew. Chem., Int. Ed.*, **2005**, 44, 744.
9. Z. Saiyed et al., *Biomagn. Res. Technol.*, **2003**, 1, 2.
10. C. Chambon et al., *Reson. Imaging*, **1993**, 11, 509.
11. O. V. Salata, *J. Nanobiotechnol.*, **2004**, 2, 3.
12. J. Baudry et al., *Proc. Natl. Acad. Sci. U.S.A.*, **2006**, 103, 16076.
13. L. F. Valadares et al., *Small*, **2010**, 6, 565.
14. D. Makarov et al., *Appl. Phys. Lett.*, **2007**, 90, 093117.
15. L. Baraban et al., *ACS Nano*, **2012**, 6, 3383.
16. A. Solovev et al., *Adv. Func. Mater.*, **2010**, 20, 2430.
17. I. Sinn, P. Kinnunen, S. N. Pei, R. Clarke, B. H. McNaughton, R. Kopelman *App. Phys. Let.* **2011**, 98, 024101.
18. M. Albrecht et al., *Nature Mater.*, **2005**, 4, 203.
19. A. M. Schmidt, *Colloid Polym. Sci.* **2007**;285:953–66.
20. D. C. F. Chan, D. B. Kirpotin, P. A. Bunn Jr, *J Magn Magn Mater* **1993**;122(1–3):374–8.
21. A. Jordan, R. Scholz, P. Wust, H. Schirra, T. Schiestel, H. Schmidt, *J Magn Magn*

- Mater* **1999**;194(1–3):185–96.
22. G. Glöckl, R. Hergt, M. Zeisberger, S. Dutz, S. Nagel, W. Weitschies, *J. Phys. Condens. Matter*. **2006**;18(38):S2935–51.
23. S. Dutz, R. Hergt, J. Mürbe, R. Müller, M. Zeisberger, W. Andrä, *J. Magn. Magn. Mater.* **2007**;308(2):305–12.
24. U. Gneveckow, A. Jordan, R. Scholz, V. Bruss, N. Waldofner, J. Ricke J, *Med. Phys.* **2004**;31(6):1444–52.
25. M. H. Falk, R. D. Issels, *Int. J. Hyperthermia*. **2001**;17(1):1–18.
26. D. G. Grier, *Nature*, **2003**, 424, 810–816.
27. R. Piazza, *J. Phys.: Condens. Matter*, **2004**, 16, S4195.
28. Z. D. Cheng, W. B. Russell and P. M. Chaikin, *Nature*, **1999**, 401, 893.
29. S. Melle, O. G. Caldero´ n, M. A. Rubio and G. G. Fuller, *Phys. Rev. E: Stat., Nonlinear, Soft Matter Phys.*, **2003**, 68, 041503.
30. H. Singh, P. E. Laibinis, T. A. Hatton, *Langmuir* **2005**;21:11500–9.
31. M. Albrecht, G. Hu, I. L. Guhr, T. C. Ulbrich, J. Boneberg, P. Leiderer, G. Schatz, *Nature Mater.* **2005**, 4, 203.
32. S. K. Smoukov, S. Gangwal, M. Marquez, O. D. Velev, *Soft Matter* **2009**, 5, 1285.
33. H. Takei, N. Shimizu, *Langmuir* **1997**, 13, 1865.
34. Q. Gao, C. Wang, H. Liu, Y. Chen, Z. Tong, *Polym Chem* **2010**;1(1):75–7.
35. A. F. Thünemann, D. Schütt, L. Kaufner, U. Pison, H. Möhwald, *Langmuir* **2006**;22:2351–7.
36. B. Luo, X. Song, F. Zhang, A. Xia, W. L. Yang, J. Hu J-H, *Langmuir* **2010**;26(3):1674–9.
37. A. Kaiser, T. Gelbrich, A. M. Schmidt, *J Phys Condens Mater* **2006**;18(38):S2563–80.
38. T. Gelbrich, M. Feyen, A. M. Schmidt, *Macromolecules* **2006**;39(9):3469–72.
39. Y. Hou YY, PhD thesis, University of Leeds, 2001.
40. Q. Zhang, H. Zhang, G. Xie, J. Zhang, *J Magn Magn Mater* **2007**;311(1):140–4.
41. J. E. Parks, *Helmholtz Coils – Uniform Magnetic Fields* University of Tennessee Press: Knoxville, TN, 2013.
42. S. Lin, M. D. Gurol *Environ. Sci. Technol.* **1998**, 32, 1417-1423.
43. M. Brzeska, M. Panhorst, P. B. Kamp, J. Schotter, G. Reiss, A. Puhler, A. Becker, H. Bruckl, *J Biotechnol* **2004**, 112:25–33
44. J. W. Choi, T. M. Liakopoulos, *Biosens Bioelectron* **2001**, 16:409–416

45. C. Liu, L. Lagae, R. Wirix-Speetjens, G. Borghs *J Appl Phys* **2007** 101:024913–024914
46. K. Smistrup, O. Hansen, H. Bruus, M. F. Hansen, *J Magn Magn Mater* **2005**, 293:597–604
47. L. E. Helseth, *Langmuir* **2005** 21:7276–7279
48. Q. Ramadan, D. P. Poenar, C. Yu, *Microfluid Nanofluid* **2009**, 6:53–62.
49. Q. Ramadan, V. D. Samper, D. P. Poenar, C. Yu, *J. Microelectromechanical Sys.* **2006**, 15: 624-63

Chapter 4: Catalytic Micromixers

Mixing in microscale is challenging as the flows are laminar and Reynolds numbers are generally low ($Re \rightarrow 0$) for example, in fluids with high viscosity or in low flow rates. Therefore, even though diffusion in this length-scale is fast, creating turbulence, to increase the contact area where the molecules can diffuse, is very difficult. To overcome this problem, various types of active and passive micromixers have been designed to facilitate mixing in microfluidic systems. In this chapter, the potential of utilising specially fabricated colloidal microswimmers which have an inherent spin, and demonstrate spiralling trajectories as nanoscale and microscale mixing devices is investigated. To determine the degree of mixing imparted to the solution surrounding these mixing devices, the diffusion coefficient and the average velocity of colloidal tracer particles adjacent to the micromixers is determined. In the absence of the fuel for the mixing particles, the obtained diffusion coefficient for the neighbouring particles is in accordance to its theoretical value and the average velocity of these particles is virtually zero demonstrating a pure Brownian motion. In the presence of the fuel for the mixer, the spiralling motion of the micromixers dramatically increases the average velocity and the diffusion coefficient of the neighbouring particles, equivalent to a change in size, an increase in “solution temperature” or a propulsive behaviour. As previous studies have shown that the propulsion velocity of catalytic swimmers is a function of fuel concentration, the rotation speed of the micromixers can also be controlled by modifying the concentration of hydrogen peroxide fuel.

4.1 Mixing in microfluidics

Mixers are among the most important components in processes that involve fluid handling [1-5]. Many industries employ chemical and fermentation reactors and the operation of these equipment depends on effective mixing [6]. The efficiency of mixing is directly proportional to the area of the interface between the fluids where molecular diffusion takes place [7]. In macroscale (where the majority of mixing processes are carried out) this interfacial area is large, plus in flows with high Reynolds numbers ($Re \sim 10^4$), mixing is enhanced by turbulence as it creates flow structures resulting in additional interfaces. On the contrary, mixing in microscale is problematic as the flows are laminar and Reynolds numbers are generally low ($Re \rightarrow 0$). Therefore, even though diffusion in these length-scales is fast, creating turbulence to increase the contact area where the molecules can diffuse is very difficult [8]. For example, in a 100 μm wide channel, a minimum mean velocity of 20 $\text{m} \cdot \text{s}^{-1}$ is required for generating a turbulent flow which is virtually impossible. Due to this restriction, microfluidic mixing is typically achieved by benefiting from rapid diffusion or via advection where motion in a mainstream fluidic media results mixing in smaller scales.

To date, various types of micromixers have been designed to facilitate mixing in microfluidic systems. These mixing devices are categorized into two main groups: active micromixers and passive micromixers. Active micromixers execute mixing either via their moving modules or by employing externally applied forces generated by gradients such as pressure [9] or electromagnetic fields [10]. Besides this external energy, these micromixers benefit from the fluid pumping energy which introduces additional stirring and perturbation to the system and accelerates the mixing process [11]. The external energy that active micromixers utilise to function can be provided

by a pressure-field gradient [9], an ultrasonic source [11] or a temperature gradient [12].

However, as integrating an actuator to these devices is required for converting the external energy source into mechanical energy, the fabrication process of active micromixers is often expensive and complicated which limits the application of these mixers on an industrial scale. Additionally, some of the aforementioned external energy sources can be damaging to biological systems. For example, introduction of high temperature gradients or strong ultrasonic waves can destroy red blood cells in a short period of time and as a result, employing these classes of active micromixers is not common for *in vivo* applications.

In contrast to active micromixers, there are no moving modules in passive micromixers and these devices do not require an external energy source. In these mixers, the geometry of the microfluidic channel is designed in a way that it either promotes advection (by laminating the fluids in-plane or out-of-plane) or improves molecular diffusion between the fluidic streams [13, 14]. Mixing in passive devices is solely depended on the energy that pumps the fluids into the channel and maximises the contact area between the streams. Various methods have been proposed to achieve efficient mixing in these devices. These methods include introduction of glass bubbles [15] or immiscible liquid droplets [16] to the stream, creating grooves and ribs on the walls of the channel to enhance advection [17] and stream splitting via parallel or serial lamination [18, 19].

As passive mixers do not have miniaturised moving parts, their life-time is typically longer than active mixers which endure the effects of wear and friction. As the only energy source running these devices is the pumping energy, they do not require an energy conversion module or an actuator. This makes fabrication of passive mixers

simpler and more cost efficient though microfabricating some complex channel topologies can be problematic [7]. A summary of these classes of devices is shown in Figure 4.1.

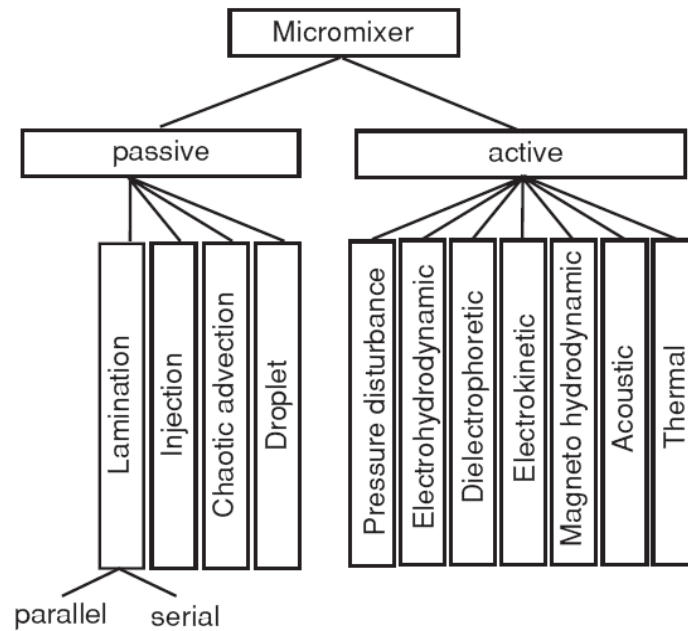


Figure 4.1 – Different classes of active and passive micromixers

While being free from wear and friction damages is an advantage for passive micromixers, lack of moving parts limits the functionality of these devices. For example, passive mixers are not switchable and after integration in a microfluidic system they perform as long as fluids are pumped into the channel. On the other hand, as active mixers operate via an external source of energy, depending on the process, they can be switched on or off either manually or automatically. Although this feature makes active mixers a suitable choice for reconfigurable microfluidic systems, it usually comes at the cost of complex fabrication and assembly procedures and the need for an on-site actuator. To conclude, there is a great potential in developing new classes of micromixers which are simple to fabricate while their functionality is controllable at different stages of the process.

4.2 Catalytic micromixers

In this chapter, a method has been proposed for fabricating catalytic micromixers which function based on the propulsion mechanism of self-motile colloidal particles. As previously reported in this thesis and as discussed by Ebbens et al [20], incorporating additional asymmetry into catalytic swimming devices can result in driven rotations or a combination of rotation and translation. This behaviour has been initially observed where the additional asymmetry was produced unintentionally. For examples, the catalytic nanorods fabricated by Fournier-Bidoz, et al. [21] have been reported to undergo circling and rotation due to surface pinning and structural defects. Vicario et al. [22] have also reported observing continuous spiralling motion of spherical particles with inhomogenous catalyst coating. Based on these findings, addition of specially fabricated catalytic devices that undergo rotary motion (and demonstrate spiralling trajectories) to a microfluidic system has the potential to create regional turbulence and enhance mixing between the streams of fluid, as shown in Figure 4.2.

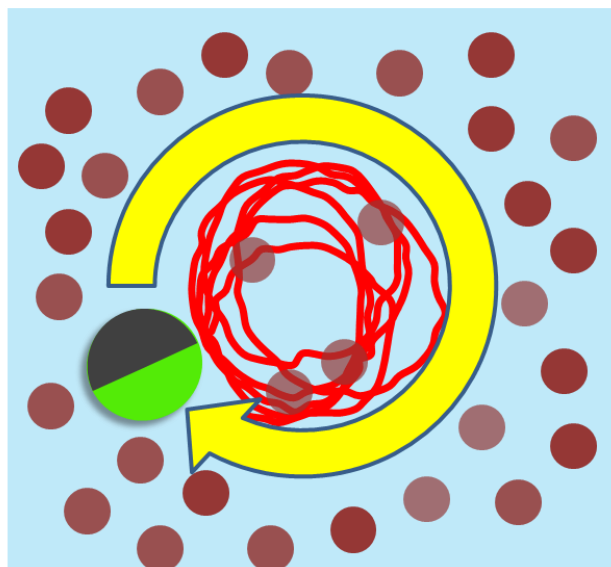


Figure 4.2 – Schematic model demonstrating the turbulence generated by the rotary motion of a catalytic swimmers.

4.3 Experimental

4.3.1 Preparation of spiralling catalytic microswimmers

The autonomous micromixers were fabricated by spin-coating a dispersed monolayer of fluorescent green (excitation/emission wavelength peaks: 468/508 nm, respectively) Thermo Scientific polystyrene colloids with a mean diameter of 1.9 μm from ethanol onto a piranha cleaned glass slide followed by thermally evaporating 5 nm of Pt onto the particles (Procedure explained in 3.2.2). This evaporation procedure has been previously reported in the fabrication of other types of propulsive and non-propulsive Janus particles [23-25]. After fabrication, particles were brushed from the glass slide using a small piece of wet lens tissue (Whatman, USA). The lens tissue containing the detached janus particles was then rubbed against the glass surface for a few times with the aim of creating additional asymmetry onto the catalyst cap by detaching small pieces of platinum from it. Finally, the particles were re-suspended in distilled water/aqueous hydrogen peroxide solution prior to the experiments.

4.3.2 Particle mixing experiment

In order to determine the mixing efficiency of spiralling catalytic micromixers, an experiment was designed to study the effect of this rotary motion has on the surrounding fluidic media. To achieve this, spiralling microswimmers were added to a solution containing 1.02 μm latex particles (fabricated by Fujii, et al. [26]) and in the next stage, the motion of the motion of microswimmers and their neighbouring latex particles was recorded and analysed in presence and absence of hydrogen peroxide fuel. This was realised by diluting 100 μl of a 1% (w/v) suspension of latex particles in distilled water into another 4 ml of distilled water and mixing 2 ml of the obtained sample with 2 ml of the sample containing suspended microswimmers

(prepared via the method describe in 4.3.1) in distilled water or in 10% (w/w) aqueous hydrogen peroxide solution so that the final hydrogen peroxide concentration was either 0% in absence of the fuel or 5% in presence of the fuel. Subsequently, 1 ml of the final solution containing the latex particles and the microswimmers was added to a quartz spectroscopy cuvette (Hellma) and 1000 frame videos were recorded from the suspending particles at 30 frames per second using an optical microscope fitted with a camera and a $\times 20$ objective. Next, the trajectory of the catalytic micromixers and their neighbouring particles were recorded and analysed using a tailor-made LabVIEW (National Instruments) program (see Figure 4.3 for a screen capture) which provided timing and the position of the particles at each frame [time, x (μm), y (μm)]. Finally, using the method described in chapter 1, the diffusion coefficient ($\mu\text{m}^2 \cdot \text{s}^{-1}$) and the velocity ($\mu\text{m} \cdot \text{s}^{-1}$) of the latex particles and the autonomous micromixers were determined from the mean squared displacement data obtained from the recorded trajectories.

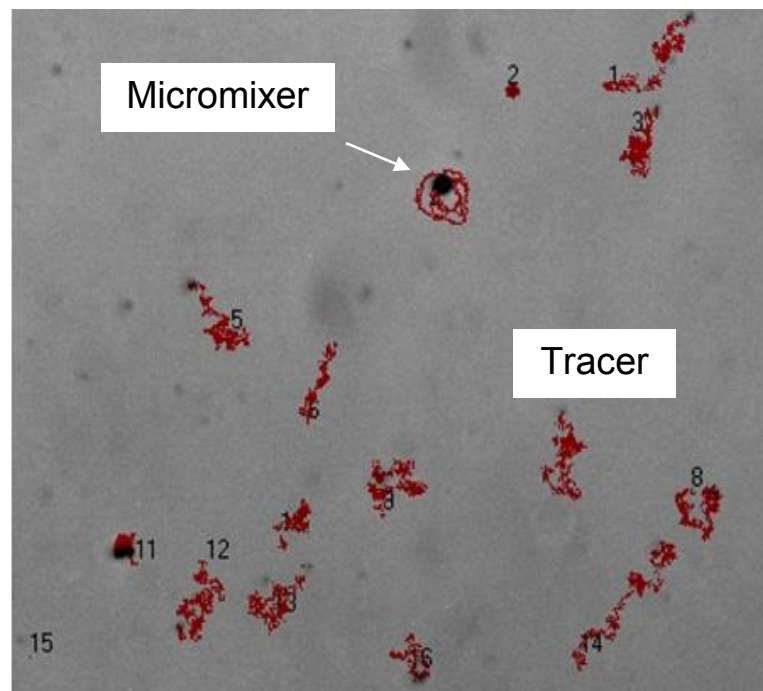


Figure 4.3 – Screen shot of the LabVIEW program recording the trajectrie of a spiralling micromixer and its neighbouring tracer latex particles

4.4 Result and discussion

To investigate the mixing efficiency of autonomous micromixers, the average velocity of the control particles surrounding each micromixer was plotted against their distance from the micromixer. After plotting the velocity vs. distance graph for each video, the results belonging to each of the experiments (in distilled water and in 5% hydrogen peroxide solution) were overlaid on a separate graph (Figure 4.3). In these graphs, the data points on the vertical axis represent the micromixers as the micromixer's distance to itself is zero. The average spinning velocity of the micromixers can also be seen and compared to the velocity of the surrounding latex particles on the graph. By comparing the graphs plotted in the presence and absence of hydrogen peroxide fuel, it can be understood that in presence of hydrogen peroxide while the catalysed decomposition reaction results in the spiralling motion of the micromixers, the motion of the neighbouring latex particles (without any catalyst coating) also becomes propulsive meaning the motion is not purely Brownian whereas in distilled water where no decomposition reaction is taking place and the micromixers are not rotating, both the micromixers and the latex particles only undergo a Brownian motion and their average velocity is nearly zero. Additionally, it can be observed that the closer the neighbouring particles are to the micromixers, the faster they move, in other words, the velocity of the control particles is directly related to their distance from the micromixer. For example, at a distance about $2.3 \mu\text{m}$ from the mixer, the velocity of the control particle increases to $2.7 \mu\text{m} \cdot \text{s}^{-1}$ where this value for a similar particle $7.4 \mu\text{m}$ away from the mixer decreases considerably to about $1 \mu\text{m} \cdot \text{s}^{-1}$. Thus, the distance where the mixing effect of the rotating particle fades can also be determined and this distance can be used in designing the geometry of the microfluidic cells.

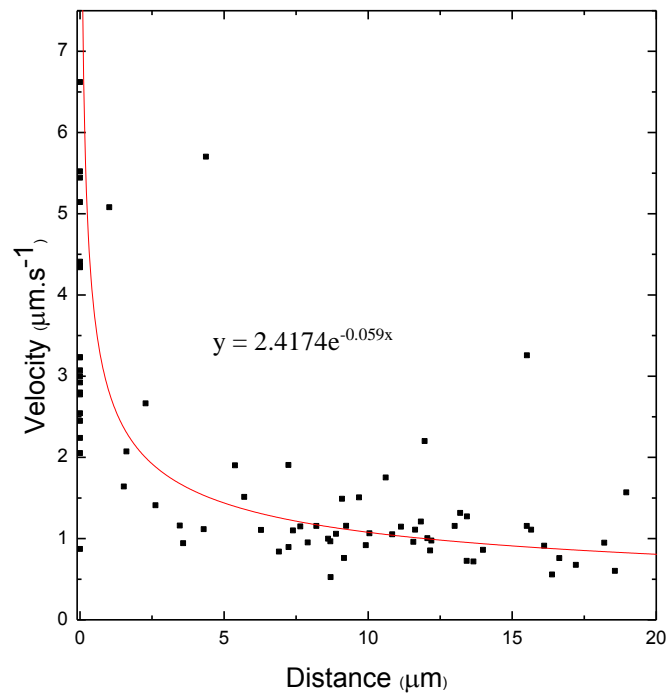
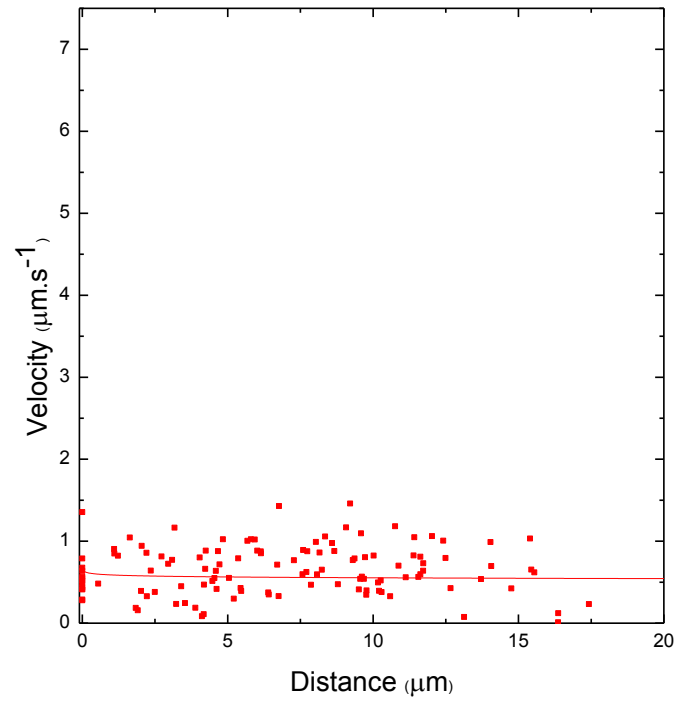


Figure 4.4 – Velocity vs distance graph for propulsive micromixers and their neighbouring latex particles in absence (top) and presence (bottom) of hydrogen peroxide fuel

The other advantage of utilising these autonomous spiralling particles in fluid mixing is the ability of controlling the spinning speed of these particles. Previously Howse, et al. have demonstrated that the velocity of propulsive autonomous swimmers is a function of the concentration of fuel in the solution they are suspended in [27]. That is, the higher the concentration of the fuel which its decomposition is catalysed by the swimmers, the faster they propel. For example, it has been reported that the velocity of a catalytic swimmer can be increased from $1 \mu\text{m} \cdot \text{s}^{-1}$ to $3 \mu\text{m} \cdot \text{s}^{-1}$ by increasing the hydrogen peroxide concentration from 2% vol to 10% vol. This is a very useful function as it can be employed for controlling the rotation speed of the micromixers and adjusting the degree of mixing between the fluids.

4.5 Summary

To sum up, the results obtained from analysing the image velocimetry data demonstrate that there is a potential to achieve efficient mixing in low Reynolds numbers at microscale by adding a small volume of a solution containing autonomous micromixers suspended in the appropriate fuel. In comparison with other active micromixer designs, these spiralling particles do not require an external source of power like an electric current or a magnetic field as the mechanical energy for their rotation is provided by the chemical reaction catalysed on their surface and additionally, these mixers do not require an external mechanism for controlling their speed as this can be also obtained by modifying the fuel concentration in the solution and adjusting the speed of the chemical reaction. Therefore, autonomous micromixers have the potential to be widely employed in biological applications where providing power and externally controlling the mixing speed is problematic.

References:

1. T. Sprogies, J. Kohler, G. Gross, *Chem Eng J* **2008**, 135:S199–S202.
2. Y. Okubo, M. Toma, H. Ueda, T. Maki, K. Mae, *Chem Eng J* **2004**, 101 (1–3):39–48.
3. K. Mae, T. Maki, I. Hasegawa, U. Eto, Y. Mizutani, N. Honda, *Chem Eng J* **2004**, 101(1–3):31–38.
4. S. Haswell, R. Middleton, B. O’Sullivan, V. Skelton, P. Watts, P. Styring, *Chem Commun* **2001**, (5):391–398.
5. D. Wilms, J. Klos, H. Frey, *Macromol Chem Phys* **2008**, 209(4):343–356.
6. F. Ullmann, *Ullmann's Chemical Engineering and Plant Design*, Volumes 1-2. John Wiley & Sons: New York, 2005.
7. L. Capretto, W. Cheng, M. Hill, *Top Curr Chem* **2011**, 304: 27–68.
8. N. T. Nguyen, Z. Wu, *J. Micromech. Microeng.* **2005** 15, R1–R16.
9. I. Glasgow, N. Aubry, *Lab Chip* **2003**, 3(2):114–120.
10. H. Bau, J. Zhong, M. Yi, *Sens Actuators B Chem* **2001**, 79(2–3):207–215.
11. G. Yaralioglu, I. Wygant, T. Marentis, B. Khuri-Yakub, *Anal Chem* **2004**, 76(13):3694–3698.
12. H. Tsai, L. Lin, *Sens Actuators A Phys* **2002**, 97:665–671.
13. A. E. Kamholz et al, *Anal. Chem.* **1999**, 71, 5340–7.
14. R. F. Ismagilov et al, *Appl. Phys. Lett.* **2000**, 76, 2376–78.
15. A. Gunther, M. Jhunjhunwala, M. Thalmann, M. Schmidt, K. Jensen, *Langmuir* **2005** 21(4):1547–1555.
16. H. Song, J. Tice, R. Ismagilov, *Angew Chem* **2003**, 115(7):792–796.
17. T. Johnson, D. Ross, L. Locascio, *Anal Chem* **2002**, 74(1):45–51.
18. N. Schwesinger, T. Frank, H. Wurmus, *J Micromech Microeng* **1996**, 6:99.
19. A. Kamholz, P. Yager, *Sens Actuators B Chem* **2002**, 82(1):117–121.
20. S. Ebbens, R. A. L. Jones, A. J. Ryan, R. Golestanian, J. R. Howse, *Phys. Rev. E* **2010**, 82, 015304
21. S. Fournier-Bidoz, I. Manners, G. A. Ozin, *Chem. Commun.* **2005**, 441–443.
22. J. Vicario, R. Eelkema, W. R. Browne, A. Meetsma, R. M. La Croisa, B. L. Feringa, *Chem. Commun.*, **2005**, 3936–3938.
23. M. Albrecht, G. Hu, I. L. Guhr, T. C. Ulbrich, J. Boneberg, P. Leiderer, and G. Schatz, *Nature Mater.* **2005** 4, 203.

24. S. K. Smoukov, S. Gangwal, M. Marquez, O. D. Velev, *Soft Matter* **2009** 5, 1285.
25. H. Takei, N. Shimizu, *Langmuir* **1997**, 13, 1865.
26. S. Fujii, P. D. Iddon, A. J. Ryan, S. P. Armes, *Langmuir* **2006**, 22, 7512-7520.
27. J. R. Howse, R. A. L. Jones, A. J. Ryan, T. Gough, R. Vafabakhsh, R. Golestanian, *Phys. Rev. Lett.*, **2007**, 99, 048102.

Chapter 5: High surface area structures

- a route for increasing the number of reaction sites in catalytic swimmers

Self-motile colloidal catalytic swimmers are promising candidates for targeted drug delivery in biological systems and small scale cargo transport in microfluidic cells since they do not require an external source of energy to propel, chemical functionalization of their surface is straightforward and they can be readily fabricated in a range of sizes depending on the application. Moreover, due to the greater capability of responsive polymeric materials in absorbing and realising chemicals, their biocompatibility and their near water densities, employing polymer-based devices is preferred to metallic devices in biological applications. Despite the advantages stated above, so far the average propulsion velocities reported for polymeric catalytic devices is considerably lower than the values reported for metallic devices such as Pt/Au nanorods. For example, the reported average velocity for a 2 μm Pt/Au nanorod suspended in 5% hydrogen peroxide aqueous solution is $7.7 \pm 0.9 \mu\text{m} \cdot \text{s}^{-1}$ [1] and this value for a 1.68 μm Pt-coated polymeric microsphere is $2 \pm 0.1 \mu\text{m} \cdot \text{s}^{-1}$ [2]. Since these velocity variations can be due to the difference between the geometry of cylindrical nanorods and spherical polymeric microswimmers, this chapter focuses on examining various methods for fabricating polymeric structures with increased surface areas. In other word, as the surface area of a cylinder is more than a sphere with the equivalent volume, the number of catalytic reaction sites per volume are higher for a nanorod compared to a microsphere resulting a faster decomposition reaction on its surface and

consequently a greater propulsion velocity. Thus a high surface area polymeric catalytic swimmer can theoretically propel faster than conventionally fabricated polymeric microswimmers.

5.1 Fabrication methods of colloidal cluster

An appealing method of achieving an increase in surface for a given overall nanoswimmer diameter is a packing smaller colloidal particles into 3D clusters [3-5]. In this technique, polymeric spheres are fused together either by chemical covalent bonds or electrostatic forces to form higher order structures such as tetrahedrons or triangular dipyramids. One of the leading papers in this field was published by Manoharan, et al. [6] who reported that under sufficient compressive force, small numbers of polymeric microspheres ($n=2$ to 15) can be packed into identical and distinct polyhedras for each value of n (See Figure 5.1). These densely packed colloidal clusters which were fabricated from 844 nm cross-linked polystyrene (PS) microspheres (with sulphate groups on their surface) as building blocks in an oil-in-water emulsion system, were prepared by dispersing the particles in toluene, adding water, mixing and creating an oil-in-water (O/W) emulsion (with oil droplet diameters ranging between 1 to 10 μm) followed by preferentially evaporating the oil phase from the system which results the PS particles in toluene droplets to pack together and form stable clusters in water. Manoharan, et al. have also mentioned that the most critical stage of the particle packing process is when the last of toluene starts to evaporate and the droplets containing the PS particles lose their spherical shape and deform. This deformation generates the capillary forces that rapidly rearrange the particles and lead to cluster formation. The drawback of this technique in fabricating colloidal clusters is the exposure of the external surface of the particles

to water at earlier stages of toluene evaporation which leads to dissociation of the surfaces of sulphate groups and prevents dense packing and cluster formation.

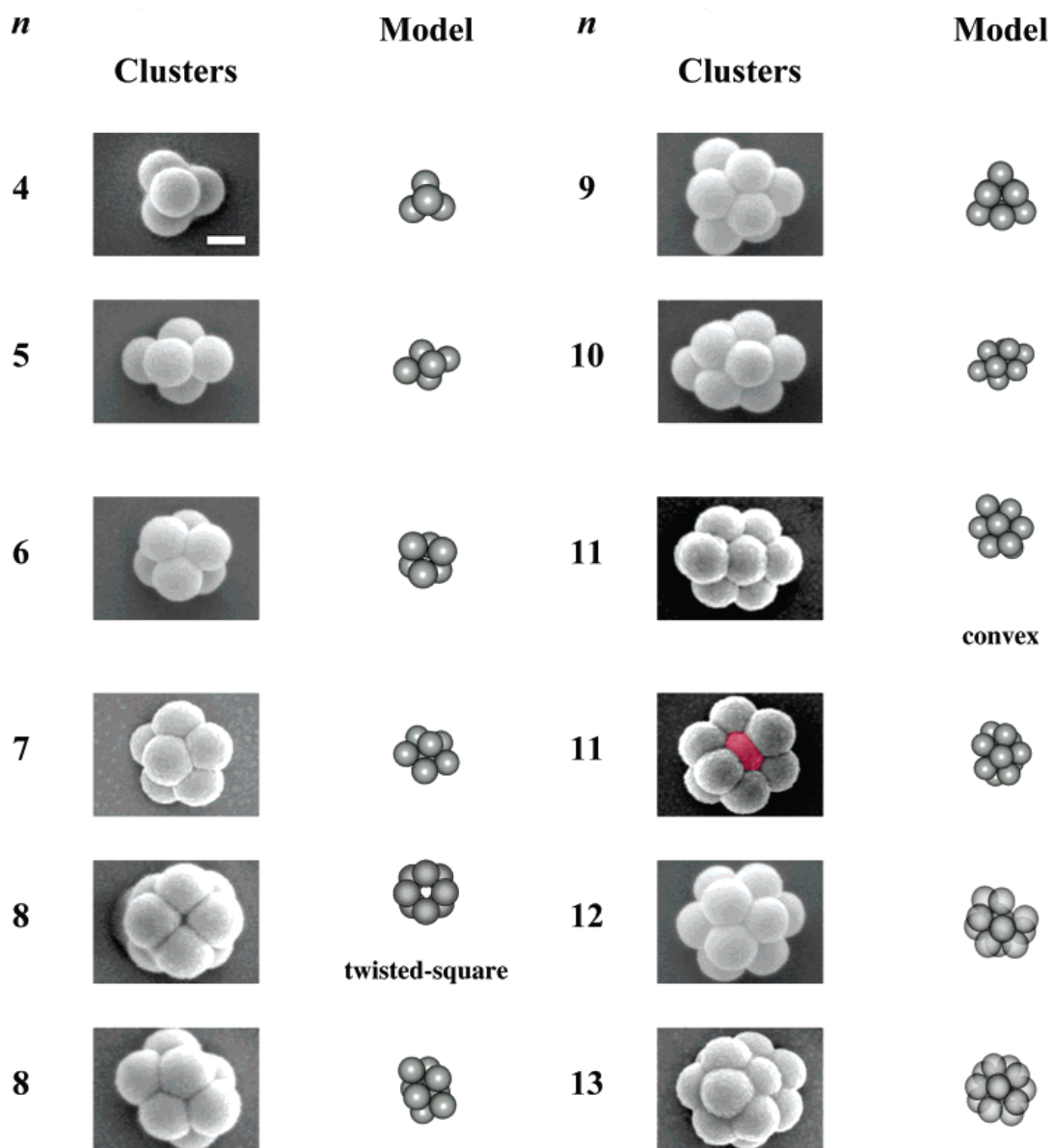


Figure 5.1– SEM images and schematic models of 3D colloidal clusters with 4 to 13 spheres in their structure. (taken from Ref. [6])

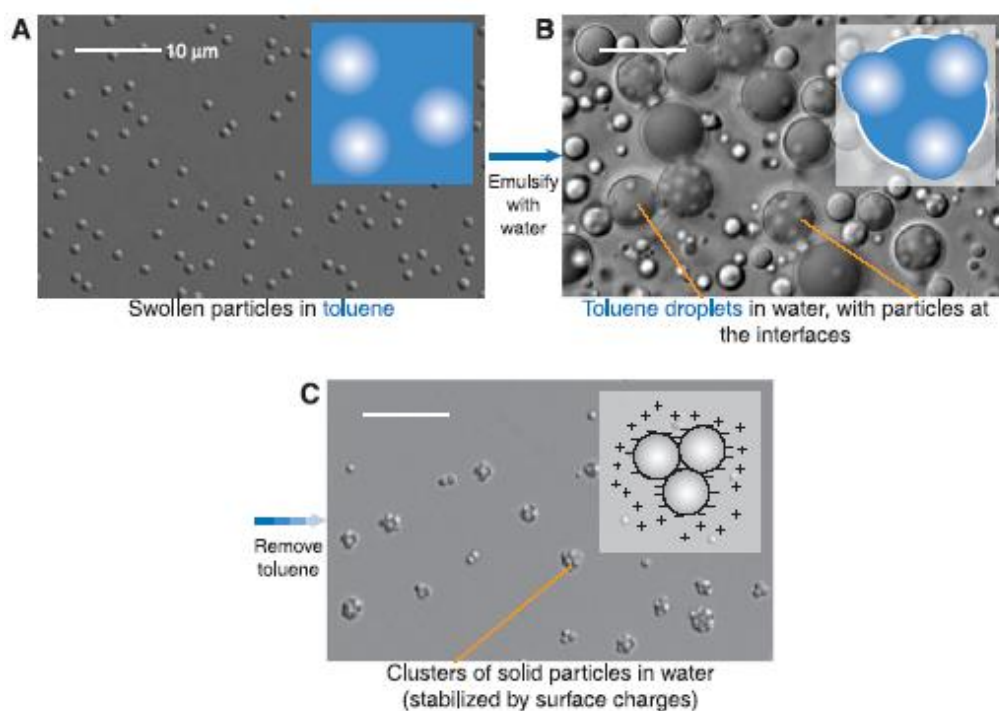


Figure 5.2 - Fabrication of PS clusters in an oil in water emulsion (A) particle dispersion in toluene (B) droplet formation after emulsification in water (C) dense packing of particles after preferential evaporation of toluene (figure taken from Ref. [5])

Cho, et al. [7] also proposed an emulsion-based method for preparing colloidal clusters. However, in their method the clusters were fabricated from a water-in-oil (W/O) emulsion. These clusters were formed by adding an aqueous suspension of 830 nm PS spheres (~1% w/w) to a solution containing toluene and Span 80 surfactant (3 mL of PS suspension added to the mixture of 1% w/w Span 80 and 17 mL of toluene.), emulsifying the mixture for with a homogenizer at 12000 rpm and finally evaporating the water phase to promote cluster formation. With this technique colloidal cluster containing 2 to 10 spheres in their structure were formed though for higher order assemblies, for example the clusters with 8 spheres, a disphenoid packing was more frequent in contrast to Manoharan, et al.'s method where for the same number of spheres the twisted square structure was dominant resulting from the different electrostatic interactions between the PS beads in W/O and O/W emulsions.

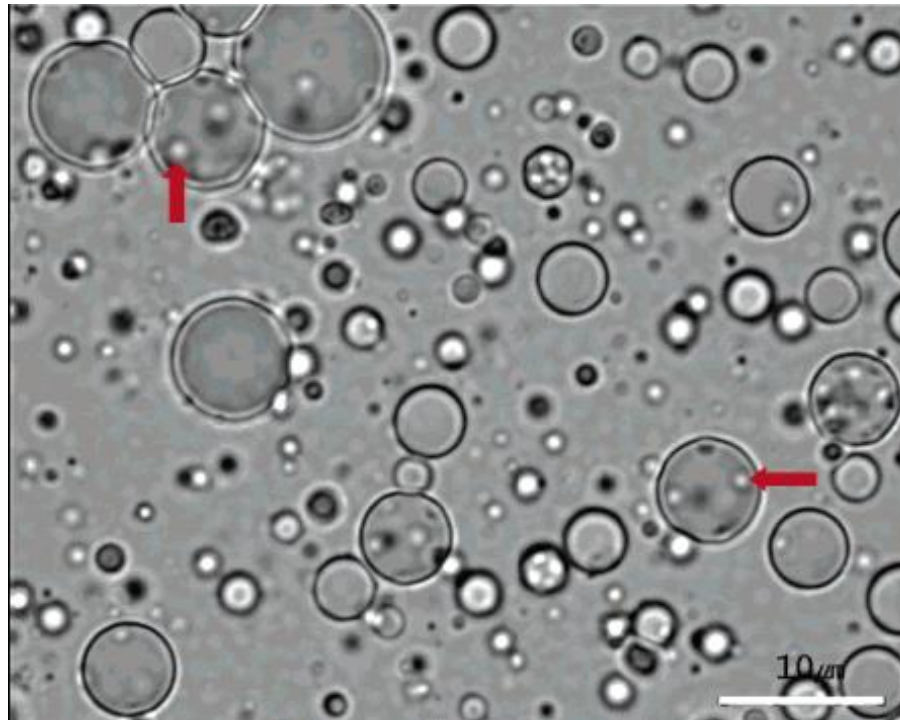


Figure 5.3 – Optical microscope image of water droplets encapsulating PS spheres in toluene media – Arrows show PS spheres at the water-toluene interface - (figure taken from Ref. [7])

A recent study based on simulations and experiments by Schade, et al. [8] suggests mixing two types of positively and negatively charged colloidal spheres with different diameters and benefiting from the electrostatic attraction between them to form 3D clusters. This study was conducted by running computational simulations to calculate the optimal ratio between the diameter of small beads and large beads followed by examining the results using oppositely charged PS spheres or functionalised particles with complementary DNA sequences on their surface. Schade, et al. [8] have noted that at a critical size ratio of $\alpha = 2.41$ between the beads, this process yields a narrow distribution of clusters with 4 spheres forming tetrahedral structures which after formation cannot rearrange to denser packings due to their electrostatic stability (Figure 5.4).

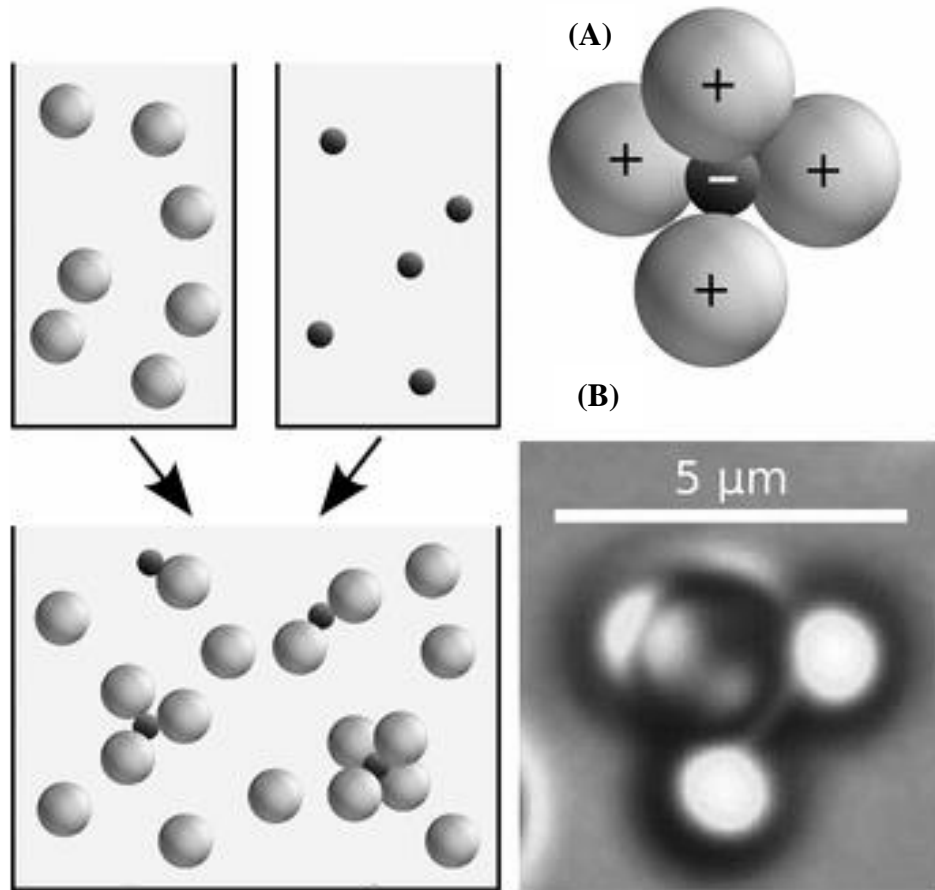


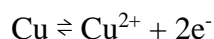
Figure 5.4 – (A) Schematic design showing the formation of tetrahedral colloidal clusters from random packing of bidisperse spheres (B) Optical image of oppositely charged polystyrene spheres forming a tetrahedral structure (taken from Ref. [8])

In addition to the methods described to this point, other techniques suggested for fabricating colloidal clusters include geometrical confinement of colloidal particles in cylindrical holes patterned into a thin film of photoresist [9] and a chemical synthesis route with controlled precipitation that produces smaller 2D cluster such as dimers, tetramers and daisy like structures [10]. As these methods are more complicated, involving expensive and time consuming preparation stages, they are generally not desired for high yield cluster fabrication.

It was therefore decided that the simpler, surfactant / emulsion approach presents one such opportunity in creating high surface area aggregates which may find use in nano- and micro-swimmers.

5.2 Catalyst deposition via redox reactions

Another method for increasing the number of reaction sites in colloidal catalytic microswimmers is through electrodeless deposition of platinum instead of the conventional vacuum vapour deposition method. A good example demonstrating the capability of electrodeless metal deposition in increasing the surface area is the reaction commonly known as the “silver tree experiment”. In this experiment, a piece of copper wire begins to get coated with silver after immersion in an aqueous solution of silver nitrate (AgNO_3). This is a redox reaction where copper (with a lower electrode potential) oxidises and gets dissolved in the solution while silver ions receive the oxidation electrons and reduce to silver on the surface of the wire:



In this reaction, silver atoms do not homogeneously coat the copper surface but they follow a growth pattern that forms several thin branches of silver covering the wire generating a silver surface of high surface area as shown in Figure 5.5.

Rhoda, et al. [11] have reported a similar technique for growing platinum crystals on a copper surface. In this patented method, catalytically active platinum branches form on copper surface after immersion in an aqueous solution of sodium hexahydroxyplatinate (IV) [$\text{Na}_2\text{Pt}(\text{OH})_6$], heated to 35°C using an oil bath. As platinum is a noble metal, this redox reaction must take place in presence of a strong reducing agent such as hydrazine hydrate to initiate and maintain the reduction reaction of platinum ions into solid platinum. As the surface area of the scattered crystal branches is higher than the area of a smooth surface coated with platinum, evaporating copper onto the surface of colloidal particles and growing platinum

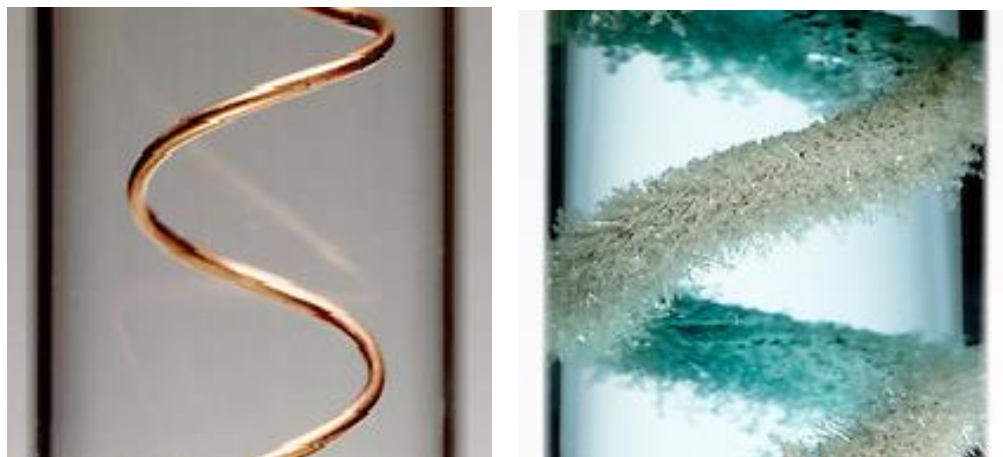


Figure 5.5 – An image showing a copper wire (A) before and (B) after immersion in an aqueous solution of silver nitrate demonstrating crystal growth on the surface of the wire

branches on them can potentially lead to formation of high surface area colloidal catalytic swimmers.

5.3 Experimental

5.3.1 Preparation of polystyrene spheres

Prior to examining the methods described earlier to fabricate high surface area catalytic swimmers, polystyrene colloidal particles which are the building blocks of these devices were prepared using a process described by Fujii, et al. [12]. In this dispersion polymerization process which was performed in the presence of poly(N-vinylpyrrolidinone) (PNVP, K90, nominal molecular weight = 360,000) steric stabiliser in batch mode at 70°C using 2,2'-azobis(isobutyronitrile) (AIBN) as the initiator, PNVP (1.0 g; 10 w/w % based on styrene) was mixed with isopropyl alcohol IPA (100 ml) in a three-necked, round-bottomed 250 ml flask fitted with a reflux condenser and a magnetic stirrer bar. This mixture was purged with nitrogen for 30 minutes at 70 °C prior to commencing the polymerisation. Next, 10 g of inhibitor removed styrene was added to the flask and the mixture was continuously stirred at 300 rpm until the temperature equilibrated back to 70 °C. Polymerisation

initiated after 100 μl of AIBN was added to the mixture of styrene, IPA and PNVP. After 24 h of nitrogen purging and continuous stirring at 300 rpm at constant temperature, synthesised PNVP-PS latex particles were separated from the solution via centrifugation at 5000 rpm for 15 minutes. Subsequently, the particles were redispersed in distilled water and washed by centrifugation-redispersion in distilled water for 3 cycles. Finally, the diameter of the beads was determined using a tailor-made optical image analysis software written in LabVIEW which reported a narrow size distribution between 1.6 and 1.7 μm for the products.

Table 5.1 – Summary of the PNVP-PS particle fabrication process

	Name	Volume
Solvent	IPA	100 ml
Monomer	Styrene	10 ml
Stabiliser	PNVP	1 ml
Initiator	AIBN	100 μl
Conditions	<ul style="list-style-type: none"> • Continuous nitrogen purge for 24h • Continuous stirring at 300 rpm • Constant temperature at 70 °C <ul style="list-style-type: none"> • Solvent reflux 	

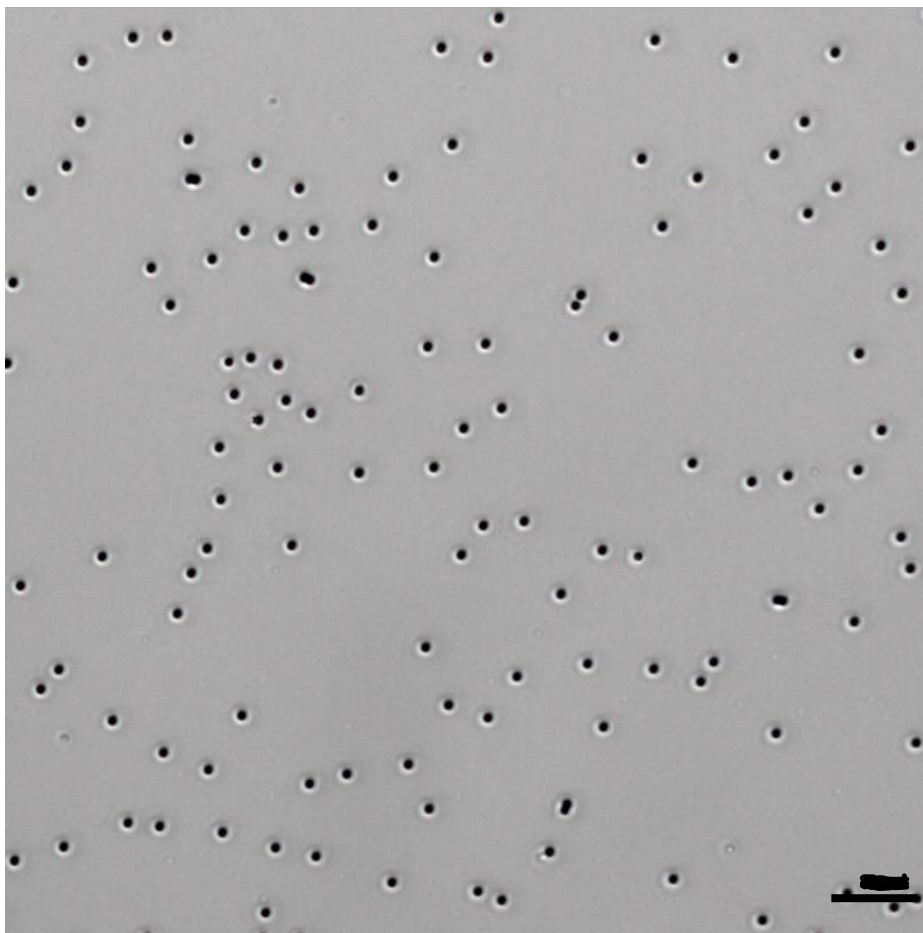


Figure 5.6 – Optical image of the 1.6 μm PNVP-PS latex particles fabricated by dispersion polymerisation (scale bar: 10 μm)

5.3.2 Preparation of colloidal clusters

5.3.2.1 SDS, water, toluene (Oil-in-Water Emulsion)

In the first attempt towards fabricating high surface area catalytic swimmers, 1.6 μm latex particles as prepared in 5.3.1 were utilised for fabricating colloidal clusters by following the method developed by Manoharan, et al. [6]. As the fabricated polystyrene particles were not cross-linked unlike the beads utilised by Manoharan, et al., toluene which is a solvent for polystyrene could not be used for preparing the oil-in-water emulsion as it resulted rapid dissolution of the beads prior to cluster formation. Consequently, the oil-in-water solution was prepared by dispersing the 1.6 μm beads in 5 ml hexane (0.1% w/w) and adding 0.5 ml of this stock solution to

a mixture of 0.1 g Span 80 surfactant in 4.5 ml distilled water. Colloidal clusters were formed after emulsifying the mixture with an ultrasonic homogeniser at 12000 rpm for 30 seconds followed by increasing the temperature to 70 °C which led to evaporation of the oil phase.

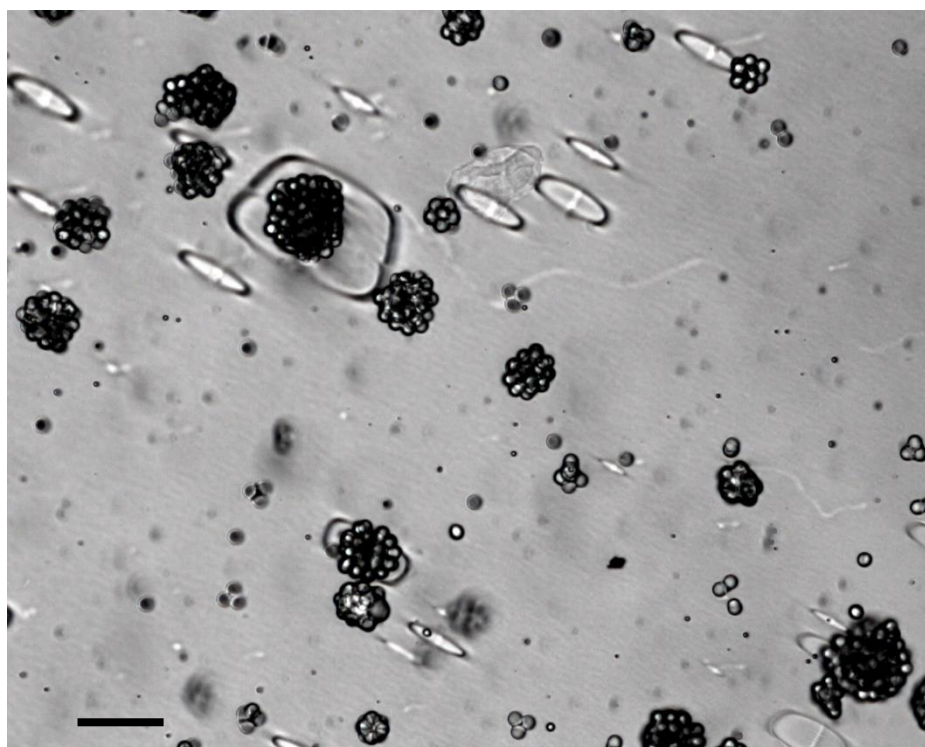


Figure 5.7 – Colloidal cluster prepared in an oil-in-water emulsion from 1.6 μm polystyrene latex particles (scale bar: 20 μm)

While the fabricated colloidal clusters were stable in water, they could not be transformed to catalytic swimmers as after drop casting them onto a glass slide from water, drying them in room temperature and evaporating platinum onto them, detaching them from the substrate led to separation of the beads from each other as the beads were only bound together by weak van der Waals force and minimal forces applied on them caused deformation and destruction of the clusters.

To overcome this issue, in a further attempt, cross-linked polystyrene beads were joined together by an adhesive medium. In this trial, 0.5 g polystyrene was dissolved

in 4.5 ml of toluene prior to adding 0.5 ml of 6 μm CA-6 latex particles (cross-linker PMMA Microbeads from Microbeads, Norway) from a 1% w/w suspension in water to the solution. The size of the utilised latex building blocks was increased from 1.6 μm to 6 μm firstly due to the availability of cross-linked colloids and with the aim of packing fewer number of beads in oil droplets and forming clusters with simpler to study assemblies. Next, 0.5 ml of the prepared stock solution containing the beads, toluene and dissolved polystyrene was added to a solution of 0.1 g sodium dodecyl sulphate (SDS) surfactant in 4.5 ml water and mixture was emulsified with an ultrasonic homogeniser at 12000 rpm for 30s. By gradual evaporation of toluene from the system, the beads were tightly packed and chemically bound together by the solidified polystyrene. Three other samples were also prepared using the same stock solution and different stock-solution:water:surfactant ratios with the aim of studying the effect of the concentration of these components on the packing and assembly of colloidal clusters. The recipes for these trials are summarised in Table 5.2.

Table 5.2 – Summary of the colloidal cluster fabrication recipes using crosslinked polystyrene particles

Sample #	Stock (ml)	Water (ml)	SDS (g)	SDS/Stock %
1	0.5	4.5	0.1	0.2
2	0.25	4.75	0.1	0.4
3	0.25	4.75	0.2	0.8
4	0.5	4.5	0.2	0.4

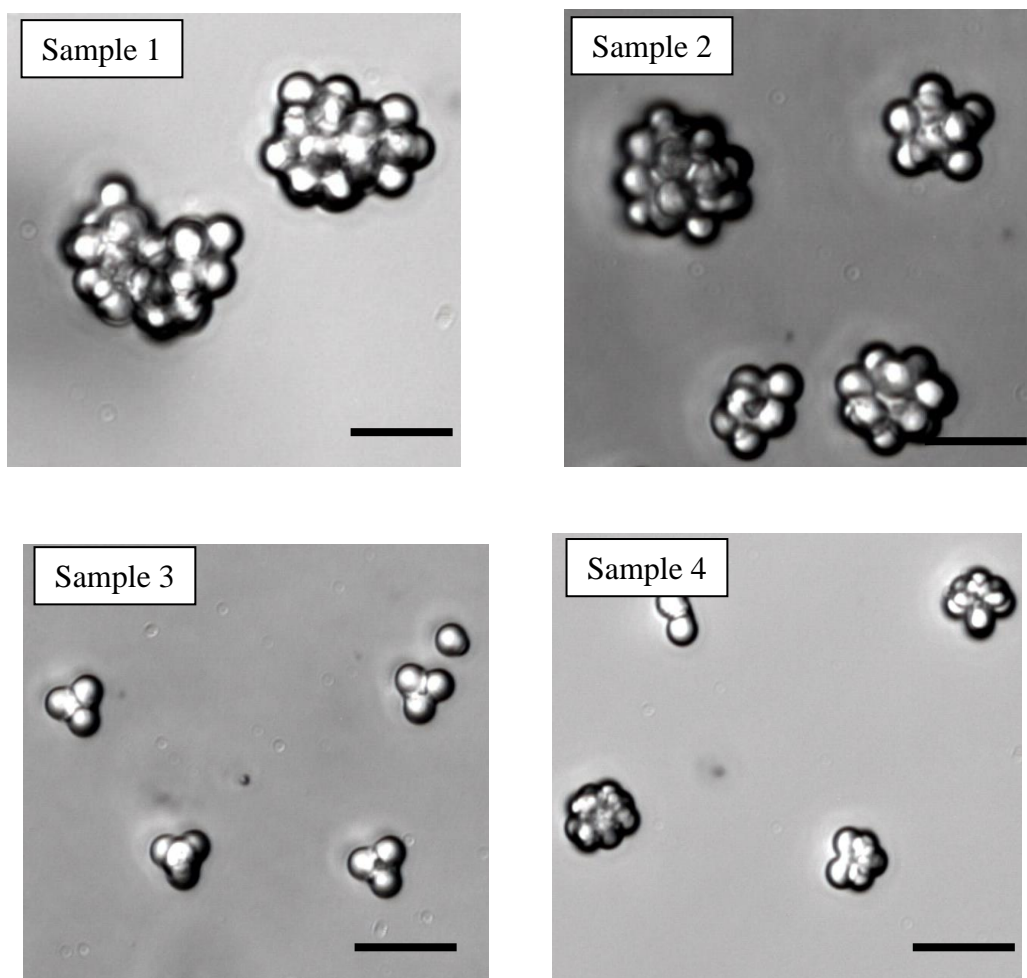


Figure 5.8 – Optical images of colloidal clusters fabricated in an oil-in-water emulsion from 6 μm crosslinked polystyrene particles (scale bar: 20 μm)

Optical images captured from these fabricated colloidal clusters with different stock-solution:water:surfactant ratios demonstrate that by increasing the surfactant:stock-solution ratio (from 0.2% to 0.8%), as there are more surfactant molecules available for a given volume of toluene, the toluene droplets formed in the emulsion are smaller therefore a fewer number of beads can fit in them, resulting smaller colloidal clusters (Sample 3). Likewise, by increasing the stock-solution:water ratio while keeping the surfactant:stock-solution the same (0.8%), as the number of beads for a given volume of emulsion increases, more beads are packed in toluene droplets and higher order clusters with more beads in their structure are formed.

In the next stage, these clusters were transformed into catalytic swimmers by evaporating 5 nm of platinum onto them and although the decomposition reaction of hydrogen peroxide took place in their presence, these particles did not propel. It is thought that it could have been due to the higher weight of the total cluster compared to previously fabricated catalytic swimmers. In another trial 10 nm of platinum was evaporated onto the clusters. Although in this trial there was enough catalyst on the clusters to make them propel, unfortunately presence of a thick layer of platinum led to a fast hydrogen peroxide decomposition reaction and rapid bubble generation in the observation cuvette, making it difficult to record videos from the propulsion of these devices. It is also worth to consider the effects of size as these aggregates, which are based on multiples of 6 micron particles, will inherently be slow compared to much smaller swimmers.

5.3.2.2 Fabrication of colloidal aggregates via partial melting

In another set of experiments a simpler approach was taken for fabricating colloidal clusters. In this approach which did not require emulsification or preferential solvent evaporation, the clusters were formed by spreading the beads onto a glass substrate and heating them until they were soft enough (beyond their glass transition temperature) to stick to the beads adjacent to them to form a cluster. In the first trial of this series of experiments, a dilute suspension (0.1 w/w%) of previously fabricated 1.6 μm polystyrene particles in ethanol was spin-coated onto microscope glass slides at 3000 rpm to distribute the beads on the substrate. Next, these samples were put into a vacuum oven at 100 mbar to avoid thermal decomposition of the beads at high temperatures and heated to 150 °C. Subsequently, optical images were taken from the samples which were heated for 5, 10, 15 and 20 minutes in the oven.

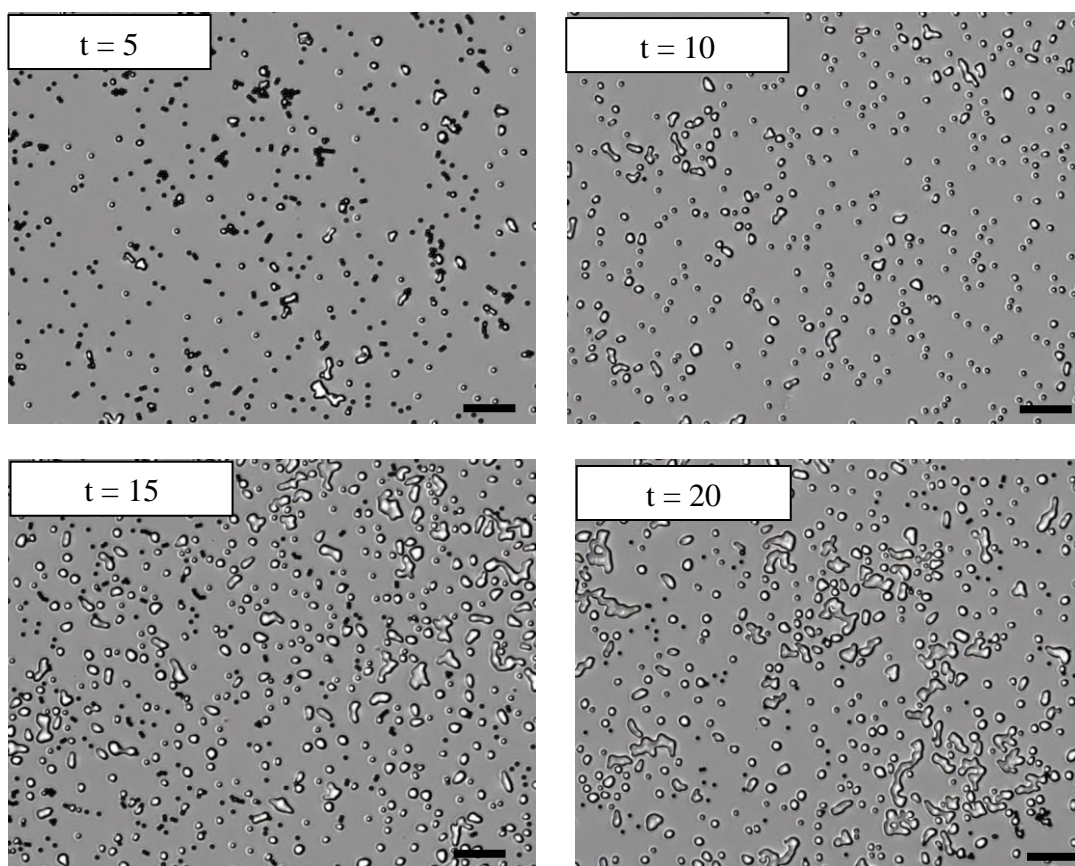


Figure 5.9 – Optical images taken from the latex beads heated to 150°C at 100 mbar at different time intervals (t=5, 10, 15 and 20 minutes) (scale bar: 10 µm)

As Figure 5.9 demonstrates, due to the rapid heating rate at 150 °C even after 5 minutes some beads were fully molten, forming amorphous polymeric aggregates which could not be detached from the glass substrate. Additionally, spin-coating the beads suspension onto the glass slide formed a dispersed monolayer of beads therefore most beads did not have other beads adjacent to them to form a cluster so the yield of this method for fabricating colloidal clusters was low.

In the next trial, the suspension of beads in ethanol was drop casted onto the glass slide and rapidly dried in the vacuum oven at 50 °C at 100 mbar. Due to the surface tension between ethanol and the glass substrate, beads were attached together at the

ethanol-air interface while the droplet containing the beads was getting smaller due to evaporation. Next the dried samples were heated to 115 °C in the vacuum oven at 100 mbar with the aim of improving the attachment of particles together and stimulating the formation of colloidal clusters. Finally, optical images were taken from the samples after heating them for 10, 20 and 30 minute in the vacuum oven.

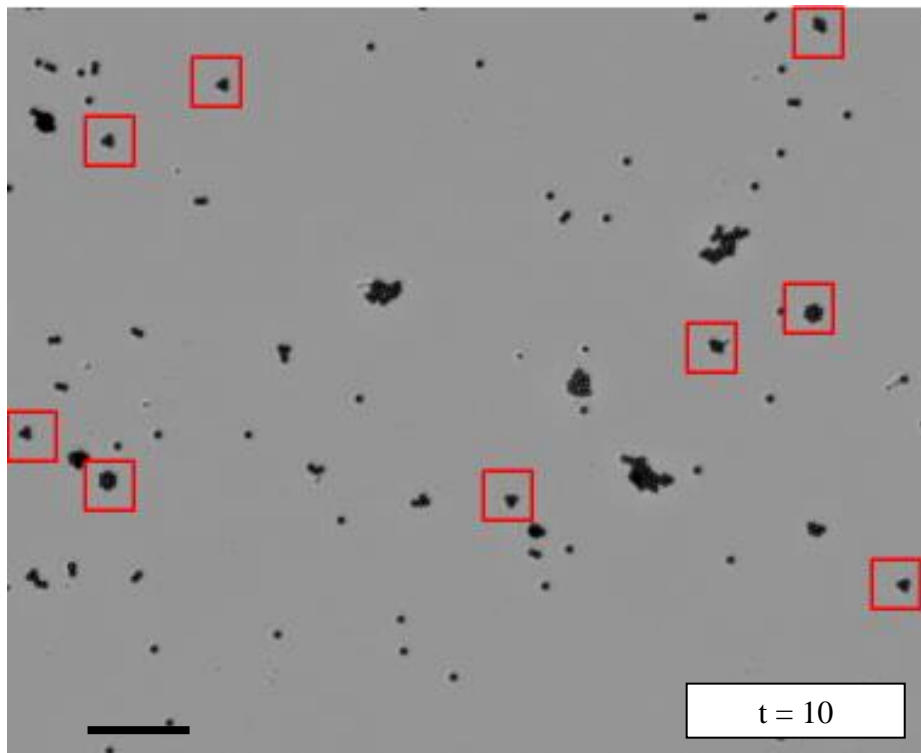


Figure 5.10 - Optical images taken from the latex beads heated at 115 °C for 10 minutes (scale bar: 20 μm)

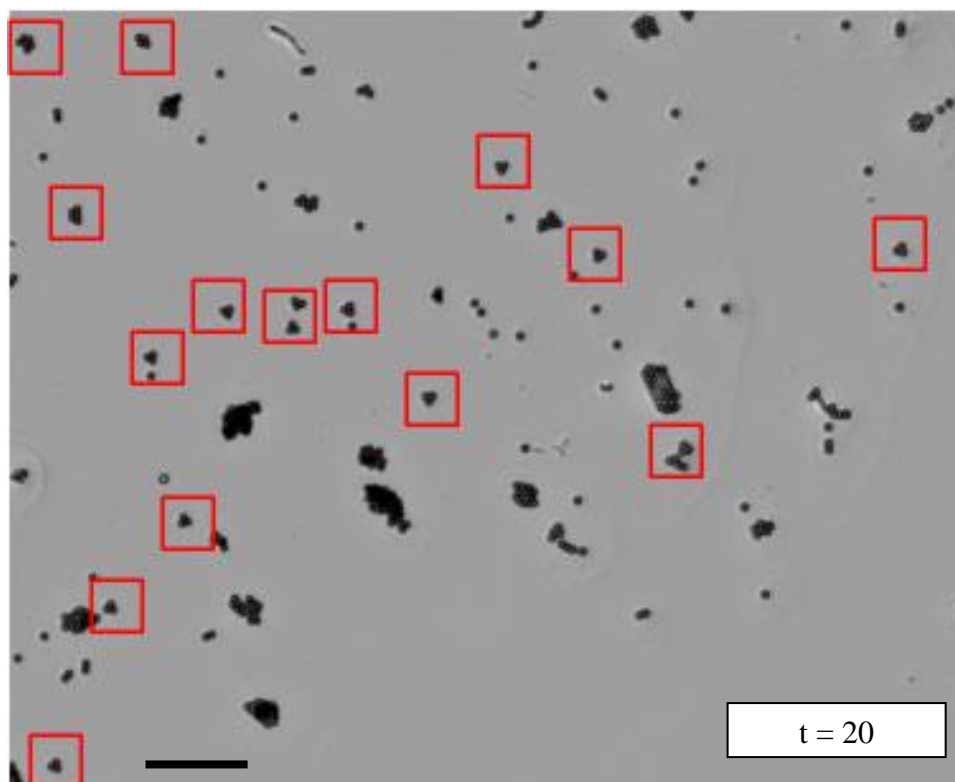


Figure 5.11 - Optical images taken from the latex beads heated at 115 °C for 20 minutes (scale bar: 20 μm)

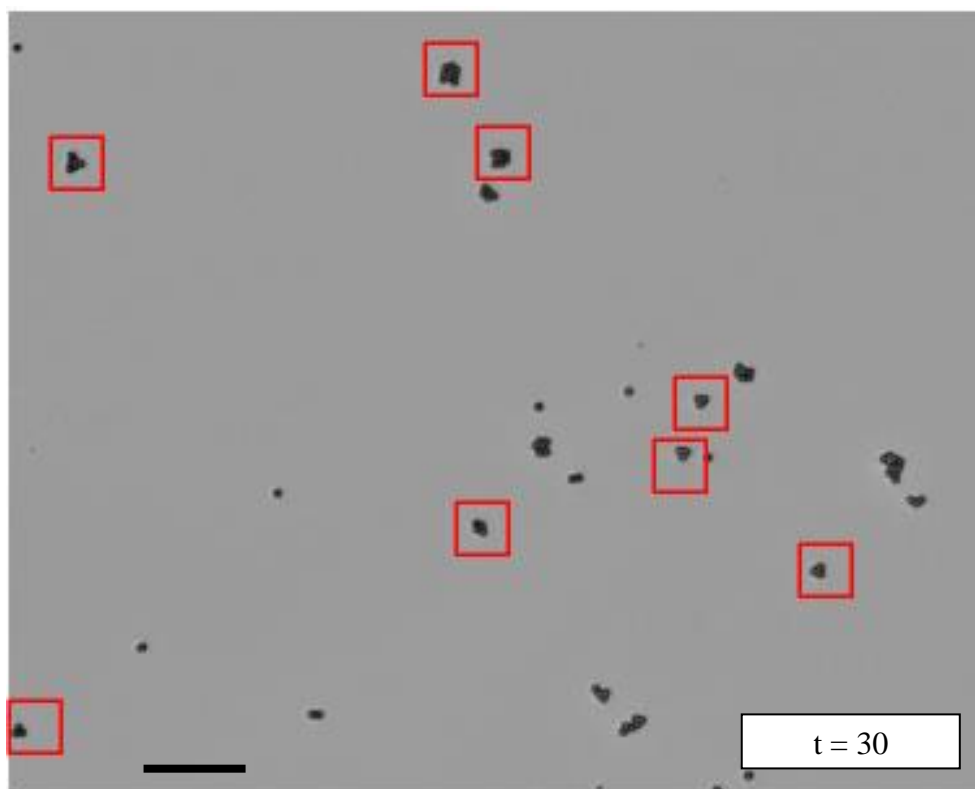


Figure 5.12 - Optical images taken from the latex beads heated at 115 °C for 30 minutes (scale bar: 20 μm)

The optimum adhesion between the beads was obtained after 20 minutes heating at 115 °C and 100 mbar (See Figures 5.10 - 5,12). The clusters formed in these conditions did not separate after detachment from the glass substrate subsequent to the platinum evaporation stage where after 10 minutes of heating the cluster were easily deformed and after 30 minutes of heating the cluster were strongly attached to the glass substrate and applying excessive force led to their deformation. Optical images taken from these clusters also indicate that this method of sample preparation which involves drop casting the bead suspension followed by rapid evaporation of the liquid media favours the formation of small 2D clusters mainly with 3 beads in their structure.

Although the results of this set of experiments were promising from a cluster formation point of view, the catalytic swimmers fabricated from these clusters propelled much slower than spherical colloidal catalytic swimmers with equivalent diameters and equal thickness of platinum on their surface. For example, the average propulsion velocity for a 2.5 μm spherical catalytic swimmer (with a 5 nm platinum cap, suspended in 10% hydrogen peroxide solution in water) reported by Ebbens, et al. [13] is 4 $\mu\text{m} \cdot \text{s}^{-1}$ where the clusters containing three 1.6 μm beads (with the same thickness of catalyst layer on their surface, suspended in 10% hydrogen peroxide solution in water) were only agitating on the substrate without any noticeable propulsion.

5.3.2.3 Fusing 6 μm PS particles to platinum coated colloids

In the third trial, catalytic colloidal clusters were fabricated by fusing a bi-disperse mixture of polystyrene particles together at 150 °C in 100 mbar vacuum. The sample

for this trial was prepared by adding 100 μl of a 1% (w/w) suspension of CA-6 latex particles in water and 100 μl of a 1% (w/w) suspension of 1 μm platinum-coated polystyrene particles (Kisker, Germany) to 5 ml of distilled water and stirring the suspension with a magnetic stirrer bar for 60 seconds. Next, the mixture was transferred into a glass test tube and left until the particles randomly settled at its bottom. The test tube was kept in the oven at 50 $^{\circ}\text{C}$ for 12 hours to ensure all the water has been removed from the sample. Subsequently, the dry sample was heated to 150 $^{\circ}\text{C}$ at 100 mbar vacuum for an hour to enhance the fusion between the particles. After the heating step, the test tube was removed from the oven and left until it cooled down to room temperature. Finally, 5 ml of distilled water were added to the test tube and the sample was sonicated for 5 minutes to redisperse the fabricated clusters in water. The yield of this method for fabricating bidisperse colloidal clusters was generally low as most of the fused particles split back into single particles after the sonicating stage. Most importantly, each of these bidisperse clusters had a distinctive assembly consisting of platinum coated particles randomly attached to one, two or rarely three CA-6 particles. This made reproducibility of the structure and the results obtained from suspending these particles in hydrogen peroxide fuel nearly impossible.

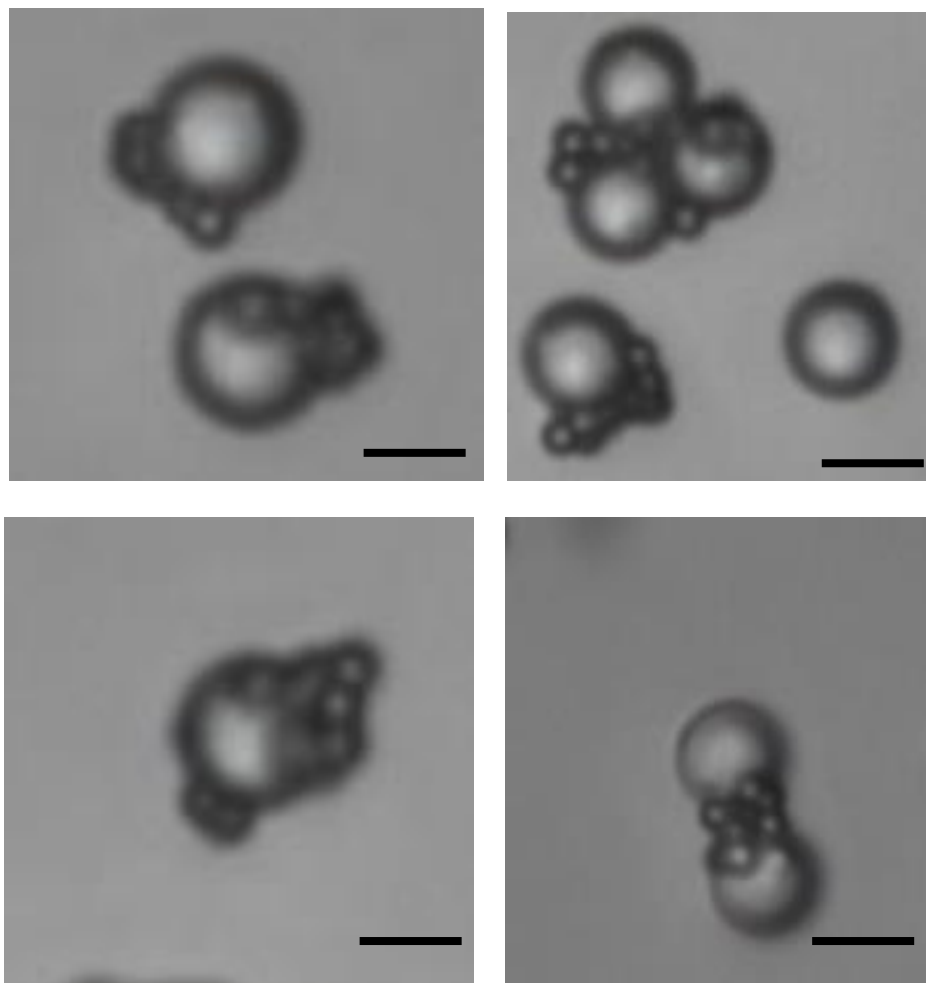


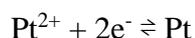
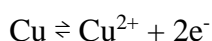
Figure 5.13 – optical images of catalytic colloidal clusters fabricated by fusing a bidisperse mixture of polystyrene particles together at 150 °C in 100 mbar vacuum (scale bar: 5 μm)

5.3.3 Electroless platinum plating of colloidal particles

In the final trial for fabricating high surface area catalytic swimmers, electrodeless platinum plating of spherical particles was examined. As platinum is a Noble metal, the reduction reaction of platinum ions in a solution to platinum atoms only takes place in presence of strong reducing agents such as hydrazine hydrate. As this reagent also reacts with polystyrene and creates a polymer foam on the surface of the solution, in this experiment polymeric beads were substituted with Spherigalss 5000 (Potters Beads, USA) glass microspheres with a mean diameter of 7-10 μm as these

particles did not react with hydrazine. As discussed earlier, Rhoda, et al. [11] developed a method for growing catalytically active platinum branches on copper, thus the Spherglass particles were partially coated with 50 nm of copper via the procedure which has been reportedly employed for the fabrication of propulsive and non-propulsive Janus particles [14-16] after being spin coated onto a glass slide (from a 1% (w/w) suspension in ethanol) prior to initiation of the redox reaction.

After coating the upper half of the surface of glass spheres with copper, these particles were detached from the glass slide using a wet sheet of lens cleaning tissue (Whatman, USA) and redispersed in 1 ml of distilled water. Next, the electroless platinum coating experiment was conducted by following the method reported by Rhoda, et al. [11]. In this experiment, which was conducted at 35 °C in an oil bath, 10 mg of $\text{Na}_2\text{Pt}(\text{OH})_6$ and 5 mg of NaOH (from solid NaOH pellets) were added to the dispersion of copper coated Spherglass particles in water and stirred with a magnetic stirrer bar until the platinum salt was fully dissolved in water. Subsequent to addition of 20 μl ethylamine which acted as the reaction stabiliser and 2 μl hydrazine hydrate, the following redox reaction was initiated:



Hydrazine hydrate was added to the mixture to maintain its concentration in the solution. After an hour, all the platinum salt dissolved in the solution was consumed and the redox reaction stopped. At this point 10 μl of the mixture was pipetted out and drop casted onto a clean glass slides. In the optical images taken from the dried drop casted sample, a few particles were seen with patches of platinum grown on their surface (Figure 5.14) but in majority of the particles the copper cap was stripped

off from the surface of the beads during the reaction which after oxidation led to formation of lumps of platinum suspended in the solution. Conducting swimming experiment on the glass beads with platinum patches on their surface was also problematic as the presence of numerous small flakes of platinum in the hydrogen peroxide solution caused excessive bubbling, making it challenging to capture videos from the motile particles.

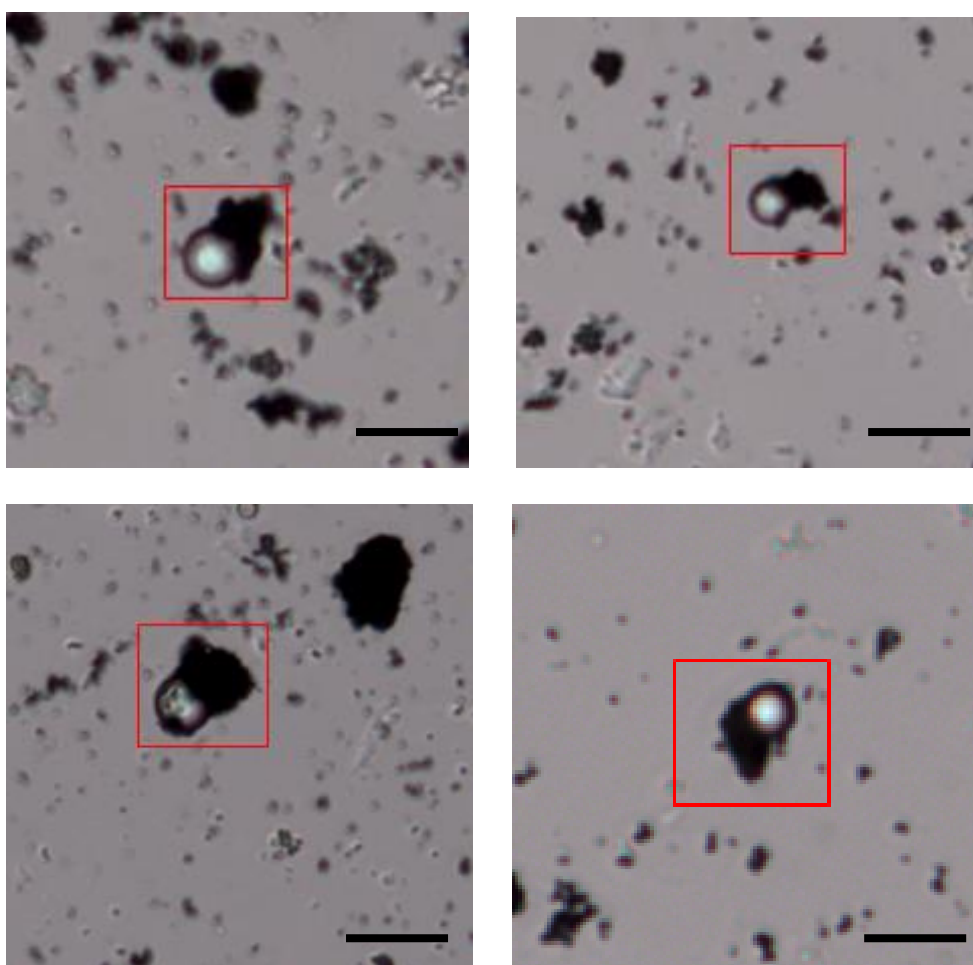


Figure 5.14 - Optical images of Spherglass particles partially coated with Cu with Pt crystals on their surface (scale bar: 10 μm)

Whilst these experiments were not as successful as hoped, they do provide a starting point for future research which is discussed further at the end of this thesis.

References

1. W. F. Paxton, K. C. Kistler, C. C. Olmeda, A. Sen, S. K. St. Angelo, Y. Cao, T. E. Mallouk, P. E. Lammert, V. H. Crespi *J. Am. Chem. Soc.* **2004**, 126, 13424-13431.
2. J. Howse, R. Jones, A. Ryan, T. Gough, R. Vafabakhsh and R. Golestanian, *Phys. Rev. Lett.*, **2007**, 99, 8–11.
3. J. H. Conway, N. J. A. Sloane, *Sphere Packings, Lattices, and Groups ed. 3* Springer: New York, 1999
4. T. C. Hales, *Discrete Comput. Geom.* **1997**, 17, 1.
5. T. C. Hales, *Discrete Comput. Geom.* **1997**, 18, 135.
6. V. N. Manoharan, M. T. Elsesser, D. J. Pine, *Science* **2003**, 301, 483.
7. Y. Cho, G. Yi, S. Kim, D. J. Pine, S. Yang, *Chem. Mater.* **2005**, 17, 5006-5013.
8. N. B. Schade, M. C. Holmes-Cerfon, E. R. Chen, D. Aronzon, J. W. Collins, J. A. Fan, F. Capasso, V. N. Manoharan, *Phys. Rev. Lett.* **2013**, 110, 148303.
9. Y. Yin, Y. Lu, Y. Xia, *J. Am. Chem. Soc.* **2001**, 123, 771.
10. C. M. Liddel, C. J. Summers, *Adv. Mater.* **2004**, 15, 1715.
11. R.N. Rhoda, R.F. Vines, US. patent 3,486,928 -**1969**.
12. S. Fujii, P. D. Iddon, A. J. Ryan, S. P. Armes, *Langmuir* **2006**, 22, 7512-7520.
13. S. Ebbens, M. Tu, J. R. Howse, R. Golestanian, *Phys Rev E* **2012** 85, 020401.
14. M. Albrecht, G. Hu, I. L. Guhr, T. C. Ulbrich, J. Boneberg, P. Leiderer, G. Schatz, *Nature Mater.* **2005**, 4, 203.
15. S. K. Smoukov, S. Gangwal, M. Marquez, O. D. Velev, *Soft Matter* **2009**, 5, 1285.
16. H. Takei, N. Shimizu, *Langmuir* **1997**, 13, 1865.

Chapter 6: Controlling the separation of polymeric microspheres by surface interactions in microfluidic devices

To date, various methods have been proposed for the separation of biological cells and soft polymeric particles. These methods often rely on controlling the transport of the particles based on specific characteristics such as density, size or surface ligands. Achieving a high degree of control over particle's transport is particularly advantageous in these systems as it enables continuous-flow separation. In this chapter, surface interactions between layer-by-layer polymeric microcapsules (with charged functional groups on their surface) rolling on adhesive, non-adhesive, and conductive substrates was studied. This study was conducted with the aim of physically realizing a computational model that demonstrated the capability of highly adhesive regions located on a non-adhesive substrate in deviating elastic particles from their path and the potential of this ability in developing a method for continuous separation of microparticles based on their mechanical stiffness and their adhesion to the surface.

6.1 Particle-substrate interactions

Common polymers are electrical insulators and any external electric charges on their surface do not flow freely. Presence of these electrostatic charges results in attractions and repulsions between polymeric microparticles and the substrate they are upon. These interactions can also generate small, large, plastic or elastic mechanical strains between the two surfaces. In addition, studying these simple

particle-substrate systems facilitates understanding of more complicated biological processes such as cell rolling and the part surface ligands play in cell adhesion on vascular surfaces.

Existing continuous-flow separation systems are founded on external control techniques where dielectrophoretic, magnetic, or other forces are utilised to separate a group of functionalised particles which respond to an applied field gradient [1,2]. These systems employ a labeling approach and are highly accurate for particle separation but are not desirable for separating cell samples as they are highly sensitive to trace amounts of contamination caused by the labeling process. Moreover, these multistage methods require several processing steps and involve special apparatus. As a result, many attempts have been made in order to develop an efficient and easy to implement label-free method for separating cells based on their own inherent physical or chemical characteristics [3].

One of the routinely employed label-based techniques for diagnosing various diseases, especially blood cancer is flow cytometry. This method involves passing cells through a microfluidic device equipped with detection apparatus which provides simultaneous sorting plus chemical and physical analysis of thousands of cells per seconds. One of the specialized types of flow cytometry that is capable of sorting a heterogeneous mixture of biological cells based on their fluorescent characteristics is fluorescence-activated cell sorting (FACS) [4].

In this method, a narrow microfluidic channel with a high flow-rate is employed for transporting the cell suspension and facilitating a primary separation based on the diameter of the cells. Subsequent to this stage, the cell suspension stream is broken into small droplets (typically with one cell in each droplet) by means of a vibrating mechanism. Next, the main stream running in the microfluidic channel breaks into

droplets but prior to that, the fluorescent character of interest of each cell is measured using light scattering techniques. After this stage, each droplet is charged based on its measured fluorescence intensity via an electrical charging ring positioned just after the droplet outlet orifice. Finally, a deflection system directs each droplet towards a container corresponding to its charge.

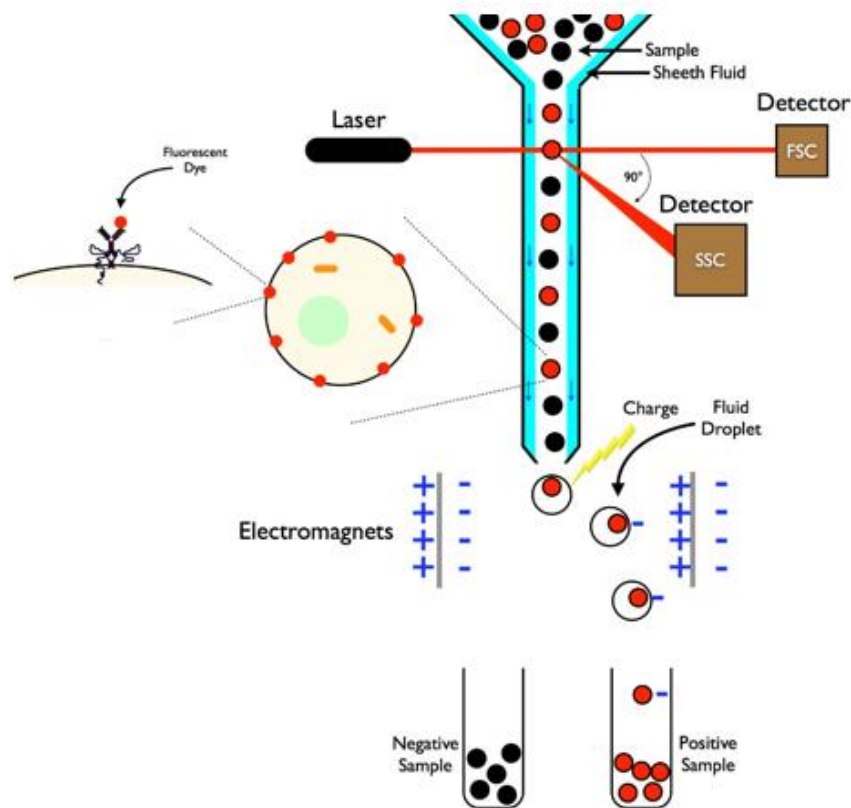


Figure 6.1 – Schematic diagram demonstrating the fluorescence-activated cell sorting (FACS) (taken from [4])

From label-free separation techniques developed in recent years, methods taking advantage from cell-rolling process have to date received the most attention [5-7]. Cell-rolling is the physiological process in which cells flowing in the blood stream form transient receptor-ligand bonds with the vascular endothelium [3]. A protein present on blood vessel inner walls (P-selectin) causes the cells that are sensitive to it to adhere to the walls of the blood vessel and to roll across them. The bonds are

formed on the leading edge of the cell while it is rolling under shear force applied by the blood flowing inside the vessel and are broken on its trailing edge. Discoveries show that neutrophils (white blood cells) slow down as they flow over a surface coated with P-selectin and roll on it where this does not happen when the surface is coated with other proteins [8].

The deliberate process of cell-rolling has the capacity to serve as the basis for fabricating a device that would interact only with certain types of cells with specific characteristics such as density, size, elasticity or surface ligands. Among physical characteristics that can be exploited to develop a cell-rolling based continuous separation system, mechanical stiffness has been proven to be a key parameter as it is a common property of both soft polymeric particles and biological cell samples that can reveal the quality of the fabricated product in the former case and the presence of disease in the latter case [9].

Additionally, as there are a number of diseases (e.g., malaria and various cancers) that alter the elasticity of biological cells [10], in addition to using this device as a continuous-flow cell separation system, by employing a therapeutic agent, this device will attain the potential to distinctively slow down and kill spreading infected cells circulating in a patient's blood.

6.2 Computational Simulations

In 2006 Alexeev, et al. [9] developed a 3D computational model to replicate the cell rolling process. In this simulation cells were modelled as fluid-filled elastic shells rolling upon substrates with various adhesive strengths. The aim of this study was to exhibit that a simple chemical variation can be exploited to design an effective separation method for cells and soft microparticles in accordance with their

compliance.

To simplify the dynamic interactions between the substrate and the surface of the microcapsule, micromechanics of these elastic solids was modeled using the lattice spring model (LSM). In the LSM, a compliant material is described by a network of harmonic “springs”, which interconnect nearest and next-nearest neighboring lattice nodes where the two surfaces interact through appropriate boundary conditions [11,12]. Next, the motion of the capsule was tracked along a flat substrate that contained two stripes with a 45° angle relative to the flow direction.

In the first set of simulations, the substrate was patterned mechanically, meaning that the capsule-substrate adhesion was constant along the substrate but the mechanical stiffness of the substrate was set 100 times higher than the stripes. This caused a significant deformation of the stripes as the capsules were rolling on them while the rest of the substrate was not distorted as a result of this motion (Figure 6.2-Top).

Figure 6.2-Bottom shows the path for three microcapsules with different rigidities on the mechanically patterned substrates. In these simulations, Δz was defined as the total lateral displacement of the microcapsule in a direction perpendicular to the fluid flow after passing both strips.

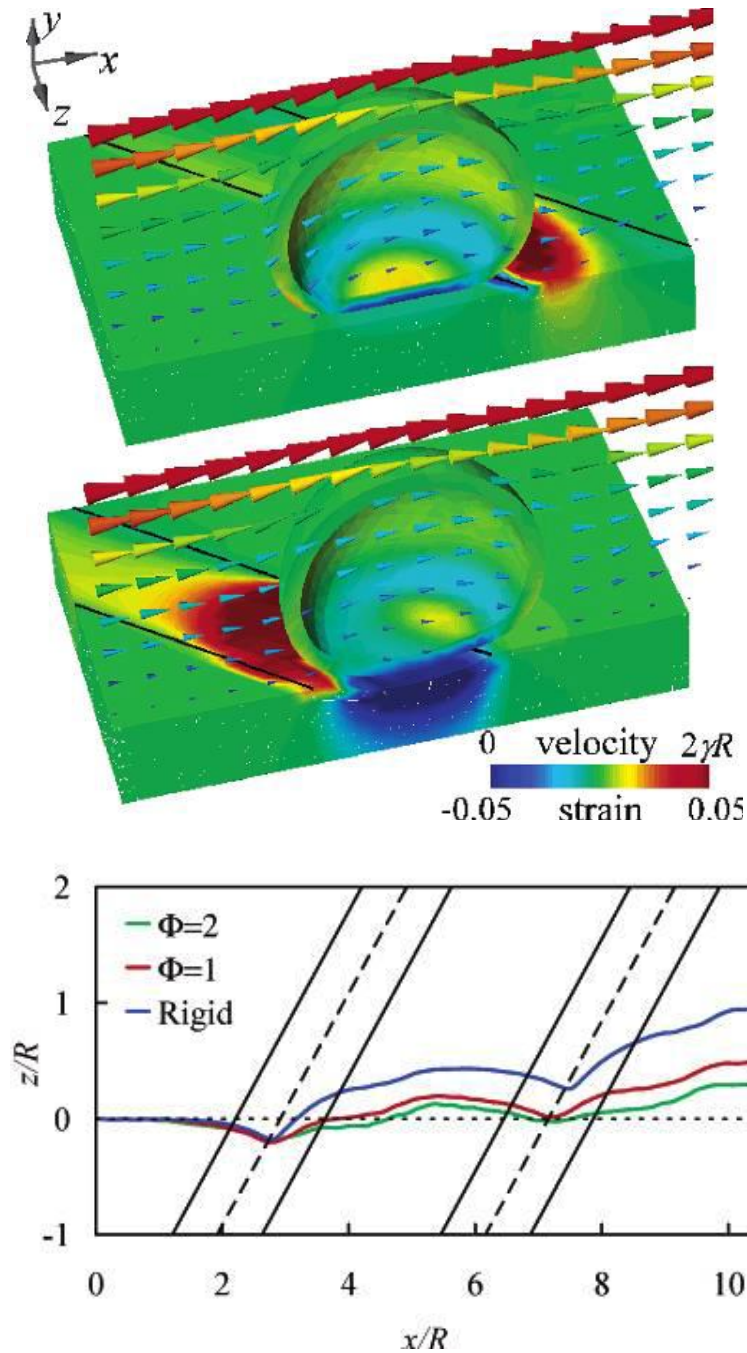


Figure 6.2 – (Top) Snapshots of an elastic capsule rolling along an adhesive, mechanically patterned substrate in shear flow. The system is shown in cross-section (made through the capsule's center of mass). The colors in the capsule and substrate reveal the strain (see color bar). The arrows indicate the flow direction, and the arrow's color indicates the magnitude of the velocity. The lines on the substrate mark the boundaries of a soft patch. The capsule approaches (upper panel) and moves past (lower panel) a soft patch. Note the strong deformation of the soft patch due to the adhesive interaction with the capsule and, consequently, the increase in contact area between the capsule and substrate. (Bottom) Trajectories of the center of mass motion for capsules with different compliancy on mechanically patterned substrates. The substrates encompass two consequent strips, which are oriented 45° relative to the flow direction. Starting from the same initial location, the capsules then move from left to right. As a result of the interaction with the patches, capsules of different stiffness gain different lateral displacements (Taken from Ref. [9]).

Subsequently, a simpler case consisting of a rigid chemically patterned substrate was simulated. In this case, the values for mechanical stiffness of the substrate and the stripes were set equal to each other (to eliminate the stripe deformation parameter) but the adhesive strength of the stripes was set 5 times bigger than the adhesive strength of the rest of the substrate while the substrate was still sufficiently strong to prevent detachment of the vesicles by a lift force (Figure 6.3-Top). Equally, Figure 6.3-Bottom shows the path of three microcapsules with different rigidities on the chemically patterned substrates. As it can be seen in Figures 6.2-Bottom and 6.3-Bottom, the outcome of the modeling confirmed that although starting from the same position, microcapsules with different mechanical stiffnesses end up in positions with remarkably different Δz from each other. However, in the first set-up where the substrates were patterned mechanically, the rigid capsules attained the largest lateral displacement in contrast to the chemically patterned substrate where the largest lateral displacement belonged to the softest capsules.

This study successfully demonstrated that a microcapsule's response to an asymmetrically patterned substrate is dictated by its mechanical stiffness and the level of adhesion between its shell and the substrate. In other words, based on their compliance with the substrate, particles that initially start at the same position, will ultimately roll to different places and thus will effectively be sorted consecutively without the need of external fields or stimuli.

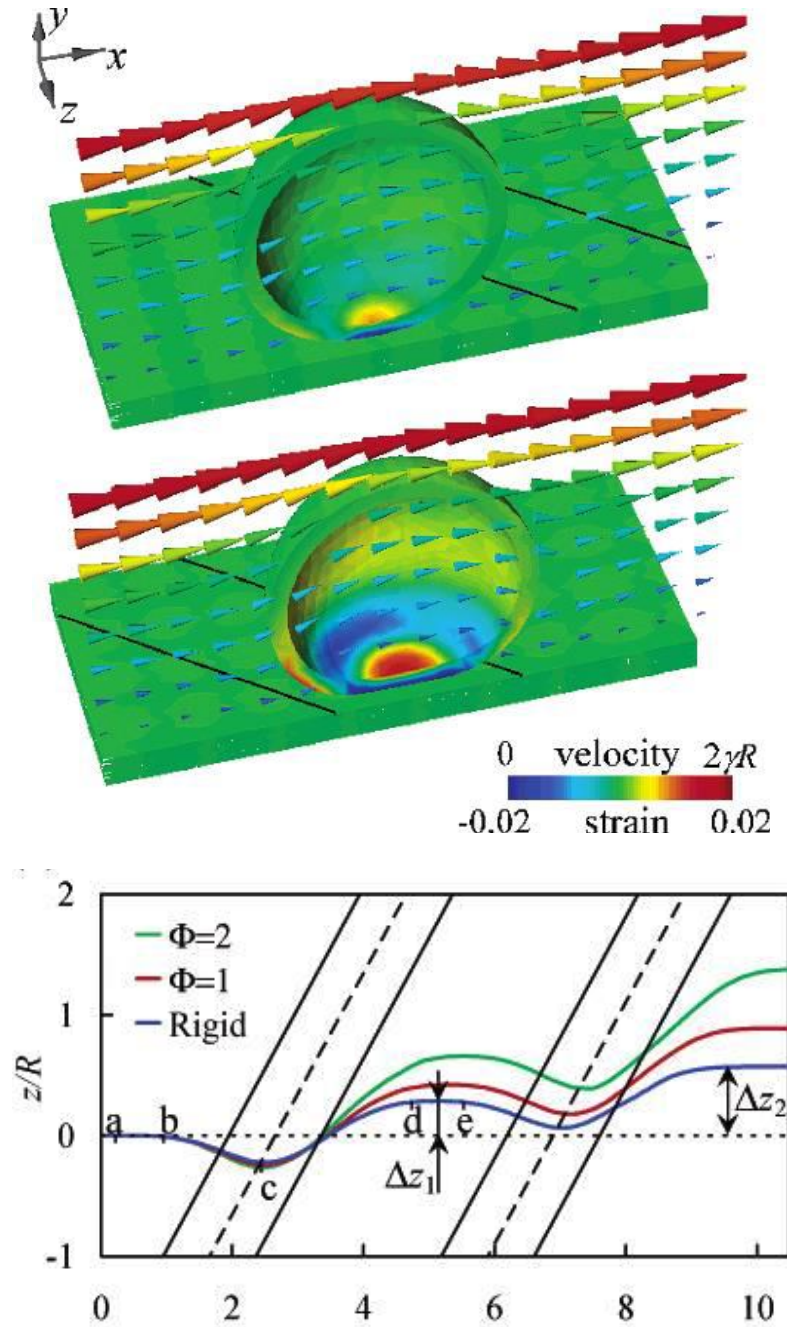


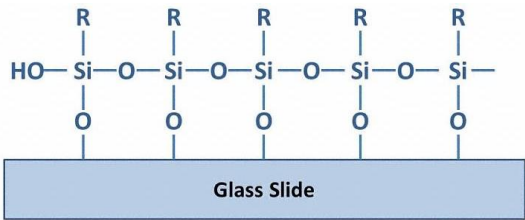
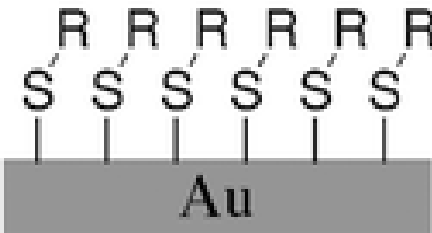
Figure 6.3 – (Top) Snapshots of an elastic capsule rolling along an adhesive, chemically patterned substrate in shear flow. The system is shown in cross-section (made through the capsule's centre of mass). The colours in the capsule and substrate reveal the strain (see colour bar). The arrows indicate the flow direction, and the arrow's colour indicates the magnitude of the velocity. The lines on the substrate mark the boundaries of a soft patch. The capsule approaches (upper panel) and moves past (lower panel) a soft patch. Note the strong deformation of the soft patch due to the adhesive interaction with the capsule and, consequently, the increase in contact area between the capsule and substrate. (Bottom) Trajectories of the centre of mass motion for capsules with different compliancy on chemically patterned substrates. The substrates encompass two consequent strips, which are oriented 45° relative to the flow direction. Starting from the same initial location, the capsules then move from left to right. As a result of the interaction with the patches, capsules of different stiffness gain different lateral displacements (Taken from Ref. [9]).

6.3 Self-assembled monolayers (SAMs): structure, preparation and patterning

Recent advances in soft lithography [13] make it possible to readily fabricate such mechanically or chemically patterned surfaces as this approach provides a relatively cost-effective method for carrying out such envisaged assays. For instance, positively or negatively charged substrates can be fabricated by taking advantage of the spontaneous self-organisation capability of atoms and molecules on compliant surfaces. These well-ordered supramolecular assemblies that normally possess both short and long-range order are named self-assembled monolayers (SAMs). Among various methods proposed for fabricating these structures and enhancing the molecule-substrate bonds, the adsorption of amphiphilic molecules (such as surfactants) on transition metal surfaces (e.g. gold and platinum) has been of great importance in the past decade [14-16].

SAMs can also be prepared using alkylsiloxane molecules on silicon and fatty acids on oxidic materials (e.g. Fe/MgO) but research in this area has been recently focused on the self-assembly of alkanethiols and related molecules on gold substrates. The reason for this growing interest is that although highly-organised SAMs can be prepared from a range of organosulphur compounds (i.e. disulphides, sulphides and alkanethiols [14]), thiol molecules form stronger bonds with gold compared to other molecules and therefore they kinetically outcompete sulphides and disulphates for available surface sites when more than one molecule is available in the solution. Additionally, compared to most transitional metals, surface oxides do not form on gold surfaces and likewise, materials adsorbed on a gold surface do not bond with it strongly. As a result, preparing SAMs can be carried out under ambient conditions.

Table 6.1 - combinations of substrates and headgroups employed in forming SAMs
(Taken from Ref. [24])

Ligand	Substrate	Ref.	Structure
ROH RHC-CH ₂	Si, Quartz, Glass	17	
RSH	Ag, Au, Cu Pd, Pt	18 19 20	

As SAMs fabricated from alkanethiol molecules interact differently with adjacent materials, these SAMs have a great potential in being utilised in various applications. For example, alkanethiol SAMs with different functional head groups can be used as model substrates in biomembrane mimetics where their interactions with biological cells and biomolecules can be studied at surfaces. These supramolecular assemblies can also be employed in selective binding of enzymes to surfaces, molecular crystal growth, corrosion protection and accurate surface patterning on the micro-scale.

6.4 Preparation of alkanethiol SAMs

The principal behind the formation of strongly hydrophobic alkanethiol SAMs is relatively simple: Firstly, the (S-H) head group which has a strong preferential adsorption to the gold substrate is attached to an alkane chain with a typical length of

10-20 (CH₂) units. Next, due to this strong preferential adsorption, the thiol molecules are densely adsorbed onto the gold from the (S-H) head group leaving the tail groups pointing outwards from the surface.

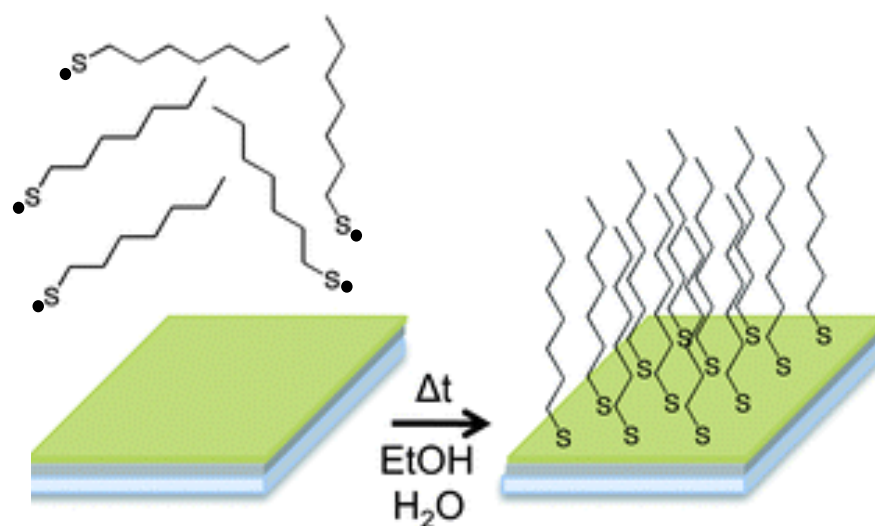


Figure 6.4 – Schematic diagram demonstrating the attachment of alkanethiol molecules on Au to form SAMs

The final chemical surface functionality of the substrate can be altered by using different functional groups and ions as the tail group or alternatively, the tails groups can be chemically functionalised after the formation of SAM on the substrate through a wide range of reactions.

A schematic diagram showing different stages of SAM formation is given in Figure 6.5. Initially, the gold substrate is fabricated by evaporating a thin film of Au onto glass or silicon with the aim of obtaining the (111) crystal face which is required for this procedure [21]. To improve the adhesion of gold onto glass and silicon substrates, a thin layer of chromium is first evaporated on the surface prior to evaporating a thicker layer of gold. Subsequently, the gold coated samples are immersed in the thiol solution which is prepared at low concentrations (1-3 mM) commonly with degassed ethanol. To obtain a defect-free, well-ordered SAM, it is

recommended to extend the adsorption time to 15 h even though the initial monolayer only requires a few seconds to form. For high purity SAMs used, the water content of ethanol is minimised via additional distillation stages to limit the incorporation of water molecules in the SAM structure and reduce outgassing.

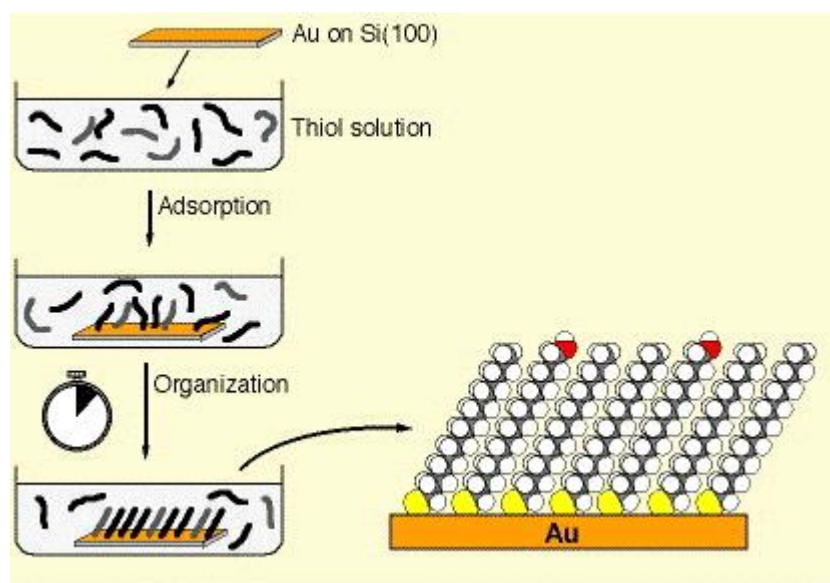


Figure 6.5 – Schematic diagram demonstrating the preparation process of SAMs.

As stated earlier, depending on the application, the tail group which represents the chemical functionality of the SAM can be modified either at this stage, after the formation of SAM or when the thiol molecules are initially synthesised. For example, CH_3 -terminated SAMs are commercially available and thiols with this non-polar tail group are mainly used for fabricating hydrophobic surfaces. On the other hand, SAMs with polar tail groups such as $-\text{OH}$, $-\text{NH}_3$ and $-\text{COOH}$ can be employed in fabricating hydrophilic substrates [22].

6.5 Patterning alkanethiol SAMs

Scientists have since examined different methods for preparing multiple component substrates with predetermined distributions of their desired SAMs. The main reason for investigating this goal was its potential in synthesising functional nanostructures with a “bottom up” approach. Additionally, fabricating patterned surfaces with chemically functionalised SAMs that possess different levels of affinity to nanoparticles, proteins and biological cells, facilitates the fabrication of higher-order structures and architectures [23].

SAMs can be patterned via various techniques such as selective *placement* of adsorbates, selective *reaction* of adsorbates and selective *removal and replacement* of one or more specific adsorbates. Removing SAMs from particular locations on a substrate can be achieved by breaking the alkanethiol-substrate bonds with energetic beams or by physical etching with atomic force microscope probes. Once SAMs are removed from the desired positions, the emptied regions can be “backfilled” with new alkanethiol molecules or left bare.

Figure 6.6 shows the techniques commonly used for patterning SAMs. To date four strategies have been widely used for this purpose:

- A. The first strategy is local deposition of the SAM onto the substrate via soft lithography (micro-contact printing) and dip-pen nanolithography techniques. Soft lithography includes transferring the solution of SAM molecules on the appropriate substrate using elastomeric pre-patterned stamps. This way, SAM molecules are only transferred on the areas of the substrate that contact the stamp and the time required for monolayers to be generated on these areas is depended on the type of SAM molecules, the amount of pressure applied and the concentration of the SAM solution [24].

B. Another method is employing the tip of an atomic force microscopy (AFM) probe for transferring the SAM molecules by initially dipping the tip into the SAM solution and then bringing it into contact with the substrate. This method is used for generating patterned SAMs with a precision of tens of nanometers [25].

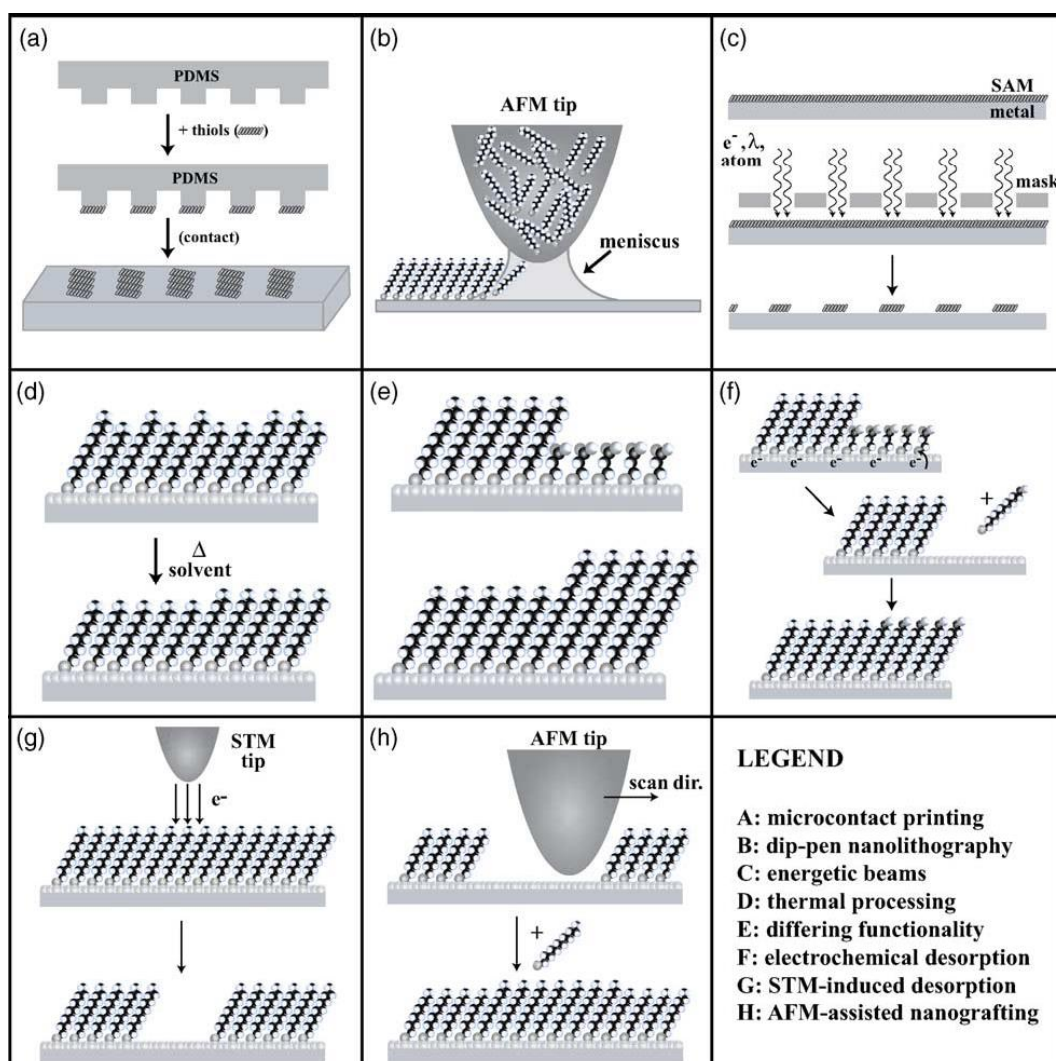


Figure 6.6 – Schematics of several techniques employed to pattern SAMs (Taken from Ref. [23])

C. The third strategy involves coating the entire substrate with SAM molecules and then removing the undesired areas via UV oxidation and shaving techniques. In UV

oxidation, the substrate fully covered with a self-assembled monolayer is exposed to UV light ($\lambda \sim 250$ nm) for at least 20 minutes. Following the UV exposure, the S-H bond in the thiol chain is broken, the SAM molecules are oxidized and only the SAMs in the areas masked with the desired pattern will remain on the substrate after washing it with a polar solvent [25]. The other method for removing the SAMs with a higher precision is dragging the tip of an AFM probe on the substrate and mechanically removing the molecules in a process called shaving [24].

- D. The fourth strategy for patterning SAMs, focuses on modification of the tail groups. This is done either by projecting UV [24] or electron beams [25] to the substrate or by creating an electrochemical reaction via the tip of a conductive AFM probe to modify the tail groups of SAM molecules.

Among these techniques, the straight-forward methods such as patterning substrates via soft lithography and by utilising energetic beams (for instance UV light) were sufficiently accurate and cost-effective to be employed in realising the computational simulation described earlier. Therefore these techniques were studied further with the aim of selecting the most suitable method for preparing the substrates with different surface chemistries for our flow experiments.

6.5.1 Patterning self-assembled monolayers using soft lithography

After the introduction of “soft-lithography” by Withsides, et al. [26] various studies have demonstrated the potential applications of this family of techniques in fabricating micro- and nanostructures [27-30]. In these techniques, flexible materials such as elastic polymers are used as a means for transferring physical and chemical features onto substrates that might get damaged by UV light or other energetic

beams. Utilisation of “microcontact printing” (which is one of the most popular soft lithography techniques) in SAM patterning has grown significantly in the past few years due to its cost-effectiveness and the simplicity of fabricating the printing stamps.

In this technique, a polymeric stamp typically fabricated from polydimethylsiloxane (PDMS) is dipped in an alkanethiol solution and subsequent to the evaporation of solvent, it is pressed onto a gold substrate or another compatible surface where the non-patterned areas can be backfilled with another alkanethiol.

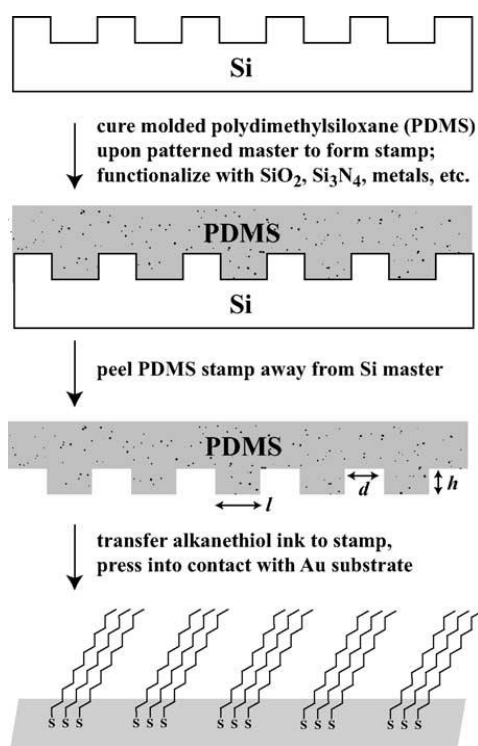


Figure 6.7 – Schematic of the microcontact printing process, adapted from [27]. The relief patterns of the silicon master are transferred as negatives to the PDMS stamp; the dimensions of post width ‘ l ’, post separation ‘ d ’, and post height ‘ h ’ are critical for proper transfer of molecules and pattern fidelity across multiple transfers.

6.5.2 Patterning SAMs with energetic beams

Although the micro-contact printing method can be applied in printing various features to different substrates, the resolution of the fabricated patterns is limited by the dimensions and properties of the stamp, plus, the reproducibility of this technique is dependent on the stamp's degradation and the contact pressure applied to the substrate [31].

One of the most cited papers on SAM patterning written by Brewer et al. [32] proposes oxidising alkanethiol monolayers on gold and silver by exposing them to UV light. This rapid photooxidation method recommends exposing SAMs to light of wavelength 254 nm for 5 minutes in order to achieve an efficient and extensive oxidation. To pattern a substrate via this technique, Brewer suggests using an electron microscope grid to mask the desired areas prior to UV exposure and immersing the SAM in a 10 mmol solution of “backfilling” thiol in ethanol.

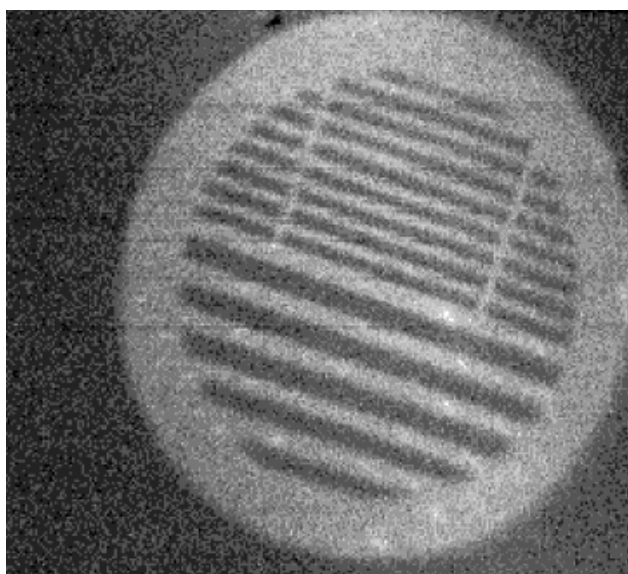


Figure 6.8 - Secondary ion mass spectrometry (SIMS) image of a photopatterned SAM, formed by mapping the O⁻ intensity. Acid terminated regions contain oxygen and thus exhibit bright contrast, while methyl terminated regions exhibit dark contrast. (Adapted from Ref. [32])

This method is perfect for displacing octanethiol with oxidised SAMs with COOH tail group such as mercaptoundecanoic acid (MUA) and mercaptopropanoic acid (MPA). In contrast, non-polar monolayers such as dodecanethiol (DDT) oxidise much slower and require longer exposure times which points to a different photochemistry for this type of alkanethiols.

6.6 Polymeric microcapsules

As many parameters are involved while conducting experiments on actual cells and as biological systems are highly sensitive to trace amounts of contamination which may result confusion in the obtained data, we decided to develop a cell-free system to investigate how surfaces with different adhesion strengths can segregate compliant particles rolling on them. This non-biological approach reduces the number of important parameters in the particle rolling process, plus, without commitment to a particular ligand-receptor pair, it also demonstrates the physics important in particle adhesion to a surface, and is very much a control system.

In recent years developing methods for fabricating soft microparticles has become a subject of investigation for scientists. Studies show that use of polymers instead of organic molecules to construct the membrane of these particles makes these systems more stable and robust. As a result, a wide variety of polymer-based microcapsules such as layer-by-layer (LbL) capsules [33-36], hollow microspheres [37-39], and hollow microcapsules [40,41] have been developed to be utilised in biomimetics and drug delivery research. Amongst these polymeric microparticles, LbL microcapsules were the most suitable replacements to biological cells for our microfluidic experiments as they were less sensitive to contamination and they could be fabricated

with a range of tailored chemical and mechanical properties to make them capable of replicating cells' behaviour. This is mainly due to them being hollow and filled with liquid.

The LbL capsules are fabricated by repeatedly depositing positively and negatively charged polyelectrolytes such as poly(allylamine hydrochloride) (PAH) and poly(styrene sulfonate) (PSS) onto spherical template particles. These template particles can be removed using appropriate solvents after the formation of the desired numbers of multilayers [42], Figure 6.9 shows the process for assembly of these polymeric layers on templates in addition to microcapsule formation, template removal and the chemical structure of two polyelectrolytes (PAH and PSS).

At first, cross-linked melamine formaldehyde (MF) or polystyrene (PS) particles were used as templates in this process but removing these materials after the formation of multilayers proved to be difficult without damaging the shell, furthermore, rapid dissolution of these templates could generate an osmotic pressure built up in the microcapsule which could rupture or even destroy the shell. As a result, some researchers are now using inorganic carbonates such as CaCO_3 , MnCO_3 and CdCO_3 more often as the metal ions in these materials easily pass the polymeric multilayer upon dissolution in ethylenediamine tetraacetate (EDTA) without generating a pressure build up [43].

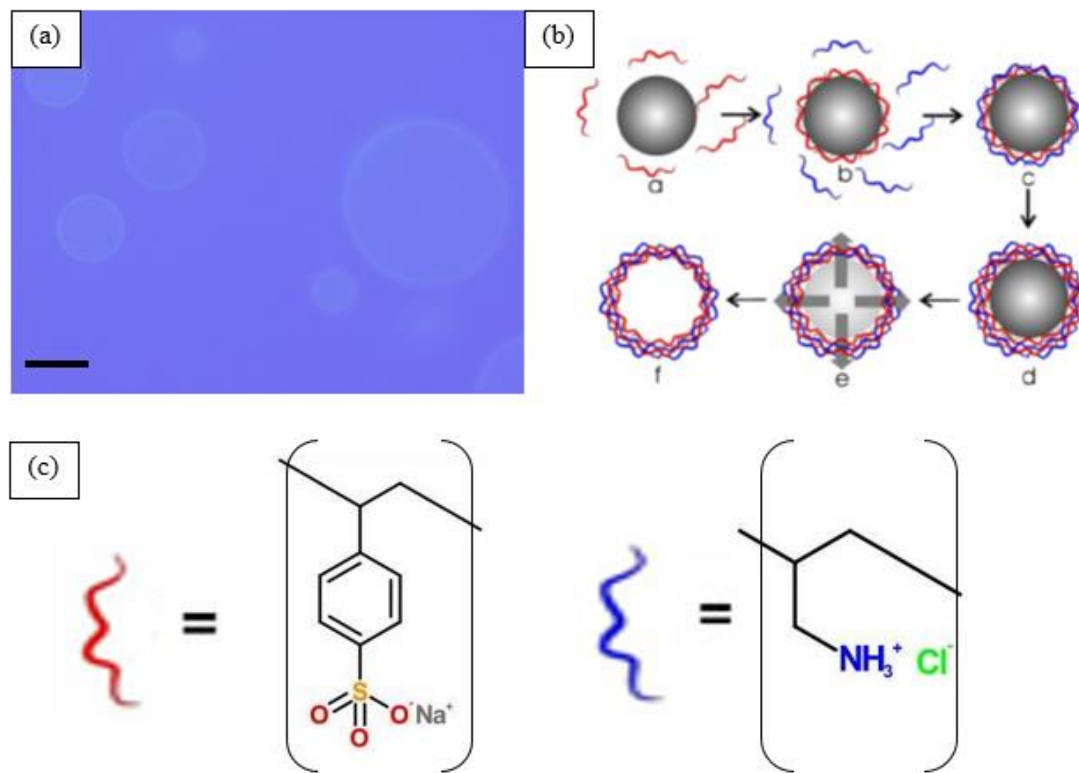


Fig. 6.9 - (a) An optical image of microcapsules fabricated via the LbL technique. (Scale-bar=10 μm) (b) Schematic illustration showing the preparation of hollow LbL microcapsules (c) Chemical structure of poly(styrene sulfonate) (PSS) (left) and poly(allylamine hydrochloride) (PAH) (right), often used polyelectrolytes to build LbL films

6.7 Experimental

6.7.1 Microfluidic flow cell design and substrate patterning using SAMs

The first preparatory stage in conducting the flow experiments was fabricating a flow channel with a laminar flow to replicate a blood vessel. From different flow channel designs and suggested pumping systems, a flow cell was built by sandwiching an adhesive sheet (Agar Scientific), which a flow channel was cut out of it, between a glass slide and a cover slip. The surface chemistry of the fabricated channel was then modified using alkanethiol SAMs before putting the microfluidic cell together. The solution containing microcapsules was pumped into the channel via a syringe pump and it was collected in a reservoir designed at the bottom of the channel.

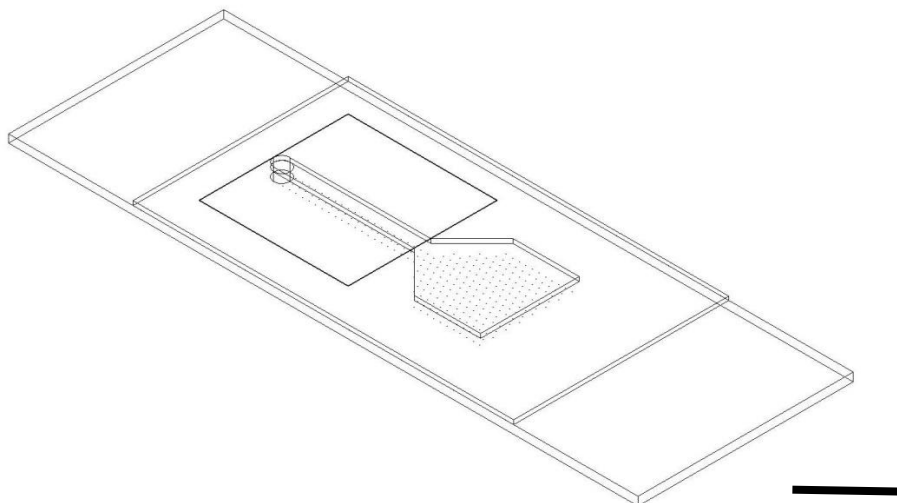


Figure 6.10 - Diagram of parallel-plate microfluidic cell used in experiments. The coated slide sits in the bottom of platform and the flow channel is cut out of the adhesive sheet. The adhesive sheet is pressed between the coated slide and a cover slip to form a sealed flow channel with an inlet and a reservoir for fluid and particles. (Scale-bar = 1 cm)

In our experiments, SAMs were prepared by thermally evaporating gold onto chromium coated glass slides then immersing the slides in 1 mmol solutions of the appropriate thiol, 1-octanethiol or mercaptoundecanoic acid (MUA), for 24h. SAMs were patterned by placing parallel bar TEM grids (100, 200 and 300 Mesh) between the SAM slide and a quartz slide and oxidizing the SAM surface for 24 h using a UV lamp with a wavelength of 254 nm [32]. The oxidised SAM regions were then back-filled with an alkanethiol with a different adhesive strength to the rolling LbL microcapsules.

6.7.2 Dex-HEMA polymeric Microcapsules

The LbL microcapsules for these experiments were fabricated by B. G. De Geest et al. [33]. To produce these particles which act as fluid-filled elastic shells, dextran-hydroxyethyl methacrylate (dex-HEMA) (400 ml; 15% (w/w)) was slowly introduced with a pipette into PEG solution (4.577 ml; 30% (w/w)) in a glass vial under slow continuous stirring using Teflon-coated magnetic stirring bar.

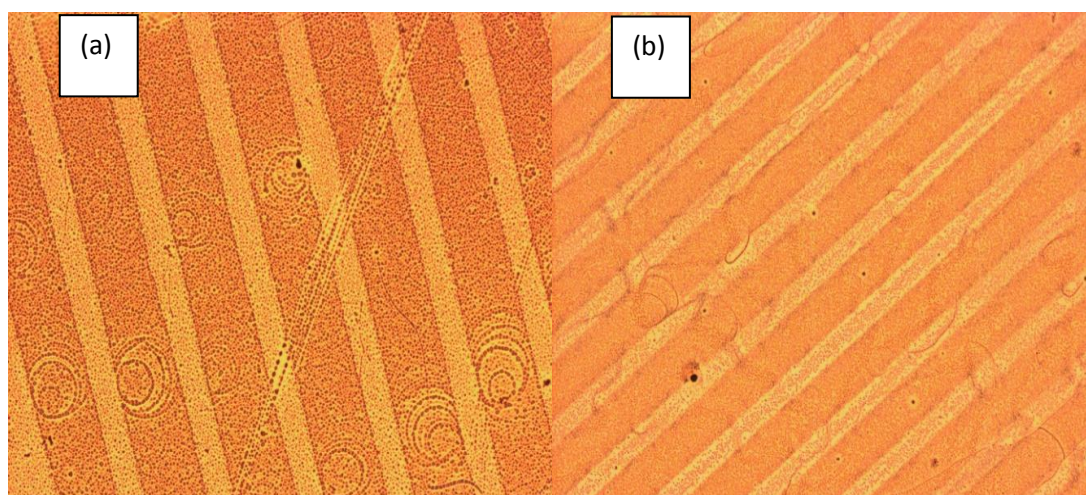


Figure 6.11 – Optical images of UV patterned 1-Octanethiol SAMs (a) 100 parallel TEM bar grids (b) 200 parallel bar grids after humidification with water vapour, showing the hydrophobic and hydrophilic regions

When a homogeneous dispersion was obtained, 35 ml dimethyl aminoethyl methacrylate (DMAEMA) was added and the mixture slowly stirred for 1 minute. Subsequently, radical polymerization was initiated by addition of N,N,N',N'-tetramethylethylenediamine (TEMED) (100 ml; pH neutralized by 4 M NaCl) and potassium persulfate (KPS) (180 ml; 50 mg ml⁻¹). The mixture was further stirred for 15 min and then allowed to stand for 30 minutes. afterwards the microgel dispersion were twice centrifuged/washed with 20 ml water and stored in 5 ml water at 20 °C until use.

Dex-HEMA microgels were alternately dispersed in 1 ml poly(styrene sulfonate) (PSS) (2 mg ml⁻¹; 0.5 M NaCl) and a 1:1 mixture of diazosresin (DAR) and rhodamine isothiocyanate labelled poly-L-arginine (P_LARG^{RITC}) (both at 1 mg ml⁻¹; 0.5 M NaCl) solutions using the layer by layer (LbL) technique. After deposition of 3 PSS/(DAR & P_LARG^{RITC}) bilayers, cross-linking was allowed to occur spontaneously under ambient light conditions. Hollow capsules with an average size

of 10 μm in diameter were acquired by dissolving the dex-HEMA core in 1M sodium hydroxide solution for 10 min followed by extensive washing with water [33].

6.8 Particle rolling experiments and results

Initial experiments were based on rolling the microcapsules on surfaces coated with gold, 11-mercaptopundecanoic acid [MUA] SAM (with a charged polar carboxyl tail group) and 1-octanethiol SAM (with a neutral non-polar methyl tail group) through an imposed flow inside the fabricated microfluidic cell. Videos were captured from microcapsules with a mean diameter around 10 μm and the motion analysis of the selected capsules was undertaken through particle image velocimetry and computer based image analysis programs written in LabVIEW. The results of this stage represent a significant difference in average rolling velocity for vesicles rolling on pure gold, MUA and 1-octanethiol surfaces.

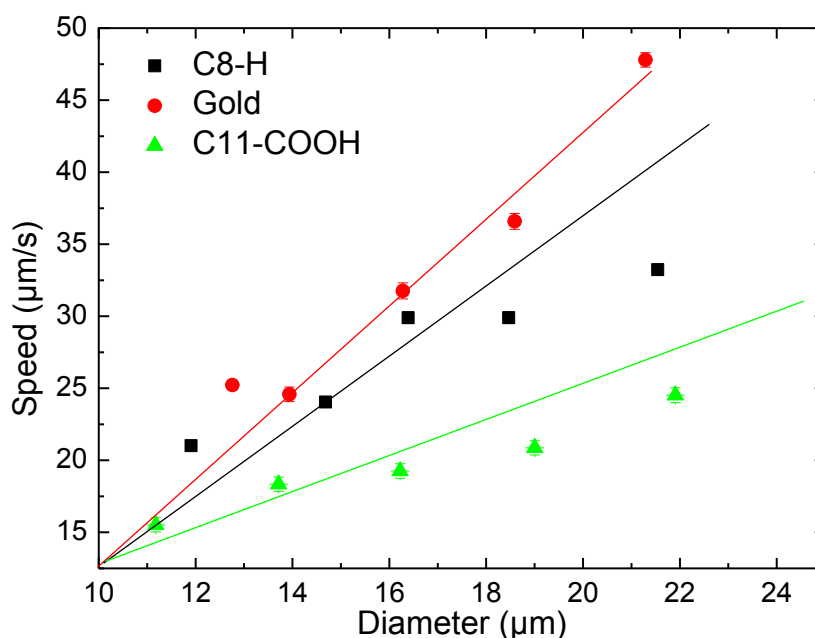


Figure 6.12 – Average speed ($\mu\text{m} \cdot \text{s}^{-1}$) vs. diameter (μm) for microcapsules rolling on surfaces with different chemistries. The lines are a guide to the eye.

This conclusion was reached by particle tracking and average velocity calculation of at least 15 vesicles on each surface (with diameters between 12 to 22 μm) rolling on the substrates in constant flow rate of 0.07 ml. h^{-1} inside identical 4 mm in 30 mm microfluidic channels (See Figure 6.12). The analysis also shows that the average velocity of microcapsules rolling on the pure gold surface is higher than 1-octanethiol and MUA surfaces respectively for a range of microcapsules with equal diameters. For microcapsules rolling on a pure gold surface, the average velocity was around $23.4 \mu\text{m. s}^{-1}$ where for 1-Octanethiol and MUA SAM surfaces this value was around $19.5 \mu\text{m. s}^{-1}$ and $13.7 \mu\text{m. s}^{-1}$ respectively.

To verify the results obtained in the first stage of the experiments, in another set of experiments, using a 15 μm microcapsule was rolled over each substrate and its instantaneous velocity was calculated in a time period of 10 seconds (Fig. 6.13). The results of this experiment confirmed the results of the initial experiments by showing that for identical microcapsules, the instantaneous rolling velocity on pure gold surface is higher than 1- octanethiol and MUA respectively in constant flow rates.

In the final stage of the experiments, a solution containing a constant concentration of microcapsules was passed over gold, 1-octanethiol and MUA surfaces for longer time periods (4, 8 and 12 min) at constant flow rate and at the end of each period the number of microcapsules captured on each surface (which were completely immobile even under the flow) was counted (Fig. 6.14).

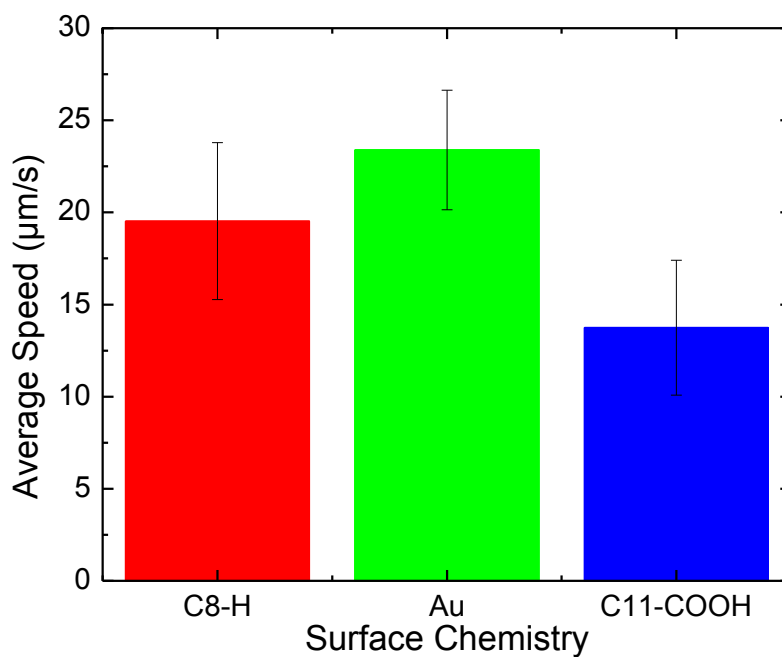


Figure 6.13 - Average speed comparison for three microcapsules with equal diameters (~15 µm) rolling on surfaces with different chemistries

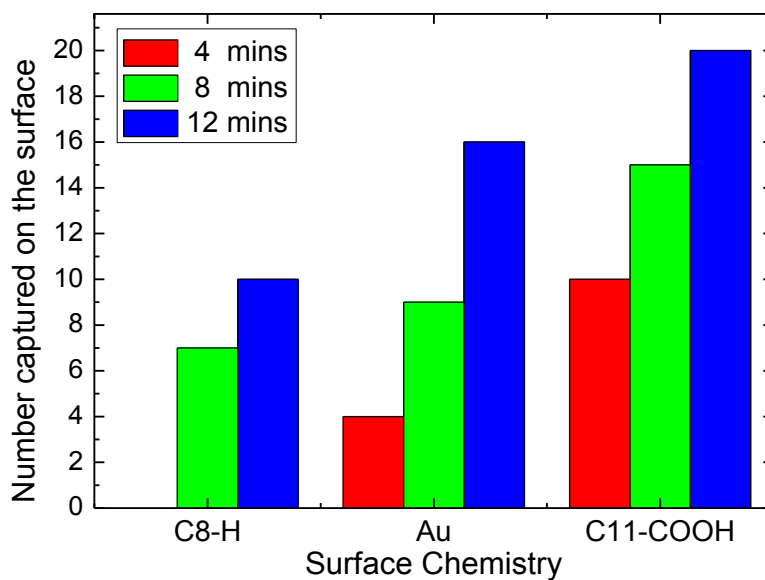


Figure 6.14 – Capture rate of microcapsules rolling on surfaces with different chemistries in equal time periods.

The results of this experiment showed that the number of microcapsules captured on the MUA surface is higher than gold and 1-octanethiol surfaces respectively both in the total number of captured microcapsules and in each individual time period. The total number of microcapsules captured on the MUA surface after 12 minutes was 46 where this value was 29 for the gold surface and 17 for the 1-octanethiol surface.

This higher capture rate for the MUA surface is possibly due to higher surface attraction between the polar COOH terminating group in the thiol and the microcapsule's shell which also has positive and negative charged groups in its structure. On the other hand, for pure gold, sticking occurs as a result of the attraction between strong electrostatic surface charges and the polar groups present on microcapsules' shells.

With the same approach it can be concluded that for 1-octanethiol, the number of microcapsules captured on the surface is significantly lower compared to other surfaces as there are no polar terminating groups or strong electrostatic charges present on the surface.

The next stage was conducting the microcapsule rolling experiments on substrates coated with the hydrophobic alkanethiol (1-octanethiol) SAM, patterned with diagonal stripes of the hydrophilic alkanethiol (MUA) SAM and vice versa (preparation of patterned SAMs is discussed in 6.7.1). While the data obtained in 6.8 demonstrated a clear difference between the velocity of particles rolling on substrates coated with hydrophobic and hydrophilic alkanethiols, in accordance with the computational modelling conducted by Alexeev, et al. [9], a divergence from their primary course was expected for particles rolling on the patterned substrates. Unfortunately no significant trajectory deviation was observed in particles rolling on the patterned substrates and additional trials to increase the width of the diagonal

stripes to enhance the particle-substrate interaction time were also unsuccessful. This was probably due to the contamination originated from the SAM patterning stage where a TEM grid (utilised as the UV mask) was sandwiched between the SAM slide and a quartz slide prior to the UV oxidation stage. Further attempts for cleaning the TEM grid by immersing it in ethanol and plasma cleaning the quartz slide did not lead to a considerable difference in the results.

References

1. D. Recktenwald, A. Radbruch *Cell Separation Methods and Applications* Dekker: New York, 1998.
2. M. Radisic, R. K. Iyer, S. K. Murthy, *Int. J. Nanomed.* **2006**, 1 (1), 3–14.
3. R. Karnik, S. Hong, H. Zhang, Y. Mei, D. G. Anderson, J. M. Karp, R. Langer *Nano Lett.* **2008**, 8 (4), 1153-1158.
4. M. R. Melamed *Flow Cytometry and Sorting*. New York, NY: Wiley-Liss; 1990.
5. L. R. Huang, E. C. Cox, R. H. Austin, J. C. Sturm, *Science* **2004**, 304 (5673), 987–990.
6. J. P. Fu, R. B. Schoch, A. L. Stevens, S. R. Tannenbaum, J. Y. Han *Nat. Nanotechnol.* **2007**, 2 (2), 121–128.
7. N. Pamme *Lab Chip* **2007**, 7 (12), 1644–1659.
8. D. N. Granger, P. J. Kubes *Leukocyte Biol.* **1994**, 55 (5), 662.
9. A. Alexeev, R. Verberg, A. C. Balazs *Langmuir* **2007**, 23, 983.
10. S. Suresh, *J. Mater. Res.* **2006**, 21, 1871.
11. A. Alexeev, R. Verberg, A. C. Balazs *Phys. Rev. Lett.* **2006**, 96, 148103.
12. A. Alexeev, R. Verberg, A. C. Balazs, *Macromolecules* **2005**, 38, 10244.
13. C. S. Chen, X. Y. Jiang, G. M. Whitesides, *MRS Bull.* **2005**, 30, 194.
14. R. G. Nuzzo, D. L. Allara, *J. Am. Chem. Soc.* **1983**, 105 4481.
15. R. G. Nuzzo, B. R. Zegarski, L. H. Dubois, *J. Am. Chem. Soc.* **1987**, 109, 733.
16. J. Sagiv, *J. Am. Chem. Soc.* **1980**, 102 92.
17. A. J. Pertsin, M. Grunze, H. J. Kreuzer, R. L. C. Wang, *Phys. Chem. Chem. Phys.* **2000**, 1729.

18. A. A. Dhirani, R. W. Zehner, R. P. Hsung, P. Guyot-Sionnest, R. L. Sita, *J. Am. Chem. Soc.* **1996**, 118, 3319.
19. D. N. Batchelder, S. D. Evans, T. L. Freeman, L. Haussling, H. Ringsdorf, H. Wolf, *J. Am. Chem. Soc.* **1994**, 116, 1050.
20. V. Chechik, R. M. Crooks, C. J. M. Stirling, *Adv. Mater.* 2000, 12, 1161.
21. N. W. Ashcroft, N. D. Mermin, *Solid State Physics* Harcourt: New York, 1976.
22. A. Ulman, *An Introduction to Ultrathin Organic Films: From Langmuir-Blodgett to Self-Assembly* Academic Press: New York, 1991.
23. S. Sun, K. S. L. Chong, G. J. Leggett, *Nanotechnology* **2005**, 16, 1798-1808.
24. J. Love et al. *Chem. Rev.* **2005**, 105, 4, 1103.
25. J. Seong et al. *Nanoscale Res Let.* **2007**, 2, 519.
26. A. Kumar, G. M. Whitesides, *Appl. Phys. Lett.* **1993**, 63, 2002.
27. Y. N. Xia, G. M. Whitesides, *Angew. Chem., Int. Ed.* **1998**, 37, 551.
28. A. Kumar, H. A. Biebuyck, G. M. Whitesides, *Langmuir* **1994**, 10, 1498.
29. B. Michel, A. Bernard, A. Bietsch, E. Delamarche, M. Geissler, D. Juncker, H. Kind, *IBM J. Res. Devel.* **2001**, 45, 697.
30. X. M. Zhao, Y. N. Xia, G. M. Whitesides, *J. Mater. Chem.* **1997**, 7, 1069.
31. T. W. Odom, V. R. Thalladi, J. C. Love, G. M. Whitesides, *J. Am. Chem. Soc.* , **2002**, 12112.
32. N. J. Brewer, R. E. Rawsterne, S. Kothari, G. J. A. Leggett *J. Am. Chem. Soc.* **2001**, 123, 4089.
33. B. G. De Geest, N. N. Sanders, G. B. Sukhorukov, J. Demeester, S. C. De Smedt, *Chem. Soc. Rev.* **2007**, 36, 636.
34. J. B. Li, H. Mohwald, Z. H. An, G. Lu, *Soft Matter.* **2005**, 1, 259.
35. G. B. Sukhorukov, H. Mohwald, *Trends Biotechnol.* **2007**, 25, 93.
36. Y. Wang, A. S. Angelatos, F. Caruso, *Chem. Mater.* **2008**, 20, 848.
37. T. Basinska, *Macromol. Biosci.* **2005**, 5, 1145.
38. S. Freiberg, X. Zhu, *Int. J. Pharm.* **2004**, 282, 1.
39. W. F. Daamen, P. J. Geutjes, H. T. B. van Moerkerk, S. T. M. Nillesen, R. G. Wismans, T. Hafmans, L. van den Heuvel, A. M. A. Pistorius, J. H. Veerkamp, J. C. M. van Hest, T. H. van Kuppevelt, *Adv. Mater.* **2007**, 19, 673.
40. S. D. Bergman, F. Wudl, *J. Mater. Chem.* **2008**, 18, 41.
41. H. N. Yow, A. F. Routh, *Soft Matter* **2006**, 2, 940.
42. G. B. Sukhorukov, E. Donath, S. Davis, H. Lichtenfeld, F. Caruso, V. I. Popov,

H. Mohwald, *Polym. Adv. Technol.* **1998**, 9, 759.

43. G. B. Sukhorukov, M. Brumen, E. Donath, H. Mohwald, *J. Phys. Chem. B* **1999**, 103, 6434.

Chapter 7: Conclusions & Future work

7.1 Conclusions

In this dissertation, the motion of polymeric microparticles at interfaces and in solution has been studied and characterised through experimental trials and computational modelling. The main contributions are:

- Demonstrating the potential to produce devices that can follow concentration gradients for a wide range of signalling chemicals in addition to rapid and autonomous accumulation at high (or low) concentration regions via predicating the behaviour of hypothetical pH-responsive catalytic swimmers modelled based on the parameters obtained from the experimental data.
- Developing a new method for navigating polymeric self-diffusiophoretic microswimmers via control of the orientation of the particles using an external magnetic field and reporting the progress made towards an autonomous technique for steering magnetic catalytic swimmers via customized magnetic entrapment.
- Discussing the ability of specially fabricated colloidal microswimmers which have an inherent spin, to be utilised as nanoscale and microscale mixing devices.
- Examining various methods for fabricating polymeric structures with high surface areas, with the aim of increasing the area at which chemical reactions takes place on the catalytic microswimmers.
- Physically realising a computational simulation that demonstrated the capability of highly adhesive regions located on a non-adhesive substrate in deviating elastic particles from their path and investigating the potential of this ability in developing a method for separating microparticles based on their mechanical

stiffness and their adhesion to the surface, whilst also offering insight into the field of cell-rolling and other related biomimetic systems.

7.2 Future work

The most apparent and pressing future work arising from these outcomes are discussed below:

7.2.1 Chapter 2: fabricating pH-responsive catalytic devices

Although the results obtained from computational modelling were encouraging, experimental attempts for fabricating pH-responsive catalytic devices were unsuccessful due to the detachment of the Pt layer deposited on the surface of the particles after their expansion in water. Another idea for coupling a catalytic module and a size changing module in a swimming device is depositing the catalyst on a rigid core particle prior to growing a pH-responsive polymer on its surface. For example, Ma, et al. [1] have developed a method for fabricating dual responsive particles with a magnetite core and a PMAA shell. Evaporating Pt onto the rigid core of these particles prior to polymerising MAA on their surface, may potentially lead to formation of Janus particles with one half acting as a catalytic module and the other half acting as the pH-responsive module.

7.2.2 Chapter 3: fabrication and navigation of magnetic catalytic swimmers

Although controlling the orientation of Janus magnetic microswimmers via an external magnetic field generated by a pair of Helmholtz coils was proven to be efficient, a considerable number of magnetic swimmers did not respond to the magnetic field in a predictable manner due to the instability of the magnetic

alignment introduced to their uniform and continuous Ni layer. Baraban, et al. [2] have recently reported that a more stable alignment on the magnetic cap of Janus particles can be obtained by evaporating *ultrathin magnetic multilayers* (consisting of [Co/Pt(Pd)] stacks) onto the particles prior to the Pt deposition. It would also be very interesting to observe the behaviour of magnetic swimmers with [Co/Pt(Pd)] stacks on their surface, propelling on the magnetic microcoils developed by Ramadan, et al. [3].

7.2.3 Chapter 4: Mixing efficiency of spiralling catalytic swimmers

While the results of this chapter demonstrated the potential ability utilising spiralling swimmers of as microscale mixing devices, further experiments can be conducted by studying the motion of these particles in microfluidic channels with co-current and countercurrent fluid streams to investigate their mixing efficiency at different flow rates, as well as further studies of the effect of fuel concentration.

7.2.4 Chapter 5: Utilising high surface area porous polymeric particles in fabricating catalytic swimmers

Another method to increase the surface area in catalytic devices is to deposit the catalyst onto initially porous polymeric microparticles. A comprehensive guide to synthesis, characterisation, functionalisation and applications of these particles has been published by Gokmen, et al. [4] including an interesting method developed by Fujibayashi, et al. [5] for fabricating hollow “golf ball-like” polymeric particles with a low density and a high surface area. It should also be noted that consideration to the deposition method will also have to be investigated as e-beam Pt evaporation results in deposition taking place in a "line-of-sight" and so only part of a porous surface

would be coated. Instead a coating method with a more diffuse direction for the coating metal should be employed such as DC or RF sputtering.

7.2.5 Chapter 6: Separation of polymeric microspheres via surface interactions

Although the data obtained from rolling LbL microcapsules on surfaces functionalised with hydrophobic and hydrophilic alkanethiols demonstrated a clear difference in rolling velocities on these substrates, no significant trajectory deviation was observed in particles rolling on the patterned substrates. As this might be due to the contamination originated from the UV patterning stage, further trials should be conducted in a clean room with minimum contamination. Determining the rolling velocity for a set of microcapsules with a narrow size distribution can also give us a better insight of the behaviour of these particles on substrates with different surface chemistries.

References:

1. W. Ma, S. Xu, J. Li, *J. Polym. Sci. A Polym. Chem.* **2011**, 49, 2725-2733.
2. L. Baraban, D. Makarov, R. Streubel, O. G. Schmidt, *ACS Nano*, **2012**, 6, 3383.
3. Q. Ramadan, V. D. Samper, D. P. Poenar, C. Yu, *J. Microelectromechanical Sys.* **2006**, 15: 624-638.
4. M. T. Gokmen, F. E. Du Prez, *Prog. Polym. Sci.* **2012**, 37, 365-405.
5. T. Fujibayashi, Y. Komatsu, N. Konishi, H. Yamori, M. Okubo, *Ind. Eng. Chem. Res* **2008**, 47, 6445-9.

Appendices

A. CCD Camera

The images and videos used in our research for studying the properties of fabricated particles and tracking their motion on the surface and in the bulk were captured using CCD cameras installed on an inverted microscope. A charge coupled device (CCD) is a sensor that converts light into electrons. A CCD chip can be described as a 2D array with millions of micron sized solar cells. Each cell accumulates an electric charge proportional to the intensity of light at its location. Following the conversion of light into electrons in cells, the accumulated charge of each cell is read by a sensor then the charge is transported across the chip to where it is read by the CCD at one corner of the array. Next, the accumulated charge value of each cell (a pixel) is converted to a digital value via an analog-to-digital (ADC) convertor. An ADC converts the input analog current or voltage generated in the pixels to digital numbers proportional to their magnitude. By connecting the CCD camera to a computer via a PCI card, the digital values can then be converted to digital images using appropriate software. For capturing images in low light conditions, typically in high magnifications, CCD cameras use an amplifier called gain. The gain increases the slope of the CCD signal and the light intensity graph resulting a brighter image. Unfortunately, brightness amplification via increasing the gain also increases the noise in the captured images therefore too high gain results saturation of the pixels to the maximum value causing loss of information required for image generation.

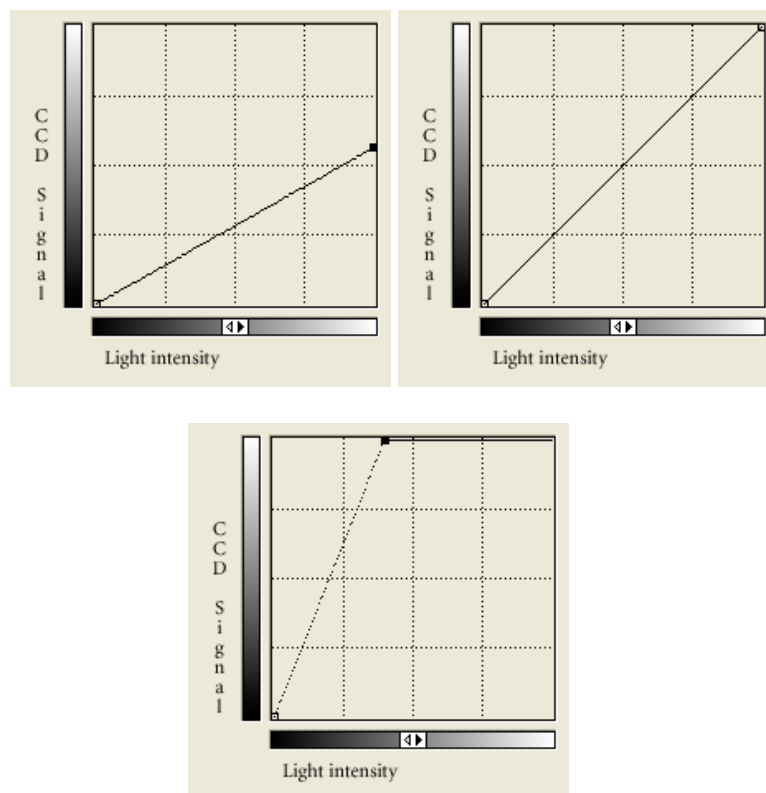


Fig. A1. Graph of the light intensity vs. the resulting pixel value (a) without gain (b) optimum gain (c) excessive gain

B. UV spectroscopy: decomposition reaction of H_2O_2 in presence of Ni and Pt

Base on a paper by Shu-Sung Lin *et al.* [Chapter 3, Ref. 42], nickel is a catalyst for the decomposition reaction of hydrogen peroxide but no propulsive motion was seen in particles with a nickel cap on their surface even in a 10% w/w solution of hydrogen peroxide in water. Therefore an experiment was conducted to compare the decomposition reaction rate of hydrogen peroxide in presence of nickel and platinum. In this experiment two glass cover slips (2×2 cm) were coated with equal thicknesses of Ni and Pt (10 nm) and immersed into glass vials containing 10% hydrogen peroxide solution in water. At different time intervals, 2 ml samples were pipetted out of the vial and their hydrogen peroxide content was measured using UV

spectroscopy. After 300 minutes nearly all of the hydrogen peroxide in the vial with the Pt covered sample was decomposed where in the vial with the Ni coated sample, the initial concentration of hydrogen peroxide was maintained.

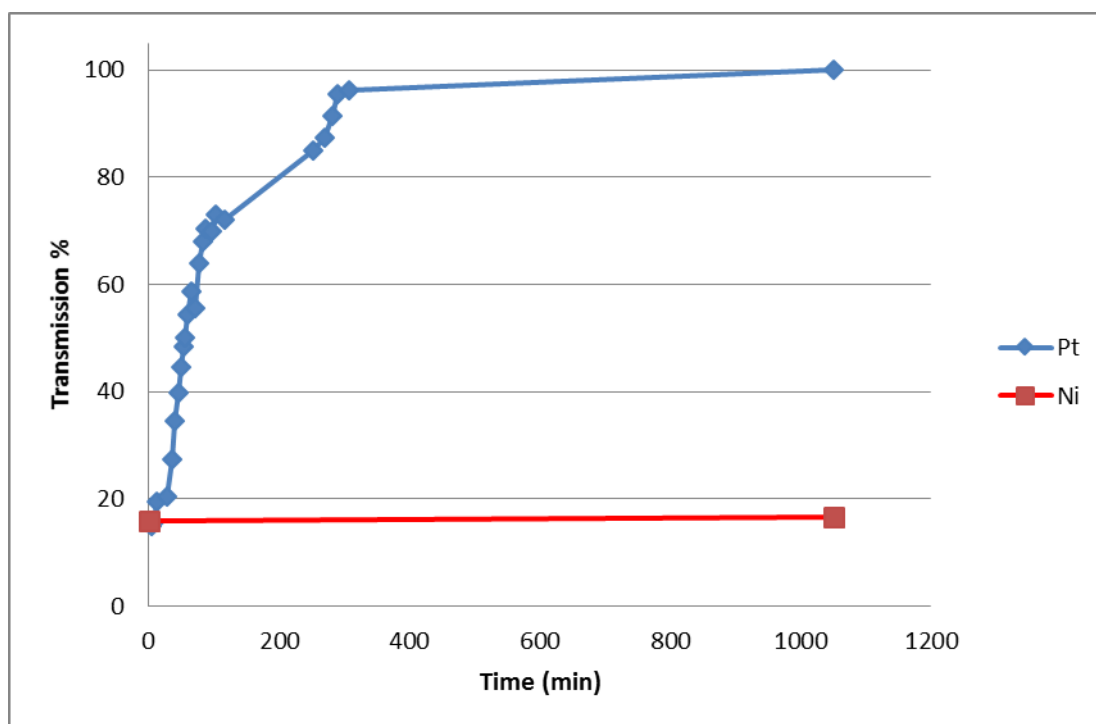


Figure A2. UV transmission graph for the decomposition reaction of hydrogen peroxide in presence of Ni and Pt

C. Particle sizing: DLS and laser diffraction technique

Dynamic light scattering (DLS) is a technique used for determining the size distribution profile of micro and nano scale particles in a suspension.¹ When light hits small particles it scatters in all directions. In case of using a coherent, monochromatic light source (a laser beam) as the light source, we will be able to observe the time-dependent fluctuation of the scattered beam. These fluctuations occur as a result of the Brownian motion of the particles suspended in the solution. The scattered light can interfere either destructively or constructively with other

particles in the solution and within fluctuation of its intensity, information is collected via a detector about the time scale of random movements of the particles.

The application of DLS in most scientific and industrial projects is limited as a result of multiple scattering where the light beam is scattered multiple times by the particles in the solution before collection at the detector. This decreases the accuracy interpretation of the obtained results particularly where samples consist of particles with large diameters with a high refractive index contrast. Although the mentioned issue limits the applications of DLS, this technique can be efficiently used for determining the size distribution of particles with small diameters suspended in dilute solutions.

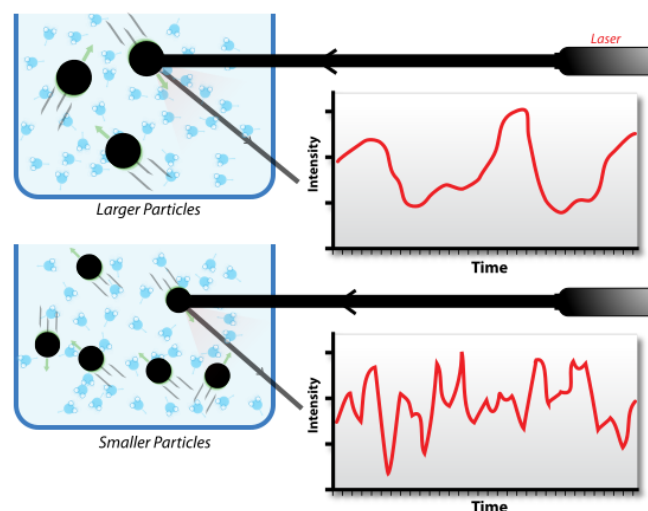


Fig. A3. Hypothetical dynamic light scattering of two samples: Larger particles on the top and smaller particle on the bottom

D. Fluorescence microscopy

Fluorescence happens when a substance absorbs a certain wavelength of light and emits a light with a different wavelength. Generally, the substance decreases the energy of the absorbed wavelength and emits a light with a longer wavelength.

In fluorescence microscopy, the sample is illuminated with a monochromatic light, generated via passing light through an excitation filter, causing fluorescence emissions in the sample, and then the emitted light by the sample is collected via a detection filter to ensure the excitation light does not reach the detector which could be an eyepiece or a CCD camera.

There are fundamental differences between the light generated in transmission or reflection microscopes (using differential interference and phase contrast techniques) and fluorescence microscopes. However, these techniques can be employed simultaneously and the generated data by one technique can improve the quality and accuracy of the data generated using other techniques.

In most fluorescence microscopes, observation and excitation of the sample takes place above the sample therefore they are called epifluorescence microscopes (-epi: above). In these microscopes the light that excites the sample is passed onto it through an objective lens and the emitted light reflected from the sample is also focused to the detector via the same objective after filtration of the reflected excitatory light by the detection filter.

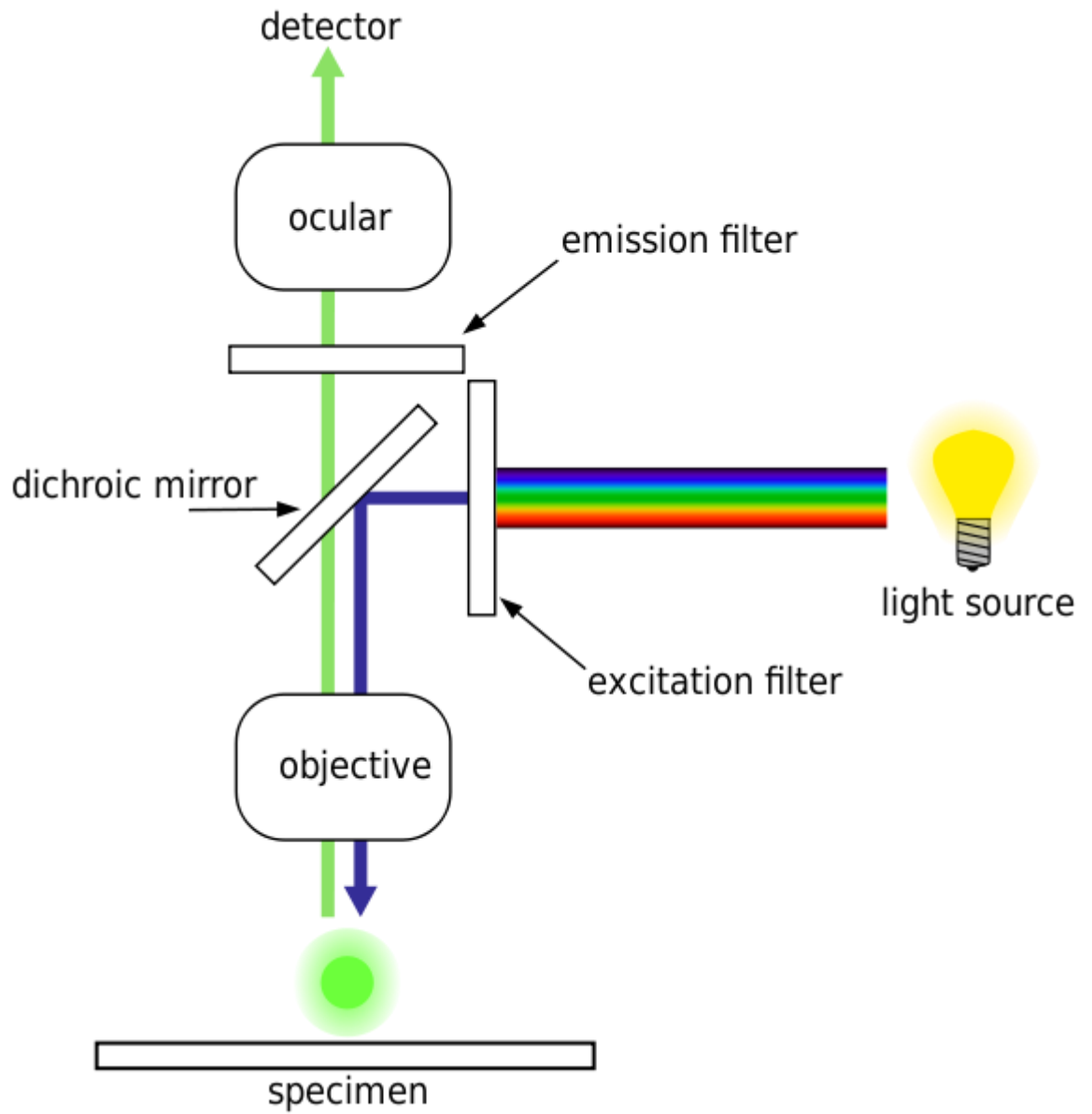


Figure A4. Schematic diagram showing different components of a fluorescent microscope